Applications of the virtual fields method to the mechanical behaviour of rubbers under dynamic loading

Sung-ho Yoon

Pembroke College

University of Oxford

A thesis Submitted for the degree of

Doctor of Philosophy

Hilary Term 2016

Applications of the virtual fields method to the mechanical behaviour of rubbers under dynamic loading

Sung-ho Yoon, Pembroke College, University of Oxford

For the degree of D.Phil. in Engineering Science, Hilary Term 2016

Experimental techniques for measuring the mechanical response of rubbers under dynamic loading are developed utilising the virtual fields method (VFM), to inversely identify constitutive behaviour from experimental observations. Rubbers and other 'soft' materials are difficult to characterize using traditional dynamic techniques such as the split Hopkinson bar: the low sound speed makes it difficult to achieve static equilibrium and the small supported forces give low signal-to-noise ratios in the experimental data. In this research, the dynamic VFM with the aid of high-speed imaging is applied to dynamic tensile experiments to resolve these difficulties. The VFM is a mathematical technique that makes use of the principle of virtual work. Manipulation of this equation enables us to remove the need for traditional force measurement, instead exploiting acceleration full-field data as a virtual load cell. Thus, the aforementioned difficulties are no longer of concern: the technique requires that the specimen is not in static equilibrium and that inertial forces are significant compared to material forces. Two dynamic tests and dynamic VFMs are developed and applied to tensile drop-weight and gas-gun driven experiments. The first uses small amplitude dynamic deformation superposed on static pre-stretching. Dynamic identifications at a number of pre-strains are collated to identify the complete nonlinear behaviour. The second utilizes a large strain amplitude of dynamic loading: one experiment characterizes the full response. Further applications of the dynamic VFM are explored in order to improve the first method and to extend the identification capability, and experiments performed at non-ambient temperatures allow a preliminary exploration of time-temperature superposition.

CONTENTS

ACKNOWLEDGEMENT

This research project has been funded by the Air Force Office of Scientific Research, Air Force Material Command, USAF, under grant number FA8655-12-1-2015.

All of my research outcomes could not have existed if Prof. Clive Siviour, my supervisor, have not given me extremely wise guidance. His supervising is always useful and creative; his advices permeated every chapters of my thesis. I am very lucky that he is my supervisor for my DPhil research. I greatly thank Prof. Fabrice Pierron of the University of Southampton for his advice. His critical view and interest on my work have improved many parts of my work. I would like also to thank S Fuller and JL Jordan of AFOSR and M Snyder and R Pollak of EOARD for their support.

I sincerely thank Richard Froud, Richard Duffin, Andy Bateman and Neil Warland for their technical support. Without them, it would not have been possible to materialize my idea. I thank Dr. Ioannis Giannakopoulos for his academic advice and training. Discussions that I had with you helped me understand the aim of my research. I would like to thank Dr. Igor Dyson for his continuous help and training for some experimental equipment. I thank for all members (Dr. Xuegang Tang, Yongchao Huang, Laure Bonfils, Heather Wilson and James Cook) of my supervisor's group. The conference in Swiss with you all is a great memory to me. I also thank Mahdi Mahmoud whose expertise was essential for my experimental work. In addition, I must thank Dr. Tae-Sung Jun of Imperial College, who have led me to have this DPhil opportunity.

Finally, I thank my father and mother who give me endless love, trust and support during my study. I thank my beloved girlfriend, Thorrung Charoensukawatana. The memory that I have with you in London and Oxford has been a great strength to me through my studying in the UK. I could not have done this research without them.

PUBLICATIONS

Journal articles

Yoon, S., Giannakopoulos, I. & Siviour, C.R., 2015. Application of the Virtual Fields Method to the uniaxial behavior of rubbers at medium strain rates. *International Journal of Solids and Structures*, pp.1–16.

Yoon, S., Winters, M. & Siviour, C.R., 2015. High Strain-Rate Tensile Characterization of EPDM Rubber Using Non-equilibrium Loading and the Virtual Fields Method. *Experimental Mechanics*.

Conferences

Yoon, S. & Siviour, C.R., 2015. The dynamic Virtual Fields Method on rubbers at medium and high strain rates E. Cadoni, ed. EPJ Web of Conferences, 94, p.01017.

Yoon, S. & Siviour, C.R., 2014. The virtual fields method to elastomeric materials under dynamic loading. In *16th International Conference on Experimental Mechanics. Cambridge*.

Yoon, S. & Siviour, C.R., 2013. The virtual fields method to the uniaxial mechanical behaviour of hyperelastic materials at medium strain rate. In *21st DYMAT Technical Meeting. London*.

NOTATIONS

Symbols and abbreviations commonly used throughout the present thesis are introduced here. Some symbols are redefined with respect to the content of each chapter.

$\mathbf{x}_0$: vector of an undeformed configuration coordinate

x_0, y_0, z_0: components of $\mathbf{x}_0$ of an undeformed configuration coordinate

$\mathbf{x}_{p0}$: vector of a pre-stretched configuration coordinate

x_{p0}, y_{p0}, z_{p0}: components of $\mathbf{x}_{p0}$ of a pre-stretched configuration coordinate

$\mathbf{x}_p$: vector of a current configuration coordinate after pre-stretching

x_p, y_p, z_p: components of $\mathbf{x}_p$ of a current configuration coordinate after pre-stretching

$\mathbf{x}$: vector of a deformed configuration coordinate

x, y, z: components of $\mathbf{x}$ of a deformed configuration coordinate

(In some chapters, $\mathbf{x}_0$ is used instead of $\mathbf{X}$)

$\mathbf{F}$: deformation tensor

$\mathbf{I}$: second-order unit tensor

$\mathbf{C}$, $\mathbf{B}$: right and left Cauchy-Green tensor

t: time

Δt: time increment

ρ: current density

ρ_0: initial density

$\boldsymbol{a}$: acceleration vector

$\mathbf{b}$: body force vector

$\boldsymbol{v}$: velocity vector

$\boldsymbol{u}$: displacement vector

$\boldsymbol{u}^*$: virtual displacement vector

$\boldsymbol{u}_0^*$: virtual displacement based on an initial coordinate

$\boldsymbol{u}_{p0}^*$: virtual displacement based on a pre-stretched state

$\boldsymbol{u}_p^*$: virtual displacement based on a current pre-stretched state

λ: principal stretch ratio

λ_{p0}: principal stretch ratio of a pre-stretched state

λ_p: total principal stretch ratio when pre-stretching is considered

$d\lambda_p$: incremental principal stretch ratio with respect to a pre-stretched state

$\boldsymbol{e}$: nominal(engineering) strain tensor

$\boldsymbol{e}_{p0}$: nominal(engineering) strain tensor of a pre-stretched state

$\boldsymbol{e}_p$: total nominal(engineering) strain tensor when pre-stretching is considered

$\boldsymbol{\varepsilon}$: true strain tensor

$\boldsymbol{\varepsilon}_{p0}$: true strain tensor of a pre-stretched state

$\boldsymbol{\varepsilon}_p$: total true strain tensor when pre-stretching is considered

$d\boldsymbol{\varepsilon}_p$: incremental true strain tensor with respect to a pre-stretched state

$\boldsymbol{\varepsilon}^*$: virtual true strain tensor

$\boldsymbol{\varepsilon}_0^*$: virtual strain based on an initial coordinate

$\dot{\boldsymbol{\varepsilon}}$: true strain rate

J: volume ratio

V_0 & v: initial and current volumes

S_0 & s: initial and current surface areas

s_f and s_u: surface area where force and displacement are prescribed

$S_{0,f}$: initial loaded surface

s_{p0}: initial surface area after pre-stretching

s_p: current surface area after pre-stretching

W: width

L: length

L_0: initial length

L_{p0}: length after pre-stretching

L_p: current length after pre-stretching

h: thickness

$\boldsymbol{\sigma}$: Cauchy (true) stress tensor

$\boldsymbol{\sigma}_{p0}$: Cauchy (true) stress tensor due to pre-stretching

$d\boldsymbol{\sigma}_p$: incremental Cauchy (true) stress tensor with respect to a pre-stretched state

$\mathbf{N}$: nominal (engineering) stress tensor

$d\mathbf{N}$: incremental nominal stress tensor

$d\mathbf{N}_{p0}$ & $d\mathbf{N}_p$: push forward terms of $d\mathbf{N}$ to initial and current pre-stretched states

$\mathbf{\Pi}$(PK1): the first Piola-Kirchhoff stress tensor

$\mathbf{S}$(PK2): the second Piola-Kirchhoff stress tensor

W: strain-energy density function

$d\mathbf{f}$: Infinitesimal force acting on the element surface

$\boldsymbol{n}$: normal vector of a current element surface

$\boldsymbol{N}$: normal vector of an initial element surface

p: hydrostatic pressure

E: Young's modulus

NE: nominal modulus

v: Poisson's ratio

G: shear modulus

K: bulk modulus

μ: Ogden model parameter (for the one-term Ogden: $G = \mu$)

α: Ogden model parameter

η: viscosity

τ: relaxation time

exp(·): exponential function

$g(t)$: normalized relaxation function

g_i: normalized modulus

Z: acoustic impedance

δ: phase lag

ω: frequency

Temp: temperature

a_T: shifting factor

E': storage modulus

E'': loss modulus

GR: grey(intensity) level of images

Φ: cost function

T: traction vector

l_f: loaded boundary for a 2D case

Q: plane-stress stiffness matrix

H: displacement interpolation matrix

B: strain-displacement matrix

$\tilde{\boldsymbol{u}}^*$: piecewise virtual displacement field

$\mathfrak{R}$: scalar zero-mean stationary (second order) Gaussian distribution

γ: amplitude of a strain measurement uncertainty

$V(\cdot)$: variance operator

ψ_i: element i^{th} location

P: transformation matrix

div & Div: divergence operators based on current and initial configuration

D: elasticity tensor

DMA: dynamic mechanical analysis

SHPB: split Hopkinson pressure bar

SHTB: split Hopkinson tension bar

TTSP: time-temperature superposition principle

VFM: virtual fields method

DIC: digital image correlation

fps: frame per second

FEM: finite element model

FEMU: finite element model updating

PVW: principle of virtual work

PVF: piecewise virtual field

VFM1: the linear VFM in Chapter 5

VFM2: the linear VFM in Chapter 7

NVFM2: the nonlinear VFM in Section 8.2

Chapter 1 INTRODUCTION

1.1 Motivation

In the context of dynamic testing, a material is often described as ‘soft’ if it has low stiffness at room temperature. One particular class of soft materials is elastomers, which consist of long, flexible molecular chains of high molecular weight, with a relatively low cross-link density. In a stress-free state, an individual chain takes a random coiled conformation; when tensile forces are applied, stretching of the coiled chains between cross-links permits high extensibility, usually accompanied by low modulus. The material response may also exhibit time-dependence, a characteristic which is known as viscoelastic behaviour.

These characteristics of elastomers have been utilized in various engineering fields. One of the common uses of elastomers is in tyre production. The usual requirements of tyres for a vehicle are to carry load with well-controlled damping and long dimensional stability. Elastomers are uniquely suited to this function: the high elasticity provides a good flexibility, and the viscoelastic characteristic enables dissipation of unwanted vibration (Rodgers and Waddell, 2005). The dissipation capability of elastomers can be also utilized as an energy absorption substance in other loading scenarios. This function is of particular interest for impact protection. One application is elastomeric coatings on concrete masonry unit walls. The elastomer layer can reduce the amount of fragmentation of a wall when it is subjected to an impulsive load (e.g. air blast from a bomb). This reduces the possibility of serious injury of occupants (Porter et al., 2002). The effect of the elastomer layer is shown in Figure 1.1 showing the comparison between the pure (left) and coated (right) masonry walls after blast loadings.

In these applications, elastomers are often subject to dynamic loading. The strain rate of the elastomer coating layer of masonry walls can reach the order of 100 s^{-1} (Davidson

et al., 2005). The mechanical behaviour of elastomers is very sensitive to deformation rate even between so-called static rates (Sarva et al., 2007). Understanding this dynamic behaviour of elastomers is important to not only achieve cost-effective use of the materials but also ensure a targeted safety level. These two aspects can be achieved by appropriate engineering design, but engineering design cannot be reliable unless material behaviour in the service conditions is well understood. Thus, it is clear that the mechanical characterization of elastomers over a wide range of strain rates is essential.

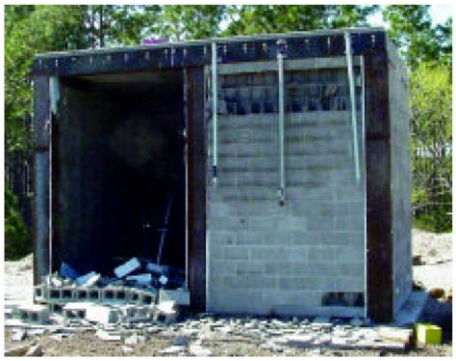

Figure 1.1 Non-coated (left) and rubber coated (right) masonry walls after blast loadings (Porter et al., 2002)

1.2 Objectives

The overall objective of this thesis is to characterize the mechanical behaviour of elastomers under dynamic loading. More precisely, the aim of this research is to develop experimental techniques able to measure physical parameters which define the stress-strain relationship of elastomers at high strain rates. Dynamic mechanical properties of elastomers have been studied using many experimental methods, which are mainly extensions of the split Hopkinson bar technique. Although efforts have been made to modify this technique for soft materials, there are still limiting factors such as a long duration at the start of the experiment in which the specimen is not in a state of static equilibrium and high noise-to-signal ratio. The limitations of the current experimental techniques will be further discussed in the next chapter.

This thesis proposes an entirely different approach from the split Hopkinson bar. The development of the proposed methods is based on the combination of two modern experimental techniques: full-field measurement and inverse identification methods for mechanical parameters. A full-field measurement method is a technique to capture experimental data from a particular region over two or three dimensions. Modern high-speed cameras are able to capture images at a very small time scale in a digitized form, in which image patterns are segmented in a digital image unit, a ‘pixel’; one advantage of digital photography over film is that distortions between images are more repeatable and therefore can, if necessary, be characterised and corrected. An imaging processing technique, so called digital image correlation (DIC) (Sutton et al., 2009), is able to analyse digitized intensity patterns, and provides deformation measurement points at a large number of independent points. The availability of this full-field deformation data allows the application of one of the inverse parameter identification methods, the Virtual Fields Method (VFM) (Pierron and Grédiac, 2012). The VFM provides the link between experimental observations and unknown constitutive parameters. It is therefore the main objective of this research to characterize dynamical stress-strain relationships of rubbers with the application of the VFM on full-field deformation data produced by high-speed experiments.

Chapter 2 BACKGROUND

Elastomer (or rubber) is defined in ASTM D 1566 (ASTM International, 2014) as “a material that is capable of recovering from large deformations quickly and forcibly”. Mechanical properties of elastomers, their constitutive relations and characterization methods are numerous and vary considerably, reflecting the range of properties and engineering applications. Dynamic mechanical properties of elastomers are of particular interest in the present thesis as they are experimentally difficult to characterize due to the low modulus; in this context often called ‘soft’. The experimental techniques developed in this thesis are not restricted only to elastomers but also to other elastomer-like material, including many biomaterials. This chapter provides a background to the mechanical behaviour of elastomers and representative constitutive models. Existing experimental techniques for elastomers are introduced with their limitations. The VFM is also introduced with regard to the definition and current state of this technique. There will be an explanation of how the current experimental limitations can be overcome by means of the VFM. Then, this chapter ends with a summary providing an overall description of the researches presented in the rest of the thesis.

2.1 Elastomers

2.1.1 Mechanical behaviour

Two of the most important mechanical properties of elastomers are high deformability and low stiffness at room temperature. An example of this typical behaviour is shown in Figure 2.1. The high deformability is mainly attributed to the large extensibility of long-chain molecules which initially exist in a randomly coiled chain due to free rotation of bonds. The randomly coiled state is stable as Brownian motion allows the freely jointed chain to recoil into a state of maximum entropy, i.e. the state that allows the chain to assume the largest number of conformations (Treloar, 1975), which then minimises the

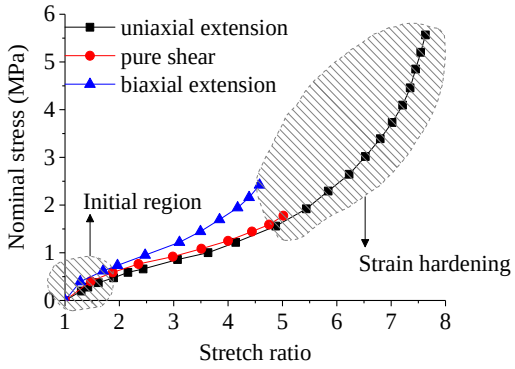

Figure 2.1 Stress-strain curve of a typical rubber (reproduced from Treloar (1944)).

Gibbs free energy at a given temperature. This entropic behaviour is the driving force for the mechanical reversibility of elastomers.

Stress-strain relations of elastomers are generally nonlinear over all strain ranges. Figure 2.1 shows typical stress-strain curves for elastomers under three different modes of loading. The linear region is very short or ambiguous. The modulus (tangent slope) generally decreases with increasing strain in the initial strain region; then, there is a transition to an upward curvature as the chain reaches its maximum extensibility (Arruda and Boyce, 1993). For some elastomers, e.g. natural rubber, the main contribution to this hardening is strain-induced crystallization (Toki et al., 2002).

In many elastomers, the degree of nonlinearity is rate dependent. One example of this rate dependency is shown in Figure 2.2. The curves at two strain rates are initially

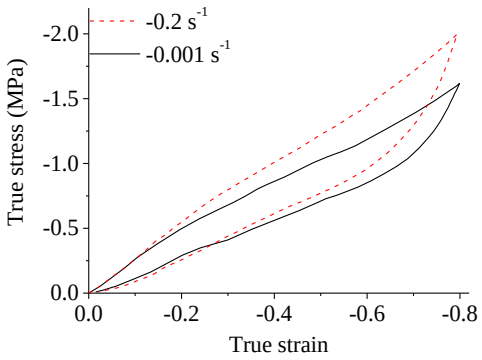

Figure 2.2 Rate dependency of an elastomer (reproduced from Bergström & Boyce (1998)).

coincident and, at about -0.2 strain, the curve with the higher strain rate exhibits stiffer behaviour with a steeper upward curve. It should be noted that although the strain rates of these two curves are still within what is often described as the 'quasi-static' rate regime (Field et al., 2004), their mechanical behaviour is clearly different. The rate sensitivity of elastomers is even more significant when comparing between high and quasi-static strain rates.

The rate dependency is related to stress relaxation behaviour in the material, which is defined as a gradual decrease in stress with time at a fixed strain. This relaxation behaviour of an elastomer is provided in Figure 2.3(a) showing a reduction in stress when deformations are interrupted for about 100 s. A longer relaxation test is given in Figure 2.3(b) where the gradual decrement of stress at a fixed strain is shown against time. The relaxation occurs over a large time range and becomes clear using a logarithmic time scale. The relaxation process can be envisaged as time-dependent motion of a free polymer chain which is topologically constrained by a molecular network. At a high enough global deformation rate, the free chain is affinely strained with the network. However, if the deformation is fixed or applied slowly, there is sufficient time for the chain to move slowly to a more relaxed conformation (Bergström and Boyce, 1998).

The mechanical behaviour of elastomers is very temperature-dependent. However, the temperature dependency is different from that of other materials (e.g., metals) due to the

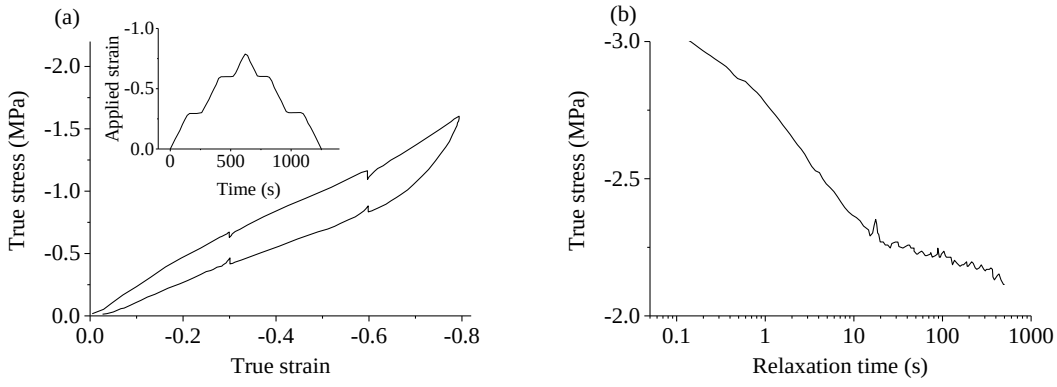

Figure 2.3 Relaxation tests of an elastomer (reproduced from Bergström & Boyce (1998)).

inherent entropic behaviour (Holzapfel, 2000). This is illustrated in Figure 2.4(a), where it is seen that the slope of the stress-temperature plot is reversed above 6 % stretch, the thermoelastic inversion point (Anthony et al., 1943). The inversion point can be also observed in Figure 2.4(b) where the stress-strain relations are replotted from the data at 20 and 70 °C in Figure 2.4(a). This behaviour can be understood in the way that a highly extended chain more stiffly responds to Brownian motion agitated by increased temperature than a loosely coiled chain. However, this observation does not mean that all elastomers are purely entropic for all situations. In fact, the behaviour is governed by a complex combination of both energetic and entropic interactions (Treloar, 1975). For some elastomers (e.g. thermoplastic rubber) or environments (e.g. crystallization at low temperatures), the contribution of the internal energy change can be more significant than the entropic interactions (Petrović and Ferguson, 1991; Rey et al., 2013).

Elastomers exhibit several inelastic behaviours. The first usual inelastic characteristic is mechanical hysteresis as shown in Figure 2.2 in which the stresses are lower for unloading. The main contribution to the hysteresis is the van der Waals forces between molecular chains; for this reason, the amount of the hysteresis is dependent on deformation (Holt, 1931; Treloar, 1975) and temperature (Kar and Bhowmick, 1997). Another usual inelastic behaviour is stress softening, the so called Mullin's effect

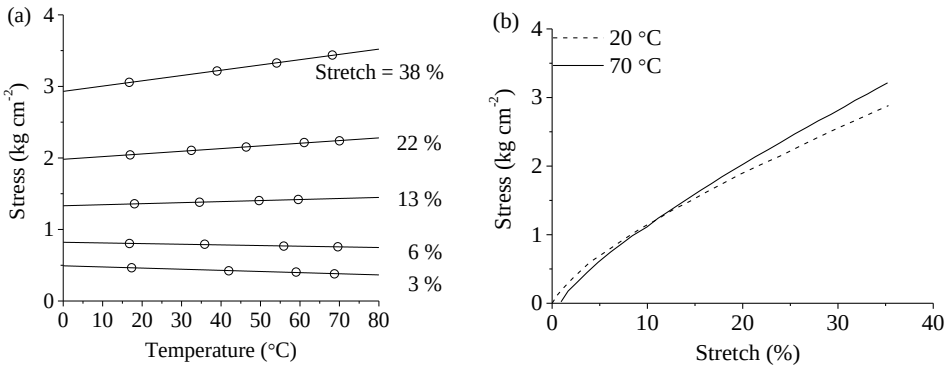

Figure 2.4 (a) Stress measurements at several deformations along temperature and (b) stress-strain relations at 20 and 70 °C (reproduced from Anthony et al. (1943)).

(Mullins, 1948). The softening can be observed for a freshly vulcanized elastomer when subjected to successive load-unload cycles. It is known that many mechanisms are involved in this softening such as chain slipping and interfacial breakage between elastomer molecules and fillers (Diani et al., 2009); however, it is not fully understood.

2.1.2 Constitutive relations

A constitutive relation can be defined as a mathematical relation describing the stress in a material as a function of applied conditions (such as strain, strain rate, temperature and time) and one or more constants which are unique to the material itself. It is these constants which we wish to characterise. It is possible to describe the stress-strain relationship of elastomers by a suitable constitutive relation. The nonlinear elastic behaviour of elastomers at large strains is described by hyperelastic models. This class of models may be divided into two groups: physically motivated (statistical) and phenomenological approaches (Treloar, 1975). The former aims to relate the deformation mechanism to the underlying microscopic structure, whilst the latter is only able to describe the observed behaviour without the consideration of the underlying mechanisms. If the structure and its physical process are known, a proper statistical model is usually able to fit the stress-strain relation with a smaller number of parameters (Boyce and Arruda, 2000). However, it can be difficult to precisely know the material structure and its evolution in various service environments. For this reason, phenomenological models are still widely applied in industry and commercial FEM codes due to their ease of use. It is a main concern of this thesis to experimentally observe the phenomenological behaviour of elastomers under dynamic loading. Thus, the scope of this section is limited to the phenomenological models. However, the techniques introduced in the present thesis could also be applied to deriving constants, or performing validation experiments, for physically based models if desired.

Prior to introducing the models, it is necessary to give the definition of strains and stresses in a continuum for large deformations. First, large deformations clearly distinguish the undeformed (initial) and deformed (current) coordinate systems. These two coordinates are described in Figure 2.5. The initial and current coordinates are respectively denoted $\mathbf{x}_0$ and $\mathbf{x}$. The relationship between them is given by the displacement field $\mathbf{U}$

$$\mathbf{x} = \mathbf{x}_0 + \mathbf{U} \tag{2.1}$$

The deformation gradient is a primary measurement of deformations in nonlinear mechanics and defined as

$$\mathbf{F} = \mathbf{I} + \mathrm{Grad}\mathbf{U} = \mathrm{d}\mathbf{x} / \mathrm{d}\mathbf{x}_0 \tag{2.2}$$

where $\mathbf{I}$ is the second-order unit tensor and 'Grad' denotes the gradient with respect to the initial configuration. A frequently used strain tensor based on the initial and current configurations can be defined using $\mathbf{F}$ according to

$$\mathbf{C} = \mathbf{F}^{\mathrm{T}}\mathbf{F} \tag{2.3}$$

$$\mathbf{B} = \mathbf{F}\mathbf{F}^{\mathrm{T}} \tag{2.4}$$

and respectively called the right and left Cauchy-Green tensor. Another useful definition of deformations is the principal stretch ratios, λ_i (i = 1, 2, 3), which are the eigenvalues of $\mathbf{F}$. This definition is very useful for describing experimental data. If the loading and

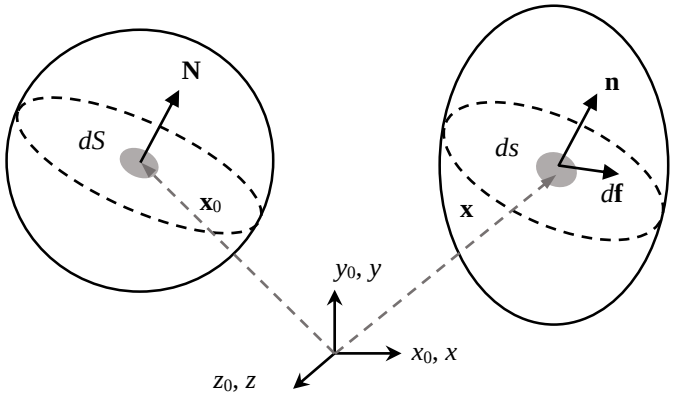

Figure 2.5 Initial and current configurations of a continuum body.

principal directions are matched and, for example, λ_1 can be a stretch ratio that is in the direction of a uniaxial loading, it is possible to define deformation terms as follows

$$e_1 = \lambda_1 - 1 \tag{2.5}$$

$$\varepsilon_1 = \ln(1 + e_1) \tag{2.6}$$

These can be referred to as uniaxial engineering (nominal) and true (logarithmic) strains. In addition, the volumetric deformation is defined by **F** as

$$J = \det(\mathbf{F}) \tag{2.7}$$

where J is known as the Jacobian determinant or volume ratio between the initial dv and current dV_0 volume elements, $J = dv / dV_0$. In fact, J is one of the principal scalar invariants of **F**. The other invariants are defined as

$$I_1(\mathbf{F}) = \lambda_1^2 + \lambda_2^2 + \lambda_3^2 \tag{2.8}$$

$$I_2(\mathbf{F}) = \lambda_1^2\lambda_2^2 + \lambda_2^2\lambda_3^2 + \lambda_3^2\lambda_1^2 \tag{2.9}$$

The stress definitions are distinguished by the coordinate system. We define d**f** as the infinitesimal force acting on the current elemental surface ds with its normal vector $\boldsymbol{n}$ in the current configuration. These two terms are denoted as dS_0 and $\boldsymbol{N}$ in the initial configuration. With respect to these terms, three stress tensors are defined as follows:

the Cauchy stress, $\boldsymbol{\sigma}$

$$\frac{d\mathbf{f}}{ds} = \boldsymbol{\sigma n} \tag{2.10}$$

the first Piola-Kirchhoff stress, $\boldsymbol{\Pi}$

$$\frac{d\mathbf{f}}{dS_0} = \boldsymbol{\Pi N} \tag{2.11}$$

the second Piola-Kirchhoff stress, **S**

$$\frac{d\mathbf{f}_0}{dS_0} = \mathbf{S}\boldsymbol{N} \tag{2.12}$$

where $d\mathbf{f}_0 = \mathbf{F}^{-1}d\mathbf{f}$. These stresses can be defined by the three principal stretch ratios; their component forms for incompressible hyperelastic models are written as (Holzapfel, 2000)

$$\sigma_i = -p + \lambda_i \frac{\partial W}{\partial \lambda_i} \quad (i = 1, 2, 3) \tag{2.13}$$

$$\Pi_i = \sigma_i / \lambda_i \tag{2.14}$$

$$\mathrm{S}_i = \sigma_i / \lambda_i^2 \tag{2.15}$$

where p is a hydrostatic pressure and W is a strain-energy function. It should be mentioned that the engineering stress $\mathbf{N}$ (or often referred to as the nominal stress) is defined as $\mathbf{N} = \mathbf{\Pi}^{\mathrm{T}}$ by the definition given by Ogden (1984).

A mathematical expression of this scalar function $W(\mathbf{F})$ is the basis of deriving phenomenological hyperelastic models. Representative classical forms of W are summarized below. These are all incompressible models which can be directly used in the stress terms introduced above.

The Mooney-Rivlin form (Mooney, 1940)

$$W = C_1\left(I_1 - 3\right) + C_2\left(I_2 - 3\right) \tag{2.16}$$

This is the first phenomenological model for hyperelastic materials. C_1 and C_2 are material parameters. When $C_2 = 0$, this model reduces to the Neo-Hookean form in which C_1 is described by a statistical approach (Treloar, 1943). This model is suitable for moderate deformations (lower than 200 %) (Marckmann and Verron, 2006).

The polynomial form (Rivlin, 1948)

$$W = \sum_{i+j=1}^{N} C_{ij}\left(I_1 - 3\right)^i \left(I_2 - 3\right)^j \tag{2.17}$$

where N is the number of terms used. This form is an extension of Eq. (2.12). Several authors (Blatz and Ko, 1962; Isihara et al., 1951) have made special modifications to this

form with high order terms but the fitting capability is not significantly better than the Mooney form (Ogden, 1972).

The Ogden form (Ogden, 1972)

$$W = \sum_{i=1}^{N} \frac{2\mu_i}{\alpha_i^2}\left(\lambda_1^{\alpha_i} + \lambda_2^{\alpha_i} + \lambda_3^{\alpha_i} - 3\right) \tag{2.18}$$

where μ_i and α_i are material parameters for each of N terms. The development of this form was initiated by the idea of simplifying the complicated polynomial form when higher order terms are required. When the Ogden model is expanded to higher order terms, each term is simply a repetition of the same equation with different parameters. The expression in Eq. (2.18) is slightly different from Ogden's initial equation, but instead is expressed in the form adopted in a commercial FEM package, ABAQUS (ABAQUS, 2011) and is a special case of the Valanis-Landel model (Bradley et al., 2001; Valanis, 1967). It has been known that the Ogden form has a good fitting capability among classical hyperelastic models, and the performance in FEM applications is also satisfactory (Kim et al., 2012; Marckmann and Verron, 2006; Martins et al., 2006; Timmel et al., 2007; Wang and Lu, 2003).

As introduced in Chapter 1, the time dependency of elastomers is a very important design factor. This dependency has been described by many viscoelastic models. Most of these models assume that the contribution of stresses may be divided into the long-term (equilibrium) and instantaneous (non-equilibrium) parts. The postulation is that the total stress consists of the long-term stress, which represents a sufficiently slow process ($t \rightarrow \infty$), and the time-dependent stresses of the instantaneous parts. The mathematical expression of the instantaneous stress is key for viscoelastic models. Many mathematical models have been developed to describe the relaxation process by using the concept of internal variables (Simo, 1987). One of the simple models for the relaxation process is

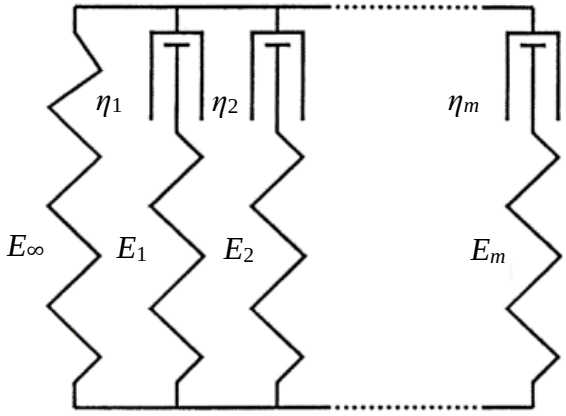

Figure 2.6 Generalized Maxwell-element (reproduced from Kaliske & Rothert (1997)).

linear viscoelasticity. The relaxation process in this model is described by the combination of mechanical analogies of springs and dashpots. One possible combination is the generalized Maxwell-element schematically described in Figure 2.6.

This mechanical analogy is able to relate the relaxation process to the equilibrium behaviour, attributed to the long-term modulus E_∞, and the non-equilibrium parts, described by m Maxwell-elements. The time-dependent elements represent the relaxation characteristic for each time scale, controlled by an internal variable: relaxation time $\tau_m = \eta_m / E_m$. If this model is applied to the one-dimensional linear elastic model, the stress is given by (Ferry, 1961)

$$\sigma(t) = \int_0^t G(t-t') \frac{\partial \varepsilon(t')}{\partial t'} \mathrm{d}t' \tag{2.19}$$

where $G(t)$ is a function representing the relaxation process and defined by a Prony series expansion

$$G(t) = E_0 - \sum_{j=1}^{m} E_j \left(1 - \exp\left(-t / \tau_j\right)\right) \tag{2.20}$$

where E_0 denotes the instantaneous modulus. The normalized form of this function is frequently used for a numerical formulation:

$$G(t)/E_0 = g(t) = 1 - \sum_{j=1}^{m} g_j \left(1 - \exp\left(-t/\tau_j\right)\right) \tag{2.21}$$

The term g_j, referred to as normalized modulus, represents the proportion of the relaxation amount assigned to each Maxwell element. This mathematical scheme is similarly used for finite viscoelasticity which can be used for hyperelastic models. According to one approach given by Holzapfel (1996), the total second Piola-Kirchhoff stress tensor **S** is separated into the volumetric and deviatoric (isochoric) parts, assuming that the volumetric one is rate-independent, as below

$$\mathbf{S} = \mathbf{S}_{\text{vol}}^{\infty} + \mathbf{S}_{\text{iso}} \tag{2.22}$$

The deviatoric stress $\mathbf{S}_{\text{iso}}$ is again divided into the long-term and viscoelastic parts:

$$\mathbf{S}_{\text{iso}} = \mathbf{S}_{\text{iso}}^{\infty} + \sum_{j=1}^{m} \mathbf{S}_{\text{vis}}^{j} \tag{2.23}$$

The viscoelastic part $\mathbf{S}_{\text{vis}}^{j}$ is defined as

$$\mathbf{S}_{\text{vis}}^{j}(t) = g_j \int_0^t \exp\left(-(t-t')/\tau_j\right) \frac{\mathrm{d}\mathbf{S}_{\text{iso}}^{0}(t')}{\mathrm{d}t'} \mathrm{d}t' \tag{2.24}$$

where $\mathbf{S}_{\text{iso}}^{0}$ is the instantaneous deviatoric stress. This definition is adopted in ABAQUS for the calculation of finite viscoelasticity. In the present research, a hyper-viscoelastic material was simulated by ABAQUS in which the combination of the Ogden form, Eq. (2.18), and the Prony series, Eq. (2.21), are applied through the finite viscoelasticity. In ABAQUS, it is assumed that the relaxation process in the Ogden form is applied only on the shear modulus term μ as

$$\mu_i(t) = \mu_i^0 \times g(t) \tag{2.25}$$

2.1.3 Properties to be considered

Elastomers are mechanically complex; several inelastic effects are simultaneously involved with hyperelastic behaviour. In fact, many phenomenological models have been

developed for these inelastic effects. Individual characterization of all these properties is excessive for the scope of the present research. The main aspect of interest to this present study is limited to the stress-strain relationship at dynamic strain rates for large strains. The stress-strain behaviour characterized by the methods presented is an apparent property, which probably includes contributions from various inelastic effects, at a specific strain rate.

2.2 High strain-rate tests

In the context of mechanical characterization, strain rates are generally divided into three regimes (Field et al., 2004): quasi-static (10^{-5} to 1 s^{-1}), medium (1 to 100 s^{-1}) and high rates (100 to 10^4 s^{-1}). Mechanical tests on elastomers at quasi-static rates can be performed by commercial screw-driven or servo-hydraulic machines and many standards are available with regard to loading modes, specimen sizes and data interpretation (Brown, 2006). For the dynamic tests (medium and high rates) on elastomers, there is no widely accepted standard. ISO 18872 (2003) could be adopted for a dynamic test on polymers. However, this standard is recommended for stiff polymers, in which clear yield behaviour is exhibited, and the strain rates are restricted to be below 10 s^{-1}. One key distinction between quasi-static and high rate loading is the presence of inertial stresses in the latter. In the current research, inertial stress is considered to be the stress required to induce rapid acceleration into the specimen, which in dynamic experiments is significant compared to the material stress described by the constitutive models. Because of these stresses, the deformation of a specimen is necessarily non-uniform for some period during dynamic loading, the specimen is no longer in quasi-static equilibrium, and calculations of constitutive parameters from experimental data become more challenging. The state in which a specimen undergoes such non-uniform deformation is referred to as a non-equilibrium state in this thesis, which is the standard, if imprecise, terminology adopted

in the high strain rate research community. The inertial effect is more significant for elastomers as the wave speed, ($\sqrt{E/\rho}$), is much lower than in stiffer engineering materials, as shown in Figure 2.7. The lower wave speed means that if a specimen is deformed at one end it takes a longer period of time for the deformation to reach the other end. The softness of elastomers and the resultant inertial effects are the primary reason for the difficulty of performing dynamic tests on these materials. Now, one of the most widespread dynamic test methods is briefly explained together with the equilibrium problem expected for elastomers.

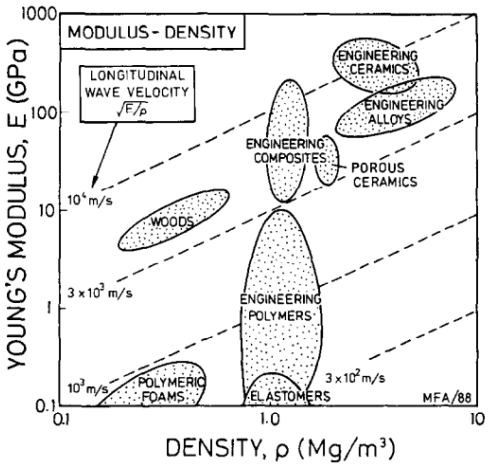

Figure 2.7 Modulus versus density of several classes of materials (dashed lines indicate a particular wave speed) (Ashby, 1989).

2.2.1 Split Hopkinson bar test

The most widely used test method for mechanical characterizations of materials at dynamic strain rates is the split Hopkinson bar. The technique was initially developed for compression experiments, in which case it is referred to as the split Hopkinson pressure bar (SHPB) by Kolsky (1949). As shown in Figure 2.8, the basic SHPB system comprises three metallic rods: the striker, incident and transmission bars. It is assumed that these bars are manufactured from the same material. The striker bar is launched at a certain initial velocity and impacts on one end of the incident bar. As a result of the impact,

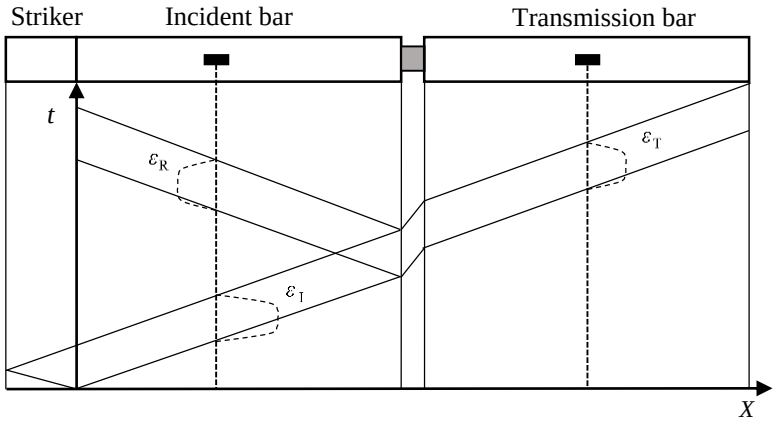

Figure 2.8 SHPB test arrangement and wave propagation diagram: the black boxes indicate the strain gauge locations.

a compression stress wave propagates into the bars, as shown in the wave propagation diagram (Figure 2.8), in which the abscissa and ordinate represent time t and the bar longitudinal position X, respectively. The strain gauge on the incident bar initially measures the incident pulse ε_I. At the specimen, part of the incident wave is reflected back to the incident bar, ε_R, and part is transmitted into the transmission bar, ε_T. These strain signals are converted to the stress waves σ_I, σ_R and σ_T using the Young's modulus E of the bars. For an elastic specimen, the relationship between σ_I and σ_R is given by the equation (Johnson, 1983; Parry et al., 1994):

$$\sigma_R = \left(\left(A_s Z_s - A_b Z_b\right)/\left(A_s Z_s + A_b Z_b\right)\right)\sigma_I = R\sigma_I \tag{2.26}$$

where A is the cross-sectional area and Z (acoustic impedance) is defined as $Z = \rho c$ (density ρ and wave speed c); the subscripts 's' and 'b' indicate the specimen and bar respectively. The multiplication factor in front of σ_I in Eq. (2.26) is called the reflection coefficient R, which is a function of the mechanical properties of the specimen and bars because $c = \sqrt{E/\rho}$. If $A_s = A_b$, the reflection coefficient is simply

$$R = \left(Z_s - Z_b\right)/\left(Z_s + Z_b\right) \tag{2.27}$$

It is possible to calculate this coefficient respectively for the cases of SHPB tests performed on high and low modulus materials by providing representative material properties Z_s and Z_b. If the pressure bars of the SHPB are made of a steel alloy, for example, of E_b =200 GPa and ρ_b = 7800 kg/m^3, and the specimen is an aluminium alloy of E_s = 70 GPa and ρ_s = 2700 kg/m^3 (Bertholf and Karnes, 1975), the reflection coefficient is approximately -0.5. This value means that if a compressive incident pulse of 1 MPa is generated, one half of this pulse (in tension) is reflected back into the incident bar. The pulse traveling along the transmission bar can be approximated by the following equation, with the assumption of the equilibrium state in the specimen (Ramesh, 2008):

$$\sigma_I + \sigma_R = \sigma_T \tag{2.28}$$

This equilibrium condition is an essential part of the traditional SHPB analysis. Using this equation, it is found that one half of the incident pulse is transmitted. The history of σ_T is directly used to obtain the stress in a specimen under the assumption of equilibrium. The nominal stress in the specimen is

$$N = \sigma_T A_b / A_s \tag{2.29}$$

In most practical cases, the specimen will not remain elastic, and the amount of the incident pulse transmitted and reflected is dependent on the flow stress of the specimen material. An example of stress pulses measured during the SHPB test on a relatively stiff polymer is shown in Figure 2.9.

It is possible to understand one difficulty of using the above SHPB analysis on elastomers by replacing the aluminium specimen with a softer material of E_s = 2 MPa and ρ_s = 1200 kg/m^3. For this assumed material, the reflection coefficient is obtained as 0.998 and, consequently, σ_T becomes about 0.002 MPa from the compressive σ_I of 1 MPa. As the impedance of a specimen is significantly lower than that of the bars, most of σ_I is reflected back and only a small portion enters the transmission bar. Such a low amplitude

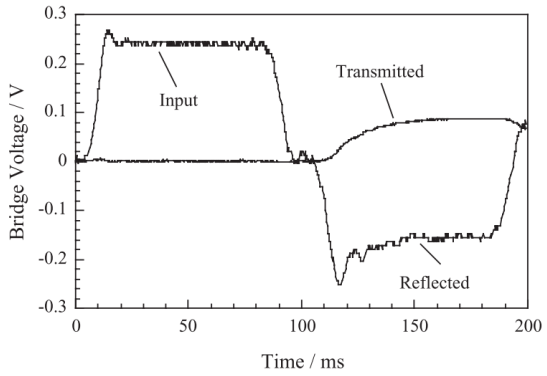

Figure 2.9 Incident, reflected and transmitted pulse in the SHPB for a polycarbonate specimen (Field et al., 2004).

pulse in the bar can prevent reliable measurement of the signal due to a high noise-to-signal ratio. Figure 2.10 shows an example of the low amplitude of σ_T due to the large impedance mismatch between a rubber specimen and metallic bars in the traditional SHPB system.

Eq. (2.28) is derived by the assumption of the equilibrium condition that the normal forces at the two specimen/bar interfaces are equal. It has been estimated that equilibrium can be achieved after three reverberations of the stress waves in a specimen (Briscoe and Nosker, 1984; Chen et al., 1999). This stress reverberation is achieved within a very short loading period for high modulus materials; for example, equilibrium of an aluminium alloy specimen ($c \approx 5000$ m s^{-1}) can be obtained after about 2.4 μs for a 4 mm thick specimen. If one generates a strain rate of 10 s^{-1} on this metal specimen, stress equilibrium is achieved after 0.002 % strain. The same calculation can be applied for elastomers; for the case of the assumed elastomer (used in the above paragraph, $c \approx 40$ m s^{-1}), the equilibrium state could be achieved after 300 ms, at which time the specimen is already deformed by 300 % strain at 10 s^{-1}. That is, for soft materials, stress equilibrium is only achieved after a large amount of deformation has already occurred, if at all. The measured signals during the non-equilibrium state should not be interpreted by the traditional SHPB analysis as the equilibrium assumption is no longer valid. It is easy to observe the non-

equilibrium state (non-uniform deformation) of elastomers in the SHPB test as shown in Figure 2.11, in which the specimen is loaded from the right-hand side. The deformation of this loading side is much larger than that of the left side; the non-uniform deformation obviously generates a different force at the two ends of the specimen. An example of the force measurement under the non-equilibrium state is presented in Figure 2.12.

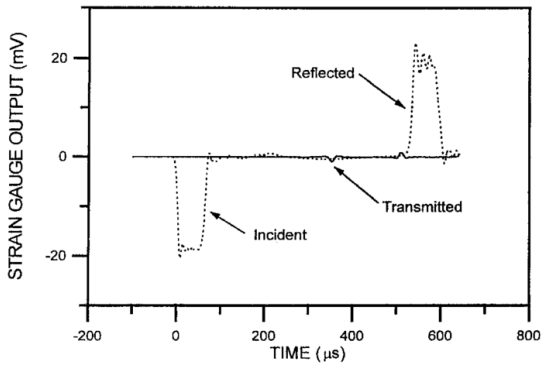

Figure 2.10 Incident, reflected and transmitted strain gauge signals of the traditional SHPB on an elastomer (Chen et al., 1999).

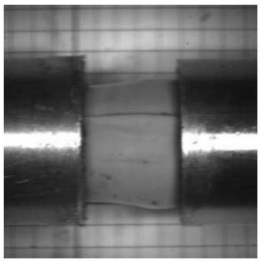

Figure 2.11 Silicone rubber dynamically loaded by the SHPB in compression (Chen and Song, 2011).

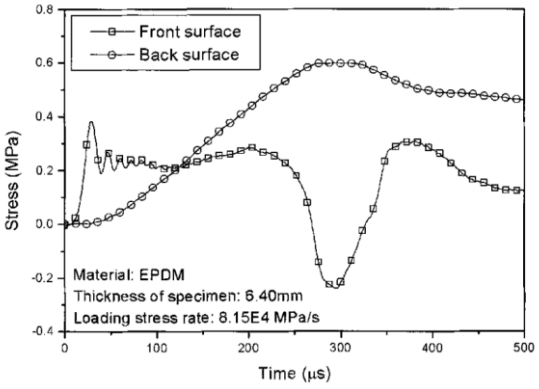

Figure 2.12 Stress measurements at both ends of an elastomer specimen in the traditional SHPB (Song and Chen, 2004).

2.2.2 Recent developments in Hopkinson bar tests for elastomers

Two limitations of the traditional SHPB experiment on elastomers are mentioned above: (1) low signal-to-noise ratio and (2) long duration of the non-equilibrium state. The achievement of equilibrium is especially difficult during the initial stages of loading; this is compounded by the fact that inaccurate force measurements due to small force signals during the initial loading can make confirmation of equilibrium difficult. These problems become more severe as the strain rate increases. These two limitations have been key factors of the modification of the SHPB or the new development of an impact experiment for elastomers. In this section, several attempts to overcome these two limitations are introduced.

The main reason of the first limitation is the large impedance mismatch between the bars and specimen. Experimental developments have therefore focused on reducing the impedance of the bars. Several authors have attempted to utilize polymer bars in the SHPB: e.g. PMMA (Bacon, 1998; Harrigan et al., 2014) and PC (Rao et al., 1997); impedances for these materials are compared to commonly used metals in Table 2.1. Because the impedance mismatch is lower when polymer bars are used, a larger portion of the loading pulse propagates into the transmission bar. Furthermore, because the polymer bars have lower Young's moduli, the strain signal resulting from this wave may be significantly larger. However, the application of polymer bars requires careful analysis

Table 2.1 Comparison of the impedance properties of commonly used bar materials for Hopkinson bar tests (Chen and Song, 2011; Rao et al., 1997).

Material	Density, ρ (kg/m^3)	Young's modulus, E (GPa)	Acoustic impedance ρc (kg/m^2/s)
Steel	8000	200	4×10^7
Titanium	5070	115	2.4×10^7
Aluminium	2810	72	1.4×10^7
PMMA	1160	2	1.5×10^6
PC	1156	2.5	1.7×10^6

to consider dispersion and attenuation of the stress waves as a result of their viscoelastic nature. In addition, this viscoelastic behaviour makes the strain signals measured using the polymer bars sensitive to other experimental factors such as strain rate, temperature and humidity. Another approach to improve the transmitted gauge signal is to design hollow metallic bars (Chen et al., 1999). The signal amplification from this design can be understood from Eq. (2.29) where the reduction of A_b leads to an increase of σ_T for the same specimen stress. Another method to increase the signal amplitude is to utilize a highly sensitive force sensor embedded in the bars instead of, or in addition to, surface strain gauges. A circular piezoelectric transducer (manufactured from PZT) has been adopted for this application (Chen et al., 2000) and showed a good sensitivity even for a very soft polymer, HTPB (Kendall et al., 2014). In order to obtain high bandwidth measurements, it is necessary to match the impedances between the bars and the PZT; for this reason, titanium alloy bars have been used for this application. The PZT is usually protected by thin aluminium or titanium discs on both sides as the transducer is very brittle. However, it has been found that additional axial inertial forces generated by the protection layers and PZT can significantly affect the actual force history (Casem et al., 2005).

Use of the polymer bars can also be a remedy for the second limitation (long duration of the non-equilibrium state). Analytical work has shown that the reduced impedance mismatch from the application of the polymer bars can significantly decrease the duration of the non-equilibrium period (Rao et al., 1997). However, the polymer bar cannot be a sole solution, especially when very soft elastomers are tested or high strain rates are required. It might be obvious that the thinner specimen reduces the non-equilibrium duration because the distance that the stress wave travels becomes shorter. Although this method is easily applicable, thickness reduction can bring several adverse effects such as

interface friction, increased confinement due to lateral inertia and poor accuracy in the strain measurement (Chen and Song, 2011; Warren and Forrestal, 2009). Moreover, when the deformation of the thin specimen is very high, the strain state can significantly deviate from the uniaxial loading that needs to be assumed for the SHPB analysis.

As well as reducing the specimen thickness, the non-equilibrium period can be minimized by shaping the incident pulse. The incident pulse shown in Figure 2.9 sharply reaches the maximum amplitude; in other words, the time (rise time) to reach the maximum amplitude is short. Such shape of the pulse will induce rapid acceleration and high strain-rate deformations concentrated on one side of the specimen so that the specimen experiences a lot of strain before reaching stress equilibrium. One technique to solve this non-equilibrium problem due to the sharp pulse is pulse shaping. A pulse shaping technique has been used to smooth the incident pulse by means of a thin polymer disk (Chen et al., 1999; Song and Chen, 2003) or layers of thin paper discs (Shergold et al., 2006) located between the striker and incident bar. Figure 2.13 shows the application of the pulse shaper in which the rise time is increased. This smooth incident pulse limits the non-equilibrium period to the initial deformation stage and allows sufficient time to achieve the stress equilibrium before the main deformation loading. This is due to two effects: firstly the more gradual loading allows equilibrium to be achieved more rapidly, and second the reduced strain rate in the early stages of deformation reduces the strain

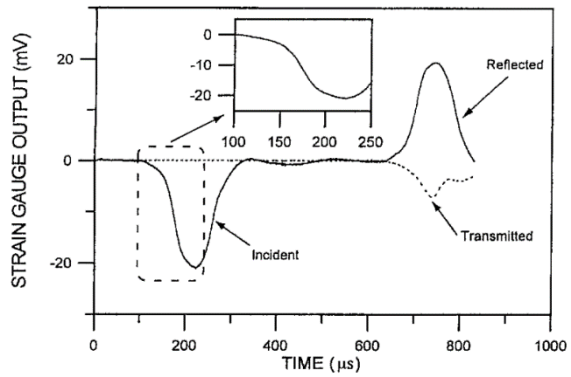

Figure 2.13 Smooth incident pulse signal by means of a polymer-disk pulse shaper (Chen et al., 1999).

induced in the specimen during this period of loading. However, the gradually increasing pulse gives the same shape to the strain rate profile. Thus, the strain rate for the initial loading period can significantly differ from the constant strain rate exhibited during the major loading stage.

The combination of the non-metallic bars, PZT sensor, thin specimen design and pulse shaping techniques can significantly improve the two limitations of the SHPB for elastomers (Jiang et al., 2015). However, it is still difficult to generalize these combinations for various soft materials. Complex soft materials, e.g. cloth-reinforced or cellular rubbers, need a certain dimensional style requirement for their specimen designs, that is, the small cylindrical specimen design of the SHPB is not suitable to fully represent their complex internal structures. For this case, a dynamic test in tension may be more appropriate as the specimen size can be larger than in compression avoiding the buckling, which is likely to occur for long and soft SHPB style specimens. However, the aforementioned two limitations of the SHPB can be even more serious for the case of a dynamic tension test on elastomers. The achievement of stress equilibrium is more difficult due to the specimen design which inevitably requires a large length-to-thickness ratio. The specimen should have at least a certain minimum length in order to experience uniaxial stress and minimise other stress states, not only triaxial but also planar or biaxial, in which elastomers exhibit different material behaviour.

A number of authors have conducted dynamic tensile tests on elastomers with some modifications to the traditional split Hopkinson tension bar (SHTB). Cheng and Chen (2003) used a short specimen and pulse shaping technique for an SHTB test on EPDM rubber at strain rate of about $3000\ s^{-1}$. A similar experiment was conducted on polyurethane using a traditional SHTB system in combination with a pendulum striker (Kanyanta and Ivankovic, 2010). Nie et al. (2008) developed a special clamping system

in an SHTB in order to use a thin tubular shape specimen with a very short gauge length of 1 mm. The authors found that this specimen design enabled them to reduce lateral and longitudinal inertia effects. Similar to the SHPB case, a smaller or short specimen shape is an applicable and effective way to decrease the duration of the non-equilibrium state; however, the reduction in the size for a tension-type specimen can cause several side effects such as inhomogeneous strain states and significant end effects from the gripping area. Apart from the conventional Hopkinson bar technique, Roland et al. (2007) developed a special drop-weight test apparatus in which a tensile load was applied at both ends of a polyurea specimen. Although in this study, stress equilibrium was confirmed by the similarity of the forces measured at each end of the specimen, the actual stress state in the middle of a specimen should be investigated. In order to overcome the equilibrium problem, a recent study has directly used the non-uniform deformation state caused by wave propagation in a specimen to obtain a dynamic strain stress curve using the nonlinear one-dimensional wave equation and jump conditions (Niemczura & Ravi-Chandar 2011a,b). However, in these studies, the material motion only along a central line of the specimen is considered, due to the one dimensional assumption, neglecting the lateral contraction. This assumption for elastomers can lead to overestimation of the stress due to high incompressibility.

2.2.3 Dynamic mechanical analysis method

DMA is a widely used technique for characterizing the temperature and frequency dependence of viscoelastic polymers, focussing on the response at small strain, which is widely accessible through commercially available devices. A schematic representation of DMA is shown in Figure 2.14(left) in which the red specimen, of thin rectangular shape, is placed on the tensile fixture. At one end of the specimen, a sinusoidal force is applied, and the resultant specimen deformation is simultaneously measured. If

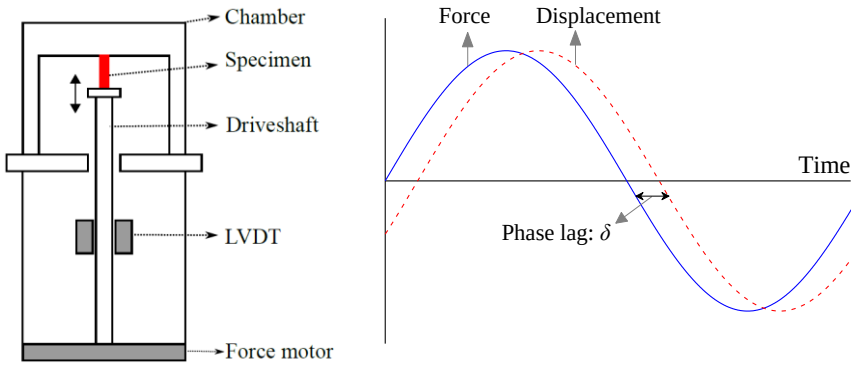

Figure 2.14 Schematic representation of a typical system of DMA and one cycle sinusoidal force and its displacement profiles along time axis.

a perfectly elastic material is tested, the force and displacement profiles are completely in phase. For the case of a viscoelastic material, a phase lag of the displacement measurement occurs with respect to the force profile. The amount of the phase lag (angle) is usually indicated by the symbol δ, which is thus a parameter characterizing the viscoelastic behaviour. If the periodical force is applied at a frequency ω (radians/sec) in the linear viscoelastic regime, the stress-strain relationship can be written (Ferry, 1961)

$$\sigma = \varepsilon_0 \left(E' \sin \omega t + E'' \cos \omega t \right) \tag{2.30}$$

where ε_0 is the strain amplitude. E' and E'' are respectively the storage and loss moduli defined as

$$E' = \left(\sigma_0 / \varepsilon_0 \right) \cos \delta \tag{2.31}$$

$$E'' = \left(\sigma_0 / \varepsilon_0 \right) \sin \delta \tag{2.32}$$

and their relationship is

$$E'' / E' = \tan \delta \tag{2.33}$$

It is desirable to characterize the viscoelastic behaviour of polymers over many decades of time, which may in practice be inaccessible or prohibitively time-consuming. In this case, the well-established time-temperature superposition principle (TTSP) may be used to extend the range of frequencies by using data obtained at different temperatures.

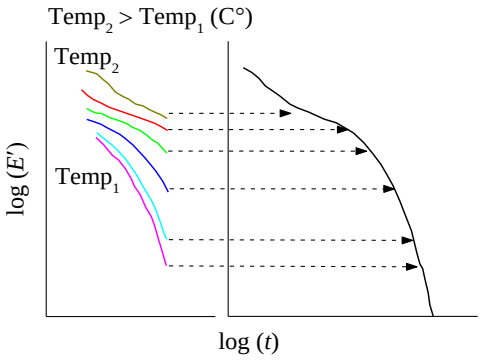

Figure 2.15 Isotherms of relaxation modulus and the construction of a relaxation master curve by means of the time-temperature superposition principle.

This method is conducted by the following procedure. The left-hand side of Figure 2.15 is a collection of the relaxation moduli obtained isothermally at several temperatures. These data are measured by a frequency sweep testing mode, which is provided by most DMA devices. The frequency used for the DMA test can be approximately converted into time as one-quarter of the period ($1 / 4\omega$). The frequency range available with a commercial DMA device is generally not large enough to give a long-range time scale for the relaxation curve. At this point, TTSP can be adopted in order to expand the time scale. This principle is based on the assumption that the reduction of the modulus due to an increase in chain movement as a result of high temperature resembles the relaxation behaviour over a long time period (Tobolsky, 1956). Similarly, there is equivalence between low temperature and high rate deformation. If the frequencies are spaced closely enough, it is observed that each isotherm overlaps with those at higher and lower temperatures. This resemblance between the isotherms makes it possible to shift curves so that they overlap in order to construct the relaxation master curve. The shifting procedure is shown in Figure 2.15. The amount of shifting is referred to as the shifting factor a_T, which is usually itself a function of temperature. A commonly used empirical function is available for a_T with respect to temperature (Williams et al., 1955) denoted as the WLF model and, given as:

$$\log a_T = -\frac{C_1(\text{Temp} - \text{Temp}_0)}{C_2 + (\text{Temp} - \text{Temp}_0)} \tag{2.34}$$

where Temp_0 is a reference temperature. In the research reported in this thesis, DMA and TTSP were utilized to support the high strain rate moduli derived from other experimental techniques.

Dynamic characterization using DMA as explained above is only limited to small strains, because the equations used for DMA are based on the assumption of linear viscoelastic behaviour. In other words, DMA is not applicable for characterizing the dynamic behaviour of elastomer at large deformations. The question might arise as to whether the relaxation master curve obtained from a set of DMA experiments can be used to describe the viscoelastic behaviour at large strain. It has been already found that the rate dependency of elastomer at large strain measured by a transient experiment (e.g. SHPB) is very different to that obtained by the application of TTSP to DMA data (Mott et al., 2011; Zhao et al., 2008). This deviation can be caused by several factors such as non-linear viscoelastic behaviour, phase changes at high or low temperatures, or time and temperature dependent structural changes with applied deformation, e.g. stress induced crystallisation. Nevertheless, the mechanical properties of elastomers measured by the combination of DMA and TTSP will be used in this research to compare with the results from transient experiments at small strain.

2.3 Virtual Fields Method (VFM)

The above section introduces modifications to the traditional SHPB or new test methods developed to overcome the current experimental limitations of dynamic tests on elastomers: (1) stress equilibrium and (2) high noise-to-signal ratio. Additionally, it is explained that the DMA technique is limited to (3) small deformations. Recently, methods to address these problems have been explored for data measurement in dynamic

experiments on polymers. With regard to the equilibrium problem, there have been several efforts to directly use the propagation of a stress wave through the specimen to obtain material properties. By means of high speed cameras and the digital image correlation (DIC) technique (Sutton et al., 2009), it is possible to track deformations in a specimen subjected to dynamic loading with a high spatial and displacement resolution, even (or especially) when the specimen is in a non-equilibrium state (Pierron et al., 2011; Siviour, 2009). This full field measurement technique opens a new way of characterizing dynamic mechanical behaviour by using inverse techniques (Stéphane Avril et al., 2008). The Virtual Fields Method, VFM, (Pierron and Grédiac, 2012) is an inverse technique which has the particular advantage that it allows inverse identification problems to be re-expressed as forward problems. The VFM is proposed as a basis for new experimental methods for overcoming the above limitations. In this section, a description of the VFM is given; actual applications are also briefly explained for static and dynamic cases. Firstly, however, a description of digital image correlation, which in this thesis is used to provide the experimental data required by the VFM, is provided. Also, a description of another popular inverse technique, finite element updating, is given for a comparison with the VFM.

2.3.1 Digital image correlation (DIC)

Many authors have performed characterization of the mechanical behaviour of materials (i.e. stress-strain relationship) using surface deformation data to obtain the required strain information. Although, it is also possible to measure volumetric deformation fields, e.g. by combining tomographic imaging with a volume correlation technique (S. Avril et al., 2008; Forsberg and Siviour, 2009), surface measurement is still popular in experimental mechanics, especially when materials are homogenous and small or thin enough to assume uniform strain states. Dynamic characterization is still limited

to surface data as the current volumetric measurement techniques are not able to achieve the required combination of temporal and spatial resolution. In the current research, the full-field measurement was conducted only on the specimen surface, and the discussion of the deformation measurement techniques is limited to the case of in-plane deformation.

Measurement methods for material surface deformations are divided into two groups: contacting and non-contacting methods. The electrical resistance strain gauge is one of the common contact measurement methods for extracting strain data on a small area where the gauge is attached on the specimen surface. The strain gauge is not applicable for elastomers exhibiting very large deformations; instead, a clip-on extensometer is often appropriate as it is able to track large relative displacements of two material locations. However, this extensometer is not applicable for dynamic tests. The weight of the clip head will cause significant inertial forces during dynamic loading and slipping of the clip-on fixture can occur.

One category of non-contact methods can be defined as techniques able to measure full-field deformations by observing an optical change on the surface of a specimen (Rastogi, 2000). The optical measurements are divided into two groups: interferometric and non-interferometric. One example of the first method is Moiré interferometry (Post et al., 1994). This method uses two coherent laser beams, the superposition of these two beams produces walls of constructive and destructive interference. This pattern, used as virtual reference grating, interacts with a geometric grating made on the specimen surface (Han et al., 2005). This interaction generates the Moiré pattern, which is recorded by a camera and then analysed to produce displacement fields. Other interferometric techniques include holography interferometry (R. Jones and C. Wykes, 1989) and speckle interferometry (Leendertz, 1970). Non-interferometric methods measure the surface deformations by comparing characteristic patterns before and after deformation. The

pattern can be made by several methods, including deposition of a thin grid, coherent light illumination on a rough surface (the laser speckle effect) and spray painting. The first of these is used in the grid method (Goldrein et al., 1995), whilst the latter two can be used in speckle photography (Sjödahl and Benckert, 1993) and digital image correlation (DIC) (Sutton et al., 2009). As the surface of the sample deforms, the changes in the pattern are recorded by a suitable imaging device. For example, digital imaging devices are widely used to record the pattern images for the DIC application. The recorded images are then typically compared to a reference image to generate displacement fields.

The DIC technique measures intensity (grey level) changes due to movement of a random grey intensity pattern made on the surface of a specimen; the pattern may be applied by, as mentioned, a spray paint or may result from natural features on the specimen surface. An example of a so-called speckle pattern is shown in Figure 2.17. The intensity changes are measured by comparison of various small regions (i.e. subsets) of two digital images before and after deformation. The commonly used numerical

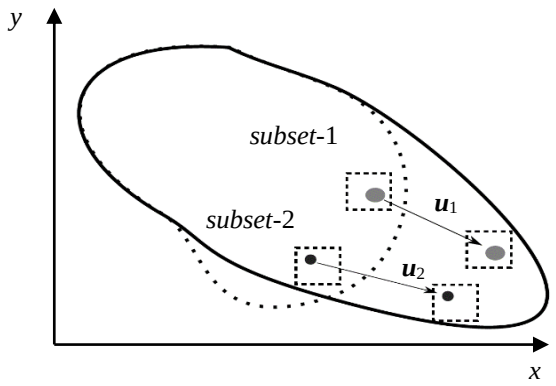

Figure 2.16 Schematic representation of the pattern matching of DIC between subsets on the reference (dashed line) and deformed (solid line) configurations.

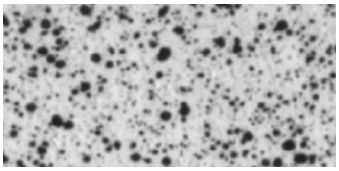

Figure 2.17 Black random speckle pattern (Lecompte et al., 2006).

algorithm for DIC was first suggested by Sutton et al. (1983). The principle of in-plane DIC involves matching the two-dimensional intensity distributions. The digital images are divided into evenly spaced subsets, and for each subset, a displacement is calculated. The subset size should be big enough to have a distinguishable pattern; a commonly used rule of thumb is that there should be three pixels per speckle and three speckles per subset (Lecompte et al., 2006). The pattern matching is conducted between subsets of the reference and deformed configurations as shown in Figure 2.16, where the two subsets include distinctive patterns: one of the dots is smaller and darker. The matching procedure is performed by evaluating the degree of similarity of the grey levels between these subsets using an objective function (Pan et al., 2009), such as

$$C_{\mathrm{SSD}} = \sum \left| GR_0(\mathbf{x}) - GR(\mathbf{x}+\boldsymbol{u}) \right|^2 \tag{2.35}$$

where GR_0 and GR represents grey levels of the reference and deformed configurations. The square difference of grey levels, C_{SSD}, is referred to as a sum of square deviation (SSD). Minimization of Eq. (2.35) is used to find locations of corresponding subsets between the two configurations. Another common correlation function is cross correlation, C_{CC}. This function is adopted in the DIC software (Davis 7.2, LaVision 2007) used throughout the present research and can be written as

$$C_{\mathrm{CC}} = \sum \left[GR_0(\mathbf{x}) GR(\mathbf{x}+\boldsymbol{u}) \right] \tag{2.36}$$

In contrast to C_{SSD}, maximization of C_{CC} is used as the correlation criterion for the pattern match. This correlation mode can be computed in the Fourier domain (Chen et al., 1993) in order to reduce computational time. The difference in the subset locations of the two configurations is a displacement vector. The agglomeration of these over the whole surface forms the full-field displacement data. The spatial derivative of this displacement field leads to the attainment of strain data; various numerical methods can also be applied

to condition or analyse the data such as FEM smoothing (Shi et al., 2004) and least-square fitting (Wattrisse et al., 2001).

The most important practical factors which affect the accuracy of DIC are lighting, speckle pattern, subset size and correlation calculation (Haddadi and Belhabib, 2008). The variation of the light source such as light flickering and brightening or dimming can cause large differences in grey level of the same subset between images. It is difficult to control this error source as the variation depends on lighting devices and the type of experiments. For the case of high speed imaging, the frequency and duration of lighting is important. One way of evaluating the sensitivity of the light variation is to use pictures of a static object. The application of DIC to static pictures should theoretically produce zero displacement and strain fields. The variation of the measured fields can be used as a parameter for the evaluation of the light source sensitivity, as well as errors owing to detector noise. A larger subset size generally produces the smallest sensitivity to measurement noise (Lecompte et al., 2006; Rajan et al., 2012). However, it also reduces the number of independent displacement measurements, and hence the data spatial resolution (number of data points), which must remain large enough to adequately represent the mechanical behaviour of the specimen. The use of static image analysis is also useful for the determination of the optimal subset size. One strategy used in the present research will be given in a later chapter. The procedure of correlation calculation is a critical factor, especially when the distortion of the pattern is very large. For this case, it may be difficult to conduct pattern matching between the initial picture and the later one. To cope with this difficulty, the incremental calculation scheme (Davis 7.2, LaVision 2007) was adopted in the present research. This method uses the correlation between two successive images to calculate an incremental displacement. These incremental data are summed to form the total deformation.

2.3.2 Applications of DIC

A common DIC application is strain measurement in mechanical tests: metals (Bastawros, 2000), composites (Périé et al., 2009) and polymers (Chevalier et al., 2001). An important advantage of DIC is a full-field data measurement. In the case of 2D DIC, it is possible to obtain five full-field data quantities: u_x, u_y and ε_{xx}, ε_{yy}, ε_{xy}. This form of analysis reveals experimental data that is difficult to be obtained by a pointwise strain gauge technique, such as large deformations (Le Cam, 2012), damage evolution (Niendorf et al., 2009) and spatial data for a large structure (Yoneyama et al., 2007). Another example is the quantitative measurement of strain localizations during mechanical testing in the case of a uniaxial tension test (Tung et al., 2010; Wattrisse et al., 2001). The application of DIC for this case is to produce an actual strain measurement, which can be approximated by averaging strain fields over a localized area. However, the determination of the averaging area can be difficult especially beyond the yield point where the spatial gradient of strain is very high (Jerabek et al., 2010). The stress-strain curve obtained from this measurement method is an averaged property between the localized and non-localized area. This averaged property significantly deviates from the actual characteristic when the localized area undergoes phase transformations (Daly et al., 2008; Delpueyo et al., 2012). Moreover, these transformations can lead to a heterogeneous strain state which is significantly different from the global strain (Kang et al., 2006). For this case, the strain-state assumption for the construction of a simple constitutive equation (e.g. one-dimensional uniaxial equation), to be used for the fitting of a stress-strain curve, is no longer valid. This heterogeneous strain state can globally occur for anisotropic materials, e.g. fibre-reinforced composites (Godara and Raabe, 2007; Pierron et al., 1998). Uniaxial tension tests for such materials and strain measurements by averaging the data field leads to the attainment of material parameters which does not

clearly represent the strain-state heterogeneity. The strain state is also an important factor for a mechanical test of rubbers. For example, a bulge test is often adopted to produce a biaxial strain state. A circular rubber sheet is clamped around the edges using two flanges; one of the surfaces is pressurized by gas or liquid (Sasso et al., 2008). As the rubber inflates, strain measurement can be conducted by DIC, especially around the central area, where it is assumed that there is a pure biaxial strain state. An averaging scheme for strain is required to conduct a fitting procedure with the biaxial stress-strain equation. However, it can be difficult to define the averaging area to exclude regions in which other strain states exist. Although this can be achieved, force data measured during this experiment are a result of heterogeneous strain states.

As explained above, the application of DIC as a simple replacement of a strain gauge has limitations for some experimental circumstances where heterogeneous strain states are expected. Often, the local strain is used as a strain measurement and assumed to correspond to the stress obtained from a global force measurement. However, it is difficult to define the direct relationship between those two measurements. Instead of using an averaged scalar value, the whole full-field data, which represent heterogeneous states over a whole specimen area, can be a solution for a better characterization of materials. One set of techniques able to utilize the complete full-field data are inverse methods.

2.3.3 Finite element model updating (FEMU)

Inverse methods are experimental analysis methods by which materials are inversely characterized through a specific relationship between the experimental data and their physical behaviour (Stéphane Avril et al., 2008). A linear inverse problem can be defined as (Aster et al., 2013)

$$\boldsymbol{d} = \Upsilon \boldsymbol{m} \tag{2.37}$$

where $\boldsymbol{d}$, $\boldsymbol{m}$ and $\boldsymbol{\Upsilon}$ are respectively a set of experimental observations, physical parameters and a matrix defining the relation between $\boldsymbol{d}$ and $\boldsymbol{m}$. The inverse problem is to seek unknown physical parameters $\boldsymbol{m}$ (e.g. Young's modulus) using observed data $\boldsymbol{d}$ (e.g. full-field displacement data and point measurement of force) and a predefined physical relation $\boldsymbol{\Upsilon}$. The conceptually simple way to estimate $\boldsymbol{m}$ is direct inversion of $\boldsymbol{\Upsilon}$; however, in practice the matrix $\boldsymbol{\Upsilon}$ is usually not invertible (Kabanikhin, 2008). Instead, the minimization of the cost function shown in Eq. (2.38) can be iteratively conducted until the function reaches its minimum value with estimated $\boldsymbol{m}'$.

$$\Phi = \boldsymbol{d} - \boldsymbol{\Upsilon}\boldsymbol{m}' \tag{2.38}$$

This concept is the main idea of the finite element model updating (FEMU) technique in which the error minimization is conducted by reducing the difference between experimental data and a numerical simulation of the experiment (Kavanagh and Clough, 1971). The first step of this technique is the construction of a finite element model which resembles the actual mechanical tests. The FEM simulation is conducted with the boundary conditions (displacement or loading) from the real test; numerical data extracted from the simulation result are compared with experimental observations, and, based on these data, changes are made to the material parameters in the simulation. This procedure continues until the numerical data match those from the experiment. The form of experimental observations for FEMU can be either full-field measurements or several point-wise discrete data.

FEMU is widely accepted for characterizing material parameters as its concept is very intuitive; the form of experimental data is very flexible; and some commercial FEM packages provide a convenient way of comparing numerical and experimental data (Ienny et al., 2012). Various materials have been characterized for the identification of material parameters: wood (Le Magorou et al., 2002), metal (Kajberg and Lindkvist, 2004;

Meuwissen et al., 1998) and polymer (Pagnacco et al., 2007). The combination of full-field measurements and FEMU is of special interest to soft materials in which stress and model parameters are very dependent on strain states (Gendy and Saleeb, 2000). FEMU has been applied to several soft materials in order to identify material parameters which reflects complex strain states obtained from full-field measurements (Genovese et al., 2006; Meijer et al., 1999). The application of DIC and FEMU has been applied to the tensile Hopkinson bar experiments on a mild steel specimen (Kajberg and Wikman, 2007). A small tensile specimen was dynamically tested with high speed photography taking a series of pictures of random speckle patterns. The full-field data (displacement and strain fields) captured heterogeneous strain states on an imaging area of the specimen surface. Material parameters for a viscoplastic model were optimized by reducing the difference between experimental and simulation data of either displacements or strains.

Although FEMU has been utilized for various materials and experimental conditions, several drawbacks remain. Firstly, the computational time can be expensive for some circumstances, for example, where the simulation size is large or a large number of material parameters need to be identified, significant effort has been put into optimising the sampling of parameter space, but if the physical effect of different parameters is highly coupled, this can still be challenging. Secondly, it can be difficult to accurately replicate the actual experimental conditions in the numerical model. This difficulty can arise when a material structure is complex or the measurements of boundary conditions are not accurate enough. Third, FEMU requires an initial estimation of material parameters due to its iterative calculation method. In order to avoid finding a local, rather than global, minimum of the cost function, the initial estimations should be within a certain range of actual material parameters, which can be difficult to assess *a-priori*.

2.3.4 Definition of the Virtual Field Method (VFM)

The VFM is an inverse method which requires full-field data of a measurement domain. The VFM provides a framework by which a relationship between experimental data and unknown parameters is mathematically constructed. The application of the VFM needs the use of a particular constitutive model in its calculation procedure. When a linear constitutive model, in which stresses and deformations are linearly defined by material parameters, is used, a linear inverse problem can be made so that it is possible to calculate the unknown parameters as

$$\boldsymbol{m}' = \Upsilon^{-1}\boldsymbol{d} \tag{2.39}$$

This means that the VFM does not require the iterative procedure using finite element simulations; thus, the aforementioned disadvantages of FEMU are no longer present in the VFM. The inverse problem of the VFM can be nonlinear when a nonlinear constitutive model is used. The VFM calculation is iteratively conducted to find material parameters. Although the iterative calculation style is required in this nonlinear VFM as in FEMU, the calculation speed is much faster for the VFM as the construction and calculation of successive finite element simulations is not required. The description of the VFM below is based on a linear constitutive relation.

The principle of the VFM is to provide a mathematical relationship between constitutive equations with unknown parameters and experimental data fields. This mathematical relationship is based on the weak form of the equilibrium equation, which is referred to as the principle of virtual work (PVW). This equation is derived from the local equilibrium equation and boundary conditions:

$$\mathrm{div}\boldsymbol{\sigma} + \mathbf{b} = \rho\boldsymbol{a} \tag{2.40}$$

$$\boldsymbol{\sigma}\mathbf{n} = \overline{\mathbf{T}} \text{ over } s_f \tag{2.41}$$

$$\boldsymbol{u} = \bar{\boldsymbol{u}} \text{ over } s_u \tag{2.42}$$

where ρ, **b** and $\boldsymbol{a}$ are the density and body force and acceleration vectors. s_f and s_u respectively represent the surface areas where loads and displacements are prescribed. The overline over displacement, $\boldsymbol{u}$, and traction, **T,** vectors indicates that they are prescribed quantities. The "div" is a divergence operator with respect the current configuration. The next step is to introduce a virtual displacement $\boldsymbol{u}^*$ which satisfies C^0 continuity (i.e. continuous fields) and kinematic admissibility, i.e. $\boldsymbol{u}^* = 0$ over s_u. The kinematic admissibility is not a compulsory requirement but a condition to remove the virtual work contribution of the reaction force at s_u. If force measurement is available over this boundary, the virtual field does not need to be kinematically admissible. The multiplication of $\boldsymbol{u}^*$ to Eq. (2.40) and its integration over the current volume v of the body with the assumption of no body force produces

$$\int_{\mathrm{v}} \mathrm{div}\boldsymbol{\sigma} \cdot \boldsymbol{u}^* \mathrm{dv} = \int_{\mathrm{v}} \rho \boldsymbol{a} \cdot \boldsymbol{u}^* \mathrm{dv} \tag{2.43}$$

Starting from this equation, the application of the divergence theorem and several mathematical procedures lead to the principle of virtual work equation (Pierron and Grédiac, 2012):

$$-\int_{\mathrm{v}} \boldsymbol{\sigma} : \boldsymbol{\varepsilon}^* \mathrm{d}v + \int_{s_f} \bar{\mathbf{T}} \cdot \boldsymbol{u}^* \mathrm{d}s = \int_{\mathrm{v}} \rho \boldsymbol{a} \cdot \boldsymbol{u}^* \mathrm{dv} \tag{2.44}$$

where

$\boldsymbol{\sigma}$	*actual stress tensor*
$\bar{\mathbf{T}}$	*actual loading* (= $\boldsymbol{\sigma n}$)
$\boldsymbol{u}^*$	*virtual displacement vector*
$\boldsymbol{\varepsilon}^*$	*virtual strain tensor* ($= \partial \boldsymbol{u}^* / \partial \boldsymbol{x}$)
v	*current volume of the body*
s_f	*current loaded surface*
':' and '·'	*the dot products for matrices and vectors*

This principle states that the equilibrium of the body with any kinematically admissible $\boldsymbol{u}^*$ applied onto the body, the sum of all virtual works imposed on the body is null. The

virtual displacement does not hold any physical relation with actual displacement; rather, it is a mathematical test function satisfying the smoothness and admissibility requirements. In Eq. (2.44), $\boldsymbol{\sigma}$ is the Cauchy (true) stress tensor and conjugated with the current configuration (i.e. deformed configuration); thus, the integration domain is based on the current coordinate. The PVW can be written in the initial configuration when the Cauchy stress tensor is replaced by the first and second Piola-Kirchhoff stress tensors, Eq. (2.11) and (2.12). For example, when the first Piola-Kirchhoff stress, $\mathbf{\Pi}$, is used, the PVW in the initial configuration is written as (Pierron and Grédiac, 2012)

$$-\int_{V_0} \mathbf{\Pi} : \frac{\partial \boldsymbol{u}_0^*}{\partial \mathbf{x}_0} \mathrm{d}V_0 + \int_{S_{0,f}} (\mathbf{\Pi} \boldsymbol{N}) \cdot \boldsymbol{u}_0^* \mathrm{d}S_0 = \int_{V_0} \rho \boldsymbol{a} \cdot \boldsymbol{u}_0^* \, \mathrm{d}V_0 \tag{2.45}$$

$\mathbf{\Pi}$	*the first Piola-Kirchhoff stress tensor*
V_0	*initial volume of the body*
$S_{0,f}$	*initial loaded surface*
$\boldsymbol{N}$	*initial normal vector of* $S_{0,\mathrm{f}}$
$\boldsymbol{u}_0^*$	*virtual displacement vector based on the initial coordinate*
$\boldsymbol{\varepsilon}_0^*$	*virtual strain tensor* $(= \partial \boldsymbol{u}_0^* / \partial \mathbf{x}_0)$

The main procedure of the VFM is a mathematical manipulation of the PVW, Eq. (2.44), in which experimental data are applied to each term. The simple analytical example of the linear VFM application for a static case is given below. In the following example, provided that the deformation is small, the configuration is based on the initial coordinate system. In addition, it is assumed that the left and right hand-side boundaries are free to contract laterally, so that $\overline{\mathrm{T}}_y \approx 0$, in order to simplify the calculation procedure.

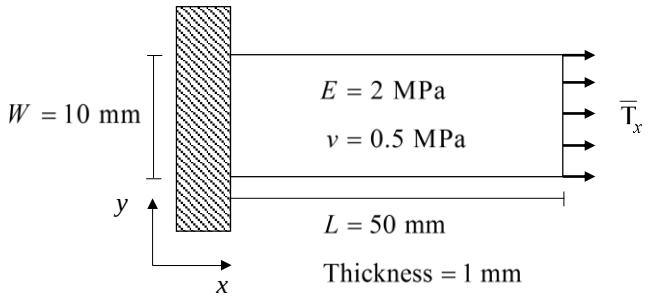

Figure 2.18 Isotropic linear elastic material in a planar rectangular shape subjected to uniaxial loading.

In the VFM application for the static case of 2D plane stress loading as shown in Figure 2.18, the PVW, Eq. (2.44), is simplified as

$$\int_s \boldsymbol{\sigma} : \boldsymbol{\varepsilon}^* \mathrm{d}s = \int_{l_f} \bar{\mathbf{T}} \cdot \boldsymbol{u}^* \mathrm{d}l \tag{2.46}$$

where s and l_f denote the current surface and loaded boundary. Its component form is

$$\int_s \sigma_{xx}\varepsilon_{xx}^* + \sigma_{yy}\varepsilon_{yy}^* + \sigma_{xy}\varepsilon_{xy}^* \, \mathrm{d}s = \int_{l_f} \bar{\mathrm{T}}_x u_x^* + \bar{\mathrm{T}}_y u_y^* \, \mathrm{d}l \tag{2.47}$$

For an isotropic linear elastic material, the Cauchy stress term is defined by the multiplication of the plane-stress stiffness matrix to a vector of the in-plane strains as

$$\begin{Bmatrix} \sigma_{xx} \\ \sigma_{yy} \\ \sigma_{xy} \end{Bmatrix} = \begin{bmatrix} Q_{xx} & Q_{xy} & 0 \\ Q_{xy} & Q_{xx} & 0 \\ 0 & 0 & G \end{bmatrix} \begin{Bmatrix} \varepsilon_{xx} \\ \varepsilon_{yy} \\ \varepsilon_{xy} \end{Bmatrix} \tag{2.48}$$

where μ is the in-plane shear modulus (= ($Q_{xx} - Q_{xy}$) / 2). It should be noted that ε_{xy} is an engineering shear strain. The insertion of Eq. (2.48) into (2.47) results in

$$\begin{aligned} Q_{xx}\int_s \varepsilon_{xx}\varepsilon_{xx}^* + \varepsilon_{yy}\varepsilon_{yy}^* + \frac{1}{2}\varepsilon_{xy}\varepsilon_{xy}^* \, \mathrm{d}s + Q_{xy}\int_s \varepsilon_{xx}\varepsilon_{yy}^* + \varepsilon_{yy}\varepsilon_{xx}^* - \frac{1}{2}\varepsilon_{xy}\varepsilon_{xy}^* \, \mathrm{d}s \\ = \int_{l_f} \bar{\mathrm{T}}_x u_x^* + \bar{\mathrm{T}}_y u_y^* \, \mathrm{d}l \end{aligned} \tag{2.49}$$

Using the simple experiment situation as in Figure 2.18, it is possible to simulate the application of the VFM in order to identify the unknown parameters Q_{xx} and Q_{xy} (or equivalently Young's modulus E and Poisson's ratio v). It is assumed that a static uniaxial test is performed in tension and in front of the specimen a digital imaging device is recording material deformations during loading. The material given in Figure 2.18 is subjected to a static tension. At the end of the tension test, the force is measured by a test machine as 0.2 N and the DIC analysis applied on digital images produces an axial strain fields ε_{xx} of 0.01 for the whole specimen surface. The complex strain states, which could occur at the end of clamping and loading sides, are ignored in this simple study. The transverse strain field ε_{yy} should be measured as -0.005 as the assumed material has a

Poisson's ratio of 0.5. The surface traction $\bar{T}_x$ in the loading direction is 0.02 MPa (= 0.2 N / cross sectional area). For a simple calculation procedure, zero strain is assumed for the shear strain ε_{xy}. After collecting the experimental data, the next step is to set up the virtual displacement $\boldsymbol{u}^*$. Two sets of $\boldsymbol{u}^*$ are required in order to create two independent PVW equations for the unknown parameters Q_{xx} and Q_{xy}. Satisfying the kinematic admissibility $\boldsymbol{u}^*(x = 0) = 0$, the virtual displacement can in principle take an infinite number of configurations. Two suitable examples of $\boldsymbol{u}^*$ are given below

$$\begin{cases} u_x^{*(1)} = x \\ u_y^{*(1)} = 0 \end{cases} \Rightarrow \begin{cases} \varepsilon_{xx}^{*(1)} = \partial u_x^{*(1)} / \partial x = 1 \\ \varepsilon_{yy}^{*(1)} = \partial u_y^{*(1)} / \partial y = 0 \\ \varepsilon_{xy}^{*(1)} = \partial u_x^{*(1)} / \partial y + \partial u_y^{*(1)} / \partial x = 0 \end{cases} \tag{2.50}$$

$$\begin{cases} u_x^{*(2)} = 0 \\ u_y^{*(2)} = y \end{cases} \Rightarrow \begin{cases} \varepsilon_{xx}^{*(2)} = 0 \\ \varepsilon_{yy}^{*(2)} = 1 \\ \varepsilon_{xy}^{*(2)} = 0 \end{cases} \tag{2.51}$$

Strictly, Eq. (2.51) is not kinematically admissible. However, if the origin of the coordinate of Figure 2.18 is located in the middle of the left-hand side edge, this virtual field is able to cancel the traction at this fixed boundary due to the symmetry of the lateral traction. These virtual fields and the assumed experimental data are substituted in Eq.(2.49), and the following PVW equations are made. The first PVW with $\boldsymbol{u}^{*(1)}$ is

$$Q_{xx} \int_s \varepsilon_{xx} \varepsilon_{xx}^{*(1)} \mathrm{d}s + Q_{xy} \int_s \varepsilon_{yy} \varepsilon_{xx}^{*(1)} \, \mathrm{d}s = \int_{l_f} \bar{T}_x u_x^{*(1)} \, \mathrm{d}l \tag{2.52}$$

$$Q_{xx} \times 0.01 \times WL - Q_{xy} \times 0.005 \times WL = \bar{T}_x \int_{l_f} u_x^{*(1)} \, \mathrm{d}l = \bar{T}_x WL \tag{2.53}$$

$$0.01 Q_{xx} - 0.005 Q_{xy} = \bar{T}_x \tag{2.54}$$

Using a similar procedure, the second PVW with $\boldsymbol{u}^{*(2)}$ is

$$-0.005 Q_{xx} + 0.01 Q_{xy} = 0 \tag{2.55}$$

Gathering Eq. (2.54) and (2.55), the following system of linear equations is constructed:

$$\mathbf{M} = \begin{bmatrix} 0.01 & -0.005 \\ -0.005 & 0.01 \end{bmatrix},\ \mathbf{Q} = \begin{Bmatrix} Q_{xx} \\ Q_{xy} \end{Bmatrix},\ \mathbf{N} = \begin{Bmatrix} 0.02\ (\text{MPa}) \\ 0 \end{Bmatrix}$$

$$\mathbf{MQ} = \mathbf{N} \tag{2.56}$$

The two material parameters are obtained by the inversion of the matrix **M** in Eq. (2.56): Q_{xx} = 2.6667 MPa and Q_{xy} = 1.3333 MPa. Consequently, the Poisson's ratio and Young's modulus are respectively 0.5 (= Q_{xy} / Q_{xx}) and 2 MPa (= $Q_{xx}(1-\nu^2)$); these inversely calculated values are equal to the assumed material parameters in Figure 2.18.

2.3.5 Applications of the static VFM

The example shown above is defined as the linear VFM. The linear VFM is a case in which the constitutive relation is linearly dependent on the material parameters so that the inversion of the matrix **M** in Eq. (2.56) is possible. Also, the VFM used in the calculation example is applied to the static test condition where inertial forces are low enough to be ignored. Thus, the method used above is referred to as the static linear VFM.

The static linear VFM is particularly advantageous for characterizing static material parameters of fibre-reinforced composite materials. The in-plane properties of an orthotropic composite are described by the four independent stiffness parameters: Q_{xx}, Q_{yy}, Q_{xy}, and G. The separated parameter identifications for such a material hold several drawbacks: redesign of composite material specimens for different mechanical test modes are expensive; it is difficult to generate homogeneous strain states, especially for a pure shear test; and this requirement limits the freedom of specimen shape (Pierron and Grédiac, 2012). The application of the VFM and full-field measurements can remedy these limitations. First, the use of full-field measurements captures heterogeneous strain states and the VFM embraces all strain states for parameter identifications. This advantage was first numerically studied for the Iosipescu in-plane shear test (Grédiac et al., 1994). Second, as shown in these studies, the VFM is able to identify the four

independent parameters from a single test as the VFM directly uses a constitutive relation including these parameters (Chalal et al., 2006).

As mentioned, an infinite number of virtual displacement fields can be designed if they satisfy the admissibility and smoothness requirements. Also, the different sets of virtual fields need to be independent. The question might arise as to what is the ideal virtual displacement for the best parameter identification. An arbitrary choice of the virtual displacement could affect the accuracy of the estimated parameters. With regard to this issue, Grédiac et al. (2002a;2002b) suggested a guideline for designing a good virtual displacement field reducing the noise sensitivity induced from the measurement errors. The method is to evaluate the independency of the matrix **M** in Eq. (2.56). The complete independency can be achieved by making **M** equal to the identity matrix **I** so that the condition number of **M** is equal to 1. Consequently, the solution of the linear system is less sensitive to small changes in the matrix **N**. The virtual fields able to make **M** = **I** are denoted as the special virtual fields. An automatic way of producing the special virtual fields has been developed for the linear VFM (Avril et al., 2004). This technique is called the optimised piecewise special virtual fields in this thesis. The meaning of "optimised" represents that the virtual displacements are determined by optimizing nodal virtual displacements by reducing the noise sensitivity of the strain measurements and satisfying the kinematic admissibility and the specialty condition, mentioned above. The term "piecewise" indicates that the virtual fields are expanded in a piecewise manner. This meaning will be clear in Section 3.3. The nodal values are then collected to form the virtual displacement fields. The optimized piecewise special virtual fields were used in some of the present research; the description will be given more in a later chapter.

If the stress term in the PVW equation is given by a nonlinear constitutive relation, it is referred to as the nonlinear VFM. A constitutive relation is nonlinear when stresses are

not linearly dependent on deformations due to rate dependency, plasticity, damage and strain-dependent stiffness. This nonlinearity makes it no longer possible to construct the system of linear equations, Eq. (2.56). Instead of using this equation, in the nonlinear VFM, the following cost function is set, e.g. for a static case (Pierron and Grédiac, 2012):

$$\left(\int_s \boldsymbol{\sigma} : \boldsymbol{\varepsilon}^* \mathrm{d}s - \int_{l_f} \bar{\mathbf{T}} \cdot \boldsymbol{u}^* \mathrm{d}l \right)^2 = 0 \tag{2.57}$$

Based on this equation, the nonlinear VFM has been adopted for identifying material parameters of the nonlinear models such as plasticity (Grédiac and Pierron, 2006; Kim et al., 2013; Pannier et al., 2006) and viscoplasticity (Notta-Cuvier et al., 2013; Pannier et al., 2006). In contrast to the linear VFM, there is no restriction about the number of independent virtual fields. Even one virtual displacement field can be used by employing the whole history of experimental data (e.g. strain field at each time, t_i) and creating the cost functions at each t_i. The parameter identifications are achieved by minimizing the sum of the residuals of all cost functions:

$$\Phi = \sum_{i=1}^{N} \left[\int_s \boldsymbol{\sigma} : \boldsymbol{\varepsilon}^* \mathrm{d}s - \int_{l_f} \bar{\mathbf{T}} \cdot \boldsymbol{u}^* \mathrm{d}l \right]^2 \tag{2.58}$$

where N is the total number of time steps. The virtual field does not need to be constant through all time steps; it is possible to adopt the optimized virtual method so that different piecewise virtual fields are created with regards to different noise sensitivity of each time step (Pierron et al., 2010).

The static VFM has been applied to a few experimental studies on elastomers. Promma et al. (2009) has used the static VFM technique for a natural rubber with equibiaxial tests. This study adopted the Mooney-Rivlin hyperelastic model in the PVW equation. Although this model gives a nonlinear relationship between stress and strain, its material parameters can be taken out from the integration term of the PVW, and the formation of the linear system is possible. Thus, this study utilized the linear VFM with the two

independent virtual fields for the two parameters. The full-field measurement was conducted by the DIC procedure, which was able to measure the complex strain states (equibiaxial tension, pure shear and uniaxial tension states). The identified parameters show a slight dependency with respect to the applied strain. This could be because the parameters identified by the linear VFM at a low strain level are not sufficient to represent the mechanical behaviour at large strain. A similar method has been used on a styrene-butadiene rubber (Palmieri et al., 2011) but with the nonlinear approach for the Ogden model parameters. In contrast to the first study, it is mathematically difficult to take out the two material parameters of the Ogden model from the integration. Thus, in this study, the nonlinear approach, Eq. (2.58), was applied to the total history of the mechanical test results with three different shapes of the specimens. The nonlinear method seems more practical for the case of elastomers because the application of the linear VFM is difficult for most hyperelastic models. Also, it is physically reasonable that the hyperelastic parameters can be more accurately identified with a total loading history (Promma et al., 2009).

2.3.6 Applications of the dynamic VFM

It should be recalled that the traditional SHPB test on elastomers has two significant difficulties: poor quality force measurements and long period of the non-equilibrium state. For these difficulties, the application of the dynamic VFM can be an ideal solution because, simply, the traditional force measurements are no longer required. Instead, the non-equilibrium state is used as a force measurement. This non-conventional measurement method is made possible by the following PVW:

$$-\int_{\mathrm{v}} \boldsymbol{\sigma} : \boldsymbol{\varepsilon}^{*} \mathrm{d}v = \int_{\mathrm{v}} \rho \boldsymbol{a} \cdot \boldsymbol{u}^{*} \mathrm{dv} \tag{2.59}$$

This PVW is made with the virtual fields specially designed to mathematically cancel the traction force term (external virtual work term). The derivation of this equation is

explained in detail in a later chapter. The development of this dynamic PVW indicates two important advantages over the traditional dynamic test: (1) the measurement of the acceleration fields during a dynamic test replaces the need of a force measurement technique, the utilization of which is difficult, in particular, for soft materials and (2) the use of the acceleration equivalently means that the stress equilibrium is no longer a compulsory requirement as a clear acceleration field is generated by a non-uniform deformation of a test specimen. Eq. (2.59) has been adopted for a dynamic characterization using both the linear and nonlinear VFM on metal (Kim et al., 2015; Louëdec et al., 2013; Pierron et al., 2011), fibre-reinforced composites (Moulart et al., 2011; Pierron et al., 2014) and concrete (Pierron and Forquin, 2012).

This VFM scheme is very advantageous for a dynamic test on elastomers. The aforementioned two advantages of the dynamic VFM can overcome the two disadvantages arising from the conventional impact test techniques. The consideration of the high noise-to-signal ratio for the measurement of low force values of rubbers, as indicated by Figure 2.10, is no longer required because traditional force measurement is not necessary. The generation of the acceleration fields requires a dynamic displacement field non-uniformly distributed over the specimen surface. The non-equilibrium state is no longer an experimental obstacle but full-field data that needs to be measured. Furthermore, the low sound speed allows stress wave propagation in these materials to be monitored at relatively low speeds, e.g. 50 000 frames per second, for which high quality images can be obtained from digital high speed video cameras. These two aspects of the dynamic VFM compared to the traditional dynamic tests are the main motivation of the present research. The dynamic VFM, Eq. (2.59), is the main technique used throughout this present research.

2.4 Summary

It is recalled that elastomers exhibit a nonlinear stress-strain curve and high rate dependency, and these properties are required to be measured for engineering applications. Several high-rate experimental techniques are introduced with their limitations for a dynamic test on elastomers. Two limitations are highlighted: high noise-to-signal ratio of the force measurement and long period of the non-equilibrium state. As a solution for these limitations, the VFM with DIC for full-field measurements is introduced. Especially, the dynamic VFM applications presented in the previous works (Moulart et al., 2011; Pierron et al., 2014) are the basis of many aspects utilized in the present research as the two experimental limitations are simply removed by the means of the non-conventional force measurement method, the use of acceleration fields. Moreover, the experimental simplification as a result of this non-conventional measurement of the dynamic VFM provides greater freedom in experimental designs for high-rate tests and so an opportunity of extracting dynamic mechanical properties of elastomers, which is not accessible by the traditional techniques. It is therefore proposed here to develop a high-rate experimental system for characterizing the dynamic mechanical property of elastomers by means of the dynamic VFM and high-speed full-field measurements. The proposed experimental technique is presented in the following chapters.

2.5 Chapter introductions

2.5.1 Chapter 3: DESCRIPTION OF THE DYNAMIC VFM

The dynamic VFM briefly introduced in this chapter is explained in more detail. The analytical example used for explaining the static VFM in Section 2.3.4 is similarly designed for the case of a dynamic experiment in tension. The calculation procedure of the PVW with respect to a discrete data field obtained from either numerical simulation

or experimental data is described. The definition of the optimized piecewise virtual fields is presented.

2.5.2 Chapter 4: THE LINEAR VFM: FEM SIMULATION

The linear VFM explained in the previous chapter is applied to FEM simulation data. The simulation was conducted with configurations given by an actual dynamic experiment. The simulation data extracted as obtained from the test were analysed by the linear VFM in order to show the identification capability. The pre-stretching method is introduced as a solution for characterizing rubber up to a large deformation level.

2.5.3 Chapter 5: THE LINEAR VFM: EXPERIMENTAL APPLICATION

The same VFM procedure is applied to the experimental data produced by a drop-weight experiment. The actual drop-weight experiment is described in terms of experiment steps and high-speed imaging configurations; also some graphical experimental data are shown. At the end of this chapter, an evaluation of the identification results of the proposed VFM technique with regard to several data calculation factors is presented.

2.5.4 Chapter 6: THE NONLINEAR VFM

The application of the nonlinear VFM is proposed as an alternative experimental technique for a dynamic test on rubbers. A gas-gun test is proposed and explained with pictures and experimental procedures. The description of the nonlinear VFM is given, showing how the material parameters of a nonlinear model are directly obtained without the use of the pre-stretching. The explanation starts with the verification of the nonlinear VFM using FEM simulations and ends with the procedure of the actual experimental application.

2.5.5 Chapter 7: THE INCREMENTAL LINEAR VFM

This chapter explores a potential improvement to the linear VFM introduced in Chapter 4. The improved linear VFM in this chapter attempts to remove the static force measurement required in the PVW. A different form of the equation of motion is adopted to derive the new VFM. FEM simulation works are presented to show the difference between the old and new linear VFM with respect to experimental error sources. In addition, some of the VFM results are compared with SHPB experiments conducted at similar strain rates.

2.5.6 Chapter 8: FURTHER APPLICATIONS OF THE VFM

This chapter consists of two parts. The first part introduces a possible way of combining the linear and nonlinear VFM procedures presented in the previous chapters. The combined VFMs are proposed as a technique to approximate a stress-strain curve prior to the actual identification so that the determination of an appropriate nonlinear model to implement in the linear VFM can be performed. The second part shows further application of the nonlinear VFM, in which a viscoelastic constitutive model is included. This new VFM is used to attempt to identify part of the relaxation behaviour of rubber. For both of the cases, FEM simulations are presented for the verification of their VFM procedures.

2.5.7 Chapter 9: CONCLUSIONS

This chapter provides summaries for all previous chapters in a condensed form. Then, possible future works are listed focusing on improvements, further analysis and applications.

Chapter 3 DESCRIPTION OF THE DYNAMIC VFM

3.1 Introduction

This chapter provides a description of the dynamic VFM in the same manner as the static VFM introduced in Section 2.3.4. An analytically solvable material model is assumed and subjected to dynamic loading in tension, which is similar to the actual experiments conducted in the research presented in the next two chapters. With this analytical experiment, the application of the dynamic VFM is mathematically described. Also, it will be explained how to generate the dynamic PVW and apply discrete full-field data in this equation. In Section 2.3.5, an automated method to determine an ideal virtual field was mentioned. At the end of this chapter, there will be a description of the automated method, the optimized piecewise virtual fields, for the application of the dynamic VFM. This description applies to the case of the linear dynamic VFM. Further information on the VFM can be found in a recent textbook, which gives a comprehensive review of the topic (Pierron and Grédiac, 2012).

The objectives of this chapter can be summarized as below:

- This chapter introduces the concept of the dynamic VFM so that readers can understand how materials can be mechanically characterized without the measurement of the traction force.
- An analytical (linear elastic) material model is assumed in order to show the mathematical procedure of the dynamic VFM and the identification capability for this assumed material.
- The identification of the VFM is sensitive to an imaging random error. This effect can be alleviated by means of the optimized piecewise virtual field. The application procedure of this method is described in this chapter. This procedure is applied to the simulation and experimental works introduced in Chapter 4 and Chapter 5.

3.2 Description of the dynamic VFM

3.2.1 Analytical description

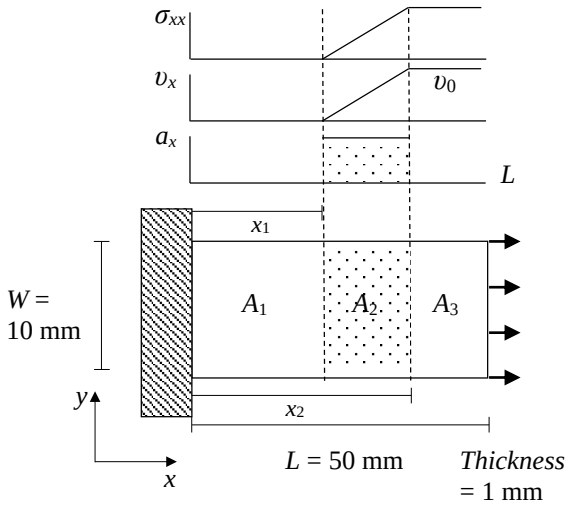

Figure 3.1 Axial stress, velocity and acceleration profiles as a function of position in the specimen at time t after loading and the resulting acceleration field. The acceleration is a_x in the region A_2 and zero elsewhere.

The simple two-dimensional geometry used in this calculation is shown in Figure 3.1. A linear elastic model is used to ensure a simple calculation. The material parameters are chosen to be similar to the general behaviour of a typical homogeneous rubber: Young's modulus E = 2 MPa, Poisson's ratio ν = 0.5, density ρ = 1200 kg m^{-3} and longitudinal wave speed 40.8 m s^{-1}, $c = \sqrt{E/\rho}$. Under the chosen applied loading, the velocity v_x of the free end rises from 0 to v_0 = 5 m s^{-1} in 10 μs (t_r) and afterward is constant. As a result of the wave propagation, the specimen may be considered as three regions with different velocity fields, as shown in Figure 3.1. At any time after t_r, the length of the area A_2 is obtained by $x_2 - x_1 = c \times t_r$ and the lengths of A_3 and A_1 can be similarly calculated. In the region A_2, assuming a linearly increasing velocity, the longitudinal acceleration can be calculated as $a_x = c(v_0 / (x_2 - x_1)) = 5\times10^5$ m s^{-2}, and the lateral acceleration is assumed to be close to zero, $a_y \approx 0$. The longitudinal stress wave field, σ_{xx}, follows the velocity profile assuming the one-dimensional stress wave equation, $\sigma_{xx} = \rho c v_x$. It should be noted that, throughout this thesis, the x and y coordinates usually indicate the lengthwise loading and transversal directions, respectively.

The first step is to write the principle of virtual work to apply the VFM, here recalled again:

$$-\int_{\mathrm{v}} \boldsymbol{\sigma} : \boldsymbol{\varepsilon}^{*} \mathrm{dv} + \int_{s_f} \bar{\mathbf{T}} \cdot \boldsymbol{u}^{*} \mathrm{ds} = \int_{\mathrm{v}} \rho \boldsymbol{a} \cdot \boldsymbol{u}^{*} \mathrm{dv} \tag{3.1}$$

In a low rate ('quasi-static') experiment, $\boldsymbol{a}$ would be negligible, and the traction $\bar{\mathbf{T}}$ would be used to calculate the material response; with dynamic loading, $\boldsymbol{a}$ is no longer negligible. In the case of a dynamic test on rubber, $\boldsymbol{a}$ can be clearly observed but $\bar{\mathbf{T}}$ is more difficult to measure due to low wave speed and stiffness. The measurement difficulty of $\bar{\mathbf{T}}$ can be removed by mathematically designing the virtual displacement fields $\boldsymbol{u}^{*}$ so that the traction term in Eq. (2.44) is removed. The following virtual fields enable the elimination of the traction term (Moulart et al., 2011):

$$\begin{cases} u_x^{*(1)} = x(x-L) \\ u_y^{*(1)} = 0 \end{cases} \Rightarrow \begin{cases} \varepsilon_{xx}^{*(1)} = 2x - L \\ \varepsilon_{yy}^{*(1)} = 0 \\ \varepsilon_{xy}^{*(1)} = 0 \end{cases}$$
$$\begin{cases} u_x^{*(2)} = 0 \\ u_y^{*(2)} = x(x-L)y \end{cases} \Rightarrow \begin{cases} \varepsilon_{xx}^{*(2)} = 0 \\ \varepsilon_{yy}^{*(2)} = x(x-L) \\ \varepsilon_{xy}^{*(2)} = (2x-L)y \end{cases} \tag{3.2}$$

The two independent virtual displacement fields are made for the identification of the two material parameters E and ν (equivalently Q_{xx} and Q_{xy}). The use of either the first or second virtual fields leads to the formation of the dynamic PVW equation:

$$-\int_{\mathrm{v}} \boldsymbol{\sigma} : \boldsymbol{\varepsilon}^{*} \mathrm{dv} = \int_{\mathrm{v}} \rho \boldsymbol{a} \cdot \boldsymbol{u}^{*} \mathrm{dv} \tag{3.3}$$

With Eq. (3.2) and the isotropic linear elastic relation, Eq. (2.48), the dynamic PVW equation, Eq. (3.3) can be transformed into the following system of linear equations.

$$\begin{bmatrix} \mathrm{M}_{11} & \mathrm{M}_{12} \\ \mathrm{M}_{21} & \mathrm{M}_{22} \end{bmatrix} \begin{Bmatrix} Q_{xx} \\ Q_{xy} \end{Bmatrix} = \begin{Bmatrix} \mathrm{N}_1 \\ \mathrm{N}_2 \end{Bmatrix} \tag{3.4}$$

$$\mathrm{M}_{11} = \int_{\mathrm{v}} \left(\varepsilon_{xx} \varepsilon_{xx}^{*(1)} + \varepsilon_{yy} \varepsilon_{yy}^{*(1)} + \frac{1}{2} \varepsilon_{xy} \varepsilon_{xy}^{*(1)} \right) \mathrm{dv} \tag{3.5}$$

$$\mathrm{M}_{12} = \int_{\mathrm{v}} \left(\varepsilon_{xx}\varepsilon_{yy}^{*(1)} + \varepsilon_{yy}\varepsilon_{xx}^{*(1)} - \frac{1}{2}\varepsilon_{xy}\varepsilon_{xy}^{*(1)} \right) \mathrm{dv} \tag{3.6}$$

$$\mathrm{M}_{21} = \int_{\mathrm{v}} \left(\varepsilon_{xx}\varepsilon_{xx}^{*(2)} + \varepsilon_{yy}\varepsilon_{yy}^{*(2)} + \frac{1}{2}\varepsilon_{xy}\varepsilon_{xy}^{*(2)} \right) \mathrm{dv} \tag{3.7}$$

$$\mathrm{M}_{22} = \int_{\mathrm{v}} \left(\varepsilon_{xx}\varepsilon_{yy}^{*(2)} + \varepsilon_{yy}\varepsilon_{xx}^{*(2)} - \frac{1}{2}\varepsilon_{xy}\varepsilon_{xy}^{*(2)} \right) \mathrm{dv} \tag{3.8}$$

$$\mathrm{N}_1 = -\int_{\mathrm{v}} \rho \left(a_x u_x^{*(1)} + a_y u_y^{*(1)} \right) \mathrm{dv} \tag{3.9}$$

$$\mathrm{N}_2 = -\int_{\mathrm{v}} \rho \left(a_x u_x^{*(2)} + a_y u_y^{*(2)} \right) \mathrm{dv} \tag{3.10}$$

In an actual experiment, the strain field data (ε_{xx} and ε_{yy}) would be calculated from the displacement field obtained from full-field measurements. For the present analytical calculation, they are obtained using the linear elastic constitutive relation, the given material parameters (E and ν), the stresses σ_{xx} ($\sigma_{yy} = \sigma_{xy} \approx 0$) and the assumption that $\varepsilon_{xy} \approx 0$. Eq. (3.4) can be further simplified to the two-dimensional case by the assumption of constant stresses through the specimen thickness, hence the volumetric integral can be converted to a surface integral. In order to simplify the calculation procedure, the initial specimen configuration is used in this integral although the integration domain in Eq. (3.3) is based on the current configuration. The integration of the components of Eq. (3.4) is conducted as follows, with the assumption of plane stress (h = thickness):

$$\mathrm{M}_{11} = h \sum_{i=1}^{3} \int_{A_i} \left(\varepsilon_{xx}\varepsilon_{xx}^{*(1)} + \varepsilon_{yy}\varepsilon_{yy}^{*(1)} \right) \mathrm{d}A_i \tag{3.11}$$

The strain fields have zero value in the area of A_1. The components of **M** and **N** have the same h term; this can be removed from Eq. (3.4). The strain in A_3 is constant (ε_{xx0}), and the linearly increasing strain in A_2 is described as $\varepsilon_{xx} = \varepsilon_{xx0}(x - x_1) / (x_2 - x_1)$, so Eq. (3.11) becomes

$$\begin{aligned}\mathrm{M}_{11} &= \int_{A_2}\left(\varepsilon_{xx}\varepsilon_{xx}^{*(1)}+\varepsilon_{yy}\varepsilon_{yy}^{*(1)}\right)\mathrm{d}A_2+\int_{A_3}\left(\varepsilon_{xx}\varepsilon_{xx}^{*(1)}+\varepsilon_{yy}\varepsilon_{yy}^{*(1)}\right)\mathrm{d}A_3\\ &= \varepsilon_{xx0}W\int_{x_1}^{x_2}\frac{x-x_1}{x_2-x_1}\left(2x-L\right)\mathrm{d}x+\varepsilon_{xx0}W\int_{x_2}^{L}2x-L\ \mathrm{d}x\end{aligned} \tag{3.12}$$

Evaluating the two integrals gives

$$\mathrm{M}_{11}=\varepsilon_{xx0}W\frac{\left(x_2-x_1\right)\left(2x_1-3L+4x_2\right)}{6}+\varepsilon_{xx0}Wx_2\left(L-x_2\right) \tag{3.13}$$

This integration procedure is similarly used for the other components of Eq. (3.4) as shown below

$$\begin{aligned}\mathrm{M}_{12} &= \int_{A_2}\left(\varepsilon_{xx}\varepsilon_{yy}^{*(1)}+\varepsilon_{yy}\varepsilon_{xx}^{*(1)}\right)\mathrm{d}A_2+\int_{A_3}\left(\varepsilon_{xx}\varepsilon_{yy}^{*(1)}+\varepsilon_{yy}\varepsilon_{xx}^{*(1)}\right)\mathrm{d}A_3\\ &= \varepsilon_{yy0}W\int_{x_1}^{x_2}\frac{x-x_1}{x_2-x_1}\left(2x-L\right)\mathrm{d}x+\varepsilon_{yy0}W\int_{x_2}^{L}2x-L\ \mathrm{d}x\\ &= \varepsilon_{yy0}W\frac{\left(x_2-x_1\right)\left(2x_1-3L+4x_2\right)}{6}+\varepsilon_{yy0}Wx_2\left(L-x_2\right)\end{aligned} \tag{3.14}$$

$$\begin{aligned}\mathrm{M}_{21} &= \int_{A_2}\left(\varepsilon_{xx}\varepsilon_{xx}^{*(2)}+\varepsilon_{yy}\varepsilon_{yy}^{*(2)}\right)\mathrm{d}A_2+\int_{A_3}\left(\varepsilon_{xx}\varepsilon_{xx}^{*(2)}+\varepsilon_{yy}\varepsilon_{yy}^{*(2)}\right)\mathrm{d}A_3\\ &= \varepsilon_{yy0}W\int_{x_1}^{x_2}\frac{x-x_1}{x_2-x_1}x\left(x-L\right)\mathrm{d}x+\varepsilon_{yy0}W\int_{x_2}^{L}x\left(x-L\right)\mathrm{d}x\\ &= \varepsilon_{yy0}W\frac{\left(x_2-x_1\right)\left(x_1^2+2x_1x_2-2Lx_1+3x_2^2-4Lx_2\right)}{12}\\ &\quad+\varepsilon_{yy0}W\frac{\left(L-x_2\right)^2\left(-L-2x_2\right)}{6}\end{aligned} \tag{3.15}$$

$$\begin{aligned}\mathrm{M}_{22} &= \int_{A_2}\left(\varepsilon_{xx}\varepsilon_{yy}^{*(2)}+\varepsilon_{yy}\varepsilon_{xx}^{*(2)}\right)\mathrm{d}A_2+\int_{A_3}\left(\varepsilon_{xx}\varepsilon_{yy}^{*(2)}+\varepsilon_{yy}\varepsilon_{xx}^{*(2)}\right)\mathrm{d}A_3\\ &= \varepsilon_{xx0}W\int_{x_1}^{x_2}\frac{x-x_1}{x_2-x_1}x\left(x-L\right)\mathrm{d}x+\varepsilon_{xx0}W\int_{x_2}^{L}x\left(x-L\right)\mathrm{d}x\\ &= \varepsilon_{xx0}W\frac{\left(x_2-x_1\right)\left(x_1^2+2x_1x_2-2Lx_1+3x_2^2-4Lx_2\right)}{12}\\ &\quad+\varepsilon_{xx0}W\frac{\left(L-x_2\right)^2\left(-L-2x_2\right)}{6}\end{aligned} \tag{3.16}$$

$$\begin{aligned} \mathrm{N}_1 &= -\rho \int_{A_2} \left(a_x u_x^{*(1)} + a_y u_y^{*(1)} \right) \mathrm{d}A_2 \\ &= -\rho a_x \int_{x_1}^{x_2} x(x-L)\, \mathrm{d}x \\ &= -\frac{\rho a_x \left(-2x_1^3 + 3Lx_1^2 + 2x_2^3 - 3Lx_2^2 \right)}{6} \end{aligned} \tag{3.17}$$

$$\mathrm{N}_2 = -\rho \int_{A_2} \left(a_x u_x^{*(2)} + a_y u_y^{*(2)} \right) \mathrm{d}A \approx 0 \tag{3.18}$$

With this integration procedure and the assumed full-field data, Eq. (3.4) is calculated at a time of 50 μs and the following material parameters are obtained

$$E = 2 \text{ MPa}$$
$$\nu = 0.5$$

These values agree exactly with the given material properties.

3.2.2 Integration procedure for an actual experiment

When applying the VFM analysis to experimental or FEM simulation results, the strain and acceleration data are not continuous but are instead an array of discrete values at a large number of locations on the specimen surface. Thus, the integral procedure for Eq. (3.4) must be approximated by discrete sums (Pierron and Grédiac, 2012). For example, M_{11} would be evaluated as follows

$$\mathrm{M}_{11} = \int_{\mathrm{v}} \left(\varepsilon_x \varepsilon_x^{*(1)} + \varepsilon_y \varepsilon_y^{*(1)} + \frac{1}{2} \varepsilon_{xy} \varepsilon_{xy}^{*(1)} \right) \mathrm{dv} \tag{3.19}$$

$$= \sum_{i=1}^{n} \varepsilon_x(\psi_i) \left(2x(\psi_i) - L \right) \mathrm{v}(\psi_i) \tag{3.20}$$

$$= \overline{\varepsilon_x(\psi_i)(2x(\psi_i) - L)}\mathrm{v} \tag{3.21}$$

In Eq. (3.20), the specimen is split into n discrete regions of volume $\mathrm{v}(\psi_i)$; $\varepsilon_{xx}(\psi_i)$ and $x(\psi_i)$ are the strain and x coordinate at the centre of the i^{th} discrete region (ψ_i). The strain and acceleration values within each discrete region are assumed to be constant for this integral procedure. Thus, the volume of this region, i.e. the total number of measurement points, is an important factor for the identification quality of the VFM. Eq. (3.20) can be simplified further to Eq. (3.21)

because v(ψ_i) does not change under the assumption of incompressibility, and it is logical to start with *n* regions of the same volume. The over bar in Eq. (3.21) indicates averaging over the integral region. Every component of the matrices **M** and **N** has v outside the averaging term so that this total volume term can be removed from Eq. (3.21).

Using the same procedure, the discrete sum for N_1 is

$$N_1 = -\rho \int_{A_2} \left(a_x u_x^{*(1)} + a_y u_y^{*(1)} \right) \mathrm{d}A_2 \tag{3.22}$$

$$= -\rho \sum_{i=1}^{n} a_x(\psi_i) \left(x(\psi_i)(x(\psi_i) - L) \right) \mathrm{v}(\psi_i) \tag{3.23}$$

$$= -\rho \mathrm{v} \overline{a_x(\psi_i) \left(x(\psi_i)(x(\psi_i) - L) \right)} \tag{3.24}$$

This integration method was adopted throughout all simulation and experimental works in the present research.

The description of the dynamic VFM presented above is used with the linear elastic constitutive relation, by which it is possible to make the system of linear equations, Eq. (3.4). In the present research, this dynamic VFM is referred to as *the linear* VFM. As briefly mentioned in Section 2.3.4, the VFM can apply to nonlinear constitutive relations; the dynamic VFM can also include nonlinear models. The dynamic VFM, in which the PVW equation is built with the nonlinear model, is referred to as *the nonlinear* VFM and presented in Chapter 6.

3.3 Optimized piecewise virtual fields

As mentioned in Section 2.3.5, one guideline for designing the virtual fields is to make the matrix **M** of Eq. (2.56) equal to the identity matrix **I** so that the solution of Eq. (2.56) is not significantly affected by a small perturbation (noise) on **M** (Grédiac et al., 2002a). Virtual fields following this guideline and easily satisfying the requirement of kinematic admissibility can be automatically made by the optimized piecewise virtual fields method. This method is well described in the VFM textbook (Pierron and Grédiac, 2012) for the case of the static VFM with

the orthotropic constitutive relation. The piecewise virtual field was utilized for the research presented in Chapter 4 and Chapter 5 where the isotropic linear elastic constitutive relation is applied to the dynamic PVW. In this section, the application method of the optimized piecewise virtual field is briefly explained. The overall description is similar to that described in the VFM textbook except for slight modifications to include the isotropic relation and the dynamic PVW. This dynamic VFM was similarly adopted in a previous VFM study: (Zhu, 2015). The first section provides the definition of the piecewise virtual field; in the next section, the automatic method of arranging the piecewise field is described.

3.3.1 Piecewise virtual fields

In FEM, the actual displacement (and strain) fields are expressed by some mathematical functions (e.g. polynomials) by which the discrete displacement values at each node of a numerical element (mesh) are interpolated. The displacement value at a particular local coordinate (ξ, ς) within this element is expanded by performing an interpolation. This approximation method can be also used for the construction of the virtual displacement $\boldsymbol{u}^*$. The example of defining the piecewise virtual fields with a quadrilateral element is given in Figure 3.2.

The interpolation of the virtual nodal displacement $\tilde{\boldsymbol{u}}^*_{(e)}$ of an element e is mathematically expressed as

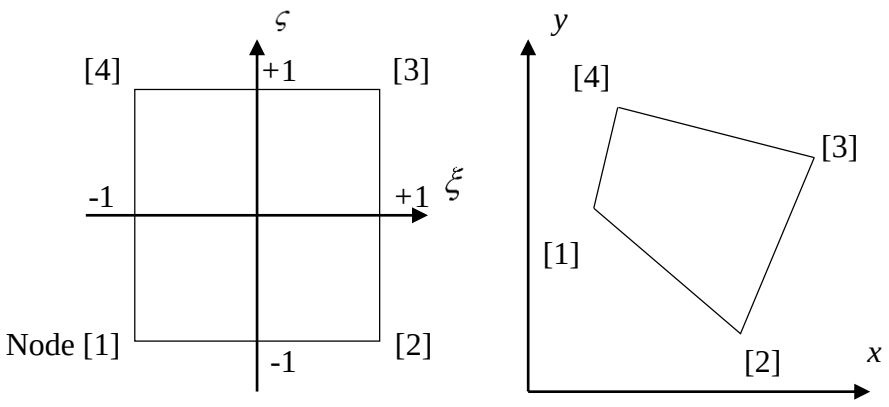

Figure 3.2 (left) Local coordinate and (right) global coordinate systems of a four-node quadrilateral element.

$$\tilde{\boldsymbol{u}}^*_{(e)} = \begin{Bmatrix} \tilde{u}^*_{x,[1]} \\ \tilde{u}^*_{y,[1]} \\ \vdots \\ \tilde{u}^*_{x,[4]} \\ \tilde{u}^*_{y,[4]} \end{Bmatrix} \tag{3.25}$$

$$\begin{cases} \boldsymbol{u}^*_{(e)}(\xi,\varsigma) = \boldsymbol{H}_{(e)}(\xi,\varsigma)\tilde{\boldsymbol{u}}^*_{(e)} \\ u^*_{x,(e)}(\xi,\varsigma) = \boldsymbol{H}_{1,(e)}(\xi,\varsigma)\tilde{\boldsymbol{u}}^*_{(e)} \\ u^*_{y,(e)}(\xi,\varsigma) = \boldsymbol{H}_{2,(e)}(\xi,\varsigma)\tilde{\boldsymbol{u}}^*_{(e)} \end{cases} \tag{3.26}$$

$$\boldsymbol{H}_{(e)} = \begin{bmatrix} \boldsymbol{H}_{1,(e)} \\ \boldsymbol{H}_{2,(e)} \end{bmatrix} \tag{3.27}$$

and for the virtual strain

$$\begin{cases} \boldsymbol{\varepsilon}^*_{(e)}(\xi,\varsigma) = \boldsymbol{B}_{(e)}(\xi,\varsigma)\tilde{\boldsymbol{u}}^*_{(e)} \\ \varepsilon^*_{xx,(e)}(\xi,\varsigma) = \boldsymbol{B}_{1,(e)}(\xi,\varsigma)\tilde{\boldsymbol{u}}^*_{(e)} \\ \varepsilon^*_{yy,(e)}(\xi,\varsigma) = \boldsymbol{B}_{2,(e)}(\xi,\varsigma)\tilde{\boldsymbol{u}}^*_{(e)} \\ \varepsilon^*_{xy,(e)}(\xi,\varsigma) = \boldsymbol{B}_{3,(e)}(\xi,\varsigma)\tilde{\boldsymbol{u}}^*_{(e)} \end{cases} \tag{3.28}$$

$$\boldsymbol{B}_{(e)} = \begin{bmatrix} \boldsymbol{B}_{1,(e)} \\ \boldsymbol{B}_{2,(e)} \\ \boldsymbol{B}_{3,(e)} \end{bmatrix} \tag{3.29}$$

where $\tilde{\boldsymbol{u}}^*_{(e)}$ is the vector of nodal displacements of the node of element *e*; $\boldsymbol{H}$ and $\boldsymbol{B}$ are respectively the displacement interpolation and strain-displacement matrices. The definition of these two matrices for a four-node quadrilateral element is given in the VFM textbook (Pierron and Grédiac, 2012) for the 2D case. The results of Eq. (3.26) and (3.28) for each virtual element are then assembled to form the following global system

$$\begin{cases} u^*_x(x,y) = \boldsymbol{H}_1(x,y)\tilde{\boldsymbol{u}}^* \\ u^*_y(x,y) = \boldsymbol{H}_2(x,y)\tilde{\boldsymbol{u}}^* \end{cases} \tag{3.30}$$

$$\begin{cases} \varepsilon_{xx}^{*}(x,y) = \boldsymbol{B}_1(x,y)\tilde{\boldsymbol{u}}^{*} \\ \varepsilon_{yy}^{*}(x,y) = \boldsymbol{B}_2(x,y)\tilde{\boldsymbol{u}}^{*} \\ \varepsilon_{xy}^{*}(x,y) = \boldsymbol{B}_3(x,y)\tilde{\boldsymbol{u}}^{*} \end{cases} \tag{3.31}$$

where $\tilde{\boldsymbol{u}}^{*}$ is a vector containing the virtual nodal displacements of all virtual nodes; $\boldsymbol{H}_{1,2}$ and $\boldsymbol{B}_{1,2,3}$ are the matrices consisting of $\boldsymbol{H}_{1,2}^{(e)}$ and $\boldsymbol{B}_{1,2,3}^{(e)}$ from the global assemblage procedure, which is introduced in the example of the MATLAB application in the VFM textbook (Pierron and Grédiac, 2012). Using Eq. (3.30) and (3.31), the integral of the dynamic PVW, for example, Eq. (3.5), can be written for the 2D case as

$$\begin{aligned} &\int_s \left(\varepsilon_{xx}\varepsilon_{xx}^{*(1)} + \varepsilon_{yy}\varepsilon_{yy}^{*(1)} + \frac{1}{2}\varepsilon_{xy}\varepsilon_{xy}^{*(1)} \right) \mathrm{d}s \\ &= \left[\frac{s}{n} \sum_{i=1}^{n} \left(\varepsilon_{xx}(\psi_i)\boldsymbol{B}_1(\psi_i) + \varepsilon_{yy}(\psi_i)\boldsymbol{B}_2(\psi_i) + \varepsilon_{xy}(\psi_i)\boldsymbol{B}_3(\psi_i) \right) \right] \cdot \tilde{\boldsymbol{u}}^{*} \end{aligned} \tag{3.32}$$

The example of the arrangement of the nodal $\tilde{\boldsymbol{u}}^{*}$, which was used for the research in Chapter 4 and Chapter 5, is shown in Figure 3.3. A 2×3 virtual quadrilateral mesh is made on a 2D uniaxial specimen. This virtual mesh includes three nodes on each end edges and the rest in the middle. The first step is to define the local coordinate of each virtual element, one of which is represented by the blue (dash) rectangle in Figure 3.3. A convenient method is introduced in the VFM textbook (Pierron and Grédiac, 2012). Each virtual element is given tag numbers, conveniently denoted as *iii* and *jjj* respectively representing the column and row of elements as shown in the numbers in the parentheses (*iii*, *jjj*) in Figure 3.3. The actual data point is given the same number of each element where they are included. The global coordinate and the tag numbers of the data point are used to obtain the local coordinate by the following relation (Pierron and Grédiac, 2012):

$$\begin{aligned} \xi &= 2x / L_{(e)} - 2iii + 1 \\ \varsigma &= 2y / \mathrm{W}_{(e)} - 2\,jjj + 1 \end{aligned} \tag{3.33}$$

After giving the local coordinate, the relations of Eq. (3.26) and (3.28) can be used so that each data point at the global coordinate x, y has its corresponding $\boldsymbol{u}^*(x, y)$ and $\boldsymbol{\varepsilon}^*(x, y)$ expanded from the virtual nodal displacement $\tilde{\boldsymbol{u}}^*$. In the next section, the automated method of the determination of $\tilde{\boldsymbol{u}}^*$ is explained; this explanation is still based on the virtual element configuration shown in Figure 3.3

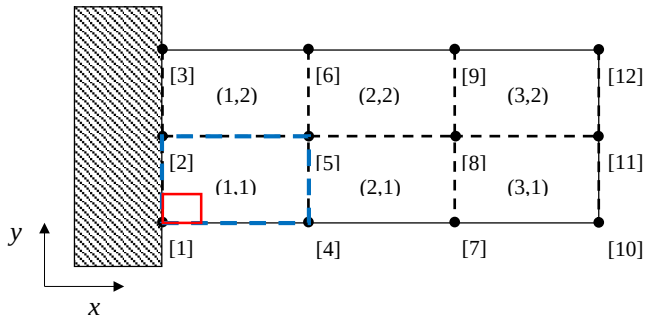

Figure 3.3 Arrangement of the virtual nodal displacements on a specimen surface: the blue rectangle is the virtual element with four nodes, and the red rectangle is the location of an actual data point.

3.3.2 Optimization method for determining the piecewise virtual field

The piecewise virtual field also has to meet the requirement of kinematic admissibility to cancel the traction at the fixed boundary. Another condition is required for the dynamic VFM in which the traction term at a loaded boundary of the PVW equation is also cancelled. These two conditions are satisfied by enforcing the following relations:

$$\tilde{\boldsymbol{u}}^*_{[1],[2],[3]} = 0 \tag{3.34}$$

$$\tilde{\boldsymbol{u}}^*_{[10],[11],[12]} = 0 \tag{3.35}$$

An additional guideline can be applied so that the virtual field is designed such that the matrix **M** of Eq. (2.56) is equal to the identity matrix **I**. However, there is still free degrees of freedom for the virtual nodal displacements. An automated method for determining $\tilde{\boldsymbol{u}}^*$, which has been first presented in (Avril et al., 2004), can help to find a virtual field simultaneously satisfying these conditions. The description of this method is given below.

The principle of this automated method is to minimize the noise sensitivity from the strain measurements. Currently, this method is developed for minimizing the effect from a white Gaussian noise distributed over a full-field measurement area. In the current research, it is also assumed that the strain measurements can be separated into the actual values and a white noise. With this assumption, the dynamic PVW, Eq. (3.3), with the isotropic linear elastic model can be rewritten as follows:

$$\begin{aligned} &Q_{xx}\int_s (\varepsilon_{xx}-\gamma\Re_x)\varepsilon^*_{xx}+(\varepsilon_{yy}-\gamma\Re_y)\varepsilon^*_{yy}+\frac{1}{2}(\varepsilon_{xy}-\gamma\Re_{xy})\varepsilon^*_{xy}\ \mathrm{d}s \\ &+Q_{xy}\int_s (\varepsilon_{xx}-\gamma\Re_x)\varepsilon^*_{yy}+(\varepsilon_{yy}-\gamma\Re_y)\varepsilon^*_{xx}-\frac{1}{2}(\varepsilon_{xy}-\gamma\Re_{xy})\varepsilon^*_{xy}\ \mathrm{d}s \\ &=-\int_s \rho(a_x u^*_x+a_y u^*_y)\ \mathrm{d}s \end{aligned} \tag{3.36}$$

where $\Re_x$, $\Re_y$ and $\Re_{xy}$ are scalar zero-mean stationary (second order) Gaussian distribution, and γ represents the amplitude of the uncertainty of the strain measurements. It is assumed that each noise component is uncorrelated for the analytical process of Eq. (3.36) (Pierron and Grédiac, 2012). This equation can be reorganized:

$$\begin{aligned} &Q_{xx}\int_s \varepsilon_{xx}\varepsilon^*_{xx}+\varepsilon_{yy}\varepsilon^*_{yy}+\frac{1}{2}\varepsilon_{xy}\varepsilon^*_{xy}\ \mathrm{d}s+Q_{xy}\int_s \varepsilon_{xx}\varepsilon^*_{yy}+\varepsilon_{yy}\varepsilon^*_{xx}-\frac{1}{2}\varepsilon_{xy}\varepsilon^*_{xy}\ \mathrm{d}s \\ &-\gamma\left[Q_{xx}\int_s \Re_x\varepsilon^*_{xx}+\Re_y\varepsilon^*_{yy}+\frac{1}{2}\Re_{xy}\varepsilon^*_{xy}\ \mathrm{d}s+Q_{xy}\int_s \Re_x\varepsilon^*_{yy}+\Re_y\varepsilon^*_{xx}-\frac{1}{2}\Re_{xy}\varepsilon^*_{xy}\ \mathrm{d}s\right] \\ &=-\int_s \rho(a_x u^*_x+a_y u^*_y)\ \mathrm{d}s \end{aligned} \tag{3.37}$$

In this equation, the two virtual fields $\boldsymbol{u}^{*(1)}$ and $\boldsymbol{u}^{*(2)}$ satisfying the specialty condition can be applied for the direct identification of Q_{xx} and Q_{xy}. For example, the use of $\boldsymbol{u}^{*(1)}$ leads to the following equation

$$\begin{aligned} &Q_{xx}\underbrace{\int_s \varepsilon_{xx}\varepsilon^{*(1)}_{xx}+\varepsilon_{yy}\varepsilon^{*(1)}_{yy}+\frac{1}{2}\varepsilon_{xy}\varepsilon^{*(1)}_{xy}\ \mathrm{d}s}_{=1}+Q_{xy}\underbrace{\int_s \varepsilon_{xx}\varepsilon^{*(1)}_{yy}+\varepsilon_{yy}\varepsilon^{*(1)}_{xx}-\frac{1}{2}\varepsilon_{xy}\varepsilon^{*(1)}_{xy}\ \mathrm{d}s}_{=0} \\ &-\gamma\left[Q_{xx}\int_s \Re_x\varepsilon^{*(1)}_{xx}+\Re_y\varepsilon^{*(1)}_{yy}+\frac{1}{2}\Re_{xy}\varepsilon^{*(1)}_{xy}\ \mathrm{d}s+Q_{xy}\int_s \Re_x\varepsilon^{*(1)}_{yy}+\Re_y\varepsilon^{*(1)}_{xx}-\frac{1}{2}\Re_{xy}\varepsilon^{*(1)}_{xy}\ \mathrm{d}s\right] \\ &=-\int_s \rho(a_x u^{*(1)}_x+a_y u^{*(1)}_y)\ \mathrm{d}s \end{aligned} \tag{3.38}$$

and

$$Q_{xx} = \gamma \Bigg[Q_{xx} \int_s \Re_x \varepsilon_{xx}^{*(1)} + \Re_y \varepsilon_{yy}^{*(1)} + \frac{1}{2} \Re_{xy} \varepsilon_{xy}^{*(1)} \, \mathrm{d}s + Q_{xy} \int_s \Re_x \varepsilon_{yy}^{*(1)} + \Re_y \varepsilon_{xx}^{*(1)} - \frac{1}{2} \Re_{xy} \varepsilon_{xy}^{*(1)} \, \mathrm{d}s \Bigg] - \int_s \rho (a_x u_x^{*(1)} + a_y u_y^{*(1)}) \, \mathrm{d}s \tag{3.39}$$

The parameters identified without consideration of the noise, but presented, are denoted as the approximated parameters and defined as

$$Q_{xx}^{app} = -\int_s \rho (a_x u_x^{*(1)} + a_y u_y^{*(1)}) \, \mathrm{d}s \tag{3.40}$$

Eq. (3.39) is rewritten with Q_{xx}^{app} as

$$Q_{xx} = \gamma \Bigg[Q_{xx} \int_s \Re_x \varepsilon_{xx}^{*(1)} + \Re_y \varepsilon_{yy}^{*(1)} + \frac{1}{2} \Re_{xy} \varepsilon_{xy}^{*(1)} \, \mathrm{d}s + Q_{xy} \int_s \Re_x \varepsilon_{yy}^{*(1)} + \Re_y \varepsilon_{xx}^{*(1)} - \frac{1}{2} \Re_{xy} \varepsilon_{xy}^{*(1)} \, \mathrm{d}s \Bigg] - Q_{xx}^{app} \tag{3.41}$$

Similarly for Q_{xy}

$$Q_{xy} = \gamma \Bigg[Q_{xx} \int_s \Re_x \varepsilon_{xx}^{*(2)} + \Re_y \varepsilon_{yy}^{*(2)} + \frac{1}{2} \Re_{xy} \varepsilon_{xy}^{*(2)} \, \mathrm{d}s + Q_{xy} \int_s \Re_x \varepsilon_{yy}^{*(2)} + \Re_y \varepsilon_{xx}^{*(2)} - \frac{1}{2} \Re_{xy} \varepsilon_{xy}^{*(2)} \, \mathrm{d}s \Bigg] - Q_{xy}^{app} \tag{3.42}$$

Assuming that the noise amplitude γ is much smaller than the norm of the strain components (Avril et al., 2004), Eq. (3.41) and (3.42) can be

$$\begin{aligned} Q_{xx} &= \gamma \Bigg[Q_{xx}^{app} \int_s \Re_x \varepsilon_{xx}^{*(1)} + \Re_y \varepsilon_{yy}^{*(1)} + \frac{1}{2} \Re_{xy} \varepsilon_{xy}^{*(1)} \, \mathrm{d}s + Q_{xy}^{app} \int_s \Re_x \varepsilon_{yy}^{*(1)} + \Re_y \varepsilon_{xx}^{*(1)} - \frac{1}{2} \Re_{xy} \varepsilon_{xy}^{*(1)} \, \mathrm{d}s \Bigg] - Q_{xx}^{app} \\ Q_{xy} &= \gamma \Bigg[Q_{xx}^{app} \int_s \Re_x \varepsilon_{xx}^{*(2)} + \Re_y \varepsilon_{yy}^{*(2)} + \frac{1}{2} \Re_{xy} \varepsilon_{xy}^{*(2)} \, \mathrm{d}s + Q_{xy}^{app} \int_s \Re_x \varepsilon_{yy}^{*(2)} + \Re_y \varepsilon_{xx}^{*(2)} - \frac{1}{2} \Re_{xy} \varepsilon_{xy}^{*(2)} \, \mathrm{d}s \Bigg] - Q_{xy}^{app} \end{aligned} \tag{3.43}$$

The noise sensitivity of Q_{xx} and Q_{xy} is evaluated by their variance written as follows where E is the expected value operator.

$$V\left(Q_{xx}\right)=\mathrm{E}\left(\left[Q_{xx}-E\left(Q_{xx}\right)\right]^2\right)$$
$$V\left(Q_{xy}\right)=\mathrm{E}\left(\left[Q_{xy}-E\left(Q_{xy}\right)\right]^2\right) \tag{3.44}$$

$$\begin{aligned}V\left(Q_{xx}\right)=\gamma^2\left(\frac{s}{n}\right)^2\Bigg[&\left(\left(Q_{xx}^{app}\right)^2+\left(Q_{xy}^{app}\right)^2\right)\sum_{i=1}^{n}\left(\varepsilon_{xx}^{*(1)}(\psi_i)\right)^2\\&+4\left(Q_{xx}^{app}Q_{xy}^{app}\right)\sum_{i=1}^{n}\left(\varepsilon_{xx}^{*(1)}(\psi_i)\varepsilon_{yy}^{*(1)}(\psi_i)\right)\\&+\left(\left(Q_{xx}^{app}\right)^2+\left(Q_{xy}^{app}\right)^2\right)\sum_{i=1}^{n}\left(\varepsilon_{yy}^{*(1)}(\psi_i)\right)^2\\&+\left(\frac{1}{4}\left(\left(Q_{xx}^{app}\right)^2+\left(Q_{xy}^{app}\right)^2\right)-\frac{1}{2}\left(Q_{xx}^{app}Q_{xy}^{app}\right)\right)\sum_{i=1}^{n}\left(\varepsilon_{xy}^{*(1)}(\psi_i)\right)^2\Bigg]\end{aligned} \tag{3.45}$$

Following the calculation procedure of the variance and the integral method for a discretized data introduced in the VFM textbook (Pierron and Grédiac, 2012), $V(Q_{xx})$, for example, is expanded as presented in Eq. (3.45), in which n is the total number of actual full-field data pairs; $\varepsilon_x^{*(1),i}$ represents the axial virtual strain value at the i^{th} data location, which is expanded through the virtual nodal displacements. The variance of Q_{xy} can be also similarly derived. One can rewrite Eq. (3.45) in the form of

$$V\left(Q_{xx}\right)=\gamma^2\left(\vartheta^{(1)}\right)^2$$
$$V\left(Q_{xy}\right)=\gamma^2\left(\vartheta^{(2)}\right)^2 \tag{3.46}$$

The variances are affected by the two coefficients γ and ϑ. The first coefficient is due to an experimental noise source, and the latter one depends on the formation of the virtual fields.

The minimization of the coefficient ϑ is used for the determination of the unknown nodal piecewise virtual displacements:

$$\mathbf{Y}^{*(i)}=\begin{Bmatrix}\tilde{u}_{x,[1]}^{*(i)}\\ \tilde{u}_{y,[1]}^{*(i)}\\ \tilde{u}_{x,[2]}^{*(i)}\\ \vdots\\ \tilde{u}_{y,[12]}^{*(i)}\end{Bmatrix}\ i=1,2 \text{ for two independent virtual field sets} \tag{3.47}$$

so that the influence on the variance from the virtual fields is minimum. The first step of this minimization problem is to set up the following relation:

$$\mathbf{A}_{\mathrm{KA}}\mathbf{Y}^{*(i)}=\mathbf{Z}_{\mathrm{KA}}^{(i)} \tag{3.48}$$

This relation is to enforce the conditions of Eq. (3.34) and (3.35) to the components of $\mathbf{Y}^{*(i)}$. This enforcement can be achieved by setting Eq. (3.48) as

$$\underbrace{\begin{bmatrix} 1 & 0 & \cdots & & & & & & & & & \\ 0 & 1 & & & & & & & & & & \\ \vdots & & 1 & & & & & & & & & \\ & & & 1 & & & & & & & & \\ & & & & 1 & & & & & & & \\ & & & & & 1 & \cdots & & & & & \\ & & & & & & \cdots & 1 & & & & \\ & & & & & & & & 1 & & & \\ & & & & & & & & & 1 & & \\ & & & & & & & & & & 1 & 0 \\ & & & & & & & & & \cdots & 0 & 1 \end{bmatrix}}_{\mathbf{A}_{\mathrm{KA}}(12\times 24)} \underbrace{\begin{Bmatrix} u_{x,[1]}^{*(i)} \\ u_{y,[1]}^{*(i)} \\ u_{x,[2]}^{*(i)} \\ u_{y,[2]}^{*(i)} \\ u_{x,[3]}^{*(i)} \\ u_{y,[3]}^{*(i)} \\ \vdots \\ u_{x,[10]}^{*(i)} \\ u_{y,[10]}^{*(i)} \\ u_{x,[11]}^{*(i)} \\ u_{y,[11]}^{*(i)} \\ u_{x,[12]}^{*(i)} \\ u_{y,[12]}^{*(i)} \end{Bmatrix}}_{\mathbf{Y}^{*(i)}(24\times 1)} = \underbrace{\begin{Bmatrix} 0 \\ \vdots \\ \\ \\ \\ \\ \\ \\ \\ \\ \vdots \\ 0 \end{Bmatrix}}_{\mathbf{Z}_{\mathrm{KA}}^{(i)}(12\times 1)} \tag{3.49}$$

The components of the matrix $\mathbf{A}_{\mathrm{KA}}$ and vector $\mathbf{Z}_{\mathrm{KA}}^{(i)}$ are zero unless specified. The 12 diagonal values of '1' of the matrix $\mathbf{A}_{\mathrm{KA}}$ is associated with each component of the vector $\mathbf{Y}^{*(i)}$. The kinematic condition, Eq. (3.34), is satisfied by giving '1' values to the first to sixth diagonal components of $\mathbf{A}_{\mathrm{KA}}$ so that the virtual nodal displacements located at the left-hand (fixed) side of the specimen (Figure 3.3) is enforced to be zero, the value of which is included in the vector $\mathbf{Z}_{\mathrm{KA}}^{(i)}$. The additional condition for the dynamic VFM, Eq. (3.35) can be also similarly achieved by giving '1' values to the 7^{th} to 12^{th} diagonal components of $\mathbf{A}_{\mathrm{KA}}$.

The specialty condition can be applied by setting the following relation:

$$\mathbf{A}_{\mathrm{SC}}^{(i)}\mathbf{Y}^{*(i)}=\mathbf{Z}_{\mathrm{SC}}^{(i)} \tag{3.50}$$

$$\mathbf{A}_{\mathrm{SC}}^{(i)}=\begin{bmatrix}\mathbf{D}_{11}^{(i)}\\ \mathbf{D}_{12}^{(i)}\end{bmatrix},\ \mathbf{Z}_{SC}^{(1)}=\begin{bmatrix}1\\0\end{bmatrix},\ \mathbf{Z}_{SC}^{(2)}=\begin{bmatrix}0\\1\end{bmatrix} \tag{3.51}$$

$\mathbf{D}_{11}$ is a row vector of 1×24, each component of which is the location of the 24 degree of freedoms of the 12 virtual nodes. This vector is constructed with the global assemblage of the integration procedure of Eq. (3.32), which is the first integration term of the dynamic PVW and associated with the parameter Q_{xx}, without the term $\tilde{\boldsymbol{u}}^{*}$. In a similar way, $\mathbf{D}_{12}$ is constructed by the second integration term associated with Q_{xy}. These two vectors represent the matrix components M_{11} & M_{12} and M_{21} & M_{22} of Eq. (3.5), respectively, when the first $\boldsymbol{u}^{*(1)}$ and the second $\boldsymbol{u}^{*(2)}$ are applied. The specialty condition $\mathbf{M} = \mathbf{I}$ can be enforced by the multiplication of the matrix $\mathbf{A}_{\mathrm{SC}}^{(i)}$ by $\mathbf{Y}^{*(i)}$ so that when $\boldsymbol{u}^{*(1)}$ is applied, then $\mathbf{D}_{11}^{(1)}\mathbf{Y}^{*(1)} = 1,\ \mathbf{D}_{12}^{(1)}\mathbf{Y}^{*(1)} = 0$ and, for $\boldsymbol{u}^{*(2)},\ \mathbf{D}_{11}^{(2)}\mathbf{Y}^{*(2)} = 0,\ \mathbf{D}_{12}^{(2)}\mathbf{Y}^{*(2)} = 1.$

The combination of Eq. (3.48) and (3.50) leads to the following form

$$\mathbf{A}\mathbf{Y}^{*(i)} = \mathbf{Z}^{(i)} \tag{3.52}$$

$$\mathbf{A} = \begin{bmatrix} \mathbf{A}_{\mathrm{KA}} \\ \hline \mathbf{A}_{\mathrm{SC}}^{(i)} \end{bmatrix},\ \mathbf{Z}^{(i)} = \begin{bmatrix} \mathbf{Z}_{\mathrm{KA}}^{(i)} \\ \hline \mathbf{Z}_{\mathrm{SC}}^{(i)} \end{bmatrix} \tag{3.53}$$

This equation is used as the compulsory (or equality) condition for the optimization procedure. The next step is to make the complete condition to minimize the coefficient ϑ. First, the coefficient ϑ takes the following form to explicitly take out the nodal virtual displacement term:

$$\left(\eta^{(i)}\right)^2 = \frac{1}{2}\tilde{\boldsymbol{u}}^{*(i)} \cdot \mathbf{H}\tilde{\boldsymbol{u}}^{*(i)} = \frac{1}{2}\mathbf{Y}^{*(i)} \cdot \mathbf{H}\mathbf{Y}^{*(i)} \tag{3.54}$$

H is a square matrix, components of which are obtained from rewriting Eq. (3.45) into the form above. The minimization of Eq. (3.54) and the requirement of Eq. (3.52) are achieved using the method of Lagrange multipliers written as follow

$$\ell^{(i)} = \frac{1}{2}\mathbf{Y}^{*(i)} \cdot \mathbf{H}\mathbf{Y}^{*(i)} + \boldsymbol{\Lambda}^{(i)} \cdot \left(\mathbf{A}\mathbf{Y}^{*(i)} - \mathbf{Z}^{(i)}\right) \tag{3.55}$$

where $\boldsymbol{\Lambda}^{(i)}$ is a vector including the Lagrange multipliers. The minimization of Eq. (3.55) is performed by the following linear system

$$\begin{bmatrix} \mathbf{H} & \mathbf{A}^{\mathrm{T}} \\ \mathbf{A} & \mathbf{0} \end{bmatrix} \begin{Bmatrix} \mathbf{Y}^{*(i)} \\ \boldsymbol{\Lambda}^{(i)} \end{Bmatrix} = \begin{Bmatrix} \mathbf{0} \\ \mathbf{Z}^{(i)} \end{Bmatrix} \tag{3.56}$$

where **0** in the matrix is a square zero matrix to fit the size of the row number of **A** and **0** in the vector is a zero vector for the size of the row of the matrix. The initial guess is given to the material parameters Q_{xx} and Q_{xy}, and the inversion of the matrix of Eq. (3.56) produces the first guess of $\mathbf{Y}^{*(i)}$. Then, this is used for the next estimation of the parameters. This iterative procedure continues until the following condition is satisfied:

$$\mathbf{Q} = \begin{Bmatrix} Q_{xx} \\ Q_{xy} \end{Bmatrix} \tag{3.57}$$
$$\chi = \mathrm{sum}\left[\left(\mathbf{Q}_{\mathrm{old}} - \mathbf{Q}\right) \cdot \left(\mathbf{Q}_{\mathrm{old}} - \mathbf{Q}\right) / \left(\mathbf{Q} \cdot \mathbf{Q}\right) \right],\ \chi < \mathrm{Tolerance}$$

The operator ‘sum’ is to sum all elements of a vector. In the present research, the initial guess for the two parameters is given as 1, and the tolerance is specified as 0.001.

This optimized piecewise virtual field is simply referred to as *the piecewise virtual field*; the manually designed virtual field, Eq. (3.2), is referred to as *the constant virtual field* through the present thesis. The piecewise virtual field was applied to the research mainly presented in Chapter 4 and Chapter 5, in which the application of the linear VFM is explained.

3.4 Summary

The dynamic VFM is described with a simple analytical example that is similar to an actual experiment. The principle of the dynamic VFM is to design the virtual displacement fields by which the traction term, requiring force measurements, can be removed from the PVW equation, but the remaining acceleration term replaces the need of force measurements. An automated method of determining the ideal virtual fields is explained based on the guideline introduced by (Pierron and Grédiac, 2012). This automated method is to seek the ideal virtual nodal displacements that can satisfy the VFM admissibility, the specialty condition and the cancellation of the acceleration term and, additionally, can minimize the sensitivity of the identification to measurement noise added to the strain fields. The optimized virtual nodal

displacements are then interpolated to produce the virtual displacement and strain fields at each full-field data location.

Chapter 4 THE LINEAR VFM: FEM SIMULATION

4.1 Introduction

This chapter provides a comprehensive application of the linear VFM to data obtained from an FEM. The purpose of this simulation work is to validate the capability of the linear VFM for the identification of Young's modulus on FEM data, which is based on the boundary conditions similar to that of an actual experiment, and it is an integral part of the design of the pre-stretching experiments presented later. The simulations were conducted using the commercial FEM package, ABAQUS (2011). The simulation was designed such that the specimen design and boundary conditions are similar to the experimental conditions observed from the actual drop-weight test presented in the next chapter. In an actual drop-weight test, the general shape of the elastomer specimen used has a uniaxial tension style design (long, thin rectangular shape), and the full-field data utilized in the VFM were measured using high-speed photography and DIC on the specimen surface during dynamic loading. Similarly, in the present simulation work, the numerical data obtained from the surface of a 2D (plane-stress) rectangular FEM model were utilized for the VFM identification. Whilst a 2D plane stress model was mainly used, a 3D model will be presented in order to validate the use of the surface data. This 3D simulation also shows the effect of the specimen thickness and the reduction of the data area owing to difficulties in obtaining DIC data near the specimen edges. Calculation of material parameters was performed with the displacement data directly obtained from the FEM and the linear VFM with constant virtual fields. After the 3D analysis, the 2D simulations are recalled again to evaluate the sensitivity of the identifications to artificial noise and, also, to see the effect of the use of the optimized piecewise virtual fields.

Further simulations were then performed to show the whole procedure of the drop-weight test. The application of the linear VFM is to find Young's modulus, which

represents only the initial part of the nonlinear stress-strain curve of elastomers. Also, the displacement amplitude (1-3 mm) applied in the drop-weight test is not sufficient to study the whole nonlinearity. Obviously, the single drop-weight test and the application of the linear VFM are not enough to extract the material parameters for nonlinear models of elastomers. In order to extend the identification capability of the linear VFM to nonlinear models, a so-called pre-stretching method has been developed. The specimen is statically preloaded to a range of fixed strains and then dynamically loaded with small amplitude stress waves; dynamic test data at different pre-strains are simultaneously used to extract the material parameters and reconstruct a stress-strain curve over a large range of strain. A similar approach has previously been employed in the literature, in which a pre-stretch was applied up to the strain hardening region in which a shock wave is propagated in an elastomer specimen (Niemczura and Ravi-Chandar, 2011b). Simulations of the present pre-stretching method were performed on a hyperelastic model and show the identification capability for the material parameters. Prior to explaining the simulation works, the framework of the linear VFM is re-explained with respect to the pre-stretching case, and its related notations are introduced. The first part of this simulation work is based on a pure-hyperelastic model; the second part of the simulation is performed on a visco-hyperelastic model. The analysis method presented in this chapter was later further explored and modified; this modified method will be provided in Chapter 7.

The objectives of this chapter can be summarized as follows:

- FEM simulation data are analysed by the dynamic VFM to assess the identification capability of the VFM under the experimental situation of a drop-weight test introduced in Chapter 5.

- FEM simulation data is polluted by a random error in order to produce an experimental-like imaging error and evaluate its effect on the VFM identification.
- The piecewise optimized virtual field is applied to FEM data polluted by a random error. The sensitivity to different error amplitudes is explored.
- The current dynamic VFM is able to characterize Young's modulus for a short loading period due to the assumption of a linear elastic behaviour over a small strain range. A so-called pre-stretching method is introduced by which a nonlinear stress-strain relationship over a large deformation range is characterized.
- The application procedure of the pre-stretching method is explained using FEM data produced by simulations with hyperelastic and visco-hyperelastic models.

4.2 Simulation: linear elastic material

4.2.1 Two-dimensional simulation

The overall simulation geometry was designed to resemble the specimen used in the drop-weight experiments. The initial geometry is similar to Figure 3.1 but the initial dimensions are now length (L) = 20 mm, width (W) = 7 mm, and thickness (h) = 1 mm. These dimensions were used for all 2D simulations in this chapter; for the 3D case, the same length and width were applied but the thickness was varied, and its specific value will be given in the later section. The left end of the specimen is fixed and a velocity boundary condition approximated from the actual dynamic displacement of the drop-weight apparatus was applied to the one end. The velocity boundary condition used for all simulations is presented in Figure 4.1.

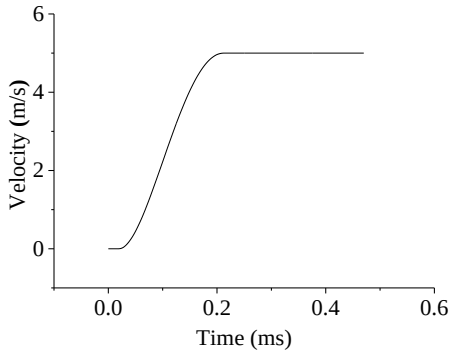

Figure 4.1 Velocity profile for the FEM simulations

On the loaded end, an additional fixed boundary condition was applied in the lateral direction. For the mechanical properties, it is assumed that $\nu = 0.49$ for the almost incompressible elastomer and $\rho = 1200$ kg m^{-3}. The Young's modulus E will be specified prior to each simulation. ABAQUS/explicit simulations were performed with a CPS4R (four-node plane stress) type and the maximum calculation time increment of 1 μs. The element size was chosen as 0.2 mm, which is similar to the distance between actual adjacent data points. The total simulation duration was 0.5 ms; the output data ($\boldsymbol{x}$, $\boldsymbol{\varepsilon}$, $\boldsymbol{a}$) were extracted every 20 μs to resemble the imaging speed, 50 000 fps, used in the actual drop-weight experiment.

The data fields extracted from the FEM result were processed in the way described in Figure 4.2. The coordinates x, y and the acceleration fields $\boldsymbol{a}$ were extracted from the nodes of all elements; interpolation was conducted using the shape function matrix **N** of the four-node element in order to obtain the data at the centre of an element. The strain fields $\boldsymbol{\varepsilon}$ at the element centre (integration points) were directly obtained from the FEM output data. The constant virtual fields $\boldsymbol{u}^{*(1),(2)}$ & $\boldsymbol{\varepsilon}^{*(1),(2)}$ based on Eq. (3.2) were made with the current coordinates. That is, the virtual fields are updated with the new coordinates at each time step during dynamic loading. The reason for this updating is because the PVW is based on the current surface area $s(t)$, which changes significantly during the loading, this is explored further below. Then, the calculation of the PVW was

performed by setting the system of linear equations using the two independent virtual fields. The inversion of the matrix **M** (as introduced in Section 3.2.1) produces the material parameters Q_{xx} and Q_{xy} and, consequently, E and v.

The simulation procedure explained above was performed with a linear elastic material model with Young's modulus of 2 MPa. An example of full-field data, from this simulation, including the first virtual displacement $u_x^{*(1)}$ are given in Figure 4.3 where the stress wave propagates from the right-hand end, and each piece of data is presented

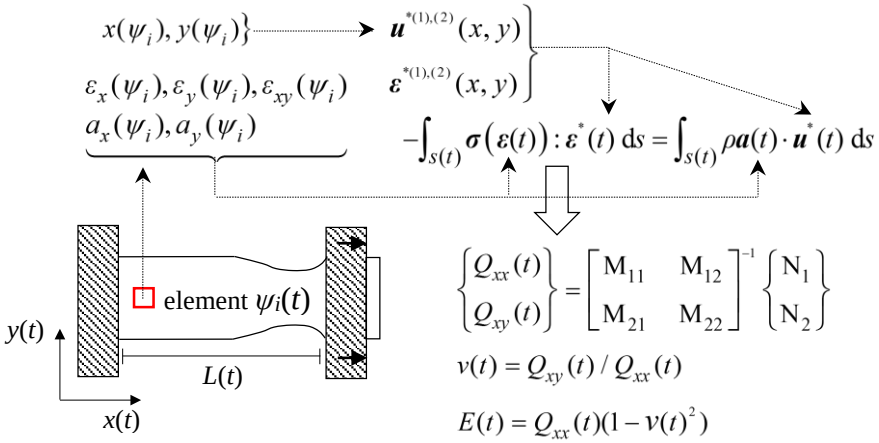

Figure 4.2 Process of the full-field data from the FEM simulations for the use of the linear VFM.

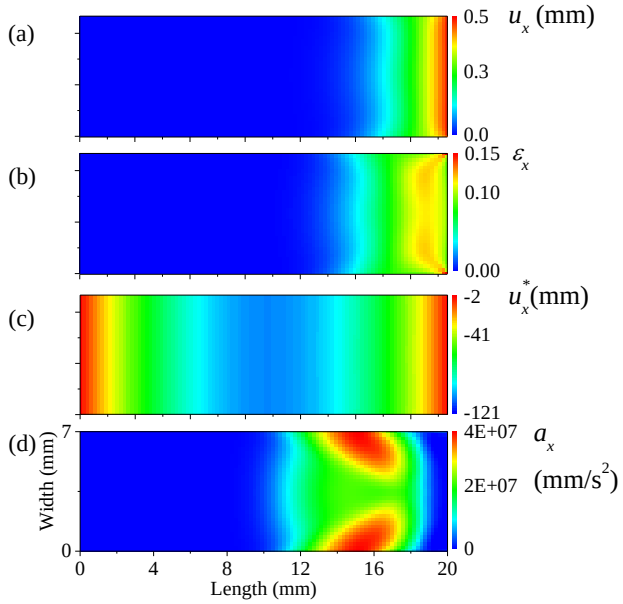

Figure 4.3 (a) Axial displacement, (b) true strain, (c) virtual displacement and (d) acceleration fields of the FEM simulation of the isotropic linear elastic material at 0.2 ms.

at its initial element location. This virtual data are generated with the current coordinates of the elements at 0.3 ms. For all time steps, the same virtual fields, Eq. (3.2), are applied so the overall shapes are the same, for example, the concave shape of $u_x^{*(1)}$ in Figure 4.3(c), but the shape of concaveness is slightly different as it is updated with the corresponding current coordinates. Figure 4.3(d) shows the propagation of the axial acceleration wave. This acceleration field is clearly observed where the displacement field gradually rises for all time steps. This observation indicates that the simulation specimen is not in a quasi-static stress equilibrium state during dynamic loading. The application of a conventional force measurement at the ends of this specimen would not lead to accurate material characterization. The linear VFM procedure described in Figure 4.2 was applied to the simulation data and the identification results are shown in Figure 4.4 in which the identifications of Young's modulus are given at each time step of the full-field data. The reference values (E = 2 MPa) are indicated by a dash line. This figure shows that the identification results (blue curve) from the present procedure are very close to the reference line. The green line represents the identification results of the linear VFM based on the initial configuration. The green line shows large deviation from the reference line compared to the blue one. This result explains that the identification of a low-modulus material requires the consideration of the coordinate system although the displacement amplitude may not appear high. For this reason, the linear VFM analysis is conducted on the simulation and experimental data based on the current configurations.

The full-field data used for the above simulation were directly extracted from the FEM results. The directly obtained data do not reflect the actual experimental procedure because the extracted data are just some among the many FEM data which are calculated at smaller time steps ($\Delta t_{\mathrm{FEM}} < 1$ μs) than the time interval between the full-field data obtained from the high-speed imaging ($\Delta t_{\mathrm{DIC}} = 20$ μs). The attainment of the actual full-

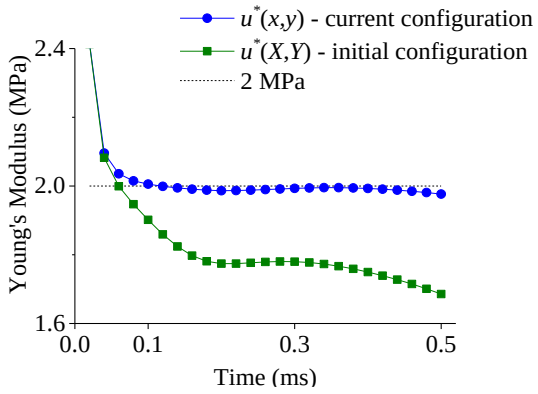

Figure 4.4 Identifications of E with the virtual fields based on the current and initial configuration.

field data is different. The displacement fields are first obtained from the DIC analysis using the digital pictures at each Δt_{DIC} and then used for the further calculation of the rest of the full-field data: $\boldsymbol{x}$, $\boldsymbol{\varepsilon}$, and $\boldsymbol{a}$. The simulation work should reflect this actual data processing. Data processing for these data field was thus adopted as described in Figure 4.5.

The four-node displacement data $\tilde{\boldsymbol{u}}(\psi_i,t)$ of each element ψ_i at all time steps t are extracted. The nodal data is then interpolated by the displacement interpolation matrix $\boldsymbol{N}$ (of the four-node quadrilateral element) to get the displacement data $\boldsymbol{u}(\psi_i,\ t)_{\mathrm{centre}}$ at the centre of each element. This central displacement data is added to the initial coordinate (central), obtained from the initial nodal coordinate, and used to calculate the current

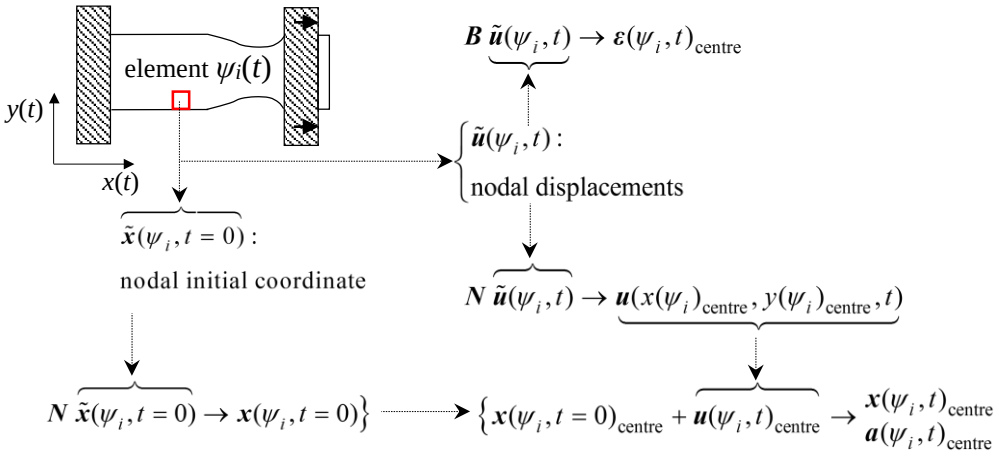

Figure 4.5 Data processing for $\boldsymbol{u}$, $\boldsymbol{x}$, $\boldsymbol{\varepsilon}$ and $\boldsymbol{a}$ fields data at the centre of elements from the nodal displacement data $\tilde{\boldsymbol{u}}$ obtained from the FEM results at each time step t.

coordinates $\boldsymbol{x}(\psi_i, t)_{\text{centre}}$. The central strain data $\boldsymbol{\varepsilon}(\psi_i, t)_{\text{centre}}$ is calculated by the strain-displacement matrix $\boldsymbol{B}$ with $\tilde{\boldsymbol{u}}(\psi_i, t)$. The acceleration field $\boldsymbol{a}$ is obtained by double temporal differentiation of $\boldsymbol{u}(\psi_i, t)$, which can be numerically approximated by a simple finite difference equation as follows:

$$\frac{\boldsymbol{u}(\psi_i, t+\Delta t)_{\text{centre}} + \boldsymbol{u}(\psi_i, t-\Delta t)_{\text{centre}} - 2\boldsymbol{u}(\psi_i, t)_{\text{centre}}}{\Delta t^2} = \boldsymbol{a}(\psi_i, t)_{\text{centre}} \tag{4.1}$$

and at $t = 0$ & $t = t_{\text{Final}}$ the acceleration fields are estimated as

$$\begin{aligned} \boldsymbol{a}(t=0) &= \boldsymbol{a}(t=0+\Delta t) \\ \boldsymbol{a}(t=t_{\text{final}}) &= \boldsymbol{a}(t=t_{\text{final}}-\Delta t) \end{aligned} \tag{4.2}$$

All of the later simulation works were conducted with the above procedure for data processing. The linear VFM analysis on the material: $E = 2$ MPa, $\nu = 0.49$ with the present data processing is compared with the result based on the pure data field in the figure shown in Figure 4.6. The VFM result with the processed data is also close to the given modulus value except that there is a sudden jump in the Young's modulus at the end. This is due to the fact that the acceleration at the last time step is approximated by Eq. (4.2).

The data processing explained above is used for further simulation work in which the effect of the imaging speed or, equivalently, time interval Δt between the data fields is studied. Four linear elastic properties (E = 2, 20, 100, 200 MPa; ν = 0.49) were used with the previous simulation configurations. The two imaging speeds were chosen (50 000 and 100 000 fps) so that there were two time intervals (Δt = 20 and 10 μs) for extracting the data field from each set of FEM simulation results. The VFM identification results from this simulation procedure are presented in Figure 4.7. The identification results from Δt = 20 μs are indicated by the filled square symbol, and the empty circular symbol for Δt = 10 μs. The identification results for E = 2 and 20 MPa are very close to the given values, and no obvious differences are shown between the two imaging speeds.

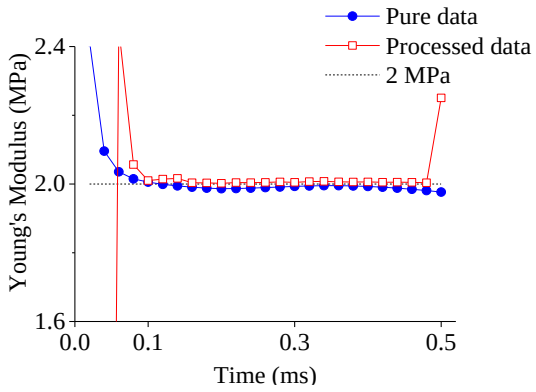

Figure 4.6 Comparison of the linear VFM based on the pure and processed data field.

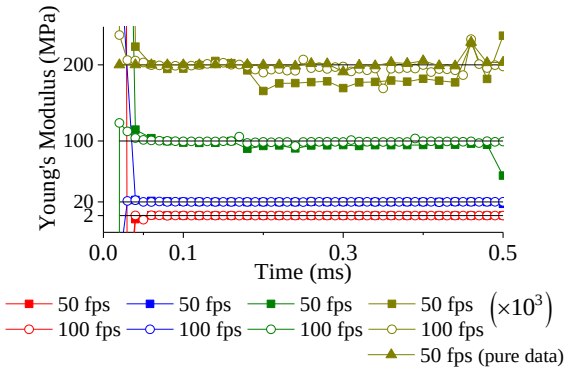

Figure 4.7 The linear VFM analysis on the several linear elastic materials (E = 2, 20, 100, 200 MPa; ν = 0.49) with the processed data; one VFM analysis shows the result of the material (E = 200 MPa) with the pure data.

Underestimation starts to be observed for the slower imaging speed for the simulation with E = 100 MPa. In the case of E = 200 MPa, this underestimation becomes clear compared to the result of Δt = 10 μs which is still close to the given modulus value. The identification result with the pure data of Δt = 20 μs is also given, which is close to the given value and demonstrates that the observed behaviour is not an effect of the FEM calculation. The results presented in Figure 4.7 indicate that a higher imaging speed is required for the stiffer materials. This is expected, as higher Young's modulus produces a faster wave propagation speed. Consequently, the time interval Δt for the temporal differentiation should be sufficiently small to have an accurate estimation of the acceleration fields. In the actual drop-weight test, the Young's moduli of the test specimens were measured as being up to 30 MPa. According to the result of Figure 4.7,

the use of an imaging speed of 50 000 fps for the drop-weight test is reasonable for the rubber specimens chosen in the present research.

4.2.2 Three-dimensional simulation

Before moving to the simulation of a hyperelastic material, it is necessary to validate the assumption of a plane-stress state and the use of the surface data. For this validation, the previous 2D simulation configuration was extended to a 3D case where the same boundary conditions and specimen dimensions were applied except for the thickness. The four elastic properties (E = 1, 5, 10, 50 MPa; ν = 0.49) were given, and for each material four thickness values (h = 0.5, 2, 4, 8 mm) were applied to the 3D geometry. The same element size was applied but with the 3D element type (C3D8R: 8-node hexahedral element with reduced integration). The simulation results for the four elastic materials are presented in Figure 4.8. For all cases, as the specimens become thicker, the

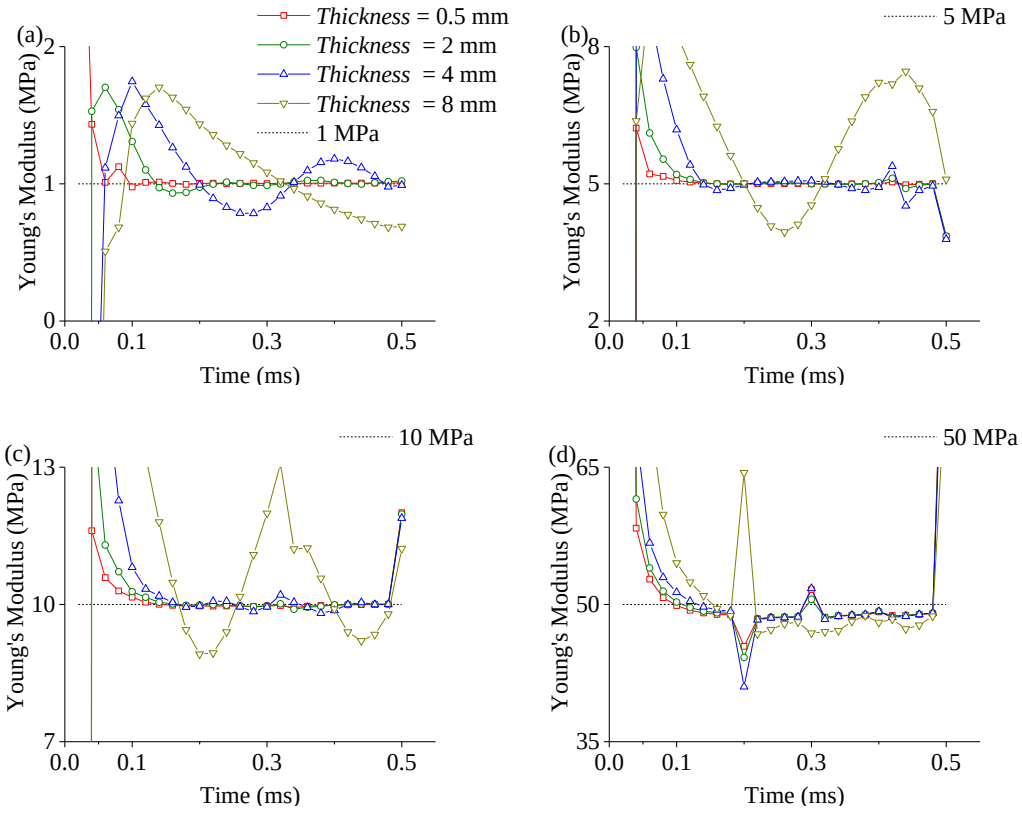

Figure 4.8 Thickness effects on the linear VFM performed on the 3D simulations with the four linear elastic materials.

identifications fluctuate around the given modulus values more than the 2D case. It was found that this fluctuation was significant when the thickness was larger than 4 mm for the present presented in Figure 4.8. For all cases, as the specimens become thicker, the identifications fluctuate around the given modulus values more than the 2D case. It was found that this fluctuation was significant when the thickness was larger than 4 mm for the present specimen geometry. It is reasonable, then, to use the 2D VFM for the specimens thinner than 4 mm in the drop-weight test. The specimens used in the actual experiments were thinner than 2 mm. Another feature can be observed in Figure 4.8: a sudden drop or rise of the identification; for example, in Figure 4.8(b) the sudden drop appears at around 0.4 ms. This drop is almost at the instant when the stress wave starts to be reflected back from the fixed boundary. At this instant, a temporally quasi-static equilibrium state is achieved, and the acceleration term of the PVW is close to zero. This means that no force information is involved in the PVW for the calculation of the material parameters. The sudden drop is not observed in Figure 4.8(a) because the wave speed is not high enough to reach the fixed end within the simulation period. For the other cases (Figure 4.8 (c-d)), it can be seen that the moment at which the sudden change occurs becomes earlier as their wave speeds are higher. Similar observations were found in the actual drop-weight test results. Later in the thesis, a VFM technique will be described that can make use of these reflections.

For the simulation work, the displacement data can be extracted from the whole area of the surface, including the nodes located at the free and boundary edges. However, in the experiment, the precise measurement of the data around the edges or its neighbourhood is difficult as speckle patterns around these areas are not clear or are affected by the boundary. In addition, the displacement data in the proximity of the clamping area should be avoided because the material properties in that region, where a

large clamping pressure is applied, could be different from the region free of clamping stress. Thus, when the VFM was applied to the actual test, full-field data slightly trimmed from the edges were utilized. Simulations to show the effect of this data range were performed with the 3D configurations with only 1mm thickness. Three different changes in the data range were applied to the initial geometry (L = 20 mm, W = 7 mm) as described in Figure 4.9.

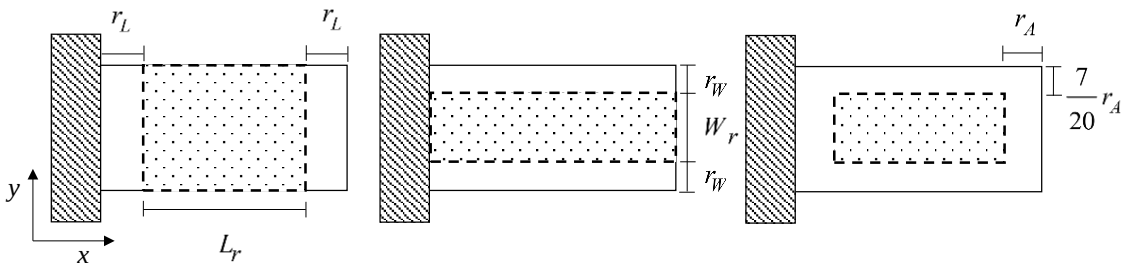

Figure 4.9 Three types of the data range reductions of the simulation geometry.

The left-hand side of Figure 4.9 describes the length reduction r_L; four reduced lengths were given: L_r = 18, 14, 10, 5 mm. In the second case, the data range was reduced in the lateral directions, and four width reductions were provided: W_r = 6.6, 6, 5, 3 mm. The right-hand side of Figure 4.9 shows the application of the third case in that the data area was reduced by shortening the length by half of the length reduction r_A on both ends, and the width also decreases by the amount of $(7/20)r_A$ in order to keep the initial aspect ratio. Four area reduction factors were given: r_A = 1, 2, 4, 5 mm. These three cases were investigated respectively with the FEM simulations of the same four linear elastic materials as used in the thickness study. It should be mentioned that when the length reduction is applied, the reduced area is considered as an initial specimen geometry. That is, the VF requirements, the kinematic admissibility and the cancellation of the traction term, are satisfied at the new ends made after the reduction. This new requirement can be achieved simply by moving the new fixed end to x = 0 for every time step so the VF,

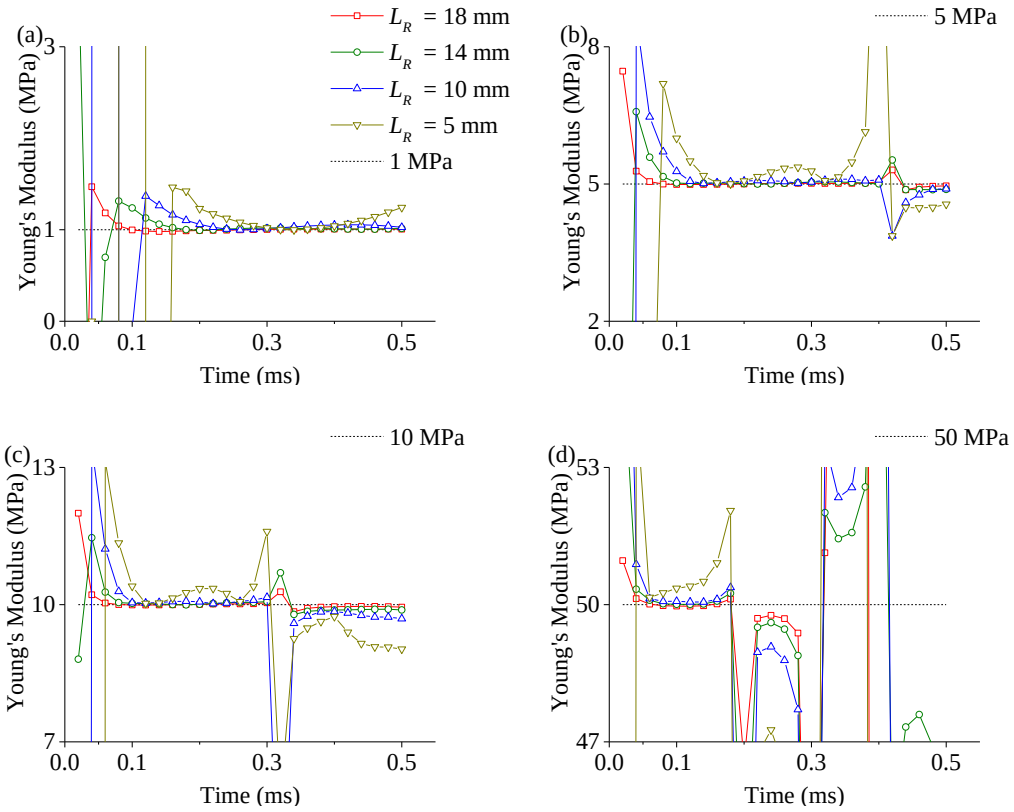

Figure 4.10 Effects of the length reduction on the linear VFM performed on the 3D simulations.

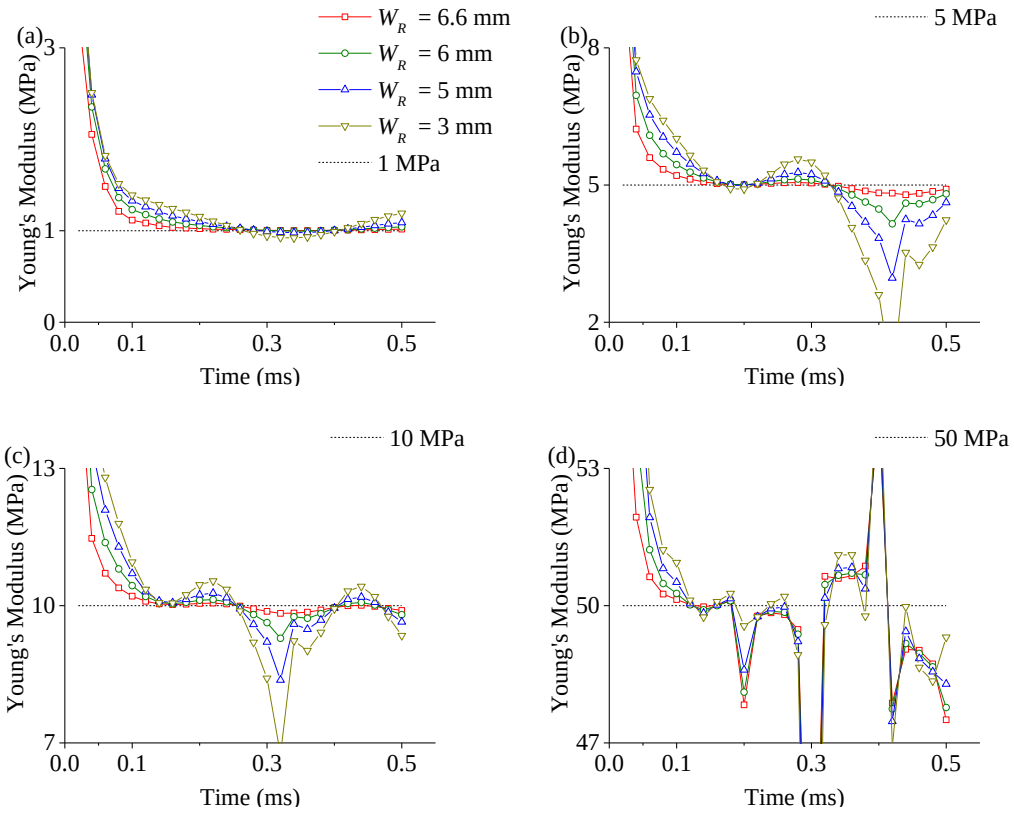

Figure 4.11 Effects of the width reduction on the linear VFM performed on the 3D simulations.

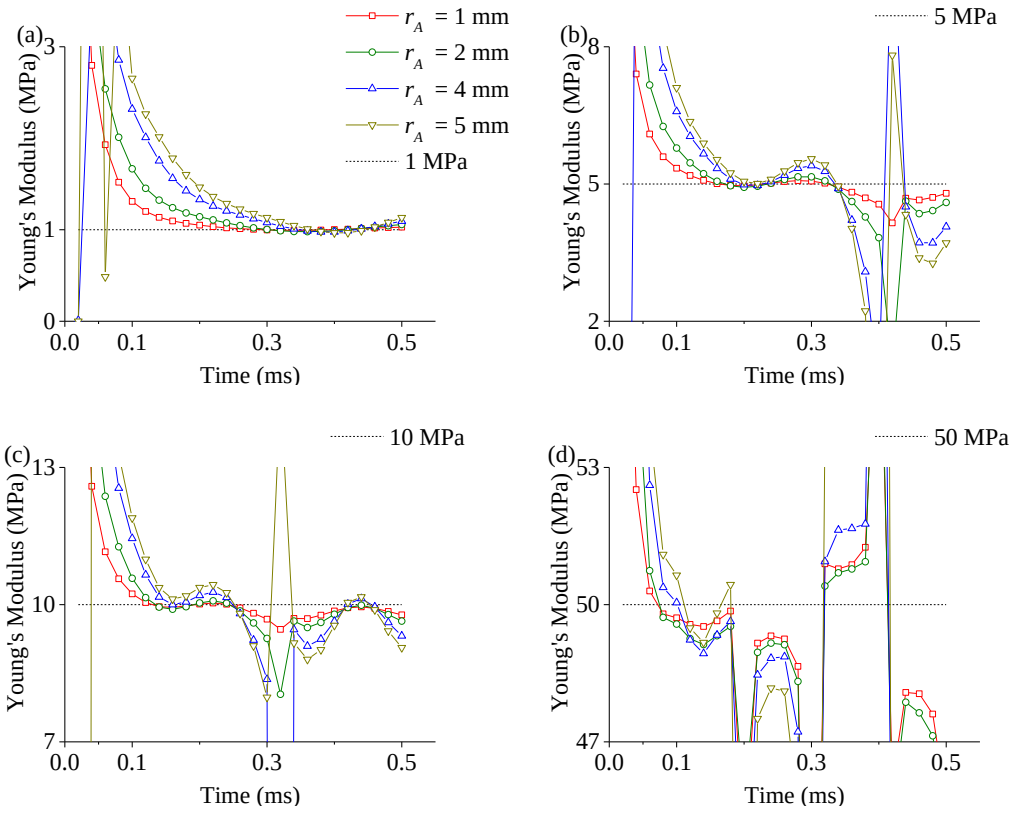

Figure 4.12 Effects of the area reduction on the linear VFM performed on the 3D simulations.

Eq. (3.2), is still applicable. The results of the linear VFM analysis on these simulations are presented below.

As observed in Figure 4.10 to Figure 4.12, it can be concluded that the data range reductions will lead to the overestimation of the Young's modulus over the first identification period. In addition, it can be seen that the identifications are more sensitive to the length reduction compared to the width. This higher sensitivity is simply due to the fact that the axial acceleration field is generated from the non-uniform deformations in the lengthwise direction and the identification of the Young's modulus is significantly dependent on the axial acceleration fields as described in the analytical description of the linear VFM. The length reduction decreases the period that the non-uniform deformation fields are captured within the data range. Considering these simulation results, the data range reduction on the experimental data used in the linear VFM was limited such that r_L, r_W < 1 mm. The meaning of these two variables is described in Figure 4.9.

The simulation results shown above can be used as a guideline with regard to the thickness and the data area reduction. The guideline mentioned above is applicable when the given length and width are used. When different dimensions are used, the guideline can be stricter or looser. For example, in the later chapter, a larger size (L = 50 mm, W = 14 mm) of the specimen was used due to the modification of the drop-weight apparatus. With these larger size specimens, the effect of the length reduction is much smaller as shown in Figure 4.13. This figure shows the comparison between the data of Figure 4.10(d) (empty symbols) and result from the same simulation with larger dimensions (filled symbols). It can be seen that the identification result with the larger dimensions is more stable for a longer period for all length reductions.

Throughout the simulation results shown in this section, it can be observed that instants of unstable identification occur and appear more frequently when a higher modulus or shorter specimen is simulated. One of the simulation results from the area reduction study (Figure 4.12(d); E = 50 MPa) is shown again in Figure 4.14 with the averaged acceleration profile used for this identification. It can be seen that the first unstable instant almost corresponds to the moment when the averaged acceleration becomes close to zero, i.e. quasi-static equilibrium state. That is, the principle of virtual work (Eq. (3.3)) does not

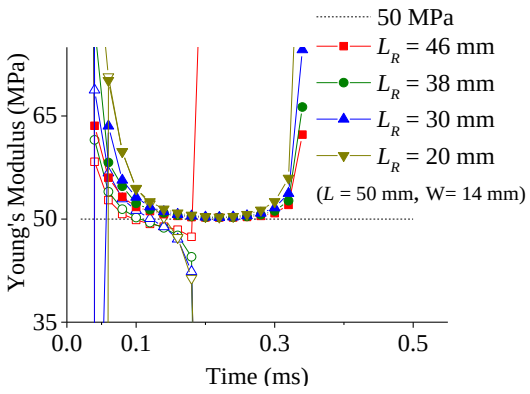

Figure 4.13 Comparison of the length reduction effects between the results of Figure 4.10(d) and the same simulation with the larger dimension (L = 50 mm, W = 14 mm); for the results of Figure 4.10(d), only the stable period is shown.

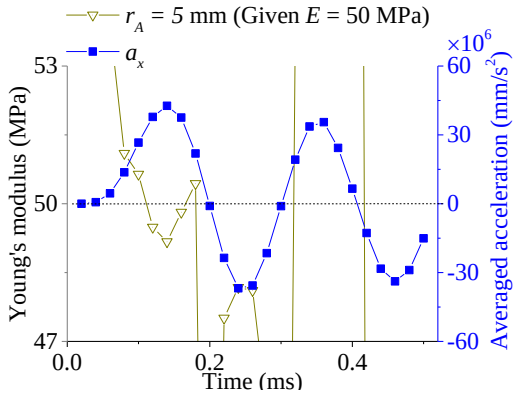

Figure 4.14 Young's modulus identification from Figure 4.12 for the case of E = 50 MPa and the averaged acceleration profile used for this identification.

have any force information for the calculation of Young's modulus. The same phenomenon is observed in the experimental result as well.

4.2.3 Piecewise virtual fields

This section presents the application of the optimized piecewise virtual fields to the 2D simulation configuration described in Section 4.2.1. The optimized piecewise virtual field is referred to as the piecewise virtual field or PVF in this section. The description of the PVF given in Section 3.3 was applied to the same FEM simulation data used to construct Figure 4.3 in which material properties of E = 2 MPa and ν = 0.49, and the pure full-field data were used. On the full-field data, PVFs were automatically generated at each time step by satisfying the kinematic admissibility, the specialty condition, the cancellation of the traction term in the PVW and the minimization of the noise sensitivity in the strain measurements. An example of the axial virtual field corresponding to that

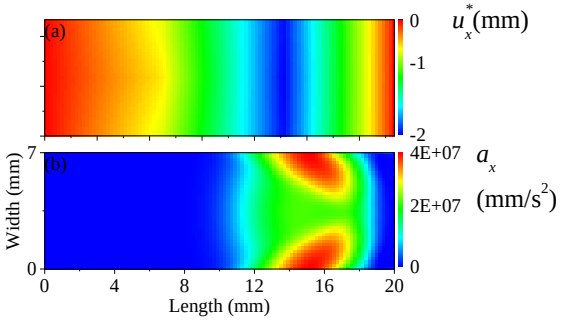

Figure 4.15 (a) Piecewise virtual displacement (2 × 3 virtual elements) and (b) acceleration fields of the FEM simulation of the isotropic linear elastic material at 0.2 ms.

shown in Figure 4.3 is shown in Figure 4.15. Figure 4.15(a) shows the field of $u_x^{*(1)}$ automatically generated from the full-field data at t = 0.2 ms. It can be observed that the virtual displacement values at both ends are close to zero. This zero-value virtual displacement at the ends confirms that the present PVF satisfies the two conditions: the kinematic admissibility and the cancellation of the traction term. The overall concave shape of this virtual field is similar to the constant virtual field shown in Figure 4.3 (c); but the peak area (blue area) of the PVF is biased to the right-hand side whereas the location of the peak area of the constant VF always remains at the centre. It was found that the peak area of the PVW approximately followed the acceleration wave front for all time steps. The identification of the linear VFM with this PVW is presented in Figure 4.16 with the result from the constant VFM (Figure 4.4) for comparison. The identified moduli are obtained by averaging the values of modulus obtained between 0.1 and 0.5 ms. The piecewise virtual field gives a mean that is closer to the given values, but the standard deviation is larger for the piecewise than the constant virtual field. This higher deviation could be an artefact of the iterative optimization procedure in determining the PVF.

The next simulation study compares the sensitivity of the identifications of the constant and piecewise virtual fields to noise in the strain measurements. It is assumed that the

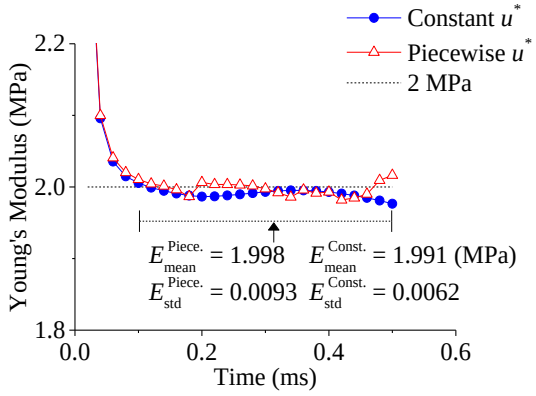

Figure 4.16 Predictions of E with the constant and piecewise virtual fields.

main noise source of the strain measurement is a white Gaussian noise as introduced in Section 3.3.2. In this simulation study, the data processing procedure described in Figure 4.5 was used but, prior to applying this procedure, the raw displacement outputs were polluted by second order white noise. The addition of the white noise was conducted by the method introduced in the VFM textbook where the MATLAB built-in function, *randn*, is adopted. This procedure can be presented as below

$$\boldsymbol{u}'(t) = \boldsymbol{u}(t) + randn(\text{nx, ny}) \times \gamma \tag{4.3}$$

where $\boldsymbol{u}'$ & $\boldsymbol{u}$ and nx & ny represent the polluted & exact displacement fields and the number of elements in the x and y directions, respectively. The term γ represents the noise level and in this present study, the 25 noise levels were given from the smallest (40×10^{-6} mm) to the highest (2000×10^{-6} mm) with an interval of 80×10^{-6} mm. The smallest and highest noise levels are denoted as levels 1 and 25, respectively. The use of the polluted displacement fields will obviously produce noisy strain and acceleration fields. With the polluted full-field data sets generated respectively from noise levels 1 and 25, the identification results of the linear VFM with the piecewise and constant VF are shown in Figure 4.17(a). This figure shows that the effect of using the PVF on the noise level 1 data is not clear. At the noise level 25, it is observed that the deviation from the given

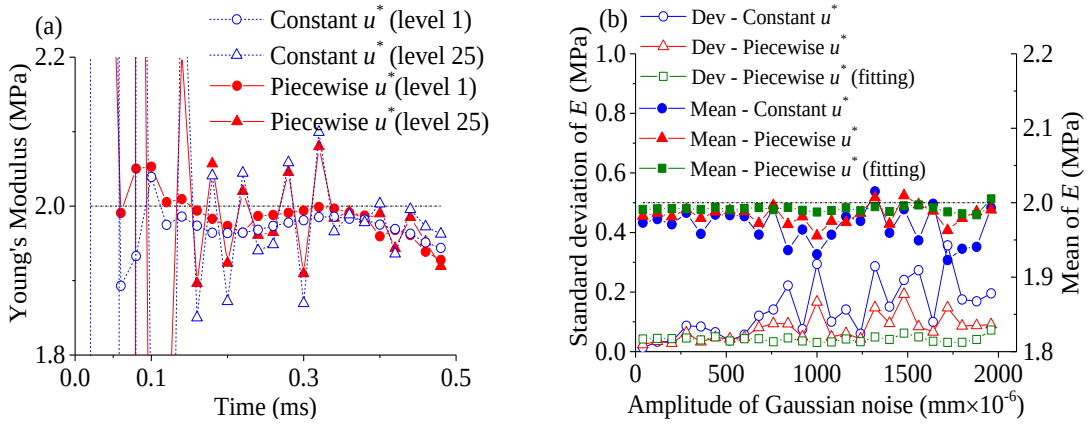

Figure 4.17 (a) Young's modulus identifications from the constant and piecewise VF with the noisy displacement fields (level 1 and 25); (b) Mean and standard deviations of the Young's modulus identifications with the constant & piecewise VF and another piecewise VF with the acceleration fields obtained from the temporal fitting.

Young's modulus is reduced for the PVF when compared to the constant VF. The benefit of using the PVF becomes clear in Figure 4.17(b) in which the standard deviation (over the loading time) of the Young's modulus identification taken from the period 0.1-0.5 ms is plotted as a function of noise amplitude for the two VFs. The standard deviation of the identification is clearly lower for the PVF than the constant one when the noise level is higher than 1000×10^{-6} mm.

The results in Figure 4.17(b) show another way in which the noise sensitivity can be reduced, by using temporal fitting in the calculation of the acceleration fields from the noisy displacements data. In this figure, the mean and standard deviation curves produced from the fitting method are denoted as 'fitting' in their legend in Figure 4.17(b). It can be seen that the deviation of the data obtained using the fitting method is significantly decreased from those of the VFMs with the simple acceleration calculation method, and this improvement is also observed in their mean curves. The PVF plus the temporal fitting method produces the best identification result. Thus, the combination of these two methods was applied to the actual drop-weight experiment data. The temporal fitting procedure was conducted by the MATLAB fitting function, *fit*. The central displacement values at each element were collected with respect to time and, then, fitted to a 9^{th}-degree polynomial using this function. These polynomials were then differentiated twice with respect to time to obtain acceleration values for each element. The degree of a polynomial can affect the fitting quality. The degree should be high enough to describe the complexity of the given curve. It is found that the use of a 9^{th}-degree polynomial is sufficient to fit the given acceleration data as shown in the figures below presenting the effect of the temporal fitting on the acceleration data generated by the displacement field polluted by noise level 25. Figure 4.18(a) and (b) show the effect of the temporal fitting on the

acceleration values averaged over the whole data surface and of a particular element at the centre, respectively.

It should be noted that the current simulation study is to observe the identification sensitivity caused by a DIC random error. However, the sensitivity with respect to reconstructive DIC errors such as intensity interpolation method, subset size & overlap and correlation function is not reflected in this study.

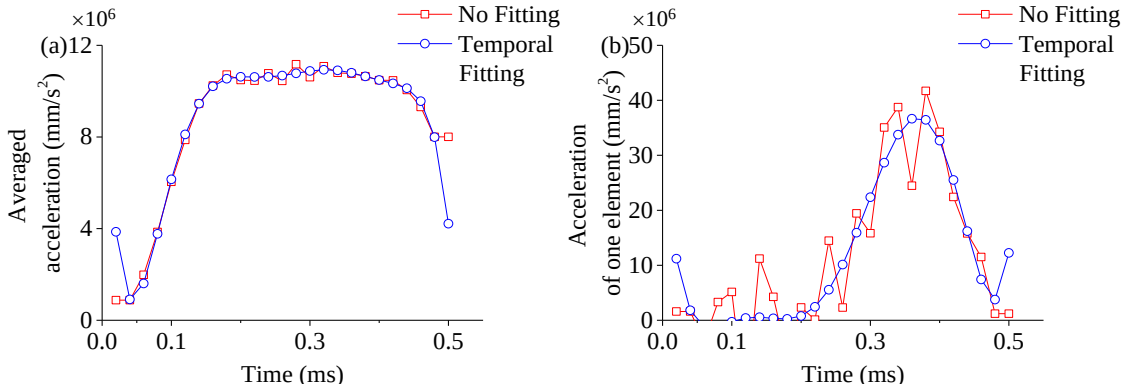

Figure 4.18 (a) Averaged accelerations over the whole data area and (b) acceleration at one particular element located around the centre of the simulation geometry; the red and blue colours represents the acceleration values before and after the temporal fitting.

4.3 Simulation: non-linear material

4.3.1 Pre-stretching method

The application of the linear VFM introduced above only provides data suitable for the identification of Young's modulus of elastomers at a very small strain range, where the materials exhibit the stress-strain linearity. Application of only the linear VFM is not sufficient to characterize the dynamic properties of elastomers over a large strain range during which nonlinearity is observed. In order to overcome this limitation, a pre-stretching method has been developed and used with the linear VFM. The pre-stretching method was adopted to characterize Young's modulus when a statically stretched specimen was dynamically loaded by the drop-weight apparatus. The pre-stretching method is briefly described by the schematic representation shown in Figure 4.19.

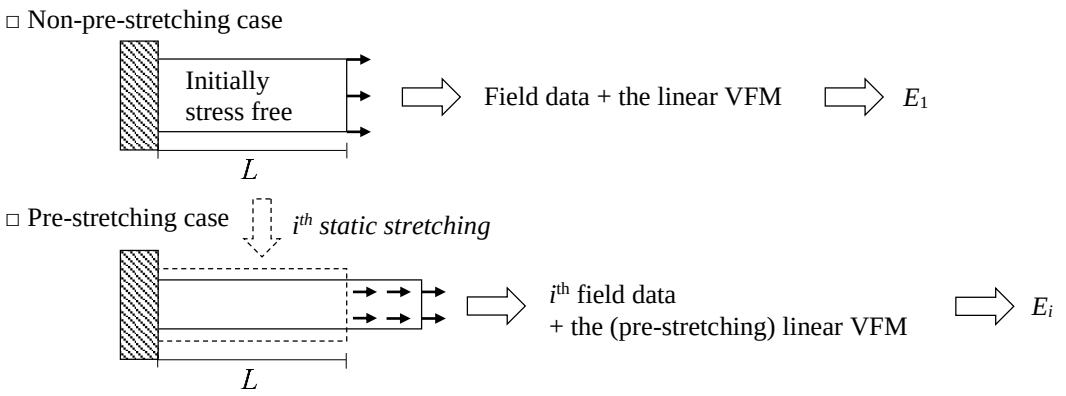

Figure 4.19 Schematic representation of the pre-stretching method.

The linear VFM explained in the previous sections was used for the identification of the Young's modulus of a stress-free (no stretching) specimen as described in the first part of Figure 4.19. The Young's modulus identified from the non-pre-stretching case is denoted as E_1. The lower part of Figure 4.19 shows a schematic of the pre-stretching method. A static stretch is applied to the initial specimen to a certain amount of end displacement. The order of the stretching is indicated numerically, for example, 2^{nd}, 3^{rd}, and 4^{th} pre-stretching; higher numbers mean a larger amount of pre-stretching. The '1^{st}' is only used for the case of the non-pre-stretching. The small arrows in Figure 4.19 represent the velocity boundary condition applied. It should be noted that the arrows are applied within the specimen for the pre-stretching case so that the effective specimen length is the same as before applying the stretching. The reason for applying such a boundary condition is to reflect the actual experimental condition of the drop-weight apparatus in which the distance between the fixtures is almost the same for all tests. This explanation will be clear when the actual experiments are described.

As indicated in Figure 4.19, the Virtual Fields Method for the pre-stretching case is written as the pre-stretching linear VFM. This is to differentiate the linear VFM used for the non- and pre-stretching cases; the linear VFM for the pre-stretching case has a slightly different form of the PVW, which will be explained here. Prior to the explanation of this

difference, it is necessary to define the notations related to the different coordinate systems. The coordinate systems are divided into two cases: the non-stretched and pre-stretched configurations as described in Figure 4.20 and Figure 4.21.

Figure 4.20 shows a schematic representation of a drop-weight test before and during dynamic loading without pre-stretching. The upper part of this figure describes the initial state where the specimen is not loaded. The notations of this initial state are indicated by a '0' subscript. The dynamic loading is applied on the right-hand side of the specimen in the *x* direction (this is the vertical direction in the actual drop-weight experiment). In the deformed (or current) state during the dynamic loading, a stress wave propagates and generates deformation fields inside the specimen. The time variable *t* is used to indicate the notations in the current state but is often omitted in the rest of the chapters. The true strain in this state is a logarithmic strain. Figure 4.21 shows the configurations of the pre-stretching experiment and its coordinate system. The specimen is statically stretched in the *x* direction by an end displacement u_p. This displacement determines a pre-strain field in the stretched specimen. Although the total specimen length is increased, this distance

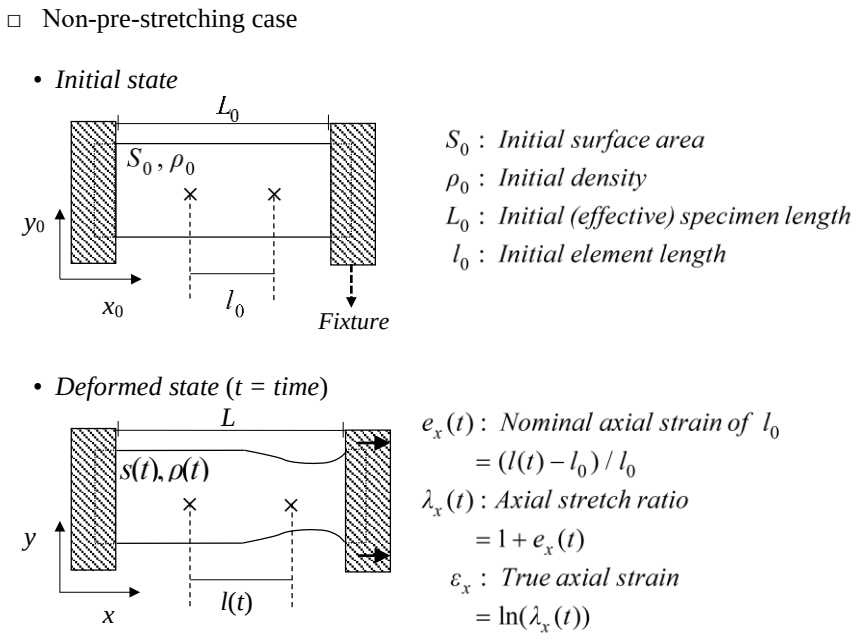

Figure 4.20 Configurations and notations for the non-pre-stretching case.

between the two fixtures does not change in the actual test; hence, the effective specimen length (or the fixture distance) remains almost the same. The pre-stretched state shown in the upper part of Figure 4.21 is regarded as a counterpart of the initial state of the non-pre-stretching case. The strains with respect to the coordinate system of the pre-stretched state are denoted as 'incremental' strain. From the incremental strain, the 'total' strain, which is based on the initial state, can be acquired by summing the true incremental strains. The definition of each strain is provided in Figure 4.20 and Figure 4.21. It should be noted that the incremental axial stretch ratio $\mathrm{d}\lambda_{x,\mathrm{p}}(t)$ is defined by Eq. (7.7) given in Section 7.2. The notations of the pre-stretched and the subsequent dynamically deformed states are denoted by the subscripts 'p0' and 'p', respectively.

The form of the PVW equation for the linear VFM is recalled here again; the component form of Eq. (3.3) is written as

$$-\int_s \sigma_{xx}\varepsilon^*_{xx} + \sigma_{yy}\varepsilon^*_{yy} + \sigma_{xy}\varepsilon^*_{xy}\ \mathrm{d}s = \int_s \rho\left(a_x u^*_x + a_y u^*_y\right)\ \mathrm{d}s \tag{4.4}$$

and with the linear elastic constitutive relation:

$$\begin{aligned} &-Q_{xx}\int_s \varepsilon_{xx}\varepsilon^*_{xx} + \varepsilon_{yy}\varepsilon^*_{yy} + \frac{1}{2}\varepsilon_{xy}\varepsilon^*_{xy}\ \mathrm{d}s - Q_{xy}\int_s \varepsilon_{xx}\varepsilon^*_{yy} + \varepsilon_{yy}\varepsilon^*_{xx} - \frac{1}{2}\varepsilon_{xy}\varepsilon^*_{xy}\ \mathrm{d}s \\ &= \rho\int_s \left(a_x u^*_x + a_y u^*_y\right)\ \mathrm{d}s \end{aligned} \tag{4.5}$$

As mentioned, in this PVW, the Cauchy stress $\boldsymbol{\sigma}$ is conjugated with the true strain $\boldsymbol{\varepsilon}$ and hence $\boldsymbol{u}^*$, $\boldsymbol{\varepsilon}^*$ and s are also defined with respect to the current coordinates of each time step. This equation is modified for the pre-stretching case by assuming that the extra stress $\mathrm{d}\boldsymbol{\sigma}$ due to a stress wave superposed on a statically deformed specimen is independent of the pre-stress. Thus, the PVW for the pre-stretching case becomes

$$-\int_{s_\mathrm{p}} \left(\boldsymbol{\sigma}_{\mathrm{p}0} + \mathrm{d}\boldsymbol{\sigma}_\mathrm{p}\right) : \boldsymbol{\varepsilon}^*_\mathrm{p}\ \mathrm{d}s_\mathrm{p} = \int_{s_\mathrm{p}} \rho\boldsymbol{a}\cdot\boldsymbol{u}^*_\mathrm{p}\ \mathrm{d}s_\mathrm{p} \tag{4.6}$$

$$-\int_{s_\mathrm{p}} \mathrm{d}\boldsymbol{\sigma}_\mathrm{p} : \boldsymbol{\varepsilon}^*_\mathrm{p}\ \mathrm{d}s_\mathrm{p} = \int_{s_\mathrm{p}} \rho\boldsymbol{a}\cdot\boldsymbol{u}^*_\mathrm{p}\ \mathrm{d}s_\mathrm{p} + \int_{s_\mathrm{p}} \boldsymbol{\sigma}_{\mathrm{p}0} : \boldsymbol{\varepsilon}^*_\mathrm{p}\ \mathrm{d}s_\mathrm{p} \tag{4.7}$$

All variables and integrations are based on the current coordinate of the pre-stretched specimen. The incremental Cauchy stress $\mathrm{d}\boldsymbol{\sigma}_{\mathrm{p}}$ is obtained through the linear elastic relation as used to derive Eq. (4.5) but associated with an incremental true strain $\mathrm{d}\boldsymbol{\varepsilon}_{\mathrm{p}}$. The component form of Eq. (4.7) is

$$
\begin{aligned}
&-Q_{xx}\int_{s_{\mathrm{p}}}\left(\mathrm{d}\varepsilon_{xx,\mathrm{p}}\varepsilon^{*}_{xx,\mathrm{p}}+\mathrm{d}\varepsilon_{yy,\mathrm{p}}\varepsilon^{*}_{yy,\mathrm{p}}+\frac{1}{2}\mathrm{d}\varepsilon_{xy,\mathrm{p}}\varepsilon^{*}_{xy,\mathrm{p}}\right)\mathrm{d}s_{\mathrm{p}}\\
&-Q_{xy}\int_{s_{\mathrm{p}}}\mathrm{d}\varepsilon_{xx,\mathrm{p}}\varepsilon^{*}_{yy,\mathrm{p}}+\mathrm{d}\varepsilon_{yy,\mathrm{p}}\varepsilon^{*}_{xx,\mathrm{p}}-\frac{1}{2}\mathrm{d}\varepsilon_{xy,\mathrm{p}}\varepsilon^{*}_{xy,\mathrm{p}}\;\mathrm{d}s_{\mathrm{p}}\\
&=\rho\int_{s_{\mathrm{p}}}\left(a_x u^{*}_{x,\mathrm{p}}+a_y u^{*}_{y,\mathrm{p}}\right)\mathrm{d}s_{\mathrm{p}}+\int_{s_{\mathrm{p}}}\sigma_{xx,\mathrm{p}0}\varepsilon^{*}_{xx,\mathrm{p}}\;\mathrm{d}s_{\mathrm{p}}
\end{aligned}
\tag{4.8}
$$

□ Pre-stretching case

• *Pre-stretched state*

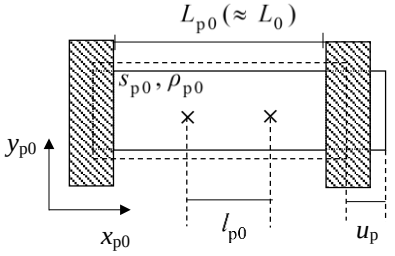

$L_{\mathrm{p}0}$: Initial (effective) specimen length after pre-stretching

$l_{\mathrm{p}0}$: Initial element length after pre-stretching

$e_{x,\mathrm{p}0}$: Nominal axial pre strain $= (l_{\mathrm{p}0} - l_0)/l_0$

$\lambda_{x,\mathrm{p}0}$: Axial pre stretch ratio $= 1 + e_{x,\mathrm{p}0}$

$\varepsilon_{x,\mathrm{p}0}$: True axial pre strain $= \ln(1 + e_{x,\mathrm{p}0})$

• *Deformed state after pre-stretching*

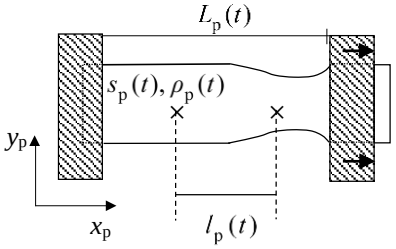

$e_{x,\mathrm{p}}(t)$: Total nominal axial strain $= (l_{\mathrm{p}} - l_0)/l_0$

$\lambda_{x,\mathrm{p}}(t)$: Total axial stretch ratio $= 1 + e_{x,\mathrm{p}}(t)$

$\varepsilon_{x,\mathrm{p}}(t)$: Total true axial strain $= \ln(1 + e_{x,\mathrm{p}}(t))$

$\mathrm{d}\varepsilon_{x,\mathrm{p}}(t)$: Incremental true axial strain $= \ln(l_{\mathrm{p}}(t)/l_{\mathrm{p}0}) = \varepsilon_{x,\mathrm{p}}(t) - \varepsilon_{x,\mathrm{p}0}$

$\mathrm{d}\lambda_{x,\mathrm{p}}(t)$: Incremental axial stretch ratio $= \lambda_{x,\mathrm{p}}(t) - \lambda_{x,\mathrm{p}0}$

Figure 4.21 Configurations and notations for the pre-stretching case.

Only the axial component $\sigma_{xx,\mathrm{p0}}$ of $\boldsymbol{\sigma}_{\mathrm{p0}}$ remains in the last term (the pre-stress term) with the assumption that the transverse and shear stress terms are sufficiently small to be ignored for a uniaxial type specimen. $\sigma_{xx,\mathrm{p0}}$ is obtained from its engineering value which can be calculated by dividing forces (measured after stretching) by an initial cross-sectional area. This procedure was identically used for both simulation and experimental analysis. With the same method in the non-pre-stretching case, either the constant VF or PVF can be applied to the linear VFM to calculate the two material parameters at each time step and for i^{th} pre-stretched state as

$$v_i(t) = Q_{xy,i}(t) / Q_{xx,i}(t), \quad E_i(t) = Q_{xx,i}(t)\left(1 - v_i(t)^2\right) \tag{4.9}$$

A series of Young's moduli E_i are produced as averaged values of $E_i(t)$ over the period where the identification is stable and $v_i(t)$ is close to 0.5, for consideration of material incompressibility. It is assumed that these averaged Young's moduli are a tangent value to the stress-strain relationship in the vicinity of the two points of their pre-strains $\varepsilon_{xx,\mathrm{p0}}$ and global final strains $\varepsilon_{xx,\mathrm{f}}$.

$$\begin{aligned} \varepsilon_{x,\mathrm{f}} &= \varepsilon_{x,\mathrm{p0}} + \mathrm{d}\varepsilon_{x,\mathrm{f}} \\ \mathrm{d}\varepsilon_{x,\mathrm{f}} &= \ln\left(L_{\mathrm{p}}(t_{\mathrm{f}}) / L_{\mathrm{p0}}\right) \end{aligned} \tag{4.10}$$

The subscript 'f' denotes the value of the final step of the averaging period. The strain amplitude $\mathrm{d}\varepsilon_{xx,\mathrm{f}}$ at t_{f} in the actual experiment is obtained by spatially averaging over a deformed area. However, this calculation method can be a cumbersome procedure for the repetitive simulation works that will be presented in this section. Thus, in the present simulation procedure $\mathrm{d}\varepsilon_{xx,\mathrm{f}}$ is approximated by Eq. (4.10). Considering the assumption of the tangent value, an optimization procedure is performed to identify model parameters of a given non-linear material model by minimizing the following cost function:

$$\Phi = \sum_{i=1}^{n}\left[\frac{1}{2}\left(\frac{\partial \sigma_x}{\partial \varepsilon_x}\left(A_1, \ldots A_j, \varepsilon^i_{x,\mathrm{p0}}\right) + \frac{\partial \sigma_x}{\partial \varepsilon_x}\left(A_1, \ldots A_j, \varepsilon^i_{x,\mathrm{f}}\right)\right) - E_i\right]^2 \tag{4.11}$$

The uniaxial stress σ_{xx} in this equation can be identified using any mechanical model suitable for elastomers. In the present study, the one-term Ogden hyperelastic model (Eq. (2.18)) is adopted, assuming that the shape of a dynamic stress-strain curve is similar to that of the static curves of the elastomers used in the present research as it was found that their quasi-static uniaxial curves in tension were well fitted by this hyperelastic model. The quasi-static curves will be presented in the chapter describing the experimental work. The material model for σ_{xx} with its material parameters A_j is differentiated with respect to the true strain ε_{xx} at $\varepsilon_{xx,\mathrm{p0}}$ and $\varepsilon_{xx,\mathrm{f}}$ in order to calculate the two tangent moduli. The optimization scheme, Eq. (4.11), is performed to find material parameters A_j by minimizing the difference between the mean value of the estimated two tangent moduli and E_i identified by the linear VFM.

4.3.2 Simulation with hyperelastic models

The VFM procedure described above was used for the identification of the one-term Ogden material in the present simulation. The two-dimensional simulation configuration used for the work presented in Section 4.2.3 was identically adopted with the PVF and the full-field data, directly obtained from the FEM simulations, to show the best capability of the pre-stretching method. The simulation studies of the present pre-stretching method with the processed data and expected experimental errors will be presented in Chapter 7. In order to define a hyperelastic material, the two coefficients for the one-term Ogden model were arbitrarily chosen as μ = 0.667 MPa and α = 1.2 and the same density value was used. The initial shear modulus of the Ogden model can be approximated by the μ term. With the incompressibility assumption, the initial Young's modulus is obtained as 2 MPa. A value of Poisson's ratio close to 0.5 was defined by choosing a large bulk modulus K = 400 MPa; this gives the Poisson's ratio, $\nu = (3K - 2\mu)/(6K + 2\mu) = 0.499$. There were 9 hyperelastic simulations, including one simulation without stretching and

eight different pre-stretching simulations with given static pre-displacements of the input end (5 mm intervals up to 40 mm). The pre-stretching was applied in a static general step, and then the deformed elements were remeshed using the MAP SOLUTION function in another static general step. This deformed and remeshed geometry was used in an explicit step for the dynamic simulation. In order to more accurately simulate the experiment, in the dynamic simulation step, the velocity boundary condition was applied along a plane 20 mm away from the fixed end (and, to prevent spurious waves, also to every element to the right of this point) as illustrated in Figure 4.19.

Figure 4.22(a) presents the modulus values obtained by applying the linear VFM to each pre-stretching simulation using the proper PVWs of Eq. (4.4) and (4.6). These values were averaged over the period where the curves are stable. Then, the nine averaged moduli values were assumed to be a tangent to the stress-strain curve in the vicinity of their pre-strain locations. These tangents are laid on the given Ogden curve in Figure 4.22(b) where it can be seen that each tangent slope is matched to the Ogden curve at their pre-strain locations. It should be noted that at this point, no constitutive relationship has been assumed in the data analysis, as the VFM calculations assume a linear elastic response to the small-amplitude dynamic strains.

The two Ogden parameters can be inversely calculated using the optimization equation, Eq. (4.11) and each identified E_i. This optimization was conducted by a built-in nonlinear equation solver (*fsolve*) with Levenberg-Marquardt algorithm in MATALB. The optimization performed with the all nine values of E_i produces $\mu = 0.6776$ MPa and $\alpha = 1.287$ (the given coefficients: $\mu = 0.667$ MPa and $\alpha = 1.2$); repeating with only the first two E_i gives $\mu = 0.6674$ MPa and $\alpha = 0.9929$. The significant difference between the α predictions demonstrates that a good identification of α requires data over a large range of strains.

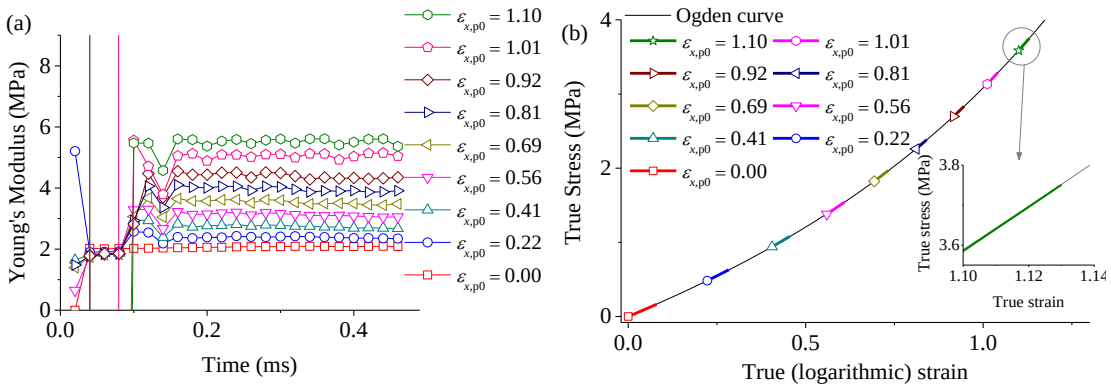

Figure 4.22 (a) Nine moduli predictions from the VFM applied to the one-term Ogden material; (b) nine tangent lines laid on the Ogden true stress-strain curve at each pre-strain location.

The same simulation procedure was applied to a visco-hyperelastic model simulation. In ABAQUS, it is possible to combine the linear viscoelastic behaviour and hyperelastic models as introduced in Section 2.1.2. The one-term Prony series model (Eq. (2.20)) was defined for the viscoelastic behaviour and embedded in the μ term of the one-term Ogden model. The rate-dependent μ term is recalled here and written as

$$\mu(t) = \mu_0(1 - g(1 - e^{-t/\tau})) \tag{4.12}$$

where the normalized shear term for the Prony series, $g = (\mu_0 - \mu_\infty) / \mu_0$, was assumed to be 0.3; this ratio defines the instantaneous shear modulus μ_0 from the given long-term value, μ_∞ = 0.667 MPa. The rate dependency was simulated by giving the four different relaxation time τ: 100, 1, 0.1 and 0.01 ms. The same simulation procedure was used but an additional implicit quasi-static step between the static, and explicit step was used for 1 second in order to ensure that the stress-state was fully relaxed.

The application of the linear VFM on the present simulations produced the four sets of the identified nine moduli. These values were then used in the same optimization procedure; this calculation gives the four Ogden parameter sets given in Table 4.1. In this table, the term μ_{apparent} gives the value of μ which would be obtained by fitting to each of the four data sets individually. When considering the material parameters, this can also be interpreted as a combination of a rate-dependent μ with the Prony series, which is the

Table 4.1 The four Ogden coefficient sets obtained by the optimization process using the four sets of the nine moduli.

τ (ms)	$\mu_{apparent}$ (MPa)	α
Instantaneous	0.953	1.2
100	0.92	1.08
1	0.89	1.10
0.1	0.76	1.15
0.01	0.69	1.19
Long-term	0.667	1.2

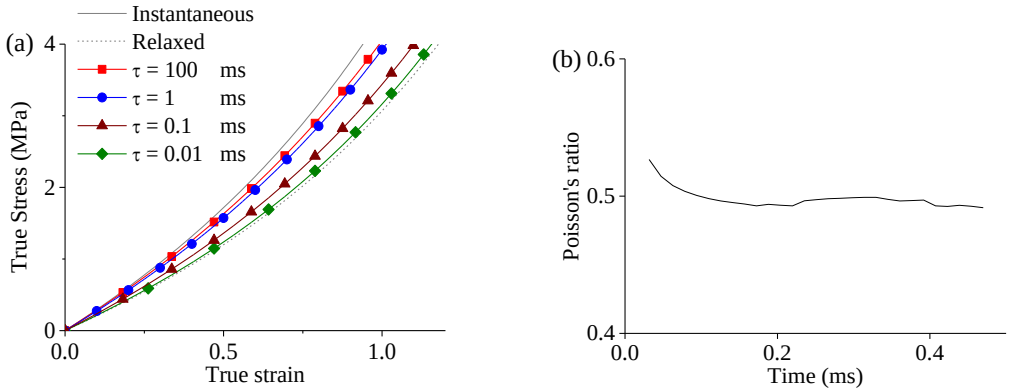

Figure 4.23 (a) Ogden curves plotted using the four sets of the optimized parameters between the given relaxed and instantaneous Ogden curves; (b) Poisson's ratio estimation curve of the visco-hyperelastic simulation (τ = 1 ms) without pre-stretching.

how the parameters are input into the FEM simulation. The true stress-strain curves plotted by these four coefficient sets shown in Figure 4.23(a); it is observed that they are placed between the instantaneous and relaxed Ogden curves, plotted using the instantaneous Ogden coefficient μ_0 = 0.953 MPa and the long-term value μ_∞ = 0.667 MPa, respectively.

It is observed that the reconstructed curve with the longer relaxation time becomes closer to the instantaneous Ogden curve and vice versa. This variation gives confidence that the present VFM procedure with the pre-stretching method is able to capture the stiffer behaviour resulting from the longer relaxation time. In addition, Figure 4.23(b) shows one of the Poisson's ratio output curves during the dynamic loading period. As incompressibility is assumed in the Ogden model by the large bulk modulus, it is

reasonable that the value is close to 0.5. Similar results were obtained in the other simulation cases.

4.4 Summary

This chapter shows the overall simulation works of the application of the linear VFM on the drop-weight experiment. The first simulation was conducted using a linear elastic material model. The identification capability of the linear VFM was investigated with regard to the several experimental factors such as the thickness of a simulation specimen, the range of the data surface and imaging speed. From these simulation studies, it can be concluded that the use of a specimen thinner than 2 mm, the removal of the full-field data by 1 mm away from specimen boundaries and the imaging speed of 50 000 fps are valid for the linear VFM on the material exhibiting stiffness up to 50 MPa. The noise sensitivity was also investigated by adding artificial random noise onto the displacement data. It was found that the use of the piecewise virtual field and the temporal fitting on acceleration fields was effective to reduce the variation of the Young's modulus identifications. All of these considerations found from these simulation works were adopted as experimental requirements for a reliable identification of the Young's modulus.

The same FEM simulation was conducted but with the one-term Ogden model in order to simulate the stress-strain nonlinearity of elastomers. The linear VFM is not sufficient to characterize the nonlinearity as it is exhibited for a long strain range. The identification capability of the linear VFM was extended by the pre-stretching method where the linear VFM is applied on the specimen that is statically stretched and, then, dynamically loaded. It is assumed that the Young's modulus identified after pre-stretching is a local tangent slope in the vicinity of each corresponding pre-strain location. Several moduli obtained at different pre-strain levels were collected and used for the particular optimization scheme for the identification of the parameters of the one-term Ogden model. Also, the

rate dependency of elastomers was simulated by combining the Ogden model and the Prony series. There were four relaxation times given to differentiate the rate dependency under the same velocity boundary condition. It was found the application of the linear VFM and the pre-stretching method was successfully able to capture the rate dependency, in that the stiffer behaviour was measured for the longer relaxation time. The pre-stretching method was identically applied to the drop-weight experiment, and this actual application is presented in the next chapter.

A summary of the present simulation outcomes is listed below and was used for the development of an actual experimental work introduced in the next chapter:

- The imaging speed of 50 000 fps (20 μs data interval) is sufficient to characterize Young's modulus up to 50 MPa.
- It is found that the combination of the piecewise optimized virtual field and the temporal fitting of acceleration fields reduces the identification sensitivity from a random error. This combination should be adopted for an actual experiment procedure.
- According to the simulation study, the VFM identification is sensitive to the specimen geometry. This study leads to two experimental requirements: a specimen should not be thicker than 2 mm; the DIC data exclusion should be limited to 1 mm.
- The principle of virtual work should be based on the current configuration for the identification of Young's modulus as the identification can be underestimated when the initial configuration is applied to the current VFM procedure.
- The identification of constitutive parameters of a hyperelastic model can be enabled by means of the pre-stretching method.

- The number of pre-stretching experiments performed is an important factor for the identification. 9 pre-stretching experiments are sufficient if the true strain range is from 0 to 1.

Chapter 5 THE LINEAR VFM: EXPERIMENTAL APPLICATION

5.1 Introduction

The experiments presented in this research mainly focus on the dynamic properties of elastomers in tension. As discussed in Section 2.2.2, the compressive properties of elastomers under high rate deformation have been relatively widely investigated in compression, usually using modified split-Hopkinson bar apparatus. However, only a small number of studies have explored the development of dynamic experiments in tension. The experimental limitations, which stem mainly from the low speed of sound in the materials, will be even more severe in the case of tensile loading than compressive. However, the same material properties make application of 'non-equilibrium' techniques more attractive, as the slower wave speed makes strain waves easier to observe. Furthermore, tensile specimens are more suited than compressive specimens to full-field analysis as larger specimens may be used without the risk of buckling and the non-static equilibrium state can be clearly captured during dynamic loading.

This chapter provides an overall description of the experimental application of the linear VFM to data obtained using a drop-weight driven apparatus that provides dynamic loading in tension. A pure silicone rubber was chosen as a model material for this study. The description starts with a quasi-static test in tension; the stress-strain curves were then fitted to the one-term Ogden model to obtain the model parameters for this slow rate case. The dynamic test is explained, including the drop-weight experimental procedure and the application of the linear VFM to the full-field data for the identification of the Ogden material parameters. A further discussion is provided with respect to the effect of the temporal fitting required to obtain acceleration fields, the number of virtual elements for

the use of the PVF and the spatial smoothing. Also, the choice of parameters for the DIC analysis is explained. At the end of this chapter, a comparison study is given, in which the initial modulus values obtained by the linear VFM, and the well-established DMA technique are compared.

The objectives of this chapter are summarised as follows:

- A pure silicone rubber is adopted for the experimental study in this chapter. In order to show the high strain-rate dependency, uniaxial tests were performed in tension with two different quasi-static strain rates.
- The dynamic experiment is performed by a drop-weight apparatus and high-speed imaging. The description of this experiment system is given with the actual pictures of the drop-weight apparatus.
- A good quality of the full-field data from DIC is essential for a precise identification of the VFM. The DIC parameters such as subset and overlap sizes are optimized in terms of the amplitude of random errors.
- The pre-stretching method introduced in the previous chapter is applied to the experimental case. This application shows that the use of several Young's moduli identified at different pre-stretching locations leads to the attainment of a nonlinear stress-strain relationship.
- The identification sensitivity of the dynamic VFM is assessed by several experimental factors: calculation methods of acceleration data, configurations of the piecewise virtual element and image smoothing.
- The Young's modulus identified by the drop-weight experiment without pre-stretching is compared with that obtained from dynamic mechanical analysis at a similar strain rate. This comparison provides confidence in the identification of the dynamic VFM.

5.2 Static experiment

5.2.1 Material

A two-part silicone rubber (Sylgard 184 silicone elastomer, Dow Corning) was cured at 100 °C for an hour in a rectangular mould. The resin to hardener ratio was 10:1. The thickness was uniformly about 0.7-1 mm. From this sheet, two flat specimen shapes were prepared respectively for static uniaxial (100×8 mm) and drop-weight (50×8 mm) tests. Black paint was sprayed to make a fine random pattern over the specimen surface; an example of this pattern is shown in Figure 5.4. The density of the silicone rubber was measured to be 1040 kg m^{-3}, obtained by weighing and measuring a specimen cut from the sheet that was used for manufacturing the dynamic and static specimens.

5.2.2 Static uniaxial test

Uniaxial static tests were conducted on the silicone rubber specimens at two different true strain rates: 0.001 and 0.01 s^{-1}. In order to prevent slipping from the test fixtures, a pneumatic grip was used to clamp both ends of the specimens. The strain was measured by a long-travel clip-on extensometer with a 25 mm gauge length in the middle of the specimens. The engineering strain measured by the extensometer was converted to the true value using the following equation

$$\varepsilon_x = \ln\left(1 + e_x\right) = \ln(\lambda_x) \tag{5.1}$$

where e_x denotes the engineering strain in the loading direction. The forces during the extension were measured by a 100 N load cell. The measured force data were divided by the initial cross-sectional area of the specimens to obtain the engineering (nominal) stresses, N_x. The true stress values were then calculated by the push forward operation written as

$$\sigma_x = N_x \lambda_x \tag{5.2}$$

The engineering stress-strain data were fitted to the one-term Ogden model to find the material parameters μ and α; its form can be derived from Eq. (2.14) and (2.18) and written as

$$\mathrm{N}_x^{Ogden} = \frac{2\mu}{\alpha}\left(\lambda_x^{\alpha-1} - \lambda_x^{-1-0.5\alpha}\right) \tag{5.3}$$

The fitting of this equation to the experiment data was conducted by the MATLAB built-in function, *fmincon*, with the conditions that μ, $\alpha > 0$ in order to satisfy material stability (Ogden et al., 2004). The cost function used for this minimization is

$$\Phi = \sum_{i=1}^{n}\left[\mathrm{N}_x^{Ogden}\left(\mu, \alpha, \lambda_x^{Exp}(t_i)\right) - \mathrm{N}_x^{Exp}(t_i)\right]^2 \tag{5.4}$$

where n is the total number of data pairs and the superscript 'Exp' denotes that the variables are experimental data. Applying this minimization to the two quasi-static experiments, the Ogden parameters are obtained as μ = 0.40 MPa, α = 4.53 for 0.001 s^{-1} and μ = 0.42 MPa, α = 5.25 for 0.01 s^{-1}. Using these parameters and Eq. (5.2) & (5.3), the fitted true stress-strain curves were reconstructed and are represented in Figure 5.1 with their actual experimental curves, which show the usual nonlinear elastomeric behaviour: a short linear region and strain hardening at large strain. The rate dependency can be observed even between these quasi-static rates and is clearly exhibited after about a true strain of 0.1.

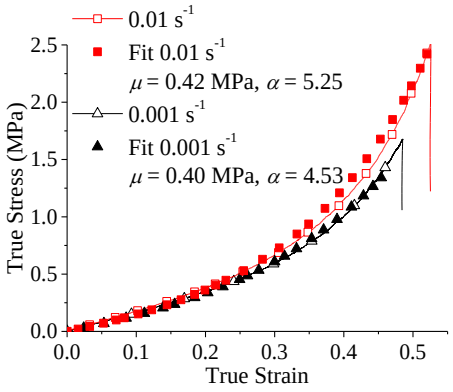

Figure 5.1 Static uniaxial tests on silicone rubbers at 0.001 and 0.01 s^{-1} and their fitted curves and parameters with the one-term Ogden model.

In addition, a simple imaging procedure was introduced to measure the global Poisson's ratio of the static specimen. The specimen was stretched in uniaxial tension at 0.001 s^{-1} true strain rate until the final true strain of 0.6. Photographs (Nikon DSLR D3100) were manually taken 17 times before, during and after the test. Then, the dimensions of the total length and central width of the specimen in each image were measured in the following way. The pictures were imported into DIC software (Davis 7.2, LaVision 2007) with the calibration information, which was obtained by taking a photo of a high precision ruler located at the same place of the test specimens. The total length was calculated by the lengthwise, *x*, coordinates of the pixels placed around the fixed and loaded boundary edges. The width was also measured in the same way using the pixels placed around the side edges. This procedure did not involve DIC analysis. With these measurements, the calculation of the Poisson's ratio was performed by the following relations

$$L_i / L_0 = \lambda_{x,i}, \; W_i / W_0 = \lambda_{y,i} \tag{5.5}$$

$$v_i = -\ln \lambda_{y,i} / \ln \lambda_{x,i}, \; v = \sum_{i=1}^{17} (v_i) / n \tag{5.6}$$

The global Poisson's ratio v is an averaged value of 17 individual v_i and was obtained as 0.490 ± 0.009.

5.3 Dynamic experiment

5.3.1 Procedure

The drop-weight apparatus and high-speed imaging system are shown schematically in Figure 5.2. This system can be separated into three parts: specimen housing, drop-weight and loading bar, and imaging devices. Actual pictures of these parts are given in Figure 5.2. The specimen housing holds the elastomer specimen between two clamps, one of which, above the specimen, is in turn connected to a static force sensor. The specimen sits above the drop-weight apparatus as shown in Figure 5.2(a). The upper clamp is tightly

closed first. In the non-pre-stretching case, before applying the bottom clamp, the specimen is slightly extended in order to prevent slight bending which occurs due to the high clamping pressure pushing the specimen out of the clamps. Figure 5.2(b) shows the high-speed camera (FASTCAM SA 5, Photron) equipped with a 105-mm Nikkor lens and two continuous light lamps (Dedocool, DEDOTEC). A feature of high-speed video cameras is that as the imaging speed increases, the resolution decreases as the field of view is reduced. Figure 5.2(c) is a picture of the bottom part of the drop-weight apparatus. It consists of the rubber stopper supporting the long steel loading bar, which is connected to the bottom clamp, and the cylindrical drop weight which is able to slide along the loading bar. Figure 5.2(d) shows the overall system, next to which there are a laptop, an oscilloscope and an amplifier.

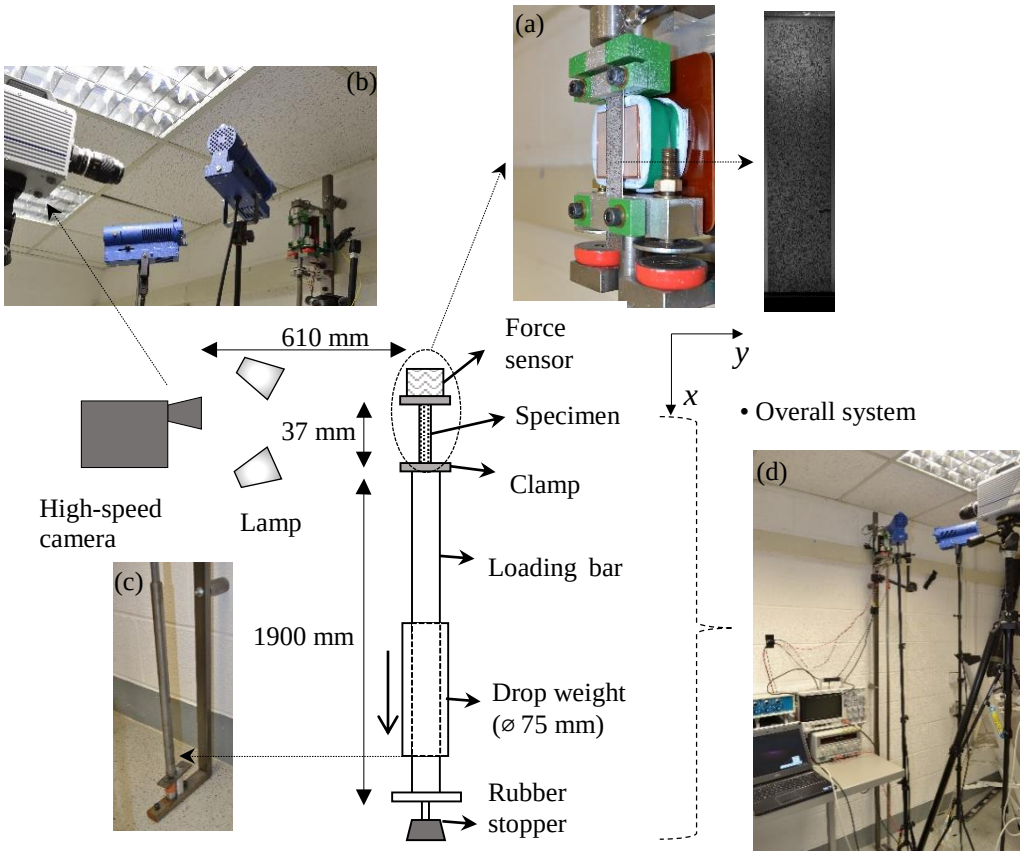

Figure 5.2 Schematic diagram of the drop-weight dynamic test and high-speed imaging system, showing actual pictures of (a) specimen between clamps, (b) imaging devices, (c) drop weight and (d) overall system (a stationary specimen picture taken by a high-speed camera is also given).

The drop-weight experiment was conducted as follows. First, the silicone rubber specimen was placed and clamped as mentioned above. The high-speed camera was set to be ready for receiving a trigger signal; the lamps were then turned on. The drop weight was manually lifted up to a pre-marked location and dropped in order to allow an impact on the flange attached at the end of the loading bar. This impact generates a tensile wave which travels along the bar past a strain gauge which is attached to the loading bar surface of about 100 mm from the specimen. The strain gauge monitors this stress wave and produces a signal which is amplified and recorded in the oscilloscope and, most importantly, used to send a trigger signal to the high-speed camera. The camera records for 3 s and is 'centre' triggered, so that half of the images are recorded before the wave arrives. The full set of images is then temporally cropped to the short duration which the loading is applied to the specimen.

As discussed in the simulation presented in Figure 4.7, it is obvious that a faster imaging speed provides better identification of the Young's modulus due to a higher temporal resolution in the calculation of acceleration fields. However, in common with all high-speed video cameras, the field of view of the camera used is reduced as the imaging speed increases. Thus, the imaging speed can affect the imaging distance and, consequently, imaging resolution. In order to determine optimal imaging speed, a preliminary study was conducted in which 10 still images taken on a stationary sample (of a similar size to the specimen used in the drop-weight test), with a random speckle pattern, at 4 imaging speeds of 10 000, 50 000, 100 000 and 232 500 fps. Then, each image set was analysed by the DIC software with a subset size of 12×12 pixels to obtain spatial standard deviations of their longitudinal displacement fields. In Figure 5.3, the mean standard deviation over the 10 images for each imaging speed is presented with the number of pixels obtained (width × length). With the consideration of these standard

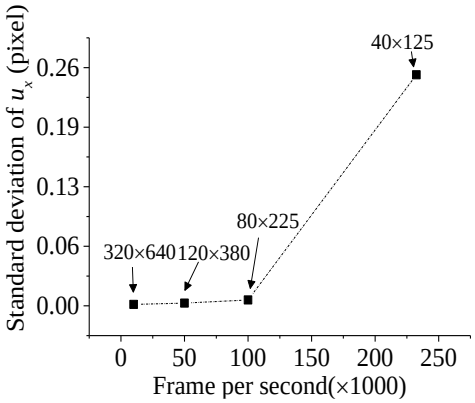

Figure 5.3 Averaged noise levels (standard deviation: 1 pixel = 0.078 mm) of the axial displacement fields from 10 still images at imaging speeds of 10 000, 50 000, 100 000 and 232 500 fps with each image size (width × length pixel).

deviations, it is reasonable to choose 50 000 fps, as 10 000 fps is too slow to capture wave propagation. This is the 'imaging speed' which was used in the simulation work. With this imaging speed, the image resolution is about 120×380 pixels in the image analysis region (8×35 mm). A still image of the actual specimen in situ is shown in Figure 5.2(a).

In the case of the pre-stretching experiment, the specimens were manually stretched before applying dynamic loading. The upper end of the specimen was fixed first and the bottom end was stretched downward. There were eight different pre-strains, as indicated in Table 5.2 in Section 5.3.2. These were achieved by first clamping the fixed end of the specimen, then stretching it, initially by 10 mm and then by 5 mm intervals up to 45 mm, before clamping to the input rod to create a gauge length of about 37 mm each time. After each pre-stretching, the axial force was recorded by an in-line force sensor installed above the upper fixture (i.e. on the fixed end of the specimen) as shown in Figure 5.2(a). Then, the procedure described above for introducing dynamic loading and taking high-speed imaging was applied to each pre-stretched specimen. It should be noted that the time between pre-stretching and application of the dynamic loading was less than 3 minutes. The effect of the relaxation time will be explained in Chapter 7. The pre-strain in the loading direction was approximated by comparing the distance of two pre-marked points

on images of the initial and pre-stretched specimen. This procedure was applied to the two test samples, referred to as SET1 and SET2, which were cut from the same silicone rubber sheet that was used for the static tests. From the images taken during dynamic loading, the commercial DIC software was used to obtain two-dimensional full-field data.

The procedure of obtaining the full-field data from the DIC software was conducted in the following way. Figure 5.4 shows part of the actual specimen surface which has a random speckle pattern made by a spray paint. Several images of these patterns taken during dynamic loading are imported to the DIC software. The DIC software provides a convenient platform to control several factors related to image correlation so that a random pattern, i.e. distinct intensity distribution, within a particular subset window can be correlated between the initial and displaced patterns. The correlation mode was chosen as cross-correlation. The multi-pass iteration mode (Davis 7.2, LaVision 2007) was used in which the window size is gradually decreased, and each window produces a displacement vector used as the starting value for the calculation in the next, smaller, window. The first and final window sizes were chosen as 64×64 (50 % overlap) and 12×12 (75 % overlap). In Figure 5.4, the final subset (red rectangle) size is shown on one of the speckle patterns on the silicone rubber specimen of Test SET1.

The final subset size was chosen by considering two conditions: Poisson's ratio and noise level in strain fields. The selection procedure of the best subset size is described in

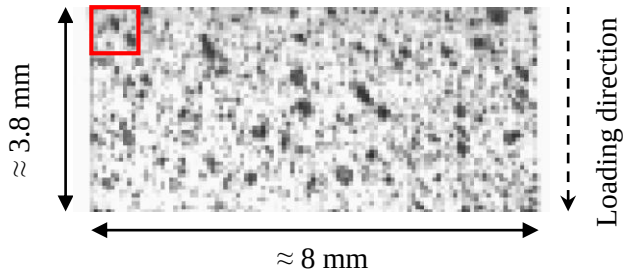

Figure 5.4 Part of the random speckle pattern made on the rubber specimen and the subset window (red rectangle) of 12×12 pixel.

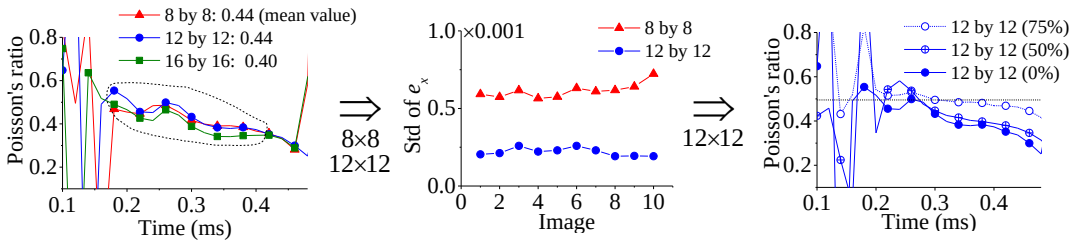

Figure 5.5 Subset size selection procedure: (first) the Poisson's ratio identifications with 8×8, 12×12 and 16×16 subset (0 % overlap) sizes on the drop-weight test data (SET1: non-pre-stretching); (second) the standard deviation of the axial strain fields of the 10 still images with 8×8 and 12×12 subset (0 % overlap) sizes, and (third) the Poisson's ratio identifications with 12×12 subset size and 0, 50 and 75 % overlap sizes.

Figure 5.5. First, three square subsets of 8, 12 and 16 pixels (0 % overlap) were chosen for analysing the drop-weight test data of SET1: non-pre-stretching. With these subset sizes, the strain (directly from the DIC software) and acceleration fields (by the temporal fitting method explained in Section 4.2.3) were applied to the VFM procedure. The averaged values of the derived Poisson's ratio was obtained as explained in Section 5.3.2; their values are 0.44, 0.44 and 0.40 respectively for 8, 12 and 16 pixel subsets. Assuming that the Poisson's ratio measured in the static test is considered as the reference value (0.49), 8 and 12 subset sizes were selected as the next possible choices. The next criterion for the best possible subset size is the noise level in the strain fields. Taking 10 still images, long before the dynamic loading began in the specimen, the spatially averaged standard deviation in their longitudinal (engineering) strain fields were obtained as presented in the middle of Figure 5.5. It is clear that the noise level with 12 subset size is lower, thus it is chosen as the best subset size.

Poisson's ratio with this subset size is still much lower than the reference value measured in the static test. It is possible to further improve the Poisson's ratio by expanding the area of the subset overlap without using smaller subset sizes in order to produce a larger number of data points. A high resolution of data points is especially required in the lateral displacement fields as the ratio of the pattern size to the width is

much larger than to the length. Figure 5.6 shows the effect of this larger overlap size on the averaged lateral strain values (over the whole surface) compared to the longitudinal strain. As can be seen in the right-hand side of Figure 5.5, the use of 75 % subset overlap leads to a value of Poisson's ratio which is the closest to the reference value. With this final DIC configuration of 12×12 subset size with 75 % overlap, the noise floors of the displacement and strain fields are presented in Figure 5.7, and it can be found that the noise amplitude in the longitudinal strain is higher than that of the 12 subset size with no overlap. However, the simulation work already shows that this noise level does not significantly affect the Young's modulus identification. Through all of the DIC analysis on the drop-weight experiment, 12×12 pixels with 75 % overlap was chosen for the final

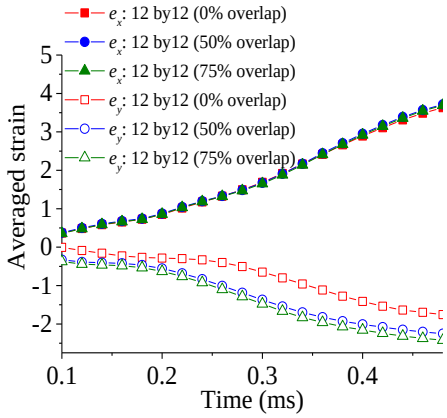

Figure 5.6 Averaged (over the whole surface) longitudinal and lateral strain curves of the drop-weight test data (SET1: non-pre-stretching) with respect to the three overlap sizes.

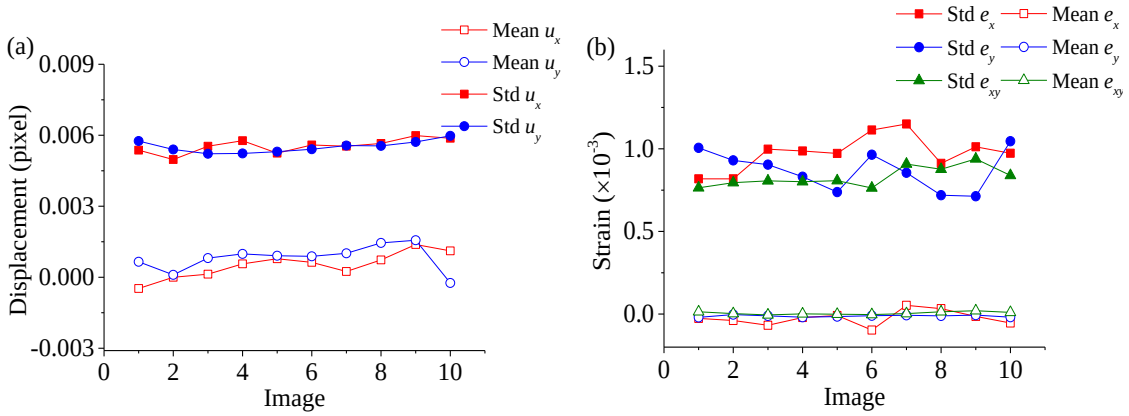

Figure 5.7 Mean and standard deviation of the (a) displacement and (b) strain fields of 10 still images with 12×12 subset size and 75 % overlap.

subset size. As a result of the choice of this subset size, the distance between each data point was 0.23 mm.

As mentioned, the strain fields were directly obtained through the DIC software. According to its manual (Davis 7.2, LaVision 2007), the strain fields are obtained from the following equation, for example for the engineering axial strain with respect to the initial coordinates x_0 and y_0:

$$e_x(x_0, y_0) = \left(u(x_0 + \Delta x_0, y_0) - u(x_0 - \Delta x_0, y_0)\right) / 2\Delta x_0 \tag{5.7}$$

In summary, Table 5.1 lists several imaging and DIC factors adopted in this chapter. The axial strain resolution is an averaged value of the standard deviation of the axial strain shown in Figure 5.7(b); the axial acceleration resolution is also obtained from its standard deviation data shown in Figure 5.13(a), which is provided in the later section.

Table 5.1 Imaging and DIC analysis factors

camera	FASTCAM SA 5, Photron
DIC software	Davis 7.2, LaVision 2007
field of view (data)	120×380 pixels
interframe time	20 μs
subset size (final)	12×12
subset overlap (final)	75 %
spatial smoothing	not applied
temporal smoothing (acceleration)	9-degree polynomial
axial strain resolution	1×10^{-3}
axial acceleration resolution	7×10^{5} mm s^{-2}

5.3.2 Results

The data set (***u***, ***e***) obtained through the procedure explained above was imported into MATLAB for the linear VFM analysis. The engineering strain data ***e*** were converted to the true value $\boldsymbol{\varepsilon}$ using the relation in Eq. (5.1). The displacement and strain fields in the longitudinal direction *x* of one of the test specimens (non-pre-stretching) are presented in Figure 5.8(a-b), in which the tensile loading was applied on the right-hand side of the

figure. For the acceleration fields in Figure 5.8(d), the temporal fitting method was applied as explained in the simulation work. Figure 5.8(e) shows the axial displacement fields before the start of the experiment and at 0.3 ms, overlayered on actual pictures of the specimen.

The linear VFM was applied to the experimental data in the same manner as described in the simulation section: Eq. (4.5) and (4.8) were used respectively for the non-pre and pre-stretching cases. One of the simulation data procedures required to obtain the central displacement values in each element was not used as the data of the DIC are obtained at the centre of each subset window. The PVF method was adopted and an example in the

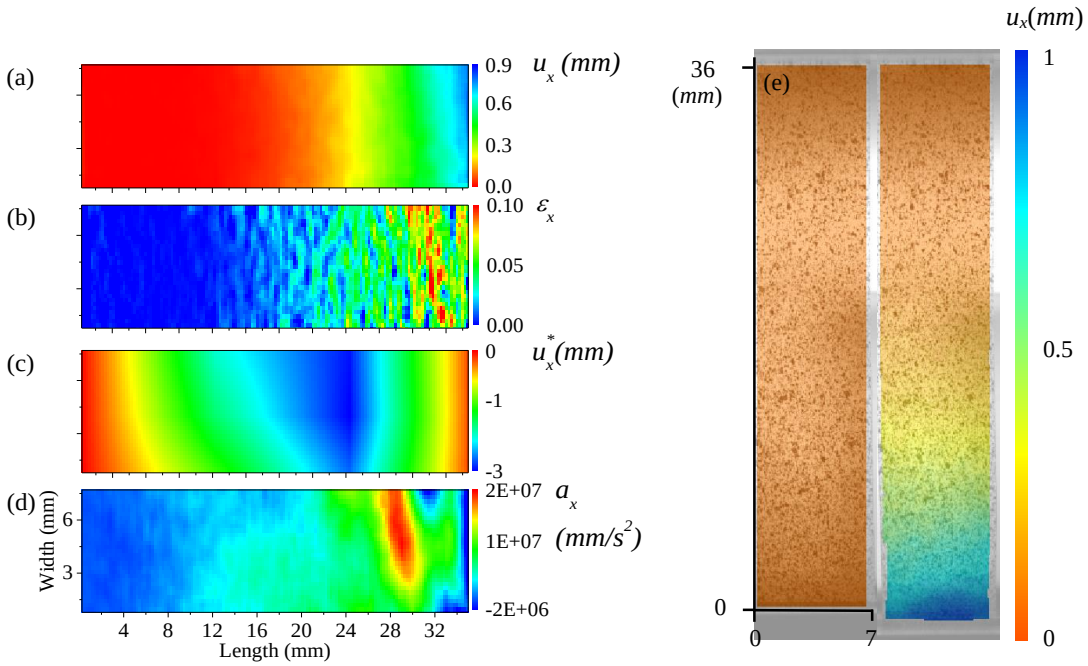

Figure 5.8 (a) Axial displacement, (b) true strain, (c) virtual displacement, (d) acceleration fields of the non-pre-stretching test at 0.3 ms and (e) the same axial displacement field overlayered on the actual picture (before and after loading) (SET1: non-pre-stretching).

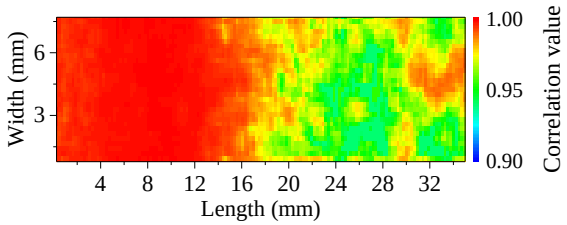

Figure 5.9 Correlation map of the non-pre-stretching test (SET1) at 0.3 ms.

longitudinal direction, u_x^*, corresponding to the actual data in Figure 5.8, is presented in Figure 5.8(c). The corresponding correlation (coefficient) map is shown in Figure 5.9. A correlation value close to 1 means a perfect correlation; when this value is higher than 0.9, it is generally accepted as an indication of a good correlation result (Ghosh et al., 2012; Pan, 2011; Pyne et al., 2014; Zhang et al., 2002; Zhu, 2015). From Figure 5.8, it can be observed that the data are similar to those from the simulation work, Figure 4.3, and the virtual field satisfies the two conditions at the left and right ends for the kinematic admissibility and the cancellation of the traction force term in the PVW. Also, it is seen that the position of the peak virtual displacement area is located around the acceleration wave front.

The Young's modulus estimation for this non-pre-stretching case is plotted with the longitudinal true strain, Poisson's ratio and averaged strain rate in Figure 5.10. For the averaged strain rate, the (true) strain rate maps were obtained in the same way used to obtain the acceleration maps from the temporal fitting, and then, the areas which have been subjected to the stress wave (i.e. excluding the undeformed area) for each time step were chosen for averaging. By the same method, the averaged true strain values were also obtained. During the stable estimation period, the strain rate and Poisson's ratio are about 130-140 s^{-1} and 0.4-0.5. Figure 5.11(a) shows the first set of all pre-stretching VFM results. As the pre-stretching amount is increased, the Young's modulus estimations gradually increase. It is also observed that the stable prediction period is continuously reduced: for example, 0.2-0.4 ms for the non-pre-stretched and 0.16-0.24 ms for an experiment in which the true pre-strain was 0.51. This reduction is due to the stiffer behaviour at higher strain so that the wave speed is higher and, consequently, the stress wave reached the fixed end of the specimen more quickly. A similar result is shown in the simulation work in Section 4.2.2. The simulation work in Section 4.3.2 does not show

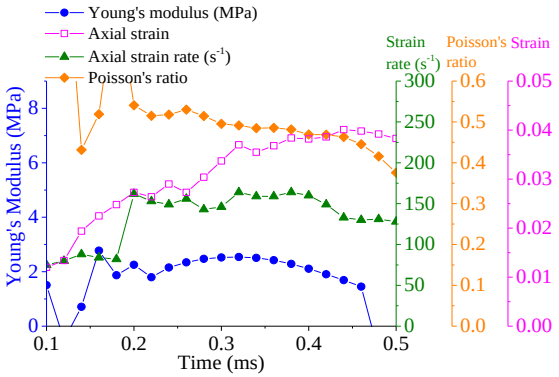

Figure 5.10 Young's modulus estimation with the Poisson's ratio, averaged strain and strain rate (SET1: non-pre-stretching).

this reduction because the stiffening due to straining is not significant in the simulation material compared to the current silicone rubber.

At the period when Poisson's ratio is between 0.40-0.50, between which the reference value lies, Young's moduli E, Poisson's ratio v, true strain ε_{xx} and strain rate $\dot{\varepsilon}_{xx}$ are averaged for all tests of SET1-2, and the mean values are given in Table 5.2. The averaging periods are presented as a hatched area in Figure 5.11. The hatched area is concentrated on the initial loading period. The reason for this concentration is to avoid the unstable prediction period which occurs when the stress wave reaches the fixed end and the averaged acceleration becomes close to zero, i.e. temporally quasi-static equilibrium. This explanation can be described by the example shown in Figure 5.11(c) in which the prediction of the last pre- stretching experiment of SET2 starts to be unstable (fall toward zero) when the averaged acceleration is close to zero (quasi-static equilibrium). The averaged moduli and their pre-true-strain values were applied to the optimization procedure of Eq. (4.11) in order to find the Ogden parameters respectively for the experiments: SET1-2. The optimized parameters are listed in

Table 5.3. These two parameters are used for reconstructing the true stress-strain curve of the Ogden model, Eq. (5.3); these curves are provided in Figure 5.12(a), in which the two dynamic curves show good repeatability. In the second optimization procedure, it is

assumed that the α term is independent of strain rate, as demonstrated in a previous study of rate dependence of a silicone rubber (Shergold et al., 2006). Using this assumption, the objective function, Eq. (4.11), is modified to include three μ terms: one each for the two static ($\mu^{0.1\%/s}$, $\mu^{1\%/s}$) and one for the set of dynamic tests (μ^{VFM}) and the same α term for all cases. The new objective function is rewritten in the following form:

$$\begin{cases} \Phi_1 = \sum_{i=1}^{16}\left[\frac{1}{2}\left(\frac{\partial\sigma_x}{\partial\varepsilon_x}\left(\mu^{\mathrm{VFM}},\alpha,\varepsilon_{x,\mathrm{p0}}^{i}\right)+\frac{\partial\sigma_x}{\partial\varepsilon_x}\left(\mu^{\mathrm{VFM}},\alpha,\varepsilon_{x,\mathrm{f}}^{i}\right)\right)-E_i\right]^2 \\ \Phi_2 = \sum_{i=1}^{n1}\left[\sigma_x\left(\mu^{0.1\,\%/s},\alpha,\varepsilon_x^{0.1\%/s}(t_i)\right)-\sigma_x^{0.1\%/s}(t_i)\right]^2 \\ \Phi_3 = \sum_{i=1}^{n2}\left[\sigma_x\left(\mu^{1\,\%/s},\alpha,\varepsilon_x^{1\%/s}(t_i)\right)-\sigma_x^{1\%/s}(t_i)\right]^2 \end{cases} \tag{5.8}$$

The first equation is to find the optimized μ^{VFM} with respect to the 16 modulus results from the SET1-2 tests; the remaining terms represent the nonlinear equations for the two quasi-static tests. The values '$n1$' and '$n2$' in these equations indicate the number of the

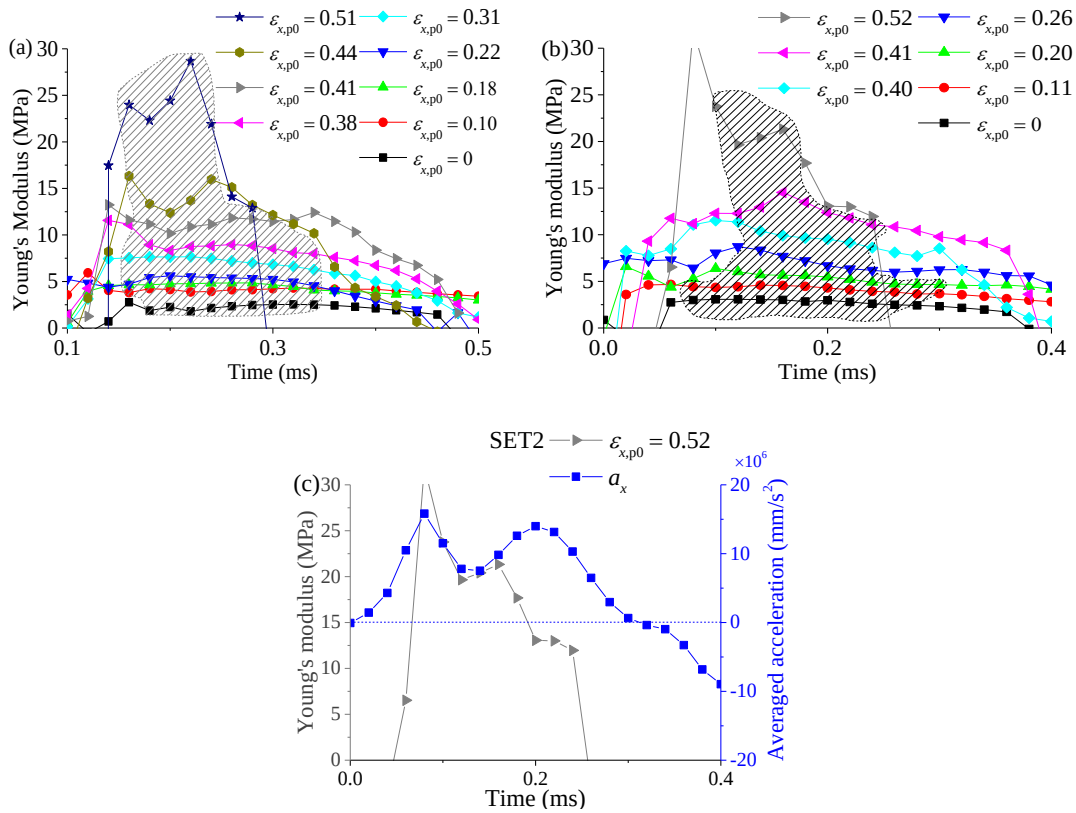

Figure 5.11 Nine moduli prediction sets for (a) SET1 and (b) SET2 (the hatched area indicates the averaging period); (c) Modulus prediction of $\varepsilon_{x,p0}$ = 0.52 from SET2 and the averaged acceleration profile.

data points for each case. These cost functions with all of the test data were simultaneously optimized by the MATLAB function, *fsolve*, to produce the Ogden parameters given in Table 5.3. Corresponding to these coefficients, Figure 5.12(b) shows the true stress-strain curves according to the one-term Ogden model. Comparison between these curves in this figure clearly shows the rate dependency of the material. In Table 5.3 (the second optimization method), this rate dependency can also be observed in the increasing μ_{apparent} term, equivalent to the initial shear modulus.

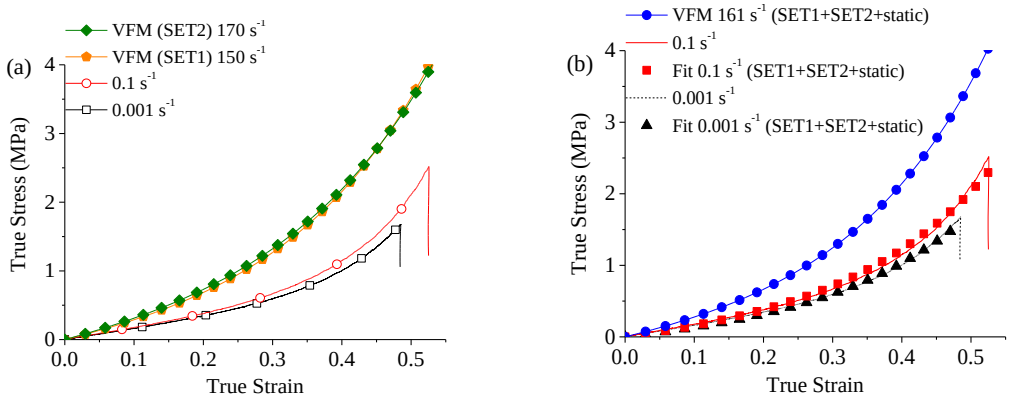

Figure 5.12 (a) Dynamic Ogden curves reconstructed from the first optimization method compared to the quasi-static tests; (b) fitting curves for the two quasi-static tests and one dynamic curve reconstructed from the second optimization method in which all rates are considered together.

Table 5.2 Averaged Young's modulus *E*, longitudinal true strain ε_x, strain rate $\dot{\varepsilon}_x$ and Poisson's ratio *v*.

SET1	*E* (MPa)	ε_x	$\dot{\varepsilon}_x (s^{-1})$	*v*	$\varepsilon_{x,p0}$	SET2	*E* (MPa)	ε_x	$\dot{\varepsilon}_x (s^{-1})$	*v*	$\varepsilon_{x,p0}$
	2.5	0.033	160	0.49	0.00		2.8	0.046	210	0.50	0.00
	4.2	0.025	160	0.50	0.10		4.5	0.023	210	0.46	0.11
	4.7	0.024	160	0.43	0.18		4.9	0.037	160	0.43	0.20
	5.4	0.028	140	0.44	0.22		6.6	0.029	160	0.49	0.26
	7.4	0.025	170	0.42	0.31		11.1	0.026	160	0.45	0.40
	8.6	0.021	160	0.46	0.38		12.4	0.019	160	0.44	0.41
	11.4	0.019	170	0.40	0.41		19.5	0.016	130	0.47	0.52
	14.3	0.014	130	0.45	0.44						
	24.3	0.018	140	0.43	0.51						
	Averaged $\dot{\varepsilon}_x$ = 150 s^{-1}, *v* = 0.45						Averaged $\dot{\varepsilon}_x$ = 170 s^{-1}, *v* = 0.46				
	Total averaged $\dot{\varepsilon}_x$ = 160 s^{-1}, *v* = 0.45										

Table 5.3 Ogden parameter sets obtained by the first and second optimization procedures.

Optimization method	Test	$\mu_{apparent}$ (MPa)	α
First	Dynamic SET1: 150 s^{-1}	0.84	4.60
	Dynamic SET2: 170 s^{-1}	0.92	4.26
Second	Static: 0.001 s^{-1}	0.39	4.78
	Static: 0.01 s^{-1}	0.46	4.78
	Dynamic SET1+2: 160 s^{-1}	0.81	4.78

5.4 Discussion of the VFM data

5.4.1 Calculation of the acceleration fields

In the final data in Figure 5.12, the VFM analysis was based on the acceleration fields formed by the temporal fitting method. It is useful to investigate the effect of this fitting method compared to the simple finite difference method. Figure 5.13(a) shows the noise floor in the axial acceleration fields from the 10 still images as used in Figure 5.7 (SET 1: non-pre-stretching). This noise floor is calculated from data obtained by the simple finite difference method. The value of this noise level (0.744×10^6 mm s^{-2} on average) compared to the acceleration amplitude, for example, 15×10^6 mm s^{-2} from Figure 5.8, is about 5 %. This noise level partially contributes to a slight variation in the averaged acceleration (over the whole specimen), which then feeds into the Young's modulus calculation. Figure 5.13(b) compares the Young's modulus identifications based on the

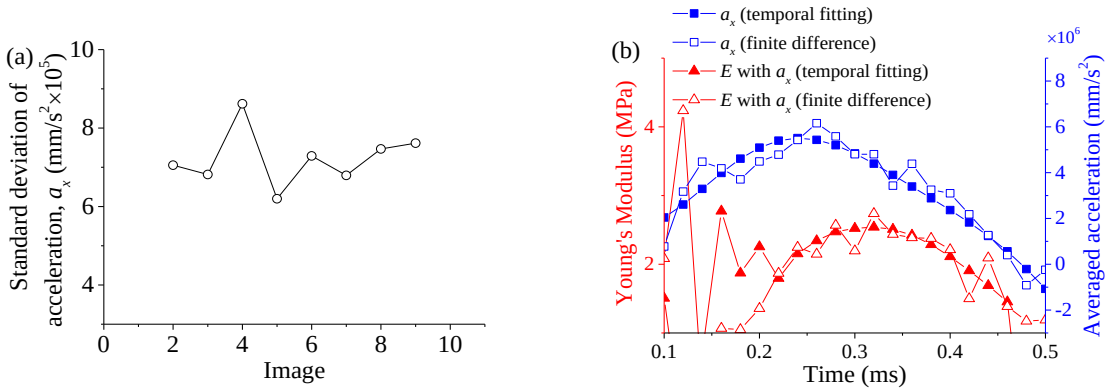

Figure 5.13 (a) Standard deviation of the acceleration fields of 10 still images; (b) averaged (over the whole surface) acceleration profile from the two acceleration calculation method and their Young's modulus identifications.

finite difference and temporal fitted acceleration fields; the standard deviation of Young's modulus (0.2-0.4 ms) is reduced from 0.15 MPa to 0.10 MPa when the temporal fitting is used.

5.4.2 Piecewise virtual field, number of elements

The experimental data from the SET1 without pre-stretching were reanalysed using different numbers of virtual elements for the PVF to evaluate the stability of the identification. Figure 5.14 shows this analysis for Young's modulus and Poisson's ratio. The identifications are rather stable, and there is a slight convergence toward 8×2. As pointed in the VFM textbook (Pierron and Grédiac, 2012), continued increasing of the number of the virtual elements does not ensure this convergence but will lead to numerical instability. The same analysis was conducted in (Pierron et al., 2014) showing a similar trend in the identification with respect to the mesh density.

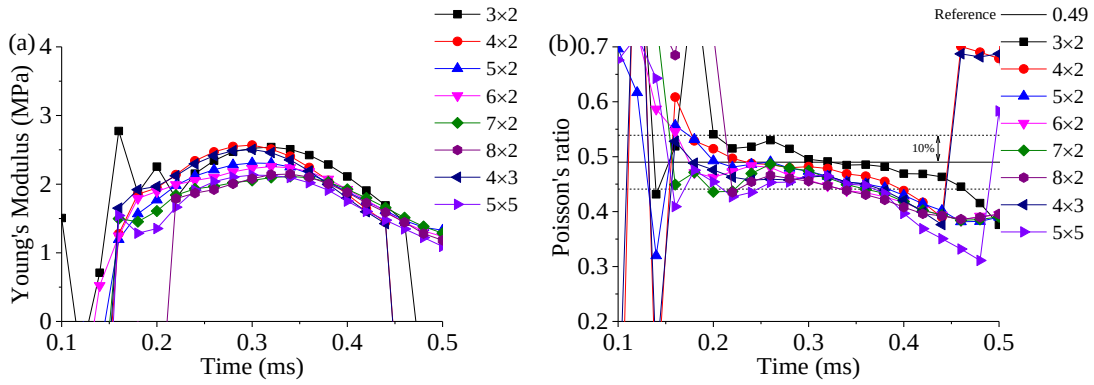

Figure 5.14 Identifications of (a) the Young's modulus and (b) Poisson's ratio of the SET1: non-pre-stretching with several virtual element numbers.

5.4.3 Effect of spatial smoothing

In the experimental work, no spatial smoothing filter was applied to the displacement fields as the simulation work shows that the VFM is able to provide good identification using the displacement fields with a noise level similar to that of the actual experiment. However, it is still worthwhile to study the effect of a spatial smoothing to the actual displacement fields. The DIC software provides a function to apply a Gaussian smoothing

filter to the displacement fields with three different filter sizes of 3×3, 5×5 and 9×9. Figure 5.15 presents the smoothing effect on the identifications of Young's modulus and Poisson's ratio. The effect of the smoothing is not significant for either Young's modulus or Poisson's ratio; the identifications are stable with respect to the size of the smoothing filter.

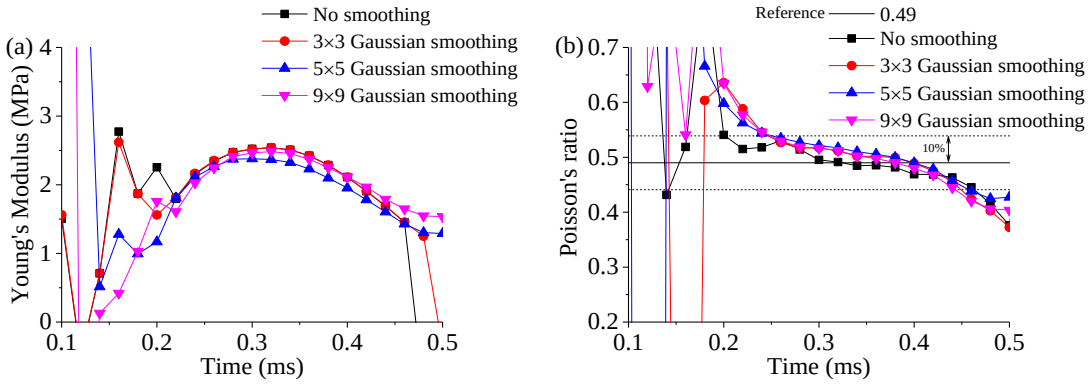

Figure 5.15 Identifications of (a) the Young's modulus and (b) Poisson's ratio of the SET1: non-pre-stretching with a Gaussian smoothing filter.

5.4.4 Overall discussion

The drop-weight test results demonstrate that the use of the linear VFM and high-speed photography in particular, to obtain acceleration fields, can replace the requirement for force measurement and static equilibrium in a dynamic tensile experiment. One advantage of the present VFM is that it is possible to capture the dynamic material behaviour at small strain amplitudes which could not be measured or properly analysed using more traditional techniques such as the SHPB. For example, the behaviour of the rubber specimens discussed in this paper can be observed reliably for strains as small as 0.05. Unlike more traditional experiments, these advantages will be even more apparent in faster experiments with smaller material forces (i.e. in which the ratio of inertial to material forces is even higher). However, in order to obtain parameters for hyperelastic materials, both small and large strain data are required. In the experiments presented here, these data were obtained by pre-stretching the material statically before applying dynamic

loading. By measuring local stiffness at a range of different strains, and applying a suitable optimization routine, it was then possible to build the full dynamic stress-strain curve for this material with a unique combination of both low strain fidelity and large strain data which cannot be obtained by any other dynamic testing method.

5.5 Comparison with dynamic mechanical analysis

Frequency dependence of mechanical properties at a small strain amplitude is often studied by the DMA technique. Here, a uniaxial multi-frequency DMA test was used to obtain temperature effects on the same silicone rubber at three different frequencies (0.5, 5, 50 Hz) between -80 to 70 °C with a strain amplitude of 0.1 %. For this tensile mode DMA, a thin film type specimen was manufactured (length = 8, width = 5.7, thickness = 0.53 mm). The DMA test was conducted by Q800 DMA instrument (TA Instruments).

Figure 5.16(a) and (b) show the multi-frequency storage modulus and tan δ versus temperature. The steep drop in storage modulus at around -60 °C is thought to reflect the melting of a crystalline phase within the silicone rubber. The three curves in Figure 5.16(a) are recognized in the form of isotherms versus the logarithmic time, which is the time to reach a maximum strain amplitude (i.e. a quarter of a loading cycle). Thus, the three frequencies, 0.5, 5 and 50 Hz correspond to 0.5, 0.05 and 0.005 s. The isotherm data are

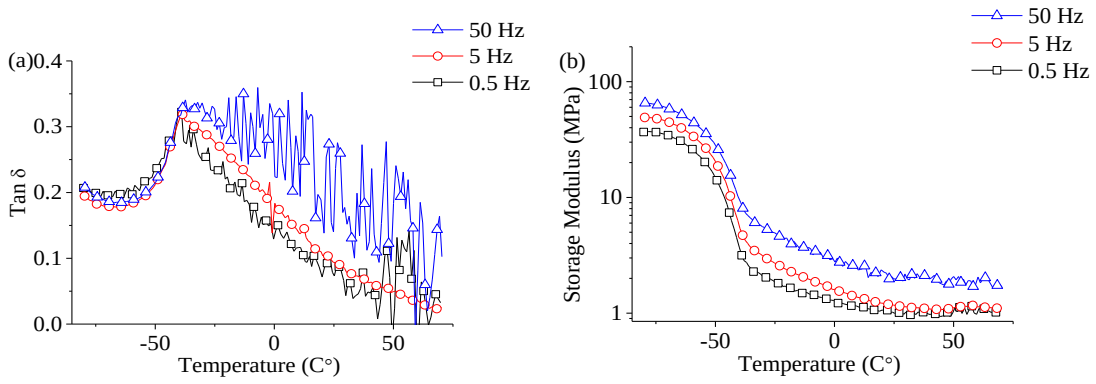

Figure 5.16 (a) Storage moduli and (b) tan δ versus temperature at 0.5, 5 and 50 Hz.

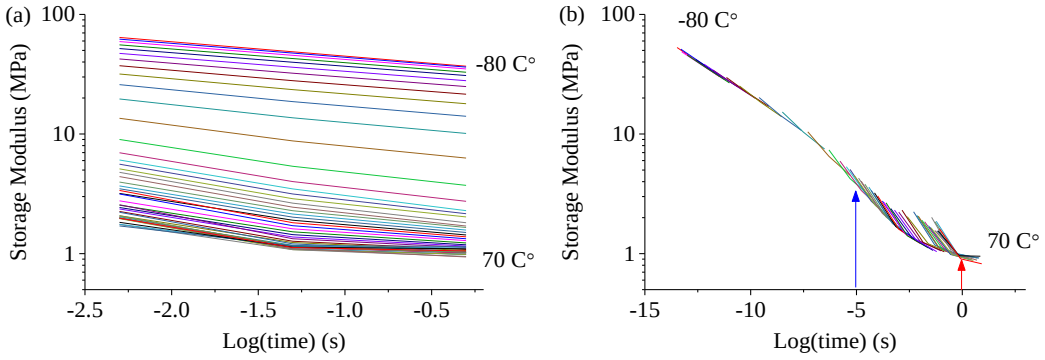

Figure 5.17 (a) Isotherm of storage modulus and (b) master curve versus the logarithmic time.

given in Figure 5.17(a). Then, these data were manually shifted to obtain the master plot, Figure 5.17(b), of the storage modulus using the reference curve at 20 °C. The difference in the shape of the storage modulus trace when plotted versus temperature or versus time is believed to be a result of the crystalline transition taking place between -60 and -30 °C. As the timescales associated with formation and melting of the crystalline phase do not have the same temperature dependence as each other or the bulk motion of the molecular chain, time-temperature superposition (TTS) is not expected to work within that temperature range. From this curve, the storage modulus at a particular strain rate can be approximated. As an example, at the strain rate, 210 s^{-1}, of the non-pre-stretching test of SET2, the time to reach the strain amplitude of 0.1 % is 4.76 μs and its logarithmic time is $\log_{10}(4.76\times10^{-6})$ = -5.32. The storage modulus at this time is approximately 4.44 MPa. Note that this rate corresponds to temperature higher than the upper bound of the crystalline transition and therefore TTS is still applicable. By the same calculation, the storage modulus at a strain rate of 0.001 s^{-1} (the logarithmic time: 0) is 1.98 MPa. Between these two rates, the ratio of the storage moduli is 2.24. This ratio can be also calculated between the static and VFM tests. For the static case, the secant modulus is obtained at a strain of 0.046 (the averaged strain of the non-pre-stretching test of SET2) as 1.51 MPa. The increment ratio between the secant modulus and the VFM result (2.75 MPa) from the

initial test of SET2 is 1.82. It can be seen that this ratio is close to the increment ratio obtained from the DMA test.

5.6 Summary

The combination of the linear VFM and the pre-stretching method was applied on dynamic test results obtained on pure silicone rubber at a strain rate of about 160 s^{-1} using a drop-weight test apparatus, high-speed imaging and the DIC technique. The two sets of pre-stretching experimental data with the application of the VFM produced the identification of 16 different moduli. The same optimization procedure as in the simulation work was utilized for these moduli, but also additionally using an objective function that includes all of the drop-weight and static test results. The optimization shows an increase in the μ term with the higher loading rate. The stress-strain curve reconstructed by the dynamic Ogden parameters clearly shows the stiffer behaviour compared to the static test curves. For comparison, the DMA technique was conducted on the same specimen. It is found that the increment ratio in the storage moduli between the strain rates similar to the current dynamics, and static tests is comparable to the ratio between the results of the drop-weight and static tests. Overall, the comparison between the different data sets illustrates the power of the VFM, combined with appropriate tensile experiments and pre-stretching procedure, to obtain the hyperelastic behaviour of elastomer specimens at strain rates that would be difficult to assess using more traditional high rate testing techniques, such as Hopkinson bar or hydraulic driven devices.

Chapter 6 THE NONLINEAR VFM

6.1 Introduction

The linear VFM introduced in the previous sections is based on the PVW in which the stress term is defined by the linear elastic constitutive model. In Section 2.3.5, it is noted that the VFM can be applied to nonlinear material models by setting up an objective function, e.g. Eq. (2.58). In addition, several studies are introduced, in which the mechanical properties of elastomers have been characterized using this VFM. The VFM procedure used in the present chapter is based on these previous studies but required modifications have been made to utilize the acceleration data in the PVW as was done in the linear VFM. The VFM procedure in the form of the dynamic PVW involving nonlinear models will be referred to as 'the nonlinear VFM' from now on.

The experimental procedure (drop-weight) used with the *linear* VFM provided discrete experimental data at each pre-stretched state. In each experiment, the dynamic strain amplitude was small so that the linear elastic model can be presumed in the PVW. Then, the collection of identified Young's moduli was used in an optimization procedure to obtain the parameters of the nonlinear model. The outcome of the utilization of the *nonlinear* VFM is also to identify the nonlinear model parameters, but a different experimental technique is applied. The PVW for the nonlinear VFM is designed so that the one-term Ogden material model can be included. The direct inclusion of this model allows the use of large and nonlinear deformations of the experimental data. In order to generate this form of experimental data, a gas-gun type experiment was developed, by which elastomer specimens were subjected to large dynamic deformations and, at the same time, high-speed imaging was conducted to record the dynamic behaviour.

In this chapter, the description of the nonlinear VFM is given in a similar manner to the explanation of the linear VFM. This chapter starts with the mathematical definition

of the nonlinear VFM and its particular form of the PVE. The next part provides the description of FEM simulations by which the capability of the present method is evaluated. The actual test procedures developed based on the simulations are described. Then, this chapter ends with a comparison between the results of the linear and nonlinear VFMs and a discussion of these data.

The objectives of this chapter can be summarised as follows:

- The description of the nonlinear VFM is given to explain the difference with the linear VFM.
- FEM simulation is conducted to provide the identification capability of the nonlinear VFM with experimental configurations of a gas-gun type test.
- Further FEM simulation is performed in order to evaluate the effect of imaging random errors, data range and material parameters on the nonlinear VFM.
- The configuration of a gas-gun experiment is described in terms of a test material (EPDM), imaging & loading system and differences with the drop-weight apparatus.
- A similar procedure for choosing imaging and DIC parameters, as used in the linear VFM, is adopted. This procedure needs to be repeated for the present case because the image resolution is much lower than that of the linear VFM.
- An actual application procedure of the nonlinear VFM on the experimental data is given, and its results are compared with the linear VFM to show different material behaviours under different loading speeds produced respectively by these two experiments.
- Further experimental study is conducted to see the effect of acceleration calculation and spatial smoothing methods on full-field data.

- Young's moduli which can be approximated from the initial deformation range of a nonlinear stress-strain curve reconstructed by the nonlinear VFM are compared with those obtained from dynamic mechanical analysis.

6.2 The nonlinear VFM

The nonlinear VFM is introduced to analyse experiments in which elastomers are subjected to large dynamic deformations. The assumption of the linear elastic model made for the linear VFM is not applicable for such data, as it is expected that significant nonlinearity of the stress-strain relation occurs during the large deformations. The identification of the nonlinear behaviour requires a proper nonlinear model, but the use of the nonlinear model in the PVW makes it difficult or impossible to construct a system of linear equations, Eq. (3.4). As introduced in Section 2.3.5, several previous studies show that parameter identification from the VFM combined with nonlinear models can be conducted by modifying the PVW to the form of an objective function and minimizing this function.

Such a VFM method, especially as used in the previous research for the characterization of elastomers, is the basis of the present nonlinear VFM (Promma et al., 2009; Sasso et al., 2013). In the present case, the same dynamic PVW was used, Eq. (3.3), but modified to convert the current coordinate system to the initial one so that the Cauchy stress term can be replaced by the first Piola-Kirchoff (PK1) stress, Eq. (2.11); the PVW of the nonlinear VFM is written as

$$\begin{aligned} &-\int_{S_0} \Pi_{xx} \frac{\partial u^*_{x,0}}{\partial x_0} + \Pi_{yy} \frac{\partial u^*_{y,0}}{\partial y_0} + \Pi_{xy} \frac{\partial u^*_{x,0}}{\partial y_0} + \Pi_{yx} \frac{\partial u^*_{y,0}}{\partial x_0} \, \mathrm{d}S_0 \\ &= \int_{S_0} \rho (a_x u^*_{x,0} + a_y u^*_{y,0}) \, \mathrm{d}S_0 \end{aligned} \tag{6.1}$$

where

$\boldsymbol{\Pi}$	*the first Piola-Kirchoff stress tensor*
$\boldsymbol{u}^*_0$	*virtual displacement vector based on the initial coordinate*

S_0 *initial surface area*

$\mathbf{x}_0$ *initial coordinate* (x_0, y_0)

The formation of this dynamic PVW is valid when the special virtual fields, in which the traction forces at both ends of a specimen cancel, are applied, e.g. Eq. (3.2). Unlike the case of the linear VFM in which the two material parameters *E* and *v* are linearly obtained with the two PVW equations (provided by the two sets of virtual fields), for the nonlinear VFM, only the first set of virtual fields of Eq. (3.2) was implemented because many PVW equations can be produced by using an entire loading history. In other words, a history of *E* and *v* estimations was obtained at each time point by setting up two linear PVW equations in the drop-weight test; in the current case, one set of the Ogden parameters, μ and α, is calculated by solving this nonlinear PVW equation set considering the whole loading history.

The nonlinear PVW equation set can be solved by building up and minimizing a cost function written as

$$\Phi = \sum_{k=1}^{n} \left[\int_{S_0} \mathbf{\Pi}(t_k) : \frac{\partial \boldsymbol{u}_0^*}{\partial \mathbf{x}_0} \, \mathrm{d}S_0 + \int_{S_0} \rho \boldsymbol{a}(t_k) \cdot \boldsymbol{u}_0^* \, \mathrm{d}S_0 \right]^2 \tag{6.2}$$

Here, *n* indicates the total number of the data field produced during a dynamic loading period, i.e. the number of time steps. In order to minimize this cost function, the MATLAB function *fmincon* was used with a lower boundary of 1×10^{-3} to find positive values of the Ogden parameters.

The PK1 stress fields in the cost function are reproduced at each loading step through a nonlinear constitutive relation defined as the one-term Ogden model. As the Ogden model is a function of the principal stretch ratio λ_i, it is convenient to express the PK1 stress in terms of the principal direction. The PK1 stress in the principal direction with the assumption of plane stress, $\Pi_3 = 0$, is

$$\Pi_1 = -\frac{1}{\lambda_1}\frac{2\mu}{\alpha}\lambda_3^{\alpha} + \frac{2\mu}{\alpha}\lambda_1^{\alpha-1}$$
$$\Pi_2 = -\frac{1}{\lambda_2}\frac{2\mu}{\alpha}\lambda_3^{\alpha} + \frac{2\mu}{\alpha}\lambda_2^{\alpha-1} \tag{6.3}$$

It can be assumed that the principal directions for Π_1, Π_2 and Π_3 respectively correspond to the longitudinal, transverse and through-thickness directions when a uniaxial type specimen is used. When this assumption and the first set of the virtual fields is used, Eq. (6.2) can be further reduced to the following form

$$\Phi = \sum_{k=1}^{n}\left[\int_{S_0}\Pi_1(t_k)\frac{\partial u_{x,0}^{*}}{\partial x_0}\,\mathrm{d}S_0 + \int_{S_0}\rho a_x(t_k)u_{x,0}^{*}\,\mathrm{d}S_0\right]^2 \tag{6.4}$$

The stretch ratio λ_3 was approximated by the assumption of incompressibility so that $\lambda_3 = 1 / (\lambda_1\lambda_2)$.

When it is expected that the principal directions deviate from the loading directions, λ_x and λ_y measured with respect to the experimental coordinate should be transformed to the principal stretch ratio λ_1, λ_2. Using these stretch ratios, the principal stresses Π_1, Π_2 are calculated and transformed back to the values based on the experimental coordinate by the following relation

$$\mathbf{\Pi}^{*} = \begin{bmatrix}\Pi_1 & 0\\ 0 & \Pi_2\end{bmatrix}$$

$$\mathbf{\Pi} = \mathbf{P}\mathbf{\Pi}^{*}\mathbf{P}^{\mathrm{T}}$$

$$\mathbf{P} = \begin{bmatrix}\mathrm{P}_{xx} & \mathrm{P}_{xy}\\ \mathrm{P}_{yx} & \mathrm{P}_{yy}\end{bmatrix} = \text{ transformation maxtrix} \tag{6.5}$$

$$\begin{aligned}
\Pi_{xx} &= \mathrm{P}_{xx}\mathrm{P}_{xx}\Pi_1 + \mathrm{P}_{xy}\mathrm{P}_{xy}\Pi_2\\
\Pi_{xy} &= \mathrm{P}_{xx}\mathrm{P}_{yx}\Pi_1 + \mathrm{P}_{xy}\mathrm{P}_{yy}\Pi_2\\
\Pi_{yx} &= \mathrm{P}_{yx}\mathrm{P}_{xx}\Pi_1 + \mathrm{P}_{yy}\mathrm{P}_{xy}\Pi_2\\
\Pi_{yy} &= \mathrm{P}_{yx}\mathrm{P}_{yx}\Pi_1 + \mathrm{P}_{yy}\mathrm{P}_{yy}\Pi_2
\end{aligned}$$

Then, the objective function is written as

$$\Phi = \sum_{k=1}^{n} \left[\int_{S_0} \Pi_{xx}(t_k) \frac{\partial u^*_{x,0}}{\partial x_0} \, \mathrm{d}S_0 + \int_{S_0} \rho a_x(t_k) u^*_{x,0} \, \mathrm{d}S_0 \right]^2 \tag{6.6}$$

6.3 Simulation

6.3.1 Two-dimensional simulation

Numerical simulations were performed and analysed to simulate the actual gas gun, which will be introduced in Section 6.4, experiment and illustrate the nonlinear VFM introduced above. A FEM simulation was conducted by ABAQUS/explicit for the 2D specimen geometry shown in Figure 6.1. The dimensions here are similar to the actual specimen design used for the gas-gun experiment. The CPS4R element type with a size of 1 mm was used. The larger element size was used, compared to the case of the linear VFM, in order to simulate the lower resolution of images taken during the gas-gun experiment. A fixed boundary condition was applied to the left end and a transversely fixed boundary condition to the right end of the specimen. For the dynamic loading applied to the right end, the velocity boundary condition, which peaked at 14 m s^{-1}, obtained from one of the actual gas-gun experiments was adopted. The total loading period was 1.4 ms, and 140 output steps were given to simulate the imaging speed of 100 000 fps which was used in the actual test. This loading period was chosen because a fracture initiation was observed at around this time on the actual specimen (EPDM rubber).

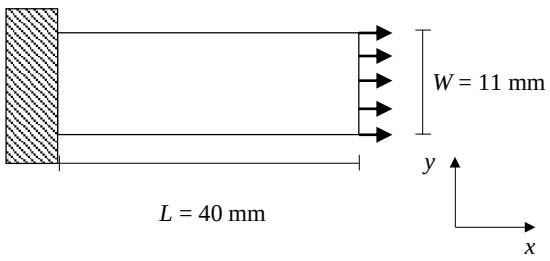

Figure 6.1 Two-dimensional simulation geometry and dimensions.

The one-term Ogden model was chosen; for its parameters μ (MPa) and α, values of 3 to 6 and 1 to 4 were respectively used with an interval of 1 so there were in total 16 simulations. This parameter range is chosen such that at least one stress wave reflection from the fixed end occurs within the simulation time; in addition, the parameters obtained from the nonlinear VFM on the gas-gun experiment are within this range. A high bulk modulus of 40 GPa was used to simulate the assumption of incompressibility. The density was set to 1370 kg m^{-3}, which was measured from the EPDM specimen. The same procedure for data processing as used in the linear VFM study was adopted to generate the full-field data, but without the addition of the noise or temporal fitting on the acceleration fields. The full-field data from each simulation were then applied to Eq. (6.4), and the result of the parameter identification set are presented in Figure 6.2. It can be found that the parameter sets (cross symbol) obtained from the VFM are well matched with the given values (intersected points of dashed lines).

The quality of the parameter extraction from the current VFM depends on the amount of loading history involved in Eq. (6.4). The history of the parameter prediction produced by the simulation work with μ = 5 MPa, α = 1 can be seen in Figure 6.3(a). The acceleration profile is an averaged value over the whole surface at each time; the sign change of the acceleration approximately indicates the moment of the wave reflection. Each Ogden parameter is obtained by solving Eq. (6.4) with the simulation data history up to each time point; for example, the μ and α at 0.8 ms are obtained using the strain and acceleration field data from 0.0-0.8 ms. During the incident wave period (0.0-0.6 ms), it can be seen that the identification of μ and α is not satisfactory with about 3 and 70 percent differences respectively from the given values. However, after the first wave reflection (after around 0.6 ms), the calculated parameters become close to the given values in a stepwise manner. The jump in this parameter estimation is due to the fact that

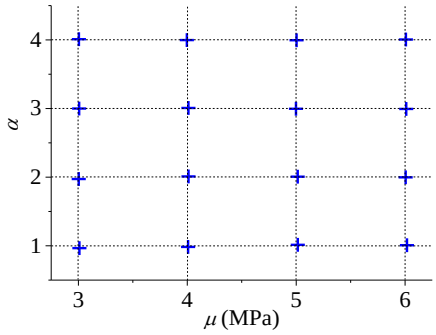

Figure 6.2 Given parameters (intersected points of dashed lines) and VFM parameter predictions (cross symbols).

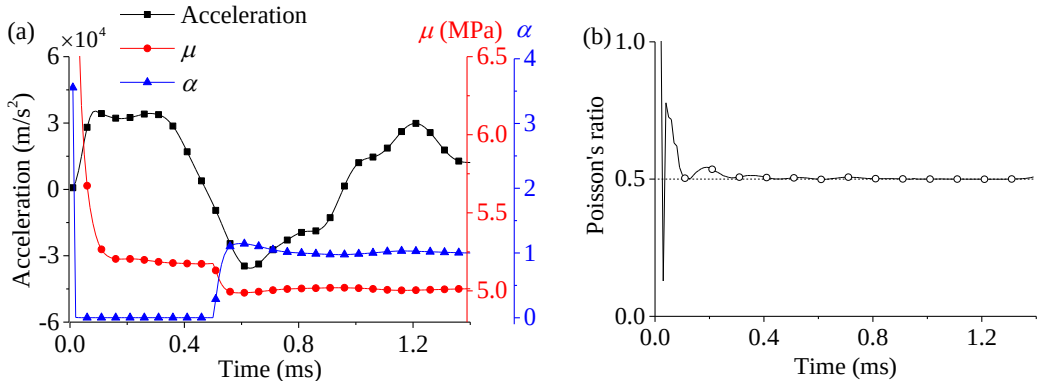

Figure 6.3 (a) Averaged acceleration profile and the history of μ and α and (b) Poisson's ratio identifications obtained from the linear VFM.

the strain amplitude in the stress wave is approximately doubled after the wave reflection from the rigid end. Figure 6.3(b) shows the Poisson's ratio obtained from the linear VFM using Eq. (3.2) and (3.3). The linear VFM was applied on the same data used to produce the result in Figure 6.3(a) with the assumption that Poisson's ratio at a particular moment is not dependent on the deformation history but on that moment. It seems that the result is well matched with the incompressibility given to the simulation material by setting a very high value of the bulk modulus. This identification procedure was also identically applied to the data from the actual gas-gun test and identified Poisson's ratios were used for the choice of the subset size in the DIC analysis.

With the same simulation configuration, simple visco-hyperelastic simulations were conducted with the one-term Prony series. The normalized shear constant g was 0.3, so

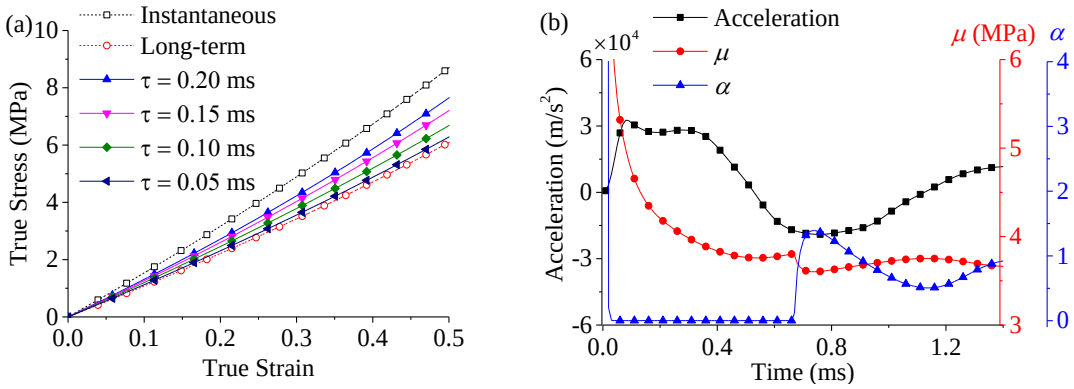

Figure 6.4 (a) Ogden curves reconstructed from the parameters given in Table 6.1 and the given instantaneous long-term curves; (b) averaged acceleration profile and the history of μ and α predictions from the visco-hyperelastic simulation with τ = 0.05 ms.

Table 6.1 Four Ogden parameter sets obtained from the nonlinear VFM analysis on the visco-hyperelastic simulation.

Relaxation time (ms)	μ (MPa)	α
0.20	4.24	1.20
0.15	4.10	1.06
0.10	3.91	0.90
0.05	3.67	0.91

that the instantaneous and long-term μ respectively were given as 5 and 3.5 MPa for the one-term Ogden model. In order to produce a different Ogden behaviour with the same velocity boundary condition, four different relaxation time constants τ were given at 0.20, 0.15, 0.10 and 0.05 ms. These constants were chosen so that the four Ogden stress-strain curves are located between the instantaneous and long-term curves. The simulation data produced by the four relaxation constants were analysed by the same nonlinear VFM procedure. The four calculated parameter sets are listed in Table 6.1. These parameters are used to reconstruct the Ogden uniaxial curves as shown in Figure 6.4(a) with the given instantaneous and long-term curves. It can be seen that the longer relaxation time produces the Ogden curve which is closer to the instantaneous one. This observation gives confidence that the present nonlinear VFM procedure is able to capture the stiffer behaviour due to the longer relaxation time given in the present model. Figure 6.4(b)

presents the estimation history of μ and α and the averaged acceleration profile from the simulation with τ = 0.05 ms. The value of μ (3.67 MPa) and α (0.91) given in Table 6.1 are obtained from the values at the end of the period (at 1.4 ms) of their profiles. The initial averaged acceleration amplitude of Figure 6.4(b) is similar to that shown in Figure 6.3(a) of the pure hyperelastic simulation work. After the incident wave period, it can be observed that the acceleration profile in Figure 6.4(b) is attenuated by about 50 % due to the viscoelastic term whereas no significant attenuation is observed in Figure 6.3(a). This attenuation is the main factor causing the variation of the Ogden parameters with the different relaxation time constants for the same velocity boundary condition.

The aforementioned simulation studies were conducted using numerical data without artificial noise on the displacement field $\boldsymbol{u}$ or the temporal fitting on the acceleration field $\boldsymbol{a}$. In order to show the effect of these on data processing, Gaussian random noise was added to $\boldsymbol{u}$ in the same way as used in the simulation work of the linear VFM; however, higher noise levels were added as the noise levels of the actual experiments are much higher than in the case of the linear VFM. The temporal fitting was also identically applied by the 9-degree polynomial function through MATLAB. It should be mentioned that the identified parameters in the simulations shown in Figure 6.3 or Figure 6.4 were obtained by the nonlinear VFM which was applied to the data from 0.0-1.4 ms and, for

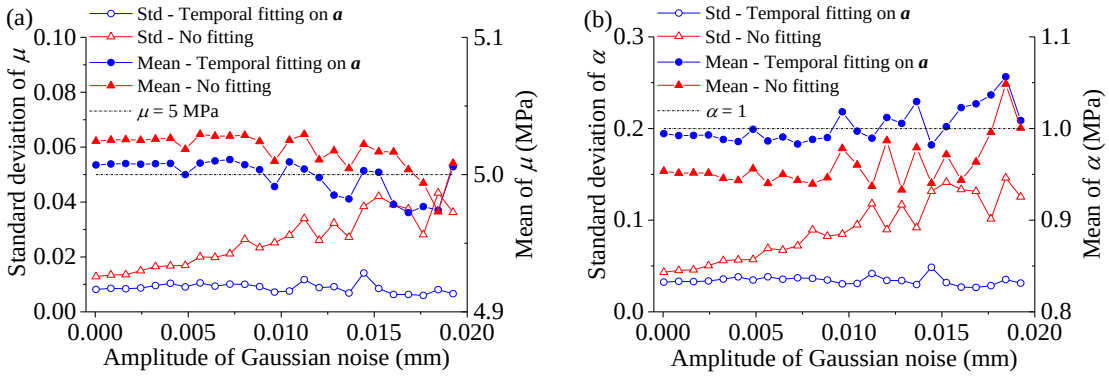

Figure 6.5 Mean and standard deviation of (a) μ and (b) α from the nonlinear VFM with the temporal fitting on $\boldsymbol{a}$ and without it.

example, for the case of Figure 6.3, the values of μ and α at 1.4 ms are taken as the identified parameters. In an actual experiment, the parameters were obtained by averaging the history values over the period when the identifications converge to certain stable values, e.g. 0.8-1.4 ms in Figure 6.3. This averaging procedure is to consider the fact that fracture nucleation was globally observed over the specimen when subjected to very large deformation. The moment when this nucleation was clearly observed was considered as the last time step for the application of the nonlinear VFM. However, it was difficult to specify when this nucleation started to occur exactly. For this reason, instead of specifying the precise nucleation moment (i.e. the last time step), the identified values during the stable period were averaged for both μ and α. The stable period for this averaging was observed to be 0.8-1.4 ms. This same period was used to obtain the mean and standard deviation of the identifications, which is presented in Figure 6.5 for the cases of the nonlinear VFM with and without the temporal fitting. For both μ and α, the mean values are closer to the given parameters when the temporal fitting is applied and also the standard deviations with respect to all artificial noise amplitudes are lower. The standard deviations of the non-fitted case become clearly higher as the noise level increases. Based on this simulation result, the temporal fitting was identically utilized for the actual gas-gun experiments introduced in Section 6.4.

A similar simulation study was conducted to show the effect of the choice of the PVW equations between Eq. (6.4) and (6.6). The previous simulation studies were all based on the PVW of Eq. (6.4), in which it is assumed that the global (experimental) coordinate *x*, *y* approximately corresponds to the principal directions by considering a uniaxial-type specimen. The nonlinear VFM (with the temporal fitting) result shown in Figure 6.5 is again presented in Figure 6.6 with the legend denoted as ‘Global direction’ in order to indicate the use of Eq. (6.4). An additional result, which is obtained from Eq. (6.6), is

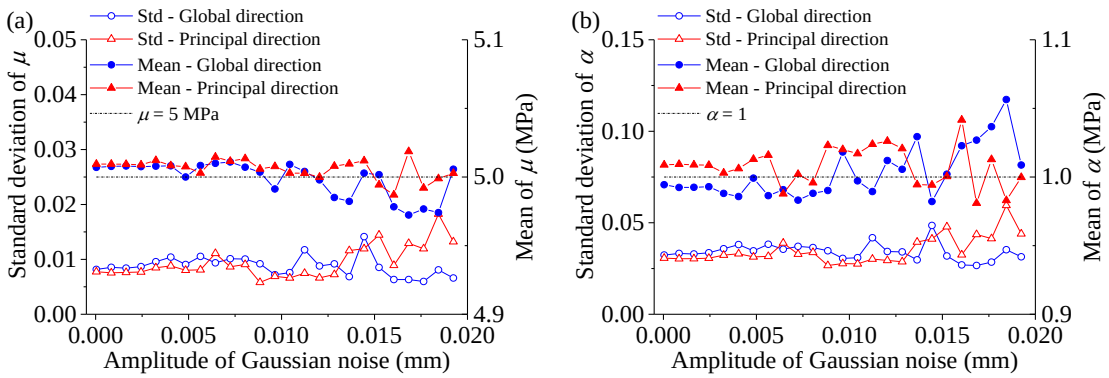

Figure 6.6 Mean and standard deviation of (a) μ and (b) α from the nonlinear VFMs with Eq. (6.4) and (6.6), which are respectively indicated by the legend of 'Global direction' and 'Principal direction'.

presented in this figure with the legend of 'Principal direction'. No significant difference between the use of Eq. (6.4) and (6.6) is observed either for μ or α; but, after the noise level of about 1500×10^{-6} mm, the identification (both μ or α) sensitivity of the principal direction case is slightly higher. This higher sensitivity can be caused by the additional procedure required to obtain the principal values and directions.

According to the result shown above, either Eq. (6.4) or (6.6) can be adopted for a long and narrow shape specimen. However, the similarity between these two equations may not be valid when a wider specimen is tested. In order to show the effects between Eq. (6.4) and (6.6) with respect to a wider geometry, the same 2D simulation was conducted but the width increased to 40 mm. The same procedure of adding artificial noise and the temporal fitting was identically applied to the simulation data. The identification results obtained from the two equations of the nonlinear VFM are presented in Figure 6.7. The identifications of μ for both cases differ by about 0.4 %, but as shown in Figure 6.7(b) the α identification from Eq. (6.4), 'Global direction', is significantly underestimated compared to the case of Eq. (6.6). This deviation is caused when the principal directions are no longer close to the global direction at which dynamic loading is applied. Thus, when it is expected that the specimen shape is not close to a uniaxial type or a constitutive equation used in the VFM is based on the principal direction like the Ogden model, the

transformation procedure shown in Eq. (6.5) should be considered. In this chapter, Eq. (6.6) was used for the analysis of all gas-gun experiments.

6.3.2 Three-dimensional simulation

The 3D simulations were conducted with a similar configuration used in the study of the linear VFM. The same geometry and boundary conditions used in the 2D gas-gun simulation was applied but three different thicknesses (h = 0.5, 2, 4 and 8 mm) were used to see the effect of thickness change. The full-field data were obtained only from the surface and then applied to Eq. (6.4). The element size for the surface was 1 mm but in the thickness direction it was set as 0.2 mm. Figure 6.8 shows the identification history of μ and α. As mentioned above, the identified parameter at a particular time is obtained using Eq. (6.4) and the whole full-field data up to that time point. The identification of μ seems stable for all thickness cases; but in the case of α, since the thickness of 4 mm, the prediction history becomes unstable, especially in the early stage of the loading period. However, the identifications at the later time period is still close to the given values for all cases. The identified values at the end of the loading period are listed in Table 6.2. Equivalent identification results for the case with μ = 10 MPa, α = 1 and μ = 15 MPa, α = 1 are also given in this table. It can be seen that the identification of μ is stable for all thickness cases but it seems that α starts to deviate from the given value when the μ term

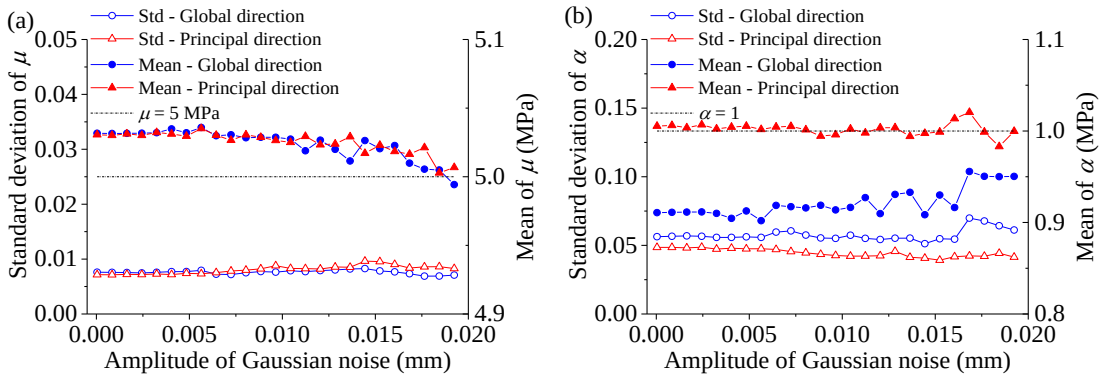

Figure 6.7 Mean and standard deviation of (a) μ and (b) α from the nonlinear VFMs with Eq. (6.4) and (6.6) on the simulation with a wider specimen (L & W = 40 mm).

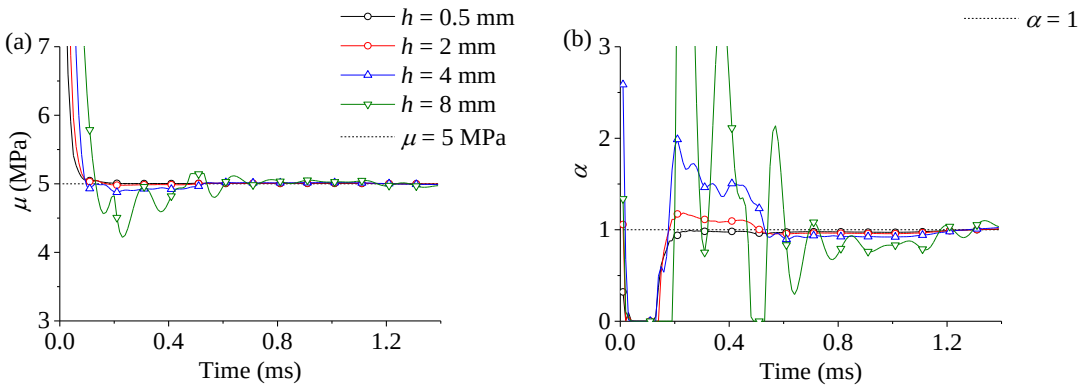

Figure 6.8 Identification histories of μ and α with respect to the thickness change of 3D FEM simulations with μ = 5 MPa and α = 1.

Table 6.2 Ogden parameter sets with respect to the thickness change for the three different simulations.

Thickness (mm)	μ = 5 MPa	α = 1	μ = 10 MPa	α = 1	μ = 15 MPa	α = 1
0.5	5.00	1.01	10.02	0.98	15.03	0.98
2	5.00	1.01	10.03	0.96	15.05	0.97
4	4.99	1.03	10.06	0.93	15.10	0.94
8	4.97	1.03	10.10	0.86	15.17	0.88

is high, and the thickness is large. The highest deviation of μ and α in Table 6.2 is 1 and 12 % respectively.

The same 3D simulation was performed but for the current case the thickness was fixed at 0.5 mm. The same boundary conditions and three Ogden materials were applied. The surface area of the full-field data was controlled to see the effect of the area reduction on the identification. A similar simulation study is introduced in Section 4.2.2 and Figure 4.12 for the case of the linear VFM. The area reduction was conducted as shown in the right-hand side figure in Figure 4.9 in Chapter 4 but, in order to simplify the mesh geometry, the length and width were reduced in 1 mm steps, which is the mesh size, up to 4 mm. For example, when a 4 mm reduction is applied, the length and width of the data area are 32 and 3 mm. Figure 6.9 shows the effect of the area reduction for the case of μ = 15 MPa, α = 1; Table 6.3 shows the identification results obtained from the whole data history for the three Ogden material cases. For all cases, the identification of μ seems

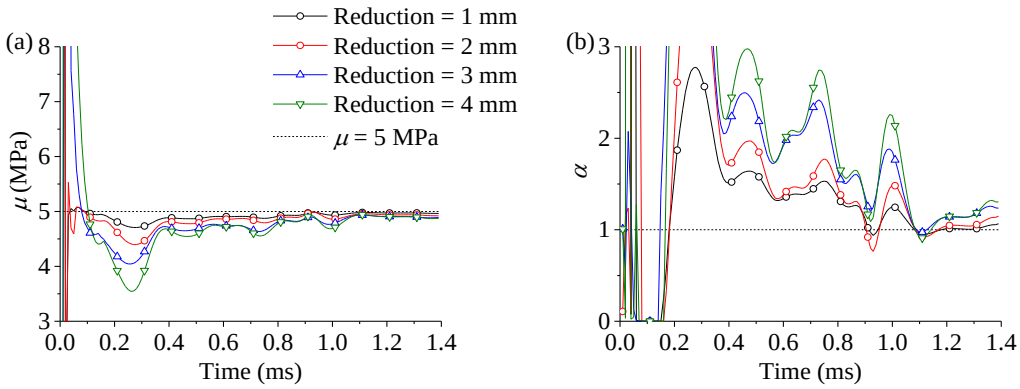

Figure 6.9 Identification histories of μ and α with respect to the data area change of 3D FEM simulations with μ = 5 MPa and α = 1.

Table 6.3 Ogden parameter sets with respect to the data area change for the three different simulations.

Reduction (mm)	μ = 5 MPa	α = 1	μ = 10 MPa	α = 1	μ = 15 MPa	α = 1
1	4.96	1.06	9.93	1.08	14.9	1.06
2	4.92	1.14	9.90	1.14	14.8	1.09
3	4.90	1.23	9.81	1.19	14.7	1.15
4	4.87	1.30	9.80	1.25	14.7	1.17

rather stable; the deviation is less than 3 %. The deviation of the α identification becomes significant (up to 30 %) when the reduction is higher than 2 mm for all material cases. This sensitivity is applicable when the specimen dimensions are close to the present simulation geometry (L = 40 mm, W = 11 mm).

In summary, the present simulation study shows that the application of the nonlinear VFM is able to identify the parameters of the chosen nonlinear model, including rate dependency as much as the linear VFM. It is found that the temporal fitting leads to a reduction of noise sensitivity so this procedure was applied to all gas-gun experiments. The full-field data obtained from the experiments were analysed by the PVW of the nonlinear VFM, Eq. (6.6). The parameters were obtained by averaging the identification history over the stable period. In addition, according to the 3D simulation works, appropriate specimen thickness and data area reduction were restricted to be less than 2 and 1 mm, respectively.

A summary of the outcomes from the present simulation work was used as a strategy for the development of a gas-gun type experiment introduced in the next section; this strategy is listed as follows:

- Use of the imaging speed of 100 000 fps is capable of characterizing material behaviour for Ogden model parameters up to μ = 6 MPa and α = 4.
- The principal coordinate system needs to be defined in order to consider the Ogden model which is based on the principal directions. It is found that for a uniaxial type specimen ($L \approx 40$ mm and $W \approx 11$ mm), the global coordinates can be assumed to be coincident with the principal directions.
- A sufficiently large deformation history is required for a proper identification of the α term of the Ogden model.
- According to the specimen geometry study using FEM data, a specimen thickness should not be more than 2 mm, and full-field data reduction should be limited to 1 mm.

6.4 Experiment

In this section, the gas-gun experiment is described with the application of the nonlinear VFM procedure identically applied to the simulations introduced above. For the present study, a sheet of commercial EPDM rubber (Amarin Rubber & Plastics Ltd) was used. The first part provides the procedure for a quasi-static test performed on this new specimen; the drop-weight and the pre-stretching method were applied and, the data were analysed by the linear VFM as introduced in Chapter 5. Then, the gas-gun procedure is described with respect to its experimental configuration. At the end of this section, the stress-strain curves measured or obtained through all tests were presented together for comparison.

6.4.1 Quasi-static experiment

For comparison with the dynamic experiments, tensile quasi-static tests were conducted. The uniaxial specimens were prepared with dimensions of gauge length = 60 mm, width = 20 mm, and thickness = 2 mm. True strain rate control was employed with three strain rates: 0.01, 0.001 and 0.0001 s^{-1}. At the time of this experiment, a USB camera (Grasshopper3 USB 3.0 Digital Camera, Point Grey Research, Inc) was available and used to capture displacement fields (at 5 fps) on the specimen surface (215×684 pixels) where a white spray was applied to make a fine speckle pattern. The full-field measurements were then analysed by the same DIC software as used elsewhere with a correlation subset size 16×16 (50 % overlap) each of which includes about three dots of the spray pattern. This subset size was the smallest able to produce high data resolution with a reasonable noise level (strain standard deviation = 0.1 %) in the axial strain fields obtained from the five static images before loading. The axial displacement

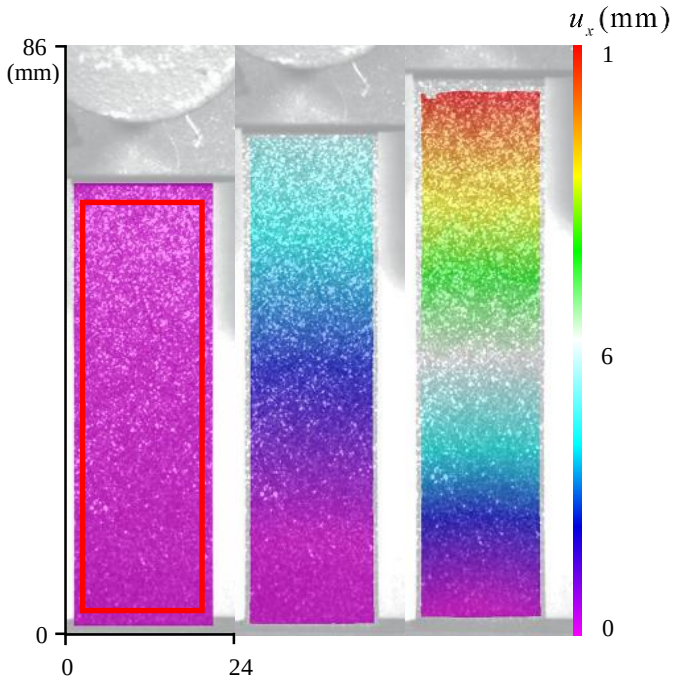

Figure 6.10 Axial displacement fields of the quasi-static test (at 0.01 s^{-1}) obtained from the DIC analysis and overlapped on the actual pictures; the red rectangle indicates the initial area where the data field is averaged.

fields obtained from this DIC analysis are presented on the actual experiment images in Figure 6.10; the red rectangle indicates the area where the strain fields are averaged.

The engineering uniaxial stress was calculated by the load measured from the tensile test machine; the engineering uniaxial strain fields obtained by the DIC analysis were averaged, and the values were interpolated to be matched with the time of the force measurement. The interpolation was conducted by the built-in MATLAB function, *interp1*. The fitting procedure of the one-term Ogden model, introduced in Section 5.2.2, was identically applied to the three quasi-static tests. The Ogden parameters from this fitting are listed in Table 6.4, and their fitted and experiment curves are presented in Figure 6.11. Similar to the case of the silicone rubber, Figure 6.11 shows the rate dependency of the EPDM specimens can be observed even between such slow rates. Also, it is found that the one-term Ogden model is capable of fitting the stress-strain curves.

It was possible to obtain Poisson's ratio from these tensile tests as the full-field data of the lateral strain corresponding to the axial strain are available. The averaged

Table 6.4 One-term Ogden model parameters obtained from the quasi-static uniaxial tests.

Strain rate (s^{-1})	μ (MPa)	α
0.0001	1.05	1.09
0.001	1.36	1.05
0.01	1.47	1.46

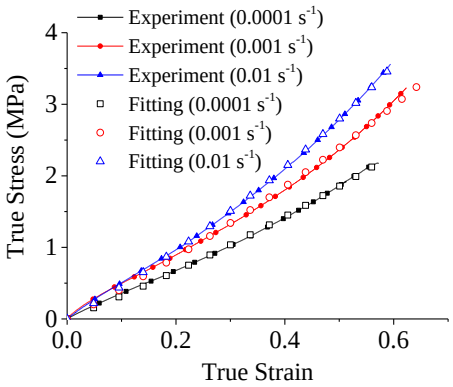

Figure 6.11 Uniaxial true stress-strain curves from the experiment (filled symbol) and fitting (open symbol).

engineering axial and lateral strain values were applied to Eq. (5.6) in order to calculate Poisson's ratio. The results for all strain-rate cases are presented in Figure 6.12 with respect to the axial true strain. Over the strain range of 0.1-0.5, the averaged Poisson's ratios for 0.01, 0.001 and 0.0001 s^{-1} are respectively obtained as 0.49, 0.46 and 0.47; the mean value is 0.47.

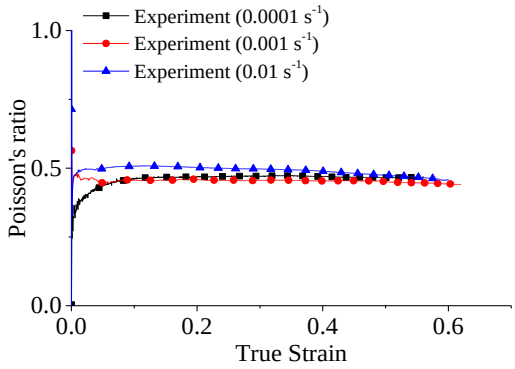

Figure 6.12 Poisson's ratio obtained from the DIC data of the three uniaxial tests.

6.4.2 Medium strain-rate test (Drop-weight test)

The same drop-weight test as described above was adopted for the procedure of the linear VFM on EPDM specimens. The following dimensions were prepared: gauge length = 37 mm, width = 11 mm and thickness = 2 mm. For these specimens, the experimental set-up and procedure introduced in Chapter 5 were applied to obtain a series of dynamic full-field measurement at a number of different pre-stretch values by means of the same high-speed camera at 50 000 fps with an image size of 420×170 pixels. The static force was measured just after pre-stretching and then applied to the PVW with the strain and acceleration fields obtained from the same DIC analysis on the dynamic displacement fields. The identical linear VFM was adopted including the piecewise virtual field. A series of Young's modulus estimation profiles from two drop-weight tests is shown in Figure 6.13, in which the hatched area indicates the period where Young's modulus, Poisson's ratio and strain rate fields are averaged; the values are listed in

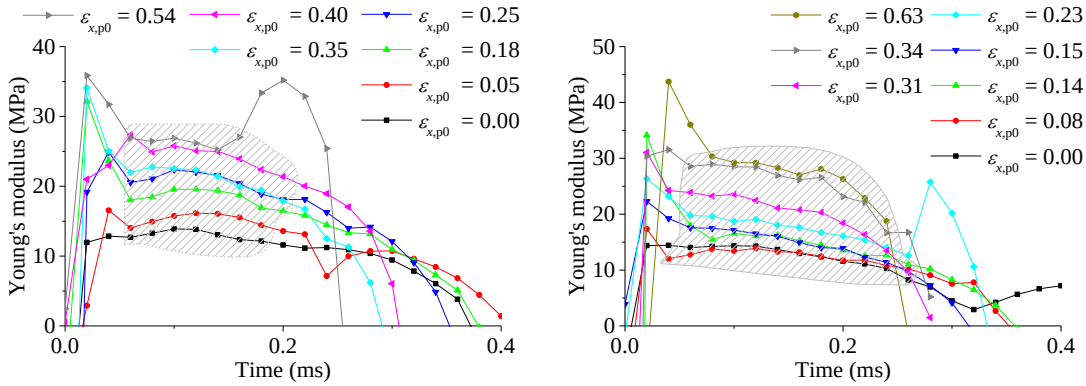

Figure 6.13 Young's modulus identifications from the drop-weight test and the linear VFM on the two EPDM specimens (the hatched area indicates the averaging period).

Table 6.5 Averaged Young's modulus, longitudinal strain rate and Poisson's ratio of the two drop-weight tests.

SET1	E (MPa)	$\dot{\varepsilon}_x$ (s^{-1})	ν	ε_x	SET2	E (MPa)	$\dot{\varepsilon}_x$ (s^{-1})	ν	ε_x
	11.8	80	0.47	0.00		12.3	103	0.45	0.00
	14.9	78	0.45	0.05		12.6	96	0.49	0.08
	17.1	86	0.47	0.18		13.0	108	0.48	0.14
	20.6	90	0.45	0.25		14.6	102	0.50	0.15
	21.0	96	0.48	0.35		17.4	122	0.48	0.23
	22.2	98	0.46	0.40		20.4	118	0.48	0.31
	26.6	120	0.49	0.54		23.4	109	0.46	0.34
						27.7	125	0.48	0.63
	Averaged $\dot{\varepsilon}_x$ = 100 s^{-1}, ν = 0.47								
	Optimized Ogden parameters: μ = 4.39 MPa , α = 1.71								

Table 6.5. This hatched area is made so that, for each profile, the Young's modulus predictions are stable and the values of Poisson's ratio are bounded between 0.4-0.5 for reasonable compressibility. All averaged E values in Table 6.5 from the test of SET1 and 2 were applied to the optimization procedure of Eq. (4.11). The optimized parameters were obtained as μ = 4.39 MPa and α = 1.71. The true stress-strain curve reconstructed from these parameters is presented in the next section with the results of the gas-gun experiment.

6.4.3 High strain-rate test (Gas-gun test)

The idea of the present gas-gun experiment is based on the high strain-rate experiment for testing a yarn of polymeric fibres introduced in the literature (Russell et al., 2013).

Here, eight uniaxial type EPDM specimens (length = 100 mm, width = 11 mm, thickness = 2 mm) were prepared. In each experiment, one end of each of two specimens was fixed on one side of a rectangular aluminium block: the specimens were superglued into a clamp. The dimensions of the aluminium block were determined so that oscillations of the specimen end due to flexure of the block were reduced. The other ends of the specimens were similarly clamped to a rigid frame attached to the barrel of a gas gun. An aluminium projectile was accelerated by the gas gun so that it impacted the block at speeds between 50 and 80 m s^{-1}. A schematic representation of the experimental configuration is presented in Figure 6.14 (upper) and the picture given at the bottom of this figure shows the actual system of the gas-gun experiment. The blue circle (dashed line) indicates the place where the aluminium block sits on a PMMA rod. In front of this block, there is a rigid frame and long gas-gun barrel. A projectile is accelerated by the pressure provided by a small chamber shown in the right-hand-side of this picture. When

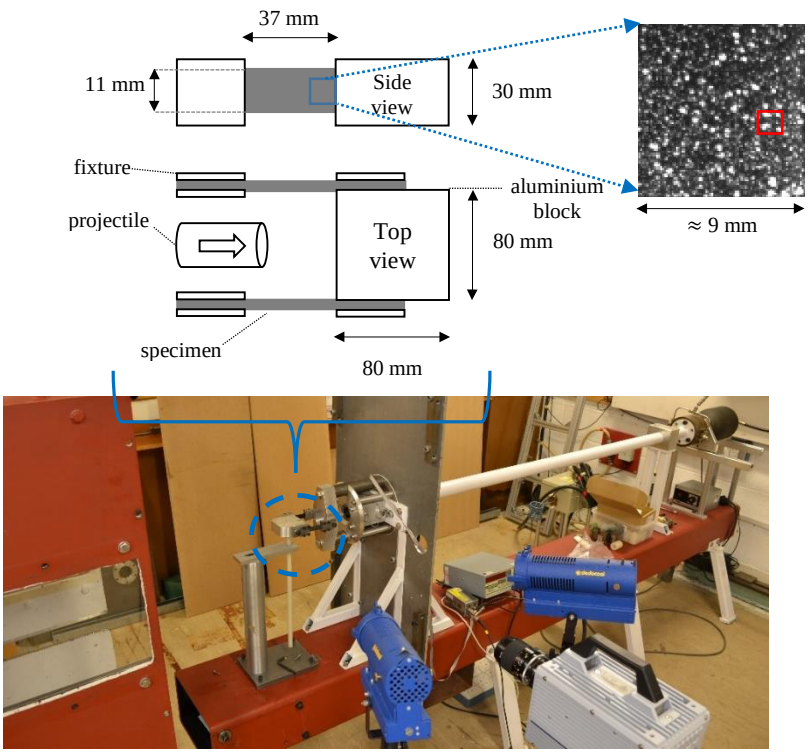

Figure 6.14 (upper) Schematic representation of the gas-gun experiment and a speckle pattern on a part of the specimen surface with a 12×12 correlation window (red rectangle); (bottom) a picture of the actual gas-gun experiment system.

the projectile approaches the rigid plate, a light sensor detects the movement and sends a trigger signal to the high-speed camera (the grey box in the picture) to capture the dynamic deformation of the EPDM specimens.

The dynamic displacement on the specimen surface, where a random speckle pattern was applied by a white spray, was captured by the high-speed camera at 100 000 fps. If two high-speed cameras are available, it is possible to obtain two dynamic displacement fields from the two specimens; however, in this study, only one of the specimen surfaces was captured by one camera. The image size over the specimen surface, for example TEST3, is 203×69 pixels. The acquired images were then analysed by the DIC software as explained in Chapter 5 but for the final subset size (12×12) a larger overlap size of 50 % was used. These subset and overlap sizes were chosen by a method similar to that

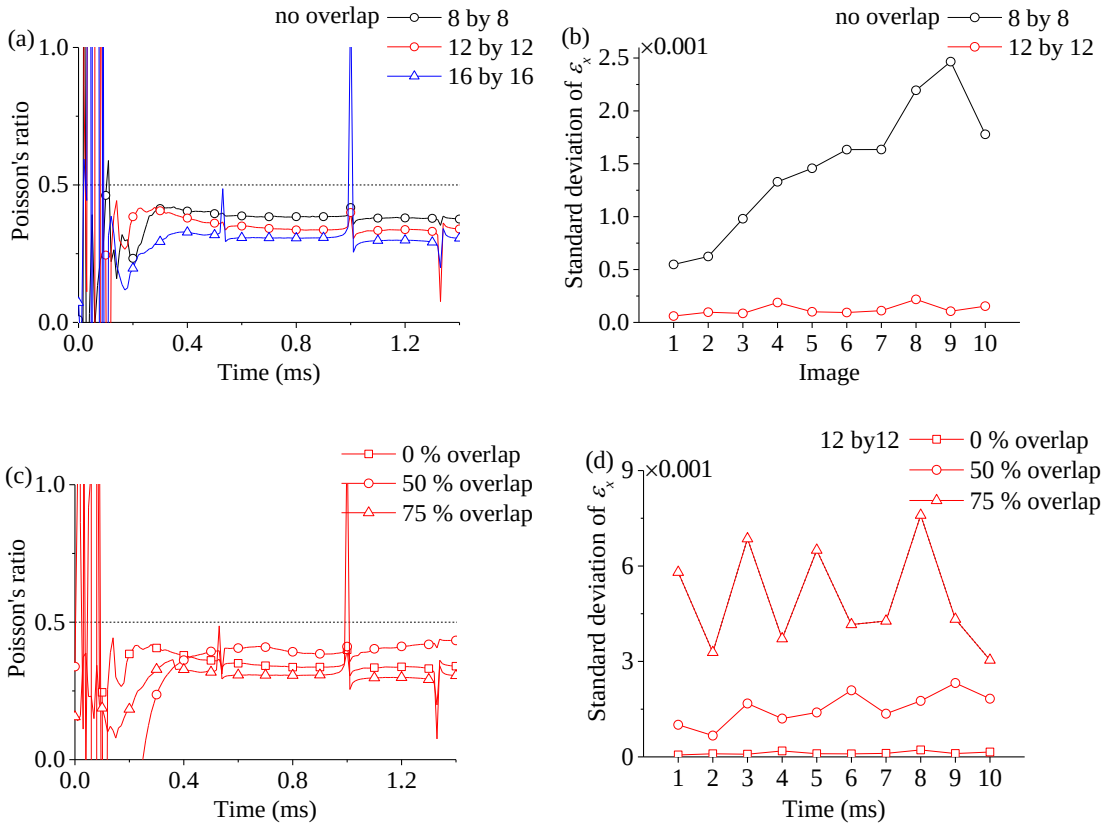

Figure 6.15 Subset size selection procedure: (a) the Poisson's ratio identifications with 8×8, 12×12 and 16×16 subset sizes on the gas-gun test (TEST 3); (b) the standard deviation of the axial strain fields of 10 still images with 8×8 and 12×12 subset sizes; (c) the Poisson's ratio identifications with 12×12 subset size and 0, 50 and 75 % overlap sizes; and (d) the standard deviation of the axial strain fields of the 10 still images with 12×12 subset size and the three overlap sizes.

used for the case of the linear VFM presented in Figure 5.5. As shown in the simulation work (Figure 6.3(b)), the application of the linear VFM to the long deformation data is able to calculate the Poisson's ratio. The identification of Poisson's ratio from one of the gas-gun tests (TEST 3) is presented with respect to the three subset sizes without overlap in Figure 6.15(a). From this result, the subset sizes of 8×8 and 12×12 are chosen for further investigation as they produce Poisson's ratio identifications close to incompressibility. With regard to these two subset sizes (no overlap), Figure 6.15(b) presents the standard deviation of the axial strain fields obtained by the 10 still images before the block is impacted. The noise level is significantly higher for the subset size of 8×8 so 12×12 is chosen as the final choice. Starting from this subset size, the overlap size increases to 50 and 75 %, and Figure 6.15(c) shows their Poisson's ratio identification results. It can be seen that, in contrast to the case presented in Figure 5.5, the increment of the overlap size to 75 % does not lead to the higher incompressibility; instead, Poisson's ratio is even lower than that of 0 % overlap. The reason for this decrement is thought to be the fact that the noise level of the strain field is significantly higher than that of 50 and 0 % overlap cases, as can be observed in Figure 6.15(d). For this reason, the subset size 12×12 and 50 % overlap was chosen for the DIC analysis on the present gas-gun experiments. The noise levels in Figure 6.15(d) becomes slightly higher as the picture number increases. This increment is due to the fact that when the projectile is shot, the air is exhaled out from the gun barrel and pushes the aluminium block and also the specimens.

The noise floors of the displacement and strain fields obtained from 10 static images of the gas-gun test with the DIC configuration introduced above are presented in Figure 6.16. The static images used in this case were not taken from the above case; instead, these were separately obtained from the situation when the specimen was located at the

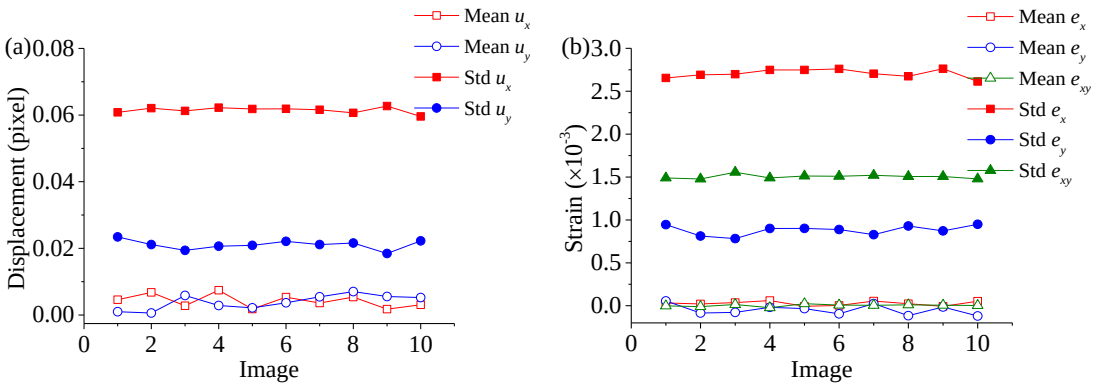

Figure 6.16 Mean and standard deviation of the (a) displacement and (b) strain fields of 10 still images with 12×12 subset size and 50 % overlap.

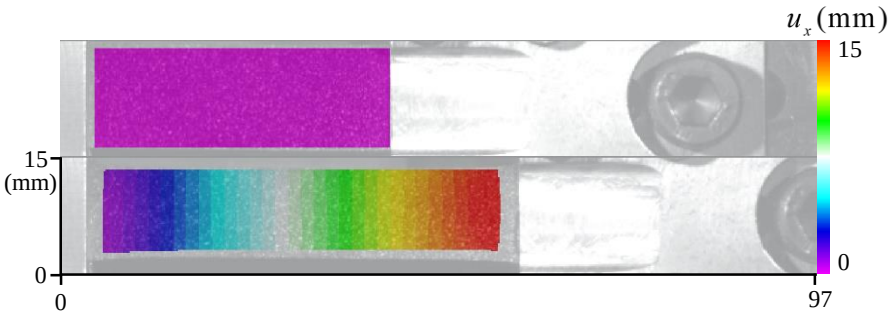

Figure 6.17 Pictures of the initial and deformed states at 1.14 ms of TEST 3 and the axial displacement fields on the surfaces.

same place but without shooting of a projectile. As can be seen in these figures, the noise levels are much higher than the case of the linear VFM presented in Figure 5.7 in Chapter 5. This higher level is an inherent characteristic of the nonlinear VFM because of the necessity of measuring large deformations. In order to capture large deformations, the initial imaging area should be much larger than the specimen length so that the whole deformation can be included at all loading levels. This explanation can be described by Figure 6.17 where two pictures show the initial state and deformed states at 1.14 ms of TEST 3. The averaged noise level (standard deviation) of the axial displacement for all pictures is 0.005 mm. Although this noise level is much higher than that of the linear VFM, according to the simulation studies shown in Figure 6.5, the application of the nonlinear VFM at this noise level is still capable of identifying the material parameters. Table 6.6 lists the DIC factors adopted in the present gas-gun experiment.

Table 6.6 Imaging and DIC analysis factors

camera	FASTCAM SA 5, Photron
DIC software	Davis 7.2, LaVision 2007
field of view (data)	203×69 pixels
interframe time	10 μs
subset size (final)	12×12
subset overlap (final)	50 %
spatial smoothing	not applied
temporal smoothing (acceleration)	9-degree polynomial
axial strain resolution	2.6×10^{-3}
axial acceleration resolution	100×10^{5} mm s^{-2}

Using this DIC configuration, the displacement and engineering strain fields were obtained for each picture. For the acceleration fields, the temporal fitting procedure (9-degree polynomial) was applied as explained in the previous chapter. The axial (loading direction) displacement, true strain and acceleration fields at loading times of 0.34 and 1.14 ms from TEST 3 are shown in Figure 6.18 with the initial coordinate. The corresponding correlation maps are shown in Figure 6.19. The axial strain values are plotted along the lengthwise position by averaging them in the lateral direction. The strain plots at several time points are presented in Figure 6.20. The strain curve at 0.24 ms shows that the initial incident strain wave propagates from the right-hand side (loading end). This incident wave starts to be reflected at around 0.54 ms. After this time, the

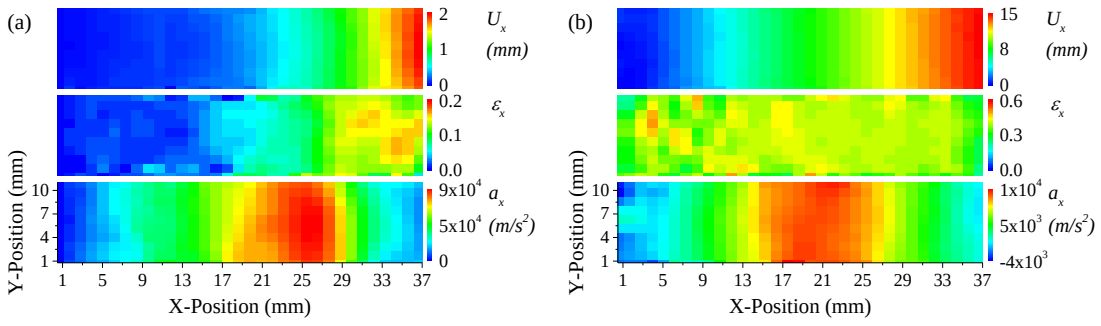

Figure 6.18 Axial displacement (upper), true strain (middle) and acceleration fields (bottom) at 0.34 (left) and 1.14 ms (right) of TEST 3.

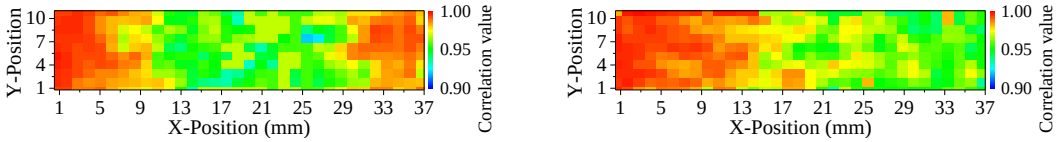

Figure 6.19 Correlation maps at 0.34 (left) and 1.14 ms (right) of TEST 3.

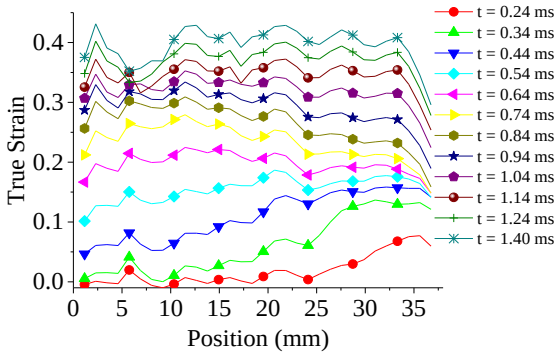

Figure 6.20 Axial true strain curves (averaged in the lateral direction) along the lengthwise position from TEST 3.

reflected wave travels back toward the loading end. The propagation of the next reflected wave is not clear and the strain along the length starts to be uniform. This wave attenuation can be caused by a viscoelastic characteristic of the specimen. The strain values around both ends of the specimen are lower than its overall behaviour (strain). This stiffer behaviour at both ends could be an artefact from the large thickness change due to the clamping fixture and a superglue layer used to improve the clamping of the specimen in the fixture. The data from this region were excluded by removing the data about 1 mm away from both ends.

The time that the strain wave just reaches the fixed end of the specimen is about 0.34 ms. From this time, it is possible to approximate the wave velocity c as 108 m/s (= 37 mm / 0.34 ms); using the one-dimensional wave theory, $c = \sqrt{E / \rho}$, the initial Young's modulus is approximately 16 MPa. Then, the initial shear modulus is obtained as 5.3 MPa with the assumption of incompressibility, ν = 0.5. The quantity μ in the Ogden model represents the initial shear modulus of the material so the μ parameter to be

obtained by the nonlinear VFM procedure should be close to this approximated initial shear modulus.

As explained in Section 6.2, the PVW, Eq. (6.6), was applied to the strain and acceleration field data up to the moment when cracks and voids are clearly observed. The VFM result of TEST 3 is given in Figure 6.21 showing the estimation history of the Ogden parameters and the profiles of the averaged acceleration and (true) strain rate. Unlike the acceleration values obtained by simply averaging whole surface data, the strain rate profile is acquired by averaging only the deformed region in the specimen during the incident strain wave period and the whole specimen after the first wave reflection. Similar to Figure 6.4(b) of the simulation work, the estimations of μ and α converge to certain values once the second acceleration wave is included in the optimization procedure of the nonlinear VFM. The period where the estimations are stable is chosen to obtain the averaged Ogden parameters as indicated by the hatched box

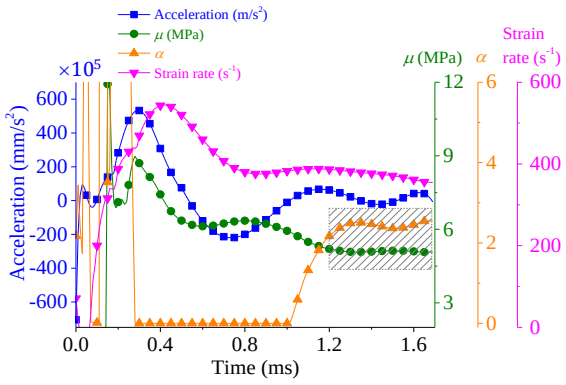

Figure 6.21 Averaged acceleration and strain rate profiles and the history of μ and α prediction from the gas-gun experiment on an EPDM specimen (TEST 3).

Table 6.7 Four Ogden parameter sets obtained from the nonlinear VFM and the averaged strain rates of the gas-gun experiments.

Test	Strain rate (s^{-1})	μ (MPa)	α
1	600	6.52	2.12
2	470	5.70	2.05
3	410	5.26	1.95
4	380	4.87	1.85

in Figure 6.21; the final strain rate is obtained by averaging its values over the period of 0.4-1.7 ms. The same procedure was repeated to obtain these parameters from all gas-gun experiments. The parameters obtained from the four gas-gun experiments are summarized in Table 6.7.

6.5 Discussion

6.5.1 Effect of the spatial smoothing

The experiment results shown above were obtained with the full-field data which was not subjected to any spatial smoothing filter. In order to see the effect of the spatial smoothing, the Gaussian smoothing function provided in the DIC software was applied on the full-field data of TEST 3 with two filter sizes of 3×3 and 5×5. Figure 6.22 shows the identification histories (μ and α) of the three cases: one from Figure 6.21 and two results of the smoothing cases. It can be seen that the identification of μ is insensitive to the given smoothing but, for the case of α, a slight variation over the stable period

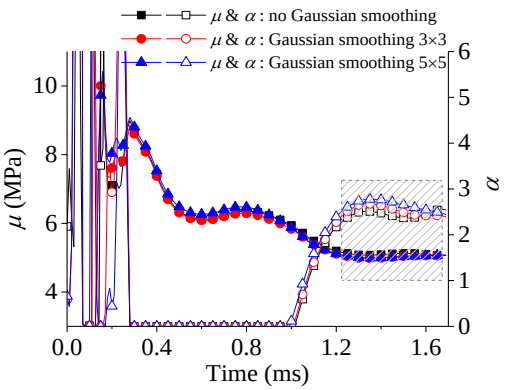

Figure 6.22 Identification histories of μ and α prediction with respect to the Gaussian smoothing (TEST 3).

Table 6.8 Ogden parameter sets obtained from the three spatial smoothing cases introduced in Figure 6.22.

Gaussian smoothing	μ (MPa)	α
None	5.26	1.95
3×3	5.20	2.10
5×5	5.20	2.21

(hatched area in Figure 6.22) is observed between the three cases. This variation could reflect the fact that the identification of α depends on the full-field data in which the deformation level is high, as this parameter describes the hardening behaviour. The optimization of Eq. (6.4) contributed by the deformation history at a later loading stage can be less than that at the initial period. The reason can be understood by Figure 6.21 in which the acceleration level is significantly reduced after about 0.8 ms. This reduction is partially due to the viscoelastic behaviour of the specimen (attenuation) but also the acceleration level can be dispersed as the stress uniformity (uniform deformation) is higher. The gradual achievement of the uniform deformation can be observed in Figure 6.20. The lower spatial gradient of the axial displacement field means the weaker level of the acceleration amplitude and, in turn, higher noise-to-signal ratio. This is one of the disadvantages of the current nonlinear VFM against the linear VFM where a non-uniform deformation state can be clearly generated at each strain level by means of the pre-stretching procedure. The identified parameters for each case, which can be obtained by averaging over the stable period (hatched area in Figure 6.22) are listed in Table 6.8, in which the differences of μ and α of each case are respectively up to 1 and 10 %.

6.5.2 Calculation of the acceleration fields

Figure 6.23(a) shows the noise level of the axial acceleration fields calculated from the displacement fields of the 10 still images used to present Figure 6.16. The calculation was conducted by the simple finite difference, Eq. (4.1). As expected, the noise level of the present case is much higher than that of the linear VFM (Figure 5.13); the averaged value is 100×10^5 mm/s^2. This noise level is significant at a later loading stage, for example, compared to the acceleration profile after 0.8 ms of TEST 3 as shown in Figure 6.21. This observation can be a reason for the slight variation of the α identification of Figure 6.22. In Figure 6.23(b), the identification histories of the two cases with and without the

temporal fitting are compared. Their final identification results are given in Table 6.9. A similar result is shown in that the μ identifications (1 % difference) are almost insensitive to the use of the temporal fitting but a slightly higher difference (4 %) is obtained for the α identifications. This higher difference can be similarly explained by the same reason as given above.

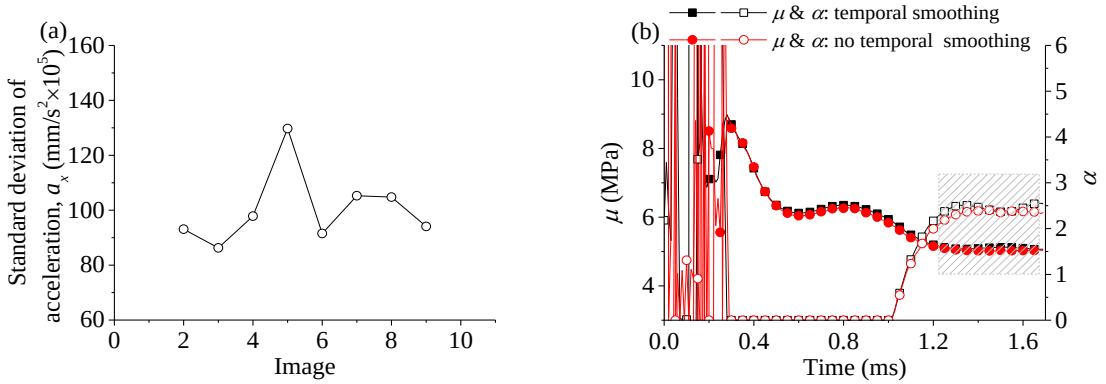

Figure 6.23 (a) Standard deviation of the acceleration fields of 10 still images (same pictures used in Figure 6.16); (b) the identification histories (μ and α) of TEST 3 with and without the temporal fitting.

Table 6.9 Ogden parameter sets obtained from the two temporal smoothing cases introduced in Figure 6.23.

Temporal smoothing	μ (MPa)	α
Applied	5.26	1.95
None	5.20	1.87

6.5.3 Comparison with the DMA

The DMA test was conducted on the same EPDM rubber. The specimen for the DMA was cut from the same EPDM sheet and its gauge length, width and thickness are respectively 12.4, 5.6 and 1.5 mm. The same DMA procedure was performed with Q800 DMA instrument (TA Instruments) but the frequency range is narrower as a preliminary test showed that the storage modulus measurement at 0.1 Hz was too noisy and for 50 Hz slipping between the specimen and the clamping was found. The same time-temperature superposition was applied to the storage moduli data shown in Figure 6.24(b). The three frequency 1, 5, 10 Hz corresponds to 0.25, 0.05 and 0.025 s. After this unit change, the

isotherm data were produced as shown in Figure 6.25(a); then each plot was manually shifted with respect to the reference isotherm curve at 20 °C. The final master curve is given in Figure 6.25(b).

The same comparison procedure can be conducted between the DMA moduli and the gas-gun & quasi-static tests. The strain amplitude of the present DMA test was 0.001. The Young's modulus of one of the quasi static test (0.0001 s^{-1}) at this strain level is approximated as a secant value of its stress-strain curve, 4.81 MPa. Young's modulus of the gas-gun TEST 4, which produced the lowest strain rate (380 s^{-1}) among the gas-gun tests, can be also similarly approximated from its reconstructed true stress-strain curve; it is obtained as 14.6 MPa. The storage moduli at this dynamic strain rate can be calculated in the following way: the time to reach the strain amplitude of 0.001 is 2.6 μs (= 0.001 / 380 s^{-1}); its logarithmic time is $\log_{10}(2.6\times10^{-6})$ = -5.6; and the storage modulus

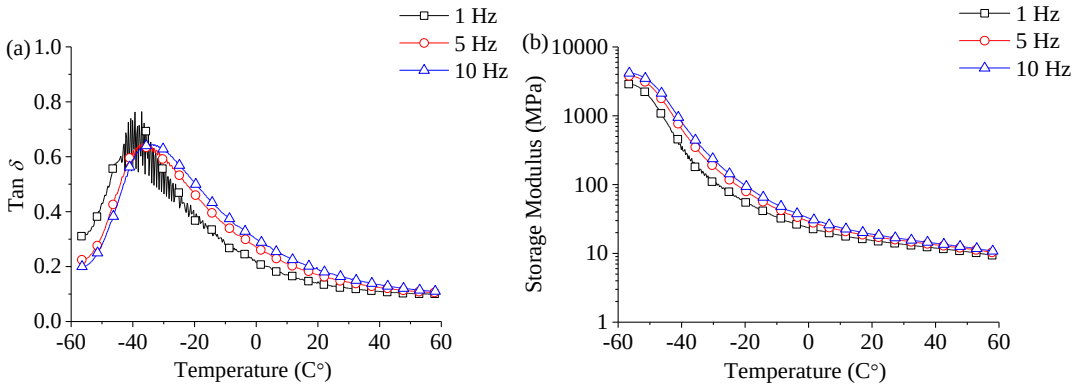

Figure 6.24 (a) Storage moduli and (b) tan δ versus temperature at 1, 5 and 10 Hz.

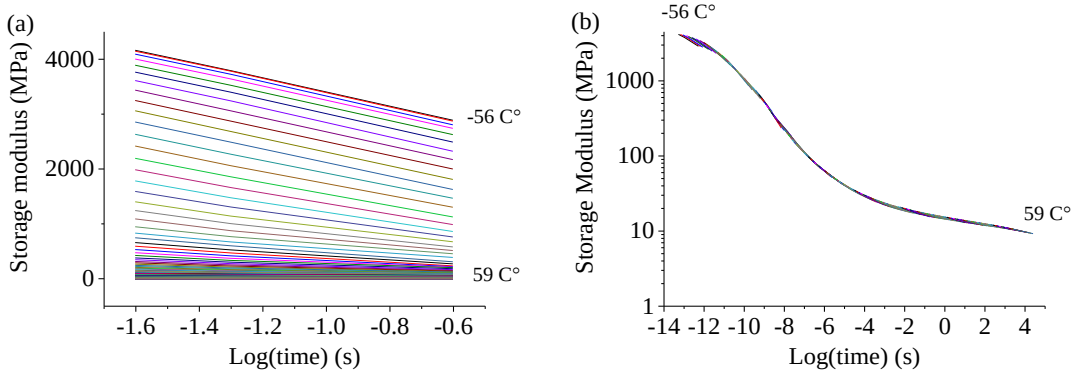

Figure 6.25 (a) Isotherm of storage modulus and (b) master curve versus the logarithmic time.

at this time is approximately 48.1 MPa. Similarly, at the quasi-static rate, the storage modulus is 13.9 MPa. The increment ratios of the transient tests (quasi-static and gas-gun tests) and the DMA are respectively 3.04 and 3.46. Using the same procedure, the increment ratio for the case of the gas-gun TEST 1 (600 s^{-1}) are 4.06 and 4.11 from the DMA. The increment ratios between the transient and DMA tests of both the two strain rate cases are comparable. In addition, the drop-weight test result can be also compared to the DMA data. The Young's modulus of the SET1 drop-weight test (no pre-stretching) is 11.8 MPa at 80 s^{-1}. The increment ratio from the quasi-static test is 2.45. The increment ratio for the DMA case at this dynamic rate and the quasi-static one is 2.81 (= 39.1 MPa (at the logarithmic times of -4.9) / 13.9 MPa). The increment ratio for this case is also comparable.

6.5.4 Overall discussion

The Ogden parameter sets obtained from the quasi-static, drop-weight and gas-gun tests are applied to the uniaxial Ogden equation, Eq. (5.2), and Eq. (5.3), to reconstruct the true stress-strain curves as shown in Figure 6.26. This figure shows the clear rate dependency of the present EPDM rubber as the stress-strain curve behaves stiffer for the higher strain rates. This stiffer behaviour can be explained by the fact that the μ term becomes larger for the higher rates. It seems that α also generally increases but is not strongly dependent on the strain rate since the α values for the drop-weight test (101 s^{-1}, α = 1.71) and one of the quasi-static tests (0.01 s^{-1}, α = 1.46) are not significantly different. The four Ogden curves from the gas-gun tests in Figure 6.26 have a solid line with symbol and a dashed line. The end of the symbolic line indicates the maximum averaged true strain of the last loading step used in the VFM; from this end, the dashed line is extended to extrapolate the gas-gun Ogden curves up to a true strain of 0.63 which is the maximum true strain of the drop-weight test.

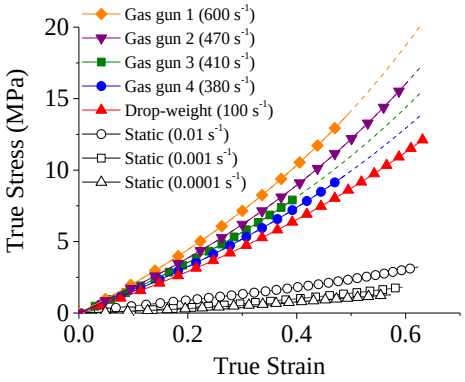

Figure 6.26 Ogden uniaxial true stress-strain curves reconstructed by the parameters of the gas-gun, drop-weight and quasi-static tests.

The identified parameters given in Table 6.7 are obtained from the dynamic full-field data produced by each single gas-gun experiment. This experimental expediency is a clear advantage of the gas-gun experiment with the nonlinear VFM in comparison to the drop-weight experiment with the linear VFM in which multiple experiments are required to introduce the pre-stretches. The identifications by the single experiment have another advantage in that complicated effects caused by the pre-stretches such as softening can be avoided. Also, it is clear that the gas-gun experiment is more suitable for high strain rates (> 300 s^{-1}) as the maximum strain rate of the current drop-weight system is limited by the mass and drop distance of the weight. However, the drop-weight test with the linear VFM and pre-stretching method is still a useful technique to fill the gap between the high strain-rate and quasi-static tests. It is experimentally complicated to introduce a single loading pulse which induces the medium strain rate of order of 100 s^{-1} whilst at the same time producing a large strain with a constant strain rate, as the final strain is not independent of the strain rate, and both are also affected by the material properties (in particular the stress wave speed). More positively, the fact that the drop-weight test produces a small strain amplitude allows use of higher resolution imaging and faster imaging speed of high-speed cameras for which the imaging size needs to be reduced for faster imaging. However, the pre-stretching can induce some inelastic effects, e.g.

Mullin's effect which requires each stretching step to have a larger amplitude than the previous.

6.6 Summary

Drop-weight and gas-gun experiments were performed on EPDM rubber to characterize the mechanical response to loading at medium and high strain rates in tension. The dynamic deformation fields captured by a high-speed camera were applied to the VFMs. The linear VFM introduced in the previous chapter was applied to a series of the short dynamic deformations fields obtained in a drop-weight apparatus with several given pre-stretches. From this procedure, a series of Young's moduli was identified at each given pre-strain and used to reconstruct an Ogden true stress-strain curve. In order to produce data at higher strain rates, the nonlinear VFM, which is directly associated with the one-term Ogden model was applied to the history of large dynamic deformation fields produced by a gas-gun experiment. The gas-gun experiment design was first simulated by finite element analysis; this simulation shows that the nonlinear VFM application on the continuous deformations fields with multiple wave reflections can successfully identify given Ogden parameters. The same nonlinear VFM procedure was used on the actual gas-gun experiments, and four Ogden parameters sets were identified at different high strain rates. The five dynamic true strain-stress curves were reconstructed by the Ogden parameters obtained from the linear and nonlinear VFMs. These dynamic curves show their clear rate dependency between the dynamic test and also from comparison to the quasi-static uniaxial experiments.

Chapter 7 THE INCREMENTAL LINEAR VFM

7.1 Introduction

In this chapter, the pre-stretching procedure used for the linear VFM (described through Chapter 4 and Chapter 5) and drop-weight test is revisited, in particular the specific requirements introduced by the pre-stretching technique and the different ways of analysing the experiment are examined. The PVW used in the VFM was based on the current (deformed) configuration of the specimen as it is loaded. The use of this PVW on a pre-stretched state requires us to account for the pre-existing stress field owing to this static deformation, as explained in Chapter 4. This static stress field was obtained by a static force measurement in the loading direction after pre-stretching and before the dynamic loading is applied. Here, an alternative VFM is introduced, which is based on an incremental form of the PVW that does not require this stress field measurement. Although these two methods have different mathematical forms of the PVW, their identification results should be consistent. However, it is expected that these two methods have different sources of experimental uncertainty as the processing of the experimental data is different in the two PVWs. This chapter describes the comparison of these two VFM procedures with regard to uncertainty in the experimental data. The linear VFM presented in the previous chapter is denoted as VFM 1 and two different approaches to the method introduced here, VFM 2 and 3. The first section provides a theoretical explanation with regard to VFM 2-3. The notations used in this section are the same used to describe Figure 4.20 and Figure 4.21 in Chapter 4 . Then, the difference between these VFMs are further studied using FEM simulations with artificially added noise. In the next section, VFM 2 is applied to the experimental data used in Chapter 5 and Chapter 6 (respectively, silicone and EPDM rubbers) so that the identification results from both VFMs can be compared. Further data are presented in order to show the effect on VFM 2

of different periods of relaxation after pre-stretching for silicone and EPDM rubbers. Additionally, a comparison study is provided, in which a compressive stress-strain curve reconstructed by material parameters identified by VFM 2 on a silicone rubber is compared with the curves measured by the SHPB at a similar medium strain-rate range on the same material.

The objectives presented in this chapter are summarized as follows:

- The incremental VFM is introduced with the description of its principle of virtual work equation based on the incremental equation of motion. This description will explain differences between the linear and incremental VFMs.
- FEM simulation study, similarly conducted in the chapter of the linear VFM, is introduced for the application of the incremental VFM. In contrast to the previous case, pre-forces produced by static stretching are not involved in the present VFM.
- The same FEM data are analysed by the linear VFM. The identification results of the linear and incremental VFMs are compared to show that the latter method is identically able to characterize a nonlinear stress-strain curve of a hyperelastic material.
- FEM simulation data, perturbed by artificial experimental errors applied on pre-strain and pre-stress data, are analysed by the linear and incremental VFMs, and its results are discussed in terms of the sensitivity to the artificial errors.
- The incremental VFM is applied on the same experimental data introduced in Chapter 5 and Chapter 6 so that the identification results can be compared with those of the linear VFM.
- In order to use the pre-stretching technique, rubber specimens are required to be quasi-statically stretched before dynamic loading. The time between

stretching and dynamic loading might influence the identification result of the VFM. This effect is studied by introducing several different stretching amounts and relaxation times.

- The same silicone rubber used in the previous chapters is tested by a SHPB technique. The description of this test is briefly given with regard to its force measurement system. Stress-strain curves reconstructed by this test are compared with that of the incremental VFM at a similar strain-rate range.

7.2 Incremental VFM (VFM 2 & 3)

The presence of a pre-stress has a strong influence on wave propagation in an elastic medium (Tang, 1967). This phenomenon is known as the acoustoelastic effect. Particularly in the context of soft materials, Ogden (2007) and Shames et al. (2011) have developed the mathematical framework to study stress wave propagation, generated by small deformations, superposed on finite pre-deformations. The small superposed deformation and its resulting stress is described by the incremental equation of motion (Shams et al., 2011)

$$\mathrm{Div}\, d\mathbf{N} = \rho \boldsymbol{a} \tag{7.1}$$

where $d\mathbf{N}$ is an incremental nominal stress tensor, $\mathbf{N} = J\mathbf{F}^{-1}\boldsymbol{\sigma}$, and Div is a divergence operator with respect to the initial state. $d\mathbf{N}_{p0}$ and $d\mathbf{N}_{p}$ are defined as push forward terms of $d\mathbf{N}$ to either the pre-stretched or current configuration (Shams et al., 2011)

$$d\mathbf{N}_{p0} = J^{-1}\mathbf{F}_{p0} d\mathbf{N} \tag{7.2}$$

$$d\mathbf{N}_{p} = J^{-1}\mathbf{F}_{p} d\mathbf{N} \tag{7.3}$$

from which it follows that

$$\mathrm{Div}_{p0}\ d\mathbf{N}_{p0} = \rho \boldsymbol{a} \tag{7.4}$$

$$\mathrm{Div}_{p}\ d\mathbf{N}_{p} = \rho \boldsymbol{a} \tag{7.5}$$

The subscripts ‘p0’ and ‘p’ in these equations denote the pre-stretched state and the current state after pre-stretching and during dynamic loading. The incremental nominal stress tensor d**N** is determined by the elasticity tensor **D** which is a function of material parameters and **F** (Ogden, 2007)

$$\mathrm{d}\mathbf{N} = \mathbf{D}\mathrm{d}\mathbf{F}_{\mathrm{p}},\ \mathbf{D} = \frac{\partial^2 W}{\partial \mathbf{F}\partial \mathbf{F}} \tag{7.6}$$

where W is a strain energy density that characterizes the properties of elastic materials. $\mathrm{d}\mathbf{F}_{\mathrm{p}}$ is the incremental deformation gradient tensor and defined as

$$\mathrm{d}\mathbf{F}_{\mathrm{p}} = \mathbf{F}_{\mathrm{p}}(t) - \mathbf{F}_{\mathrm{p0}} \tag{7.7}$$

In a similar way, the axial component $\mathrm{d}\lambda_{x,\mathrm{p}}$ of $\mathrm{d}\mathbf{F}_{\mathrm{p}}$ is obtained as presented in Figure 4.21. Using this incremental stretch ratio, Eq. (7.6) can be written in the axial direction

$$\mathrm{dN}_x(t) = \frac{\partial^2 W}{\partial \lambda_x^2}(t)\mathrm{d}\lambda_{x,\mathrm{p}}(t) \tag{7.8}$$

The double derivative term $\partial^2 W / \partial \lambda_x^2$ in this equation is an instantaneous nominal modulus, designated as *NE,* and the material parameter to be identified in this incremental VFM scheme.

Previous studies have used the VFM based on the first Piolar-Kirchhoff stress $\mathbf{\Pi} = \mathbf{N}^{\mathrm{T}}$, and The PVW, Eq. (6.1), used in the nonlinear VFM presented in Chapter 6 is recalled here again

$$\begin{aligned} &-\int_{S_0} \Pi_{xx}\frac{\partial u^*_{x,0}}{\partial x_0} + \Pi_{yy}\frac{\partial u^*_{\mathrm{y},0}}{\partial y_0} + \Pi_{xy}\frac{\partial u^*_{x,0}}{\partial y_0} + \Pi_{yx}\frac{\partial u^*_{\mathrm{y},0}}{\partial x_0}\ \mathrm{d}S_0 \\ &= \int_{S_0} \rho\left(a_x u^*_{x,0} + a_y u^*_{y,0}\right)\mathrm{d}S_0 \end{aligned} \tag{7.9}$$

The virtual displacement fields are defined in terms of the initial configuration, $\boldsymbol{u}^*_0 = \boldsymbol{u}^*(\boldsymbol{x}_0)$. The use of the first virtual field $\boldsymbol{u}^{*(1)}$, Eq. (3.2), introduced in Chapter 3 and the relation $\Pi_x = \mathrm{N}_x$ simplifies Eq. (7.9) to

$$-\int_{S_0} \mathrm{N}_x \frac{\partial u_{x,0}^{*(1)}}{\partial x_0}\ \mathrm{d}S_0 = \int_{S_0} \rho a_x u_{x,0}^{*(1)}\ \mathrm{d}S_0 \tag{7.10}$$

$u_{x,0}^{*(1)}$ is the first axial virtual displacement field with respect to the initial configuration as indicated by the subscript '0'. Eq. (7.10) can be rewritten to be based on the pre-stretched state ($x_{\mathrm{p}0}$, $y_{\mathrm{p}0}$) and the current state after pre-stretching (x_{p}, y_{p}) by using Eq. (7.4) and (7.5) as shown below

$$-\int_{s_{\mathrm{p}0}} \mathrm{dN}_{x,\mathrm{p}0} \frac{\partial u_{x,\mathrm{p}0}^{*(1)}}{\partial x_{\mathrm{p}0}}\ \mathrm{d}s_{\mathrm{p}0} = \int_{s_{\mathrm{p}0}} \rho a_x u_{x,\mathrm{p}0}^{*(1)}\ \mathrm{d}s_{\mathrm{p}0} \tag{7.11}$$

$$-\int_{s_{\mathrm{p}}} \mathrm{dN}_{x,\mathrm{p}} \frac{\partial u_{x,\mathrm{p}}^{*(1)}}{\partial x_{\mathrm{p}}}\ \mathrm{d}s_{\mathrm{p}} = \int_{s_{\mathrm{p}}} \rho a_x u_{x,\mathrm{p}}^{*(1)}\ \mathrm{d}s_{\mathrm{p}} \tag{7.12}$$

Using the relation of Eq. (7.2), (7.3) and (7.8), the final form of the PVW equations for the incremental VFM is obtained as

$$\frac{\partial^2 W}{\partial \lambda_x^2}(t) = -\frac{\int_{s_{\mathrm{p}0}} \rho a_x(t) u_{x,\mathrm{p}0}^{*(1)}\ \mathrm{d}s_{\mathrm{p}0}}{\int_{s_{\mathrm{p}0}} \lambda_{x,\mathrm{p}0} \mathrm{d}\lambda_{x,\mathrm{p}}(t) \frac{\partial u_{x,\mathrm{p}0}^{*(1)}}{\partial x_{\mathrm{p}0}}\ \mathrm{d}s_{\mathrm{p}0}} \tag{7.13}$$

$$\frac{\partial^2 W}{\partial \lambda_x^2}(t) = -\frac{\int_{s_{\mathrm{p}}} \rho a_x(t) u_{x,\mathrm{p}}^{*(1)}\ \mathrm{d}s_{\mathrm{p}}}{\int_{s_{\mathrm{p}}} \lambda_{x,\mathrm{p}}(t) \mathrm{d}\lambda_{x,\mathrm{p}}(t) \frac{\partial u_{x,\mathrm{p}}^{*(1)}}{\partial x_{\mathrm{p}}}\ \mathrm{d}s_{\mathrm{p}}} \tag{7.14}$$

By means of either Eq. (7.13) or (7.14), the instantaneous axial nominal modulus $NE_n(t) = \partial^2 W / \partial \lambda_x^2$ is acquired as an identified material parameter. The VFM schemes using Eq. (7.13) and (7.14) are denoted as VFM 2 and 3 in this chapter. The averaged values of NE_n can be calculated by the same method that was used for the attainment of E_n in Chapter 4 and Chapter 5. Each NE_n from one non-pre-stretching and several pre-stretching cases is used for the optimization procedure in order to obtain the model parameters by minimizing the cost function below:

$$\Phi = \sum_{j=1}^{n}\left[\frac{1}{2}\left(\frac{\partial^2 W}{\partial\lambda_x^2}\left(A_1,\ldots A_i,\lambda_{x,\mathrm{p0}}^{j}\right)+\frac{\partial^2 W}{\partial\lambda_x^2}\left(A_1,\ldots A_i,\lambda_{x,\mathrm{f}}^{j}\right)\right)-NE_j\right]^2 \tag{7.15}$$

The strain energy density term W is defined by the given material model. W is described by the same one-term Ogden model. In this study, it is assumed that the principal direction and the experiment coordinate (i.e. x: loading direction) are coincident. W of the one-term Ogden model is recalled below

$$W = \frac{2\mu}{\alpha^2}\left(\lambda_x^{\alpha}+\lambda_y^{\alpha}+\lambda_z^{\alpha}-3\right) \tag{7.16}$$

The form of the instantaneous axial nominal modulus expressed by this Ogden model under an in-plane stress condition is

$$\frac{\partial^2 W}{\partial\lambda_x^2} = \frac{2\mu}{\alpha^2}\left(\alpha\left(1+\frac{\alpha}{2}\right)\lambda_x^{-2-\frac{\alpha}{2}}+\alpha\left(-1+\alpha\right)\lambda_x^{-2+\alpha}\right) \tag{7.17}$$

This expression is used in Eq. (7.15) for the optimization procedure to find the material parameters μ and α.

Compared to Eq. (4.8), the PVW used for VFM 1, the pre-stress term $\sigma_{xx,\mathrm{p0}}$ is not involved in Eq. (7.13) and (7.14). However, these equations of VFM 2-3 include the pre-strain term $\lambda_{x,\mathrm{p0}}$. From this difference, it is expected that the identifications of VFM 2-3 have a different sensitivity to error sources in experimental measurements. In the next section, this sensitivity is studied by a finite element simulations of a drop-weight experiment.

7.3 Simulation work

The simulation works presented in Chapter 4 demonstrated that VFM 1 is able to identify given material parameters of the one-term Ogden model. In the present study, the same simulation analysis was extended to simulate the analysis procedure of VFM 1-3 and study their sensitivity of experimental errors. The simulation geometry is slightly different as there was the modification of a drop-weight apparatus so that a longer

specimen can be tested; hence, the dimensions for the present simulation are length = 38 mm and width = 8 mm. The whole procedure is exactly the same as the 2D pre-stretching simulation procedures presented in Chapter 4. The same data processing procedure was applied to mimic the imaging speed of 50 000 fps (Figure 4.5) and to add random noise (white Gaussian noise) to the displacement fields (Eq. (4.3)). For the acceleration fields, the same temporal fitting procedure was used with a 9-degree polynomial. Seven different amounts of pre-stretching were applied, corresponding engineering strains of 0.1 to 0.7. For the material model, the one-term Ogden model was used but with a higher bulk modulus of 40 GPa in order to retain incompressibility for a stiffer behaviour which was exhibited by the material parameter adopted in the present study. With the field data from one simulation, one Young's modulus from VFM 1 and two nominal moduli from VFM 2 and 3 are produced. Each VFM analysis includes three sets of 8 different moduli from one non- and seven pre-stretching simulations. These modulus sets are then used for the optimization procedure to obtain three sets of μ and α. Throughout the present simulation studies, the density ρ used in the VFMs is assumed to be 1370 kg/m^3 which is the actual value of the EPDM specimen.

7.3.1 Identification capability

In the data presented in this section, the pure displacement fields were polluted only by noise level 1 (40×10^{-6} mm) so that the best identification capability of each VFM can be evaluated. The first simulation was conducted with one-term Ogden parameters of μ = 4 MPa and α = 2. These parameters are of the order of the actual identification results of the EPDM rubber presented in Chapter 6. The identification results of Young's and nominal moduli are shown in Figure 7.1 for the case of VFM 1 and 2. Next to each figure, the amount of true axial strains $\varepsilon_{xx,\mathrm{p0}}$ are given.

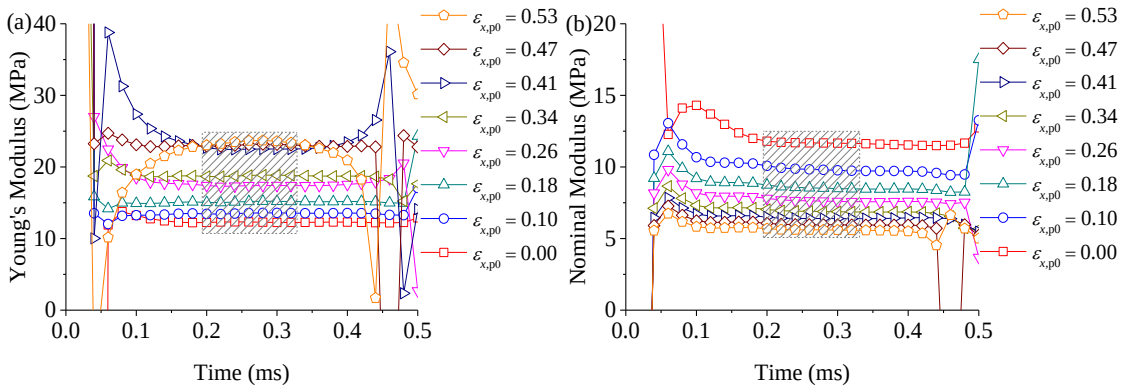

Figure 7.1 (a) Young's and (b) nominal moduli identifications at each true pre-strain location for VFM 1 and 2.

The hatched box in each figure indicates the area in which the averaged modulus values are obtained. This area is chosen so that the modulus predictions are stable, and the Poisson's ratios are bounded between 0.4 and 0.5. The length of this averaging area depends on material stiffness and, consequently, its wave speed as the unstable identification occurs when a stress wave is reflected from the fixed end of the specimen, for example, the sudden drop in the Young's modulus identification at 0.44 ms of the pre-stretching simulation with $\varepsilon_{xx,p0} = 0.53$. Although the length of the averaged period can be changed with respect to the material parameters and pre-stretching amount, in this study its length was fixed at 0.2 to 0.32 ms in all cases in order to automate the analysis. Each 'run' of the identification procedure including the 8 simulations and three VFMs was automatically conducted by linking MATLAB and ABAQUS. The global final axial deformations: $\varepsilon_{xx,f}$ in Eq. (4.11) for VFM 1 and $\lambda_{x,f}$ in Eq. (7.15) for VFM 2-3 are taken at the last step of the averaging period, $t = 0.32$ ms.

In Figure 7.1(b), it can be seen that the identified nominal modulus becomes lower as the pre-stretching increases while the opposite trend is shown in the Young's modulus identification. This difference can be understood from Figure 7.2, in which the true and nominal stress-strain curves are shown with two sets of 9 slopes laid on true and nominal stress-strain curves at the pre-strain locations. These slopes were the averaged modulus

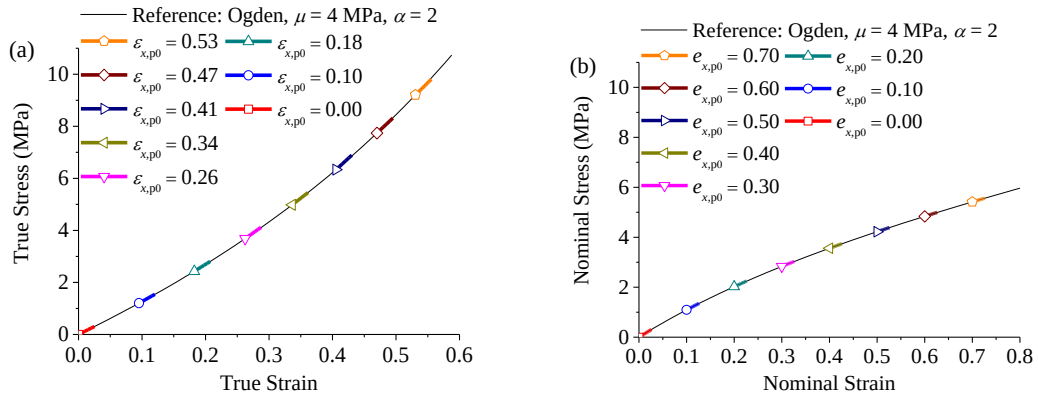

Figure 7.2 (a) True and (b) nominal stress-strain curves of the one-term Ogden model (μ = 4 MPa, α = 2) and nine (true and nominal) slope lines at each pre-strain location.

Table 7.1 Identified Ogden parameters from VFM 1-3 on the FEM simulations.

VFM	μ (MPa)	α
VFM 1	4.05	1.99
VFM 2	4.01	2.04
VFM 3	4.01	2.04
Given μ = 4 MPa, α = 2		

values obtained from Figure 7.1. It can be seen that the slopes on the true curve of Figure 7.2(a) increases with increasing strain whilst the opposite trend is shown on the nominal curve in Figure 7.2(b). These increasing and decreasing tendencies depend on the material parameters; for some parameters the nominal curve can also show increasing slope with increasing strain.

One set of the averaged Young's moduli (VFM 1) and two sets of the averaged nominal moduli (VFM 2-3) were then used for the optimization procedure of Eq. (4.11) and (7.15). The identified Ogden parameters in each case are given in Table 7.1. All of the identified material parameters from VFM 1-3 are close to the given values. This result leads to the conclusion that the use of VFM 2-3, which does not require the measurement of the pre forces, has the capability to obtain the Ogden material parameters as well as VFM 1.

The same simulation and VFM procedures were applied to other combinations of μ and α. The range of these parameters were 1 to 4 with an interval of 1 so there were in

total 16 pre-stretching simulation & VFM analyses. This range includes the identified parameter from the actual drop-weight experiments on silicone and EPDM rubbers. For all simulations, noise level 1 was applied to the displacement data. Figure 7.3 shows that the identification results of VFM 1-3 on these multiple simulations are well matched to their given μ and α parameters (intersection points of dashed lines). The slight deviations can occur due to the fixed averaging period, since the stable identification periods may change and the use of a constant bulk modulus which will give a slight variation in the Poisson's ratio.

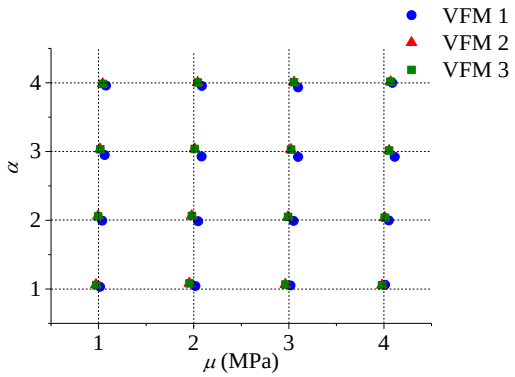

Figure 7.3 Identified parameters from VFM 1-3 for the multiple simulations with the given parameters (intersection points of dashed lines).

7.3.2 Noise on displacement fields

The effect of the white noise on the identification of Young's modulus was studied using the same FEM simulation method as applied to VFM 1 in Chapter 4. In the present section, this study is extended to include noise effects on the identification of the material parameter (μ = 4 MPa, α = 2) using the same simulation procedure as in the previous section but with higher amplitudes of white Gaussian noise on the displacement fields. For each noise level, 15 pre-stretching simulations were conducted and analysed by VFM 1-3. Then, the 15 sets of μ and α obtained from each VFM were taken for the calculation of the mean and standard deviation in the parameter identifications; the results of these calculations are shown in Figure 7.4.

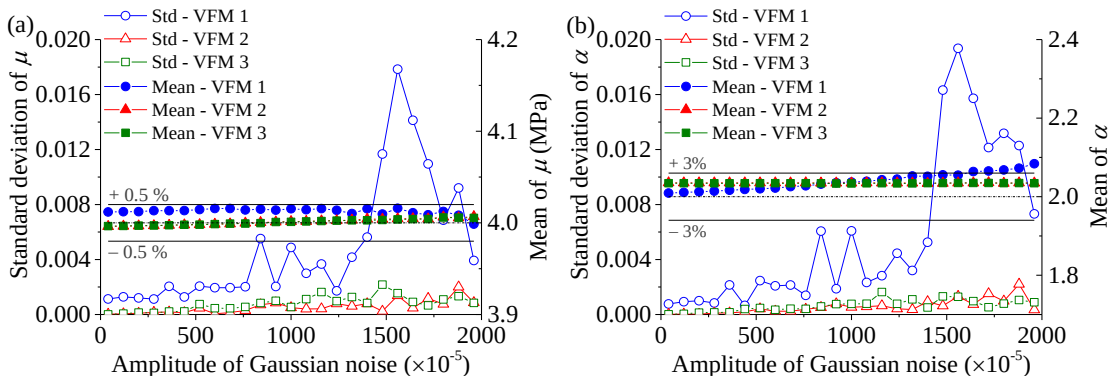

Figure 7.4 Mean and standard deviation of the identified values of (a) μ and (b) α from VFM 1-3 applied to the FEM simulation with white Gaussian noise.

The mean values of the identified μ and α of VFM 1-3 are bounded approximately between, respectively, 0.5 and 3 % error (solid lines) from the given values (dashed line). It can be seen that the standard deviation of μ and α obtained from VFM 1 is higher for all noise levels compared to that of VFM 2-3. Even at noise level 1 (40×10^{-6} mm), VFM 1 produces about 40 times higher standard deviation in its identification than VFM 2-3. This higher noise sensitivity of VFM 1 toward the displacement noise can be explained by the number of the virtual fields used in each PVW equation. Two sets of virtual fields were used in the PVW for VFM 1 but only the first set was applied to Eq. (7.13) and (7.14) for VFM 2-3. In other words, for the VFM 1 procedure the first and second virtual fields are multiplied by the data field in the x and y direction, i.e. $\varepsilon_{xx}, \varepsilon_{yy}, \varepsilon_{xy}$, $a_{x,y}$. This calculation of VFM 1 brings white Gaussian noise in all directions into its identification. Thus, the PVW of VFM 1 includes more noise source than VFM 2-3 which are affected only by the noise in ε_{xx} and a_x.

7.3.3 Measurement error in pre-strains and pre-static forces

The pre-strains $e_{xx,p0}$ or stresses $\sigma_{xx,p0}$ are used throughout the analysis procedures of VFM 1-3. The actual measurement of $e_{xx,p0}$ was conducted by comparing distances of pre-marked points on the un- and pre-deformed specimen. $e_{xx,p0}$ is involved in three ways in the optimization procedure of VFM 1-3 (Eq. (4.11) and (7.15)); in the calculation of $\sigma_{xx,p0}$

from its nominal value for VFM 1; and in the PVW of VFM 2-3. The nominal pre-stress was obtained by dividing a static force, measured after pre-stretching, by the initial cross-sectional area. Obviously, the measurement error in the pre-strains and static forces can affect the identification quality of μ and α. However, the identification sensitivities of VFM 1-3 with respect to these error sources are different as VFM 1 is affected by both of the measurement, but VFM 2-3 only by $e_{x,\mathrm{p0}}$.

This identification sensitivity is studied in this section by artificially introducing measurement errors of the pre-strains and forces on the simulation work of Section 7.3.1 (μ = 4 MPa, α = 2). It is assumed that the pre-strains and forces may be inaccurately measured with an error of up to $\pm$ 10 %. First, $\pm$ 10 % errors were added to all engineering pre-strain measurements; then, these polluted values were used to calculate $\varepsilon_{xx,\mathrm{p0}}$ and $\lambda_{x,\mathrm{p0}}$ which were in turn, used in the optimization procedures, respectively for VFM 1 and 2-3. The polluted $\lambda_{x,\mathrm{p0}}$ was also used in the PVW of VFM 2-3 and for the multiplication to the nominal pre-stress in order to obtain $\sigma_{xx,\mathrm{p0}}$ used in VFM 1. In addition, prior to this pre-stress calculation, the measurement of the pre-force was polluted by ± 10 % error.

The introduction of these measurement errors produces two Ogden curves which form the maximum and minimum error boundaries, shown as red and blue dashed curves in Figure 7.5. Next to each boundary curve, their identified μ and α parameters are provided with the same colour. Between these boundaries, the reference Ogden curve made by μ = 4 MPa, α = 2 is located. In each figure, *Area* means the area between the two error boundaries and represents the approximate quantification of the identification sensitivity of VFM 1-3. The area in the case of VFM 1 is larger than those of VFM 2-3. This larger area indicates the higher sensitivity of VFM 1 with respect to the measurement error sources; the same observation can be found from the larger deviation of μ and α of VFM 1 compared to those of VFM 2-3. The higher sensitivity of VFM 1 is simply due to the fact

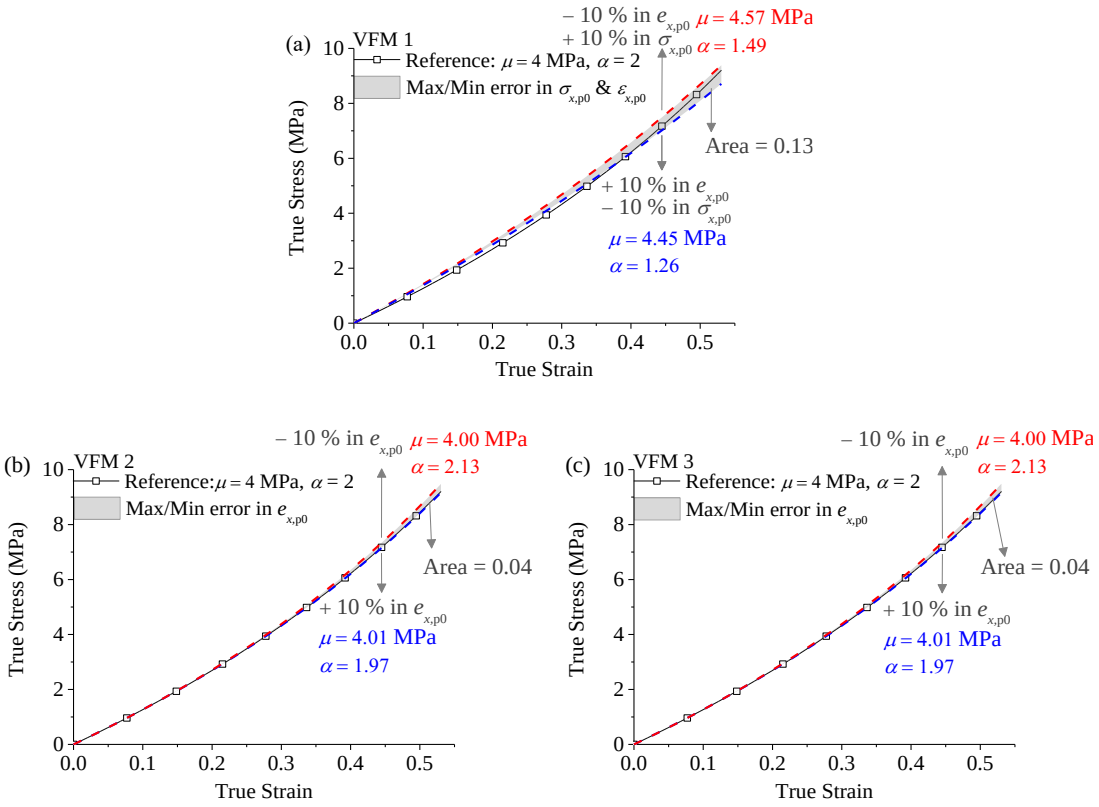

Figure 7.5 Influence of the $e_{xx,p0}$ and $\sigma_{xx,p0}$ measurement errors on the μ and α identification: (a) VFM 1 with $e_{xx,p0}$ & $\sigma_{xx,p0}$ error, (b-c) VFM 2-3 with $e_{xx,p0}$ error (*Area* indicates the area between the error boundaries).

that both the pre-strain and force measurements are simultaneously involved but only the former is required in VFM 2-3. The addition of the pre-force measurement error on VFM 1 gives another observation that the downward deviation of the minimum error boundaries of VFM 1 is larger than the case of VFM 2-3, which shows relatively small downward deviation.

7.3.4 Discussion of the simulation work

The identification capabilities of VFM 1-3 are almost the same if no noise sources are applied as shown in Figure 7.3. This result means that the pre-force measurement does not need to be enforced when using either VFM 2-3 which are based on the incremental VFM. With regard to the displacement field noise, Figure 7.4(a) and (b) shows that the identifications of VFM 1 is more sensitive with respect to the spatial noise on the displacement fields. This higher noise sensitivity could make VFM 1 difficult to apply to

a dynamic test requiring very high imaging speed, in which the noise amplitude usually becomes larger for a given high-speed camera. Measurement errors in the pre-strains and forces have an influence on the identification quality of VFM 1-3 as shown in Figure 7.5. The identification sensitivity is higher for VFM 1 because of the additional measurement error in the pre-force. When VFM 1 is applied to an actual drop-weight test, the downward deviation from the reference curve in Figure 7.5(a) is more likely to appear because stress relaxation as pre-stretching on a rubber specimen can induce an underestimation in the actual measurement of the pre-force. From the present simulation study, it can be concluded that VFM 2-3 are capable of characterizing a stress-strain curve of rubbers without the pre-force measurements; their identifications are more reliable with respect to the measurement error sources than those from VFM 1. However, VFM 1 still has its usefulness in that it can provide the identification of Poisson's ratio which can be used as one of the identification quality factor. For example, Poisson's ratio of rubber measured by a static test can be used for the reference value for evaluating the VFM identification with the assumption of rate-independent and very large bulk modulus.

In summary, the present simulation work leads to the following two conclusions:

- The incremental VFM is able to identify the stress-strain curve of a hyperelastic model as well as the linear VFM.
- The linear incremental VFM is insensitive to the uncertainty in pre-stress measurement.

7.4 Application of VFM 2-3 to actual experimental data

Drop-weight experiment data presented in Chapter 5 and Chapter 6 are used for the application of VFM 2-3 in this section. The identification result from only VFM 2 is given in the present study because VFM 2 and 3 produce almost identical identifications, as also shown in the simulation study. Figure 7.6 presents the comparisons of the Young's and

nominal moduli, respectively obtained from VFM 1 and 2, of the silicone and EPDM rubbers. The hatched area in each figure indicates the period for obtained the averaged moduli as explained in the simulation work. These periods were already chosen in the previous studies by considering the stable identifications and incompressibility so that the identified Poisson's ratio is bounded between 0.4-0.5. The same averaging periods from Figure 7.6(a) and (c) were applied to the nominal modulus identification of Figure 7.6(b) and (d).

The average of E_n and NE_n were applied to the optimization procedures of VFM 1 and 2, Eq. (4.11) and (7.15), in order to obtain the optimized Ogden parameters. These parameters were used for plotting the uniaxial stress-strain curves presents in Figure 7.7. The two identified parameters respectively from VFM 1 and 2 for the silicone and EPDM rubbers are given in the legend of each figure. The true and nominal curves are produced with identical parameters but shown to highlight their different shapes and how these

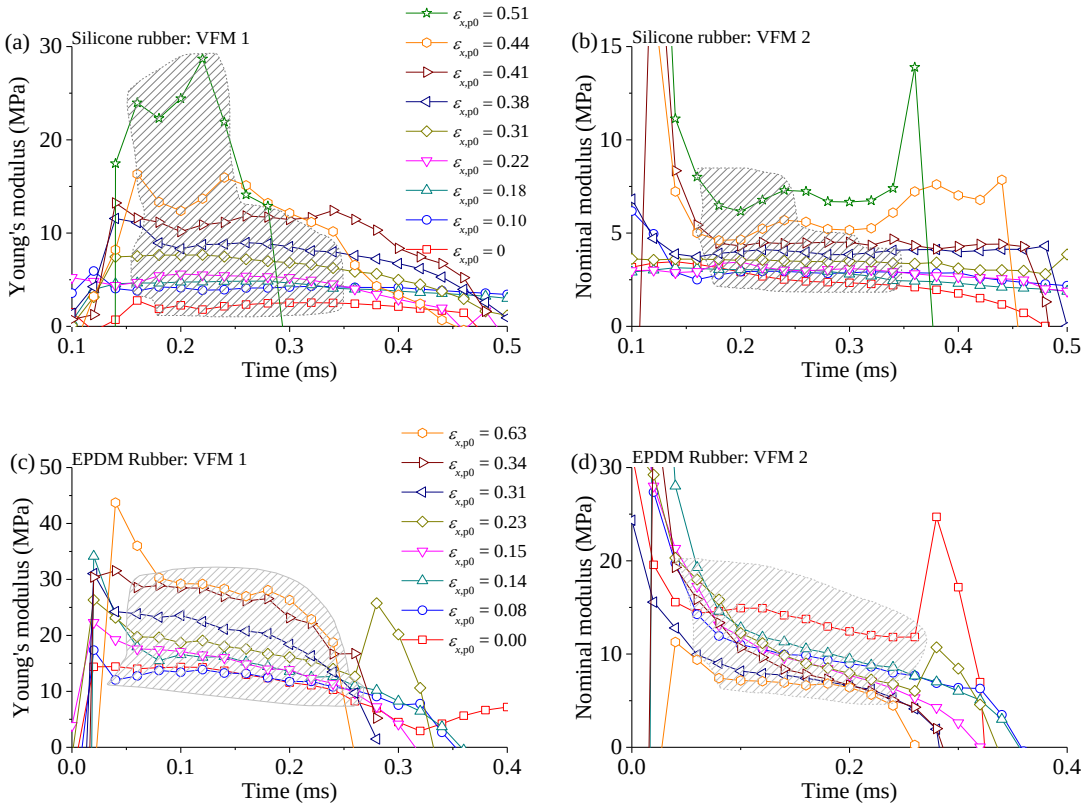

Figure 7.6 Identifications of the Young's and nominal moduli of VFM 1 and 2 on: (a, b) silicone and (c, d) EPDM rubbers (the legends in (a, c) figures are identically used for (b, d)).

relate to the tangent moduli obtained. Similar to Figure 7.2(a-b), lines corresponding to the averaged E_n and NE_n values are laid on top of the true (for VFM 1) and nominal (VFM 2) curves. For example, in Figure 7.7(a), the Ogden curve (solid line) from VFM 1 is shown with the slope E_n at each true pre-strain. This description shows the reason for the continuously increasing E_n for a higher pre-strain, observed in Figure 7.6(a), which determines the convex-upward shape of the true stress-strain curve in Figure 7.7(a). In the same way, from Figure 7.7(b), it is observed how the values of NE_n constructs the

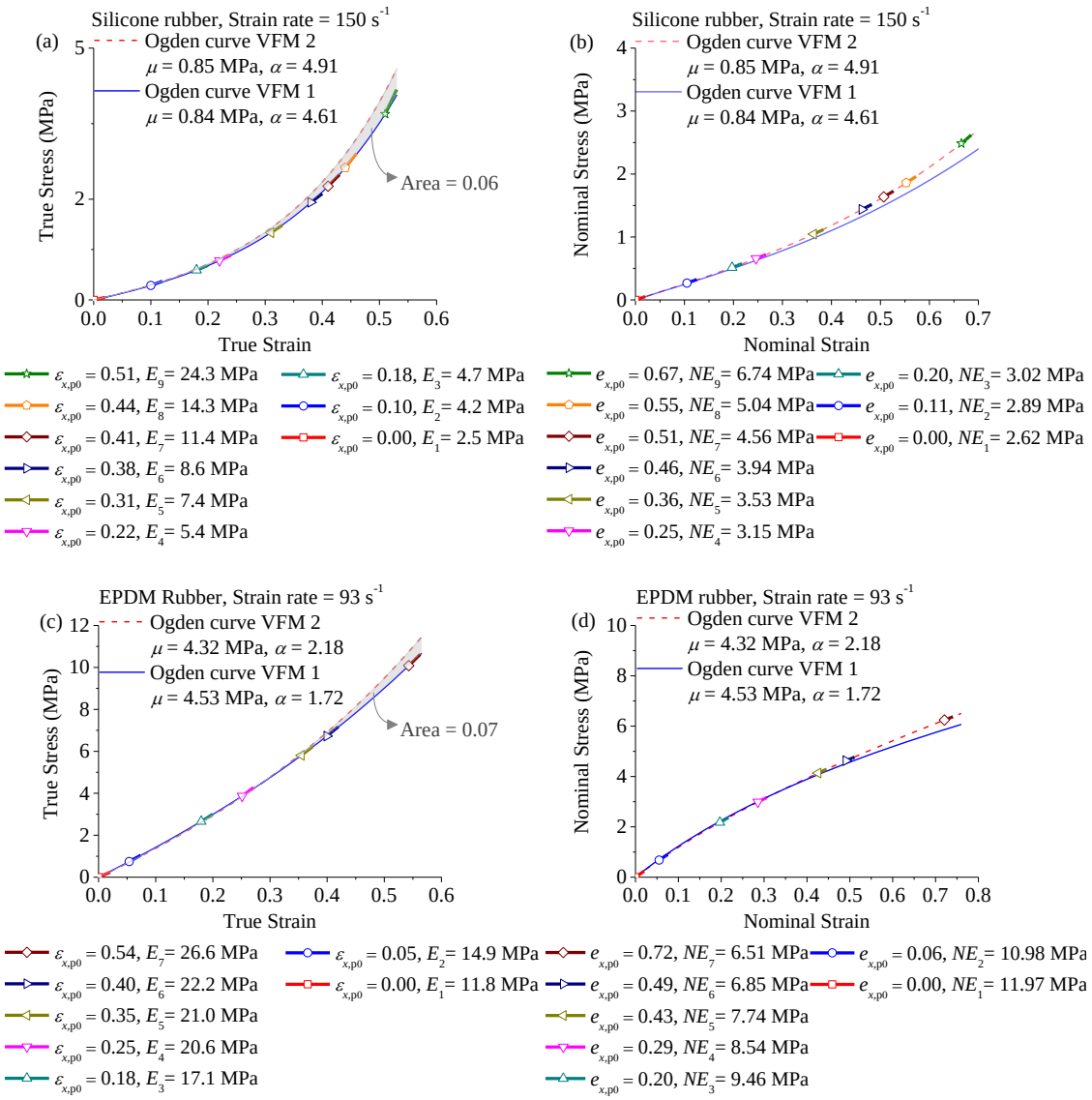

Figure 7.7 True and nominal stress-strain curves constructed by the one-term Ogden model and its parameters obtained from VFM 1-2 on the silicone and EPDM rubbers.

nominal curve (dashed line) shape obtained from VFM 2. The increasing trend of NE_n shown in Figure 7.6(b) corresponds to the concave-upward nominal curve in Figure 7.7(b). In contrast to the silicone rubber, the *NE* values of the EPDM are in a decreasing trend with increasing pre-strain. This difference is also observed in the nominal curve (Figure 7.7(d)) showing the concave-downward shape. From the comparison of Figure 7.6(b) and (d) or Figure 7.7(b) and (d), it can be concluded either VFM 1 or 2 is able to catch the different characteristics of these two rubbers in this medium strain-rate experiment.

It is observed that the Ogden curve from VFM 1 exhibits lower stresses than that of VFM 2 in the high strain region ($\varepsilon_{xx} > 0.3$) for both the silicone and EPDM rubbers. This result agrees with those from the simulation study with measurement errors in the pre-strains and forces. There is a need to use $\varepsilon_{xx,\mathrm{p0}}$ in both VFM 1 and 2 procedures; thus, its measurement errors can affect the identified parameters of both VFM 1 and 2. Spatial noise on images obtained during the loading might also influence the parameter identifications of VFM 1 and 2; but it is expected that this noise effect is insignificant because the spatial noise level on displacement fields is about 4×10^{-4} mm, which does not have a significant effect on the identifications of μ and α as shown in Figure 7.4(a) and (b). The measurement error in the pre-forces is unique only to VFM 1. The simulation study shows that the pre-force measurement error can expand the error boundary which is already affected by the pre-strain measurement; and in the particular experiment where the pre-force measurements are likely to be underestimated due to stress relaxation, the identified curve tends to be softer than an actual one. This tendency is a probable reason for the lower stress curves of VFM 1 observed in Figure 7.7.

7.5 Discussion

7.5.1 Repeatability of the drop-weight test

One potential weakness of the pre-stretching method described above is that there is a short delay between applying the static preload and the subsequent dynamic loading, this was approximately 2 to 3 minutes. During this time the specimen relaxes. In this section the potential effects of this relaxation are observed. Firstly, the effect of intermittent relaxations on data obtained from quasi-static experiments is explored. Then, drop-weight experiments are performed with different relaxation times between the application of the static and dynamic loads.

The uniaxial (nominal) stress-strain and intermittent relaxation curves of the pure silicone rubber are shown in Figure 7.8. These tests were conducted at $\dot{e}$ = 5 % s^{-1}, and the controlling software for a quasi-static experiment machine, Bluehill 3, in which only nominal strain rate control is available for an intermittent relaxation test. The strain values were measured by means of a USB camera and the DIC software as introduced in Section 6.4.1 in Chapter 6. Each relaxation was performed for 30 minutes, reloading was applied up to the next relaxation point. The reloading curve follows the continuous uniaxial curve after about a nominal strain of 0.4, which is equivalent to a true strain of 0.34.

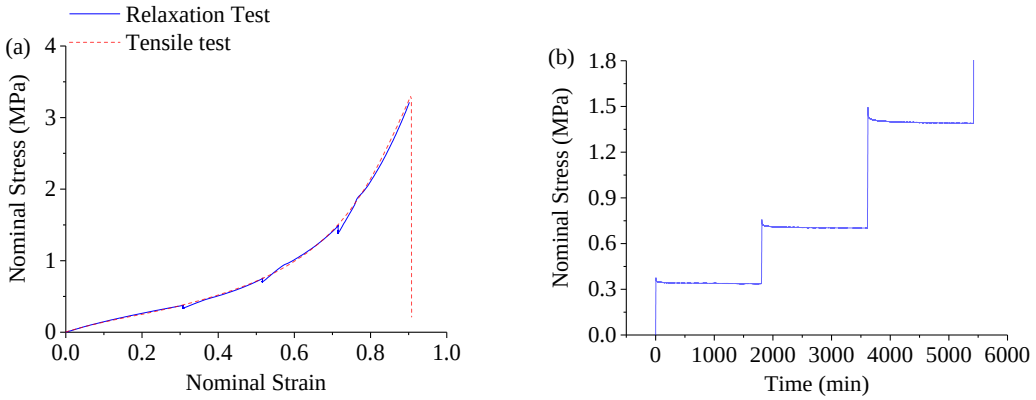

Figure 7.8 Uniaxial stress-strain obtained monotonically and with intermittent relaxations at $\dot{e}$ = 5 % s^{-1}; (b) stress-time response for the intermittent relaxation curve.

Although this transition is within the range of the uniaxial true strain fields which varies up to 0.1, during the averaging period, produced by the drop-weight test, this transition is relevant only at quasi-static strain rates. For the consideration of the effect on the drop-weight data, it is necessary to study the transition in a dynamic experiment following pre-stretching and relaxation. In order to investigate the effect of the total relaxation time on the stress transition period, the drop-weight test was conducted on the same pure silicone rubber with three relaxation times ($t_{1,2,3}$ = 3, 15 and 30 min) after pre-stretching and clamping. The specimens used for this test and the previous study were not manufactured in the same batch of material; their actual properties may be slightly different although the manufacturing procedure was nominally the same. Twelve specimens were prepared; for each set of four specimens, three axial pre-stretches were given: $e_{x,\mathrm{p}0}^{\mathrm{intended}}$ = 0.2, 0.3 and 0.5. These intended pre-strains were approximately applied by manually stretching the specimens; their actual $e_{x,\mathrm{p}0}$ were measured by comparing the distance between two pre-marked points on images of the un- and deformed specimen. After clamping the specimens, the relaxation time was measured. When each desired relaxation time was reached, the dynamic loading was applied, and the same imaging and DIC procedures were used.

The VFM 2 procedure was adopted to obtain the estimation profile of the nominal modulus *NE* as shown in Figure 7.9 for the case of $e_{x,\mathrm{p}0}^{\mathrm{intended}}$ = 0.2. Similar results were obtained for the other amounts of pre-stretching, and the mean values of the nominal modulus and true strain were obtained by averaging over the time period of 0.2-0.4 ms. Their values are listed in Table 7.2. At the end of this table, the averaged values for four specimens in each pre-strain case are also provided. It seems that there is no strong relation between the relaxation time and the averaged nominal modulus for all pre-strain cases although the instantaneous modulus, i.e. the slope of the stress-strain curve, during

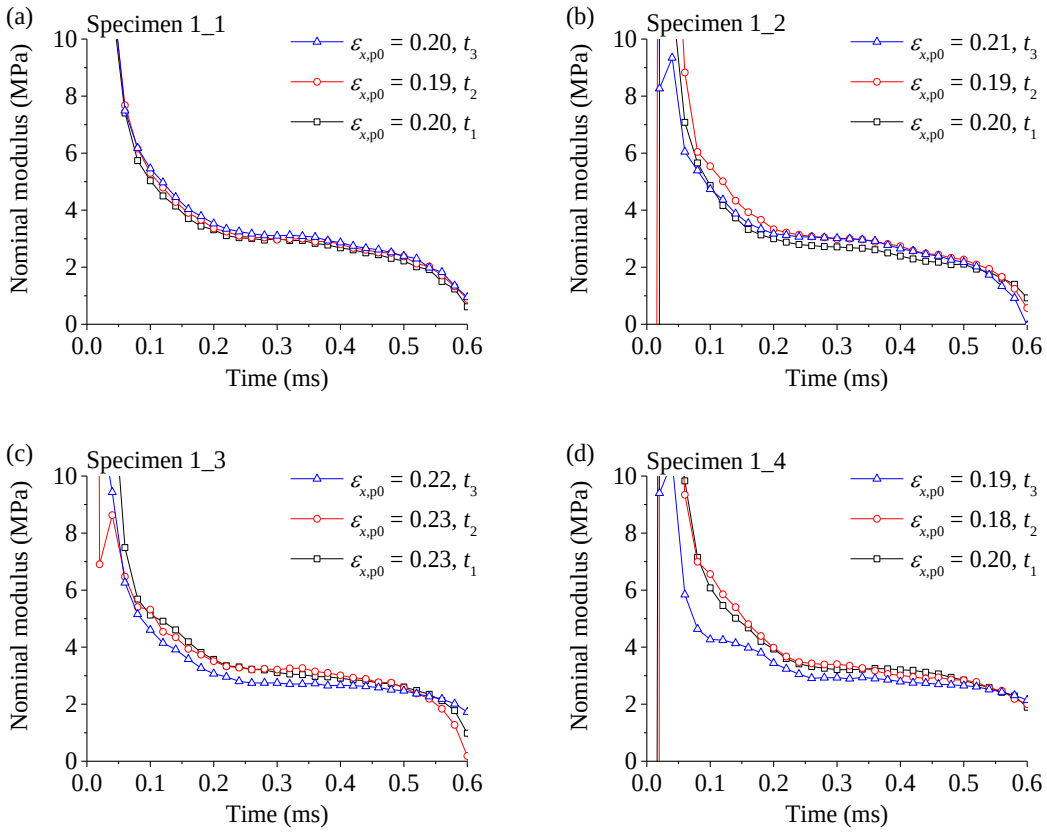

Figure 7.9 Nominal modulus estimation profiles obtained from VFM 2 on the silicone rubber at three different relaxation times ($t_{1,2,3}$ = 3, 15 and 30 min).

the transition period depends on the amount of relaxation, as shown in the intermittent tests on rubber from other studies (Bergström and Boyce, 1998; Lion, 1997; Shim and Mohr, 2011). The present result indicates that the transition period is limited to an early stage of the modulus estimation history. However, this observation is only valid for the present medium strain-rate range produced by the drop-weight experiment. When much higher strain rates are expected to be used, the same study should be conducted.

The same repetition tests with different relaxation times were conducted on the EPDM rubber. It was found that this rubber had become slightly stiffer at the time of the repetition test, compared to the original experiments performed a few months earlier, probably due to ageing. However, for the purpose of these experiments, this property change is not important. The multiple use of one specimen for the three relaxation times at approximately the same pre-strain is not suitable for the EPDM rubber because the

Table 7.2 Averaged nominal moduli and strain rates obtained from VFM 2 on the silicone rubber with the relaxation times ($t_{1,2,3}$) at given three pre-strains.

$e_{x,\mathrm{p}0}^{\mathrm{intended}} = 0.2$				$e_{x,\mathrm{p}0}^{\mathrm{intended}} = 0.3$				$e_{x,\mathrm{p}0}^{\mathrm{intended}} = 0.5$			
Relaxation time	$e_{x,\mathrm{p}0}$	*NE* (MPa)	$\dot{\varepsilon}_x$	Relaxation time	$e_{x,\mathrm{p}0}$	*NE* (MPa)	$\dot{\varepsilon}_x$	Relaxation time	$e_{x,\mathrm{p}0}$	*NE* (MPa)	$\dot{\varepsilon}_x$
Specimen 1_1				Specimen 2_1				Specimen 3_1			
t_1	0.22	2.90	117	t_1	0.30	3.09	113	t_1	0.49	3.88	109
t_2	0.21	2.97	113	t_2	0.30	3.04	100	t_2	0.50	4.02	109
t_3	0.22	3.07	117	t_3	0.29	3.07	90	t_3	0.51	3.96	92
Specimen 1_2				Specimen 2_2				Specimen 3_2			
t_1	0.22	2.64	113	t_1	0.33	3.36	94	t_1	0.50	4.22	95
t_2	0.21	2.95	111	t_2	0.30	3.39	100	t_2	0.50	4.11	96
t_3	0.24	2.93	120	t_3	0.31	3.43	105	t_3	0.51	4.04	95
Specimen 1_3				Specimen 2_3				Specimen 3_3			
t_1	0.26	3.09	121	t_1	0.32	3.62	93	t_1	0.48	4.04	100
t_2	0.26	3.18	125	t_2	0.32	3.18	104	t_2	0.49	4.11	100
t_3	0.25	2.74	116	t_3	0.32	3.44	93	t_3	0.48	4.03	96
Specimen 1_4				Specimen 2_4				Specimen 3_4			
t_1	0.22	3.28	104	t_1	0.33	3.22	101	t_1	0.52	4.12	114
t_2	0.20	3.29	126	t_2	0.34	3.41	106	t_2	0.54	4.12	103
t_3	0.21	2.93	105	t_3	0.34	3.27	106	t_3	0.53	4.21	105
Averaged				Averaged				Averaged			
t_1	0.23	2.98	113	t_1	0.32	3.32	100	t_1	0.50	4.07	105
t_2	0.22	3.10	118	t_2	0.31	3.26	103	t_2	0.51	4.09	102
t_3	0.23	2.92	114	t_3	0.32	3.34	99	t_3	0.51	4.06	97

Table 7.3 Averaged nominal moduli and strain rates obtained from VFM 2 on the EPDM rubber with the relaxation times ($t_{1,2,3}$) at three given pre-strains.

$e_{x,\mathrm{p}0}^{\mathrm{intended}} = 0.2$				$e_{x,\mathrm{p}0}^{\mathrm{intended}} = 0.3$				$e_{x,\mathrm{p}0}^{\mathrm{intended}} = 0.4$			
Relaxation time	$e_{x,\mathrm{p}0}$	*NE* (MPa)	$\dot{\varepsilon}_x$	Relaxation time	$e_{x,\mathrm{p}0}$	*NE* (MPa)	$\dot{\varepsilon}_x$	Relaxation time	$e_{x,\mathrm{p}0}$	*NE* (MPa)	$\dot{\varepsilon}_x$
t_1	0.22	15.8	85	t_1	0.28	14.2	83	t_1	0.41	13.4	84
	0.21	15.6	80		0.31	15.0	81		0.43	11.9	84
	0.20	16.0	81		0.28	14.9	71		0.42	12.0	75
	0.23	15.4	82		0.27	14.9	72		0.42	12.2	81
t_2	0.22	14.9	80	t_2	0.29	15.6	78	t_2	0.39	11.5	91
	0.22	16.8	80		0.29	13.8	81		0.40	13.8	78
	0.21	15.2	79		0.28	13.5	71		0.41	13.1	71
	0.23	16.4	82		0.28	15.0	76		0.43	12.7	76
t_3	0.21	14.6	83	t_3	0.28	15.5	79	t_3	0.41	12.2	84
	0.22	17.0	79		0.30	14.6	79		0.42	12.1	78
	0.23	16.5	84		0.28	14.8	70		0.42	13.9	78
	0.21	15.6	81		0.27	14.0	80		0.42	13.0	75
Averaged				Averaged				Averaged			
t_1	0.22	15.7	82	t_1	0.29	14.7	77	t_1	0.42	12.4	81
t_2	0.22	15.8	80	t_2	0.29	14.5	77	t_2	0.41	12.8	79
t_3	0.22	15.9	82	t_3	0.28	14.7	77	t_3	0.42	12.8	79

Mullin's effect can be exhibited, causing a softening at lower or similar strain. Therefore, new EPDM specimens were used for every experiments. The result of these repetition test is given in Table 7.3, in which it can be seen that no strong relation is found between the relaxation times and the identifications.

7.5.2 Comparison to data from compressive Hopkinson bar

The Ogden parameters (μ = 0.85 MPa, α = 4.91) of the silicone rubber obtained from VFM 2 were used to reconstruct its true stress-strain curve in compression to compare it with data obtained from dynamic compression experiments. Although it is known that the identification of hyperelastic model parameters is affected by strain states exhibited during the test (Gendy and Saleeb, 2000), their overall behaviour should be comparable over a similar range of strains. In order to provide other set of Ogden parameters at a higher strain rate, the nonlinear VFM and the gas-gun experiments introduced in Chapter 6 were applied to the same silicone rubber and the Ogden parameters were obtained as μ = 0.99 MPa, α = 4.97 at a strain rate of 350 s^{-1}. For the comparison with these tension data, a dynamic compression test was performed using the split Hopkinson compression bar (titanium alloy) equipped with piezoelectric stress gauges at the bar-specimen interface, lead zirconium titanate (PZT). One of the benefit of using of a piezoelectric sensor on the SHPB is high signal to noise ratio in force measurements on soft materials (Chen et al., 2000), furthermore, direct measurements at both faces of the specimen allow static equilibrium to be confirmed. The modified SHPB apparatus employed in this study was previously used for dynamic test experiments on HTPB (hydroxyl terminated polybutadiene) rubber and described in a previous paper (Kendall et al., 2014). The same experimental procedure was performed except that in the present experiments, the strain was calculated by measuring the displacements of the bar-specimen interface by means of the high speed imaging and DIC; this procedure is briefly explained below. This

comparison study was performed only on the silicone rubber because it is possible to manufacture a cylindrical-shaped specimen (diameter = 8 mm, length = 4 mm) for this rubber.

It was difficult to measure such large strains in Figure 7.10(a) using the gauge signal because of the wave reflection and overlapping during the dynamic deformations; unfortunately a longer Hopkinson bar system, which would have eliminated this problem,

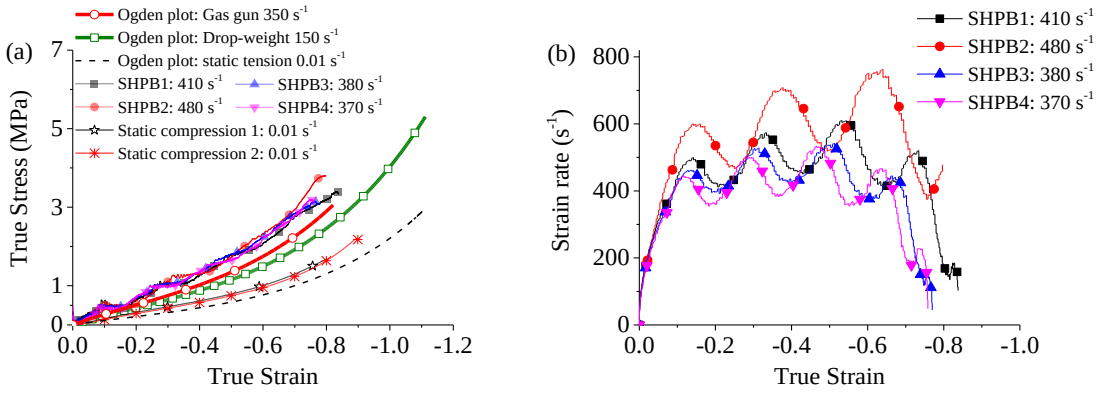

Figure 7.10 (a) Dynamic stress-strain curves in compression of the pure silicone rubber from split Hopkinson compression bar tests (SHPB1-4), two uniaxial compressible quasi-static tests and the one-term Ogden plots obtained from: VFM2 shown in Figure 7.7 and the previous uniaxial tensile quasi-static test in Chapter 5 and the gas-gun test with the application of the nonlinear VFM; (b) true strain rates profiles versus true strains for each SHPB test.

Figure 7.11 High speed imaging on the modified SHPB: the printed speckle pattern is attached on the surface of the bars near the PZT sensors, a silicone rubber specimen sits in the middle.

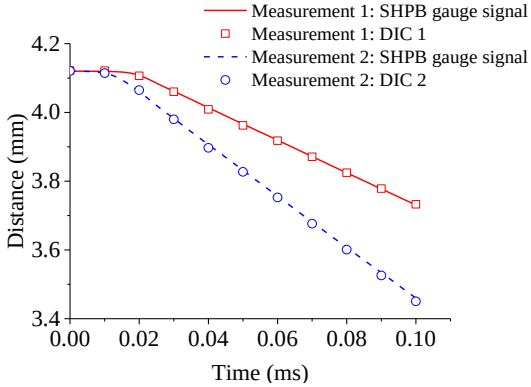

Figure 7.12 Comparisons of the bar distance measurement obtained from the strain gauge signal and the DIC.

was not available. For this reason, the strain measurements were achieved by means of high speed imaging (100 000 fps) in the vicinity of the bar interface. The bar interface is shown in one of the high-speed images, Figure 7.11, showing digital speckle patterns (Speckle Generator, Correlated Solutions, Inc.) printed on a paper and attached to the incident and transmitted bar surfaces. The displacement fields over the patterns dictated by the bar moment were obtained by the DIC method using the same analysis software. It is assumed that the averaged value over the displacement fields is the same as the actual bar interface movement. The subtraction of the two averaged displacements produced the bar distances, and these data were used for the strain calculation. Figure 7.12 shows the comparison of the bar distances measured by the gauge signal and the DIC method. The impacting speed (measurement 1 and 2: $\dot{\varepsilon}_x \approx$ 1200 and 1700 s^{-1}) were much faster than the actual tests of Figure 7.11 in order to generate clear gauge signals. The time period in Figure 7.12 is approximately the initial incident wave period. As can be seen in this figure, the measurements of the bar distances from the gauge signal and the DIC method are well matched.

In Figure 7.10(a), the thick green (empty square symbol) profile is a stress curve reconstructed by the Ogden parameter obtained from the drop-weight test with VFM 2 on the silicone rubber. This stress curve is plotted by the uniaxial one-term Ogden equation up to a strain range of the final pre-strain amount. The final engineering pre-stretching was $e_{x,\mathrm{p0}} = 0.67$. This tension value is taken as the final compressive engineering strain by making it negative and, thus, the final true compressive strain is approximated as -1.11. In the same way, the Ogden parameter obtained by the nonlinear VFM is used to plot the stress-strain curve, which is the thick red (empty circular symbol) profile Figure 7.10(a). There are four stress-strain curves from the SHPB tests, their strain rate profiles versus strains are given in Figure 7.10(b). The strain rates of the SHPB tests given in the legend

are averaged values of these profiles up to the largest strain-rate peaks. The fluctuation in the strain rates is due to the fact that the whole deformations of the SHPB tests were produced by a multiple wave reflection in the incident bar. The wave overlap is no longer a concern as the stress and strain data were measured respectively by the PZT sensor and DIC analysis. The curve denoted as "Ogden plot: static tension" is obtained from the Ogden parameters (μ = 0.42 MPa, α = 5.25) from the quasi-static tension test at 0.01 s^{-1} shown in Figure 5.1 in Chapter 5; the two compressive quasi-static curves at the same strain rate were obtained using the same commercial testing apparatus and the same dimensions as the SHPB test. The strain measurement for this quasi-static test in compression was conducted by a clip-on style extensometer which was attached in the vicinity of the compression platens.

Figure 7.10(a) shows that the reconstructed curves of the drop-weight and gas-gun tests are reasonably comparable to the one from the SHPB tests up to a true strain of about 0.3, after which the SHPB curves exhibit larger strain hardening. A similar trend is observed between the static curves where the stress-strain curves from the compressive test is stiffer. The stiffer behaviour in compression can be caused by the lateral friction between the sample and the platens. With regard to this issue, Bechir et al. (2006) have shown that Poisson's ratio measured (on the specimen surface) during compressive tests was much lower than the tension case in spite of using a low viscosity lubricant, and they have presented a test result showing the same trend as in Figure 7.11(a); Day and Miller (2000) presented FEM simulations showing that even small levels of lateral friction can significantly influence the stress measurement, i.e. stiffer measurement from higher levels of the friction. If it is assumed that the levels of the lateral friction in the SHPB and quasi-static tests are similar, the deviation level between the SHPB and the dynamic VFM should be similar to that of the quasi-static case. The stress curve obtained from the SHPB

at 370 s^{-1} is over a similar strain rate range to the gas-gun test (350 s^{-1}). The deviation between them should be close to that of the quasi-static curves, e.g. the deviation level between 'Static compression 2' and the reconstructed quasi-static curve. It should be mentioned that for the specimens used for the quasi-static compression and SHPB tests, a thin layer of Vaseline was applied on the both surfaces.

The deviation level can be quantified by the coefficient of friction between the specimen and the metal platen. The quantification of the deviation was studied by FEM simulations which were conducted in the following way. Using ABAQUS, a rubber specimen was modelled with similar dimensions of that used for the SHPB and quasi-static compression tests (diameter = 8 mm, length = 4 mm). The specimen was meshed with an 8-node linear brick (reduced integration) and an element size of 0.5 mm. The one-term Ogden model was applied with the parameters obtained from the quasi-static tension test (μ = 0.42 MPa, α = 5.25). Two platens were also modelled with the dimensions of 16 mm diameter and 3 mm thickness and meshed with the same element type but 2 mm element size. The material of the platens was assumed to be a general steel alloy with the linear elastic parameters of E = 200 GPa, ν = 0.3. A static simulation was conducted, in which one of the faces of the cylindrical geometry was compressed by the platen with the final displacement of 18 mm, and the other face was supported by the fixed platen. The nodal values of reaction forces obtained from the contacted surface of the movable platen were extracted, and the sum of these values were divided by the initial surface area of the specimen in order to calculate the engineering stress. The corresponding engineering strains were simply obtained by dividing the displacement by the initial length of the specimen; the true strains were assumed to be the logarithmic one. The contact between the specimen and platens was defined by surface-to-surface contact and coefficients of lateral friction, γ.

When the coefficient of friction was set to zero and the Ogden parameters of the quasi-static tension were applied, the true stress-strain curve (square symbol) obtained from the current simulation is coincident with the analytically plotted curve (black dashed line) with the same parameters as shown in Figure 7.13(a). The coefficient of friction was iteratively increased until the stiffer curve as a result of the higher friction is well matched with the curve of the quasi-static compression test. The objective function for this match was given as

$$\sum_{i=1}^{n}\left[\sigma_x^{FEM}\left(\varepsilon_i,\gamma\right)-\sigma_x^{Exp}\left(\varepsilon_i\right)\right]^2=0 \tag{7.18}$$

The minimization of this objective function was conducted using MATLAB and its built-in function *fmincon*, with uncertainty values of 0 to 0.5 for the coefficient. The simulation explained above was called by MATALB and the coefficient was provided to ABAQUS. As a result of the present method, the coefficient of friction was optimized as 0.11 and the stress-strain curve obtained from the simulation with this coefficient is shown in Figure 7.13(a) as a triangle symbol scatter, which is close to the curve of the quasi-static compression test. It is found that this coefficient is within the range of 0.09 to 0.2 that was reported in a previous study where the coefficient of friction between a lubricated rubber and steel sphere was studied (Greenwood and Tabor, 1958). The same simulation

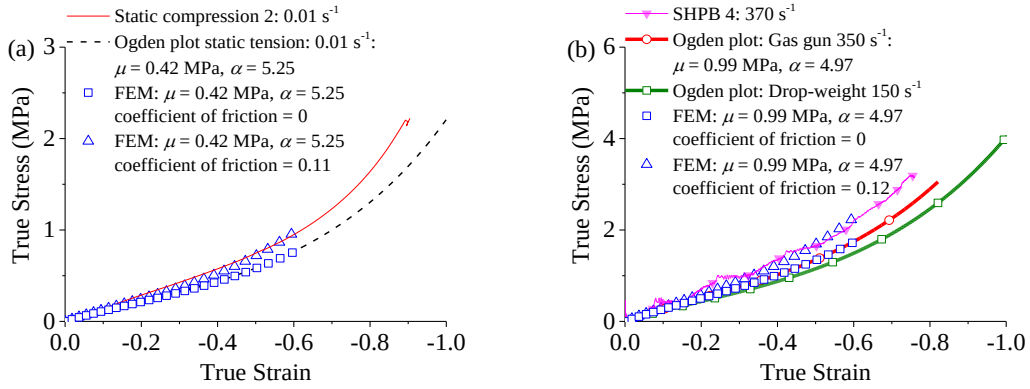

Figure 7.13 Re-plotted true stress-strain curves from Figure 7.10(a) respectively for (a) the quasi-static and (b) the dynamic cases; in each figure, the scatter (triangle and square symbols) lines represent the true stress-strain curves obtained from the FEM simulations with the effect of friction.

study was conducted for the case of the dynamic experiments. The Ogden parameters (μ = 0.99 MPa, α = 4.97) of the gas-gun experiment were given to the simulation, and the coefficient was iteratively updated until the resultant stress-strain curve was matched with that of the SHPB 4 test. The coefficient value was obtained as 0.12, and its corresponding stress curve is shown in Figure 7.13(b). The coefficients between the quasi-static and dynamic cases are comparable. That is, the deviation levels of both the quasi-static and dynamic cases can be quantified by almost the same value of the coefficient. As shown in Figure 7.13, it can be seen that the stress measurement of soft materials is sensitive even to such small values of the coefficient of friction. This result may indicate that the stiffer measurement of the compression tests could be induced by the lateral friction. This study is not to show how to exactly correct the compressive test data but to describe the possible reason of the stiffer measurements, which can be identically applied to both the quasi-static and dynamic cases.

7.6 Summary

A modification was proposed to the linear VFM presented in Chapter 4 and Chapter 5. This previous VFM procedure, here referred to as VFM 1, requires a static force measurement after applying pre-stretching. In the current chapter, it is found that the application of the incremental equation of motion for constructing the principle of virtual work equation leads to the removal of the pre-force requirement. This new VFM procedure is denoted as VFM 2 or 3 in this chapter. The same simulation study was conducted to evaluate the identification capability of this new method. The simulation work shows that the qualities of the parameter identifications of the old and new VFMs were almost identical where pure simulation data were used. Further simulation works were performed in order to see the effect of expected noise source on experimental data such as displacement field and pre-force & strain measurements. This noise study reveals

that the identification quality of VFM 1 was more sensitive to all noise sources. In particular, when the underestimation of the pre-force measurement was added, the identified parameters from VFM 1 produced a downward deviation of the stress-strain curve relative to a reference produced by the given parameters, at large strain. This observation is expected due to the fact that the pre-force measurement is likely to be underestimated because of stress relaxation after pre-stretching.

Dynamic test data from the silicone and EPDM rubbers shown in the previous chapters were applied to the new VFM (VFM 2) with the use of the one-term Ogden model. It is observed that the true stress-strain curves from VFM 2 are slightly stiffer at large strain than those from the old VFM. It is speculated that this identification difference between the old and new VFMs is caused by the underestimation of the pre-force measurements used for the old VFM as the similar tendency is shown in the simulation work. A repetition test of the drop-weight experiment was conducted on the same rubbers to see the effect of relaxation on the new VFM. The test results show the relaxation time does not have a strong influence on the identification of the new VFM. The parameters of the one-term Ogden model from the new VFM on a silicone rubber were used to reconstruct the true stress-strain curve in compression. These data were compared with other stress-strain curves measured by the split Hopkinson bar (equipped with PZT sensors) in compression on the same material at similar strain-rate ranges. It is found that the stress-strain curves from these two methods are comparable.

Chapter 8 FURTHER APPLICATIONS OF THE VFM

8.1 Introduction

In the present chapter, further applications of the VFMs introduced in the previous chapters are described. This chapter is divided into two parts. The first part describes the application of a new VFM by which the shape of a nonlinear stress-strain curve can be approximated. This new method could be a supporting technique in situations when it is difficult to identify a suitable constitutive model to be assumed in the optimization procedure, e.g. Eq. (7.15), of the linear VFM. In most of the previous chapters, the one-term Ogden model was adopted in the optimization procedure as the quasi-static stress-strain curves of the silicone and EPDM rubbers were well described by this model. This assumption is based on the observation in previous papers (Pouriayevali et al., 2012; Shergold et al., 2006; Song and Chen, 2003) that these two rubbers exhibit similar shapes for their stress-strain curves between quasi-static and medium strain rates ($\dot{\varepsilon} < 1000\ \mathrm{s}^{-1}$). However, this assumption may not be valid for other rubbers, the stress-strain curve of which has various shapes at different strain rates. Moreover, even if the loading rate is the same, the shape can be also different at different temperatures (Lion, 1997). The actual shape of the stress-strain curve is unknown until it is measured for a particular condition. The VFM procedure proposed in the first part of this chapter is based on the two previous techniques: the nonlinear VFM (Chapter 6) and the incremental VFM (Chapter 7). The combination of these two methods provides an identification of the shape of the stress-strain curve. The observation of the curve shape obtained from this technique can give an opportunity to evaluate the suitability of a chosen nonlinear constitutive model used in the optimization procedure. The first part starts with the quasi-static test in tension on a new material (nitrile rubber), the stress-strain curve of which was clearly described by the two-term, but not the one-term Ogden model. The two-term Ogden model and its

parameters obtained from this quasi-static experiment were adopted in the same simulation work as shown in Chapter 7. The new VFM was applied to this simulation data, and the identification procedure of the curve shape is described. For comparison, the two-term Mooney-Rivlin model was also adopted for this simulation procedure. The same drop-weight experiment was conducted on the new rubber. The experimental data were analysed by means of the new VFM technique with regard to the shape of the stress-strain curve. In order to show the case that the curve shape can change at a fixed loading rate at different temperatures, a new experimental device is introduced to vary the specimen temperature between 9 to 60 °C.

The second part of this chapter presents the application of the nonlinear VFM to the linear viscoelastic behaviour of rubbers. The idea of the dynamic VFMs presented in the previous chapters is based on the utilization of the acceleration field, which is clearly generated when specimens are subjected to a non-uniform deformation. This means that the whole data field, including strain, displacement and acceleration, varies during the non-uniform deformations. This data variation can also include strain rate fields, although in the previous chapters the strain rate for a particular drop-weight test was obtained by spatially averaging it for each time step. The existence of the variation of strain rate could give more information than the previous cases where a rate-independent model was applied. Moreover, in the previous drop-weight experiments, only the initial loading period was adopted for the analysis of the linear VFM; in fact, multiple reloading was available from a single drop-weight experiment, which overall explored a larger deformation range. The multiple reloading data can allow consideration of the stress-strain nonlinearity and, simultaneously, the rate-dependent behaviour, i.e. viscoelastic characteristics. Using these two observations: (1) strain rate variation during a particular loading step and (2) multiple reloading data, the linear viscoelastic model was utilized in

the framework of the nonlinear VFM. Few previous studies have explored the application of the VFM for the viscoelastic behaviour of soft materials. Sasso et al. (2013) utilized the nonlinear VFM in order to identify several inelastic behaviours of a rubber but the parameters of a viscoelastic model (Prony series) was separately calibrated out from the VFM technique. Connesson et al (2015) have shown that the dynamic VFM (linear VFM) was able to identify the viscoelastic parameters based on a frequency scale for a soft biological material. Here, the application of the nonlinear VFM to the viscoelastic behaviour is to identify the parameters of the Prony series model, Eq. (2.20). The viscoelastic behaviour which can be exhibited during the drop-weight experiment is limited by the time scale of the total data and also the imaging speed. In order to extend this limitation, a temperature controlling device was used for the drop-weight experiment so that each relaxation curve constructed by the Prony parameters obtained from different temperatures can be shifted using the principle of time-temperature superposition. The second part starts with the description of the DMA data and relaxation curves of the nitrile and silicone rubber. The Prony model was fitted to these two relaxation curves to obtain their parameters. The obtained parameters were applied to the same simulation work as in the first part but without pre-stretching. Simulation data were analysed by the nonlinear VFM to identify the relaxation curve at a particular temperature. Each relaxation curve was shifted to build a master curve, which was then compared to the given relaxation behaviour. The same analysis procedure was applied to the actual drop-weight experiment data of nitrile and silicone rubber. Their reconstructed relaxation curves were compared to the one obtained from the DMA technique.

The objectives of the first part of this chapter can be summarized as follows:

- There is a brief description of the situation where a prior assumption of a constitutive model in the VFM procedure leads to poor constitutive model fitting.
- In order to resolve this limitation of the VFM, the combined linear and nonlinear VFM is introduced. The application procedure is explained with regard to the purpose of this method, by which possible complex nonlinear stress-strain curves are approximated by means of a simple one-term Ogden model.
- The combined method is applied to FEM simulation data to show its identification capability. Also, the simulation includes a viscoelastic model in order to explain why the present simulation is to approximate a stress-strain curve, not to characterize it at a particular strain rate. The same procedure is used to analyse experimental data produced by the drop-weight experiment.

The objectives of the second part are listed as below

- In the second part, silicone and nitrile rubbers are used as test specimens. Their relaxation behaviours are obtained by dynamic mechanical analysis. These results are used for FEM simulation and the comparison with the identification result of the nonlinear VFM introduced in the second part.
- The nonlinear VFM is re-described in order to introduce the linear viscoelastic model (Prony series) into the PVW equation.
- FEM simulations are conducted as similarly shown in Chapter 5 but the loading period is much longer so that a relaxation behaviour for a certain period can be captured. The simulation data is applied to the nonlinear VFM; the identified relaxation behaviour is compared with the DMA data given to the simulation.

- The identified result obtained from a single dynamic loading, which can be produced by the drop-weight apparatus, represents the relaxation behaviour only over a short period of time. One possible way to extend the time scale of the relaxation behaviour is introduced, in which time temperature superposition is adopted. The application procedure of this method is described with FEM simulation.
- Based on the description of the present nonlinear VFM in the simulation part, actual experimental data produced from the drop-weight test are analysed; the identification results are compared with the DMA relaxation data of the silicone and nitrile rubbers.

8.2 Estimation of the shape of a stress-strain curve

8.2.1 Quasi-static test of a nitrile rubber

A commercial nitrile rubber sheet (Coru118, Coruba) of 1 mm thickness used. The density of this rubber was measured as 1480 kg m^{-3}. The experimental procedure presented in Section 6.4.1 was used; the specimens were cut in the same dimensions and loaded in tension at 0.01 and 0.001 s^{-1}, and strains were measured by a USB camera and DIC analysis. Nominal stress-strain curves are shown in Figure 8.1.

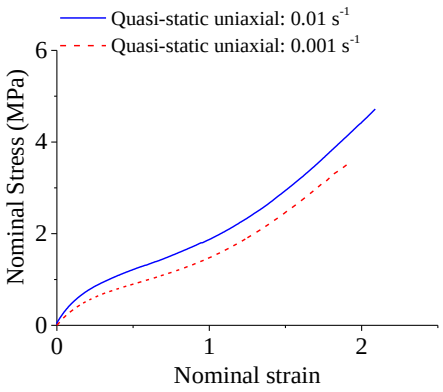

Figure 8.1 Uniaxial true stress-strain curves from the quasi-static tension tests at 0.01 and 0.001 s^{-1}.

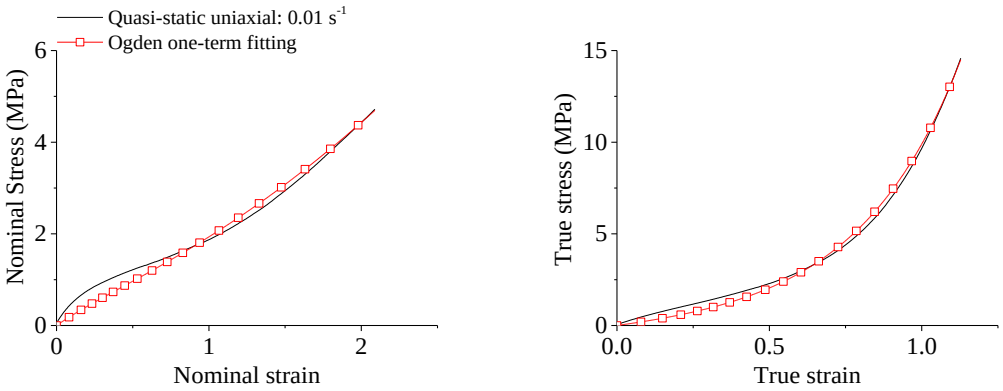

Figure 8.2 One-term Ogden model fitting on the stress-strain curve of 0.01 s^{-1} (left: nominal curve, right: true curve).

The stress-strain curve at 0.01 s^{-1} was fitted by the procedure presented in Section 5.2.2. The first fitting was conducted with the uniaxial stress-strain equation from the one-term Ogden model, Eq. (5.3), and the optimized parameters, μ = 0.78 MPa and α = 2.95. The fitting results are shown in Figure 8.2. It seems that the one-term Ogden model fairly well describes the overall concave upward behaviour. However, it can be observed that the fitted and experimental curves are not well matched during the initial loading stage (e_x < 1). It seems that the one-term Ogden model is not sufficient to describe a stress-strain curve in which there is a significant change in the tangent slope; the tangent slope of the nominal curve decreases until a nominal strain of 0.5 and starts to increase after about 0.8 strain.

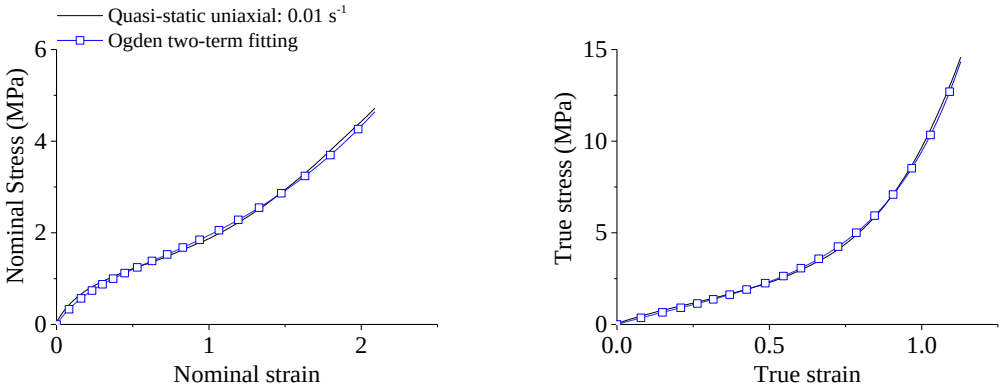

Figure 8.3 Two-term Ogden model fitting on the stress-strain curve of 0.01 s^{-1} (left: nominal curve, right: true curve).

The same fitting procedure was conducted but with the uniaxial stress equation from the two-term Ogden model

$$N_x^{Ogden} = \frac{2\mu_1}{\alpha_1}\left(\lambda_x^{\alpha_1-1} - \lambda_x^{-1-0.5\alpha_1}\right) + \frac{2\mu_2}{\alpha_2}\left(\lambda_x^{\alpha_2-1} - \lambda_x^{-1-0.5\alpha_2}\right) \quad (8.1)$$

The optimized parameters are obtained as μ_1 = 0.10 MPa, α_1 = 4.66, μ_1 = 1.51 MPa and α_2 = -3.62. The reconstructed stress-strain curve from these parameters is shown in Figure 8.3. It can be clearly observed that the two-term model is able to describe the increasing and decreasing tangent slope respectively of the initial and later loading stage of the actual experimental data. Comparison between Figure 8.2 and Figure 8.3 indicates that if the actual material behaviour in the drop-weight test is as presented, the assumption of the one-term Ogden model for the optimization procedure, Eq. (7.15), will produce parameters that are not able to completely describe the actual behaviour. The good fitting result of the two-term model to the quasi-static experimental data does not mean that the assumption of this model in the optimization procedure is validated. The shape of the stress-strain curve can change at different strain rates or temperatures. With regard to this difficulty, in the next section, one possible way to approximate the curve shape is introduced.

8.2.2 Combination of the linear and nonlinear VFM

The linear (dynamic) VFM introduced in Chapter 5 and Chapter 7 is a method to identify Young's (VFM 1) or nominal instantaneous modulus (VFM 2). In the PVW, the linear elastic constitutive equation is adopted with the assumption that this model is sufficient to describe the mechanical behaviour of rubbers at a particular time step, but not for long deformation histories. The use of the linear elastic model is one advantage of the linear VFM as there is no need of the assumption of a constitutive model in the PVW regardless of the actual behaviour of rubbers. However, as mentioned above, the assumption of a constitutive model is required in the optimization procedure. The

nonlinear VFM introduced in Chapter 6 requires the assumption of the nonlinear model in its PVW equation, which can be used to build the objective function for the identification of the parameters of that model. One advantage of the nonlinear VFM is that not only the entire nonlinearity exhibited during long deformation histories but also the possible nonlinearity within a particular time step can be considered simultaneously. Again, the assumption of a nonlinear constitutive model in the PVW without the knowledge of the actual curve shape can be its disadvantage.

The new VFM to approximate the shape of a stress-strain curve is based on the idea of the combination of the two advantages respectively from the linear and nonlinear VFMs. Thus, the combination of these two VFMs will lead to the identification of the curve shape without the consideration of the choice of a constitutive model and with the consideration

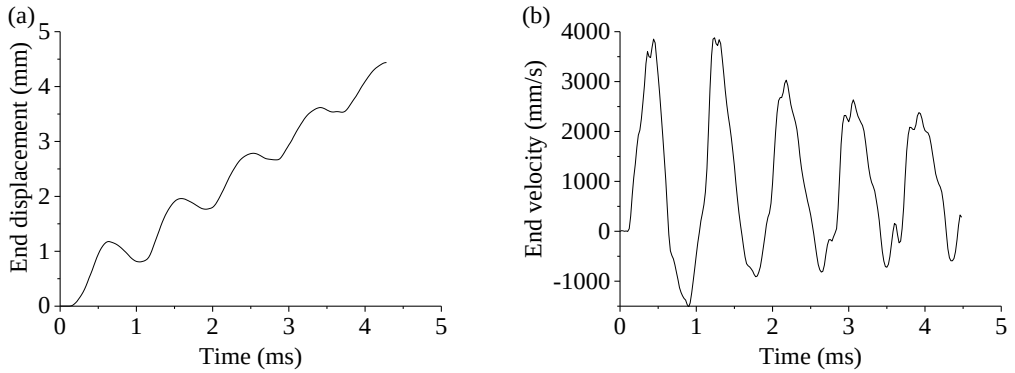

Figure 8.4 (a) End displacement and (b) velocity profile of the drop-weight test on a nitrile rubber.

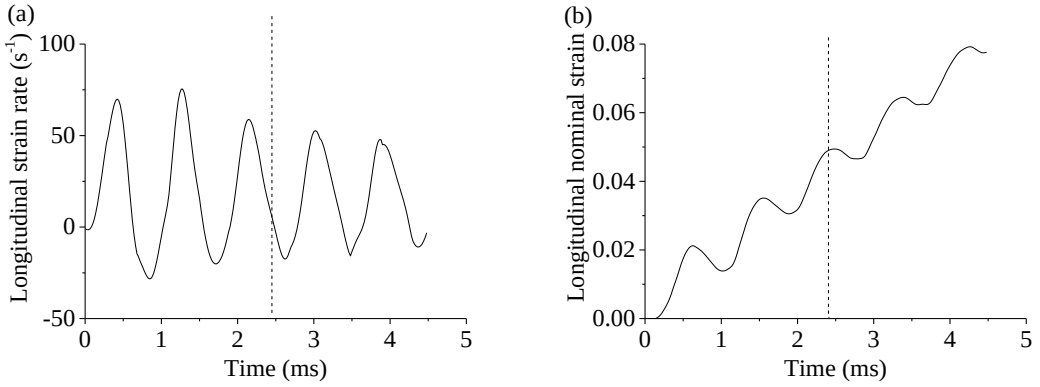

Figure 8.5 (a) Global averaged strain rate and (b) strain profiles in the longitudinal direction (the dash line indicates the deformation range applied in the new VFM).

of the nonlinearity exhibited during a certain deformation range.

The meaning of this certain deformation range is explained here. In the previous section, the linear VFM was applied to the deformation data during the initial loading period. Then, the identified moduli at each time step was averaged to obtain the mean value. In fact, after the first loading from the drop-weight apparatus, there are multiple reloadings on a specimen due to the wave reverberation within the long loading bar, and the high-speed camera is able to capture these multiple deformations. The longitudinal displacement profile obtained from the end of a nitrile rubber tested for the present drop-weight experiment (non-pre-stretching case at room temperature) is shown in Figure 8.4(a), and Figure 8.4(b) shows its velocity profile calculated by the simple finite difference equation

$$v_x(t) = \frac{u_x(t_{i+1}) - u_x(t_{i-1})}{2\Delta t} \tag{8.2}$$

The detailed experimental procedure is given in a later section but the overall procedure was identical to that conducted in the previous chapter. For the simulation work, which will be described later in this section, the velocity boundary condition shown in Figure 8.4(b) was applied. From the experimental data, the averaged (longitudinal) strain rate profile was also obtained by averaging the whole spatial strain rate field, which was acquired in the way used in Chapter 5; the profile is presented in Figure 8.5. It should be noted that the averaged strain rate in this figure and the one shown in the previous chapters are different because the previous one was obtained by spatial averaging only over the deformed area, which has been subjected to the stress wave. As can be seen in Figure 8.5(a), after the second strain-rate peak (at around 1.3 ms), the peaks start to reduce in amplitude. In order to provide reasonably uniform strain rate peaks from each loading period to the new VFM, the deformation range was chosen as indicated by the dashed

line in Figure 8.5. The same procedure was applied to the deformation range used in the new VFM for all experiments and simulations.

The assumption made in the VFM analysis described here is that a part of any stress-strain curve, which is long enough to describe a part of the nonlinearity but limited by the deformation range defined above, can be expressed by the one-term Ogden model. In other words, it is assumed that the part of the stress-strain curve in Figure 8.1, for example a nominal strain range of 0 to 0.05 (as indicated by the dash line in Figure 8.5(b)), can be described well by the one-term Ogden model, even though this is not sufficient to describe the whole stress-strain curve. Also, if a static pre-stretching is applied, e.g. 0.1 of a nominal strain, it can be assumed that the nonlinearity during the short strain range of 0.1 to 0.15 is well expressed by the one-term Ogden model. Using this assumption, the PVW of the present VFM for the approximation of the curve shape is taken from the same equation used in the nonlinear VFM in Chapter 6 for a non-pre-stretching case. In the present VFM procedure, it is assumed that the principal directions and experiment coordinates are coincident; thus, Eq. (6.4) is adopted and here rewritten again with the one-term Ogden model below

$$\Phi = \sum_{k=1}^{n_{[1]}} \left[\int_{S_0} \left(-\frac{1}{\lambda_x} \frac{2\mu_{[1]}}{\alpha_{[1]}} \lambda_z^{\alpha} + \frac{2\mu_{[1]}}{\alpha_{[1]}} \lambda_x^{\alpha-1} \right) \frac{\partial u_{x,0}^*}{\partial x_0} \, \mathrm{d}S_0 + \int_{S_0} \rho a_x(t_k) u_{x,0}^* \, \mathrm{d}S_0 \right]^2 \tag{8.3}$$

where $n_{[1]}$ indicates the final time step of the deformation range of a non-pre-stretching case. The subscript [1] of the model parameters represents that these are the parameters of a non-pre-stretching case. The calculation of this PVW can be identically conducted as explained in Chapter 6. For pre-stretching cases, the incremental VFM (VFM 2) introduced in Chapter 7 is adopted. The PVW of VFM 2 is recalled here again with the expansion of $\mathrm{dN}_{x,\mathrm{p0}}$

$$-\int_{s_{\mathrm{p}0}} \lambda_{x,\mathrm{p}0} \frac{\partial^2 W}{\partial \lambda_x^2}(t)\mathrm{d}\lambda_{x,\mathrm{p}}(t) \frac{\partial u_{x,\mathrm{p}0}^{*(1)}}{\partial x_{\mathrm{p}0}} \, \mathrm{d}s_{\mathrm{p}0} = \int_{s_{\mathrm{p}0}} \rho a_x(t) u_{x,\mathrm{p}0}^{*(1)} \, \mathrm{d}s_{\mathrm{p}0} \tag{8.4}$$

This equation can be converted to the form of the nonlinear VFM with the use of the definition of $\partial^2 W/\partial \lambda_x^2$, Eq. (7.17):

$$\Phi = \sum_{k=1}^{n_{[i]}} \left[\int_{s_{\mathrm{p}0}} \lambda_{x,\mathrm{p}0} \frac{\partial^2 W}{\partial \lambda_x^2}(t_k)\mathrm{d}\lambda_{x,\mathrm{p}}(t_k) \frac{\partial u_{x,\mathrm{p}0}^{*(1)}}{\partial x_{\mathrm{p}0}} \, \mathrm{d}s_{\mathrm{p}0} + \int_{s_{\mathrm{p}0}} \rho a_x(t_k) u_{x,\mathrm{p}0}^{*(1)} \, \mathrm{d}s_{\mathrm{p}0} \right]^2 \tag{8.5}$$

$$\frac{\partial^2 W}{\partial \lambda_x^2}(t_k) = \frac{2\mu_{[i]}}{\alpha_{[i]}^2} \left(\alpha_{[i]} \left(1 + \frac{\alpha_{[i]}}{2} \right) \lambda_{x,\mathrm{p}}^{-2-\frac{\alpha_{[i]}}{2}}(t_k) + \alpha_{[i]} \left(-1 + \alpha_{[i]} \right) \lambda_{x,\mathrm{p}}^{-2+\alpha_{[i]}}(t_k) \right) \tag{8.6}$$

where [i] indicates each pre-stretching case. It should be noted that in Eq. (8.6) the stretch ratio term, $\lambda_{x,\mathrm{p}}$ represents the total stretch ratio that is defined in Figure 4.21 in Chapter 4. The meaning of the use of this stretch ratio term in Eq. (8.5) and (8.6) is that the part of the stress-strain curve after pre-stretching up to the given deformation range is fitted by the one-term Ogden curve defined under the same deformation range. For example, if the first pre-stretched case is generated with a nominal pre-strain of 0.05 and a final nominal strain of 0.10, the curve shape supposed to be exhibited during this deformation interval (0.05 to 0.10) is identified by the one-term Ogden model defined within the same deformation interval. Thus, the optimized parameter of a particular pre-stretched state using Eq. (8.5) and (8.6) describes the curve shape only within the deformation interval. This procedure will be clearer in the simulation section. In this section, the use of Eq. (8.4)-(8.6) is referred to as the second nonlinear VFM or NVFM 2. The application of NVFM 2 for the approximation of the curves shape is described in the next section using the simulation data resembling the drop-weight experiment.

8.2.3 Application of NVFM 2: simulation

The same 2D simulation procedure presented in Chapter 6 was used but the velocity boundary condition shown in Figure 8.4(b) was applied. The two-term Ogden model was

adopted and the optimized parameters: μ_1 = 0.10 MPa, α_1 = 1.51, μ_1 = 4.66 MPa and α_2 = -3.62, which are obtained from the model fitting shown in Section 8.2.1, were used; the density measured from the nitrile rubber was applied. The specimen dimensions (length = 50 mm and width = 14 mm) were slightly larger than in the previous cases because the drop-weight apparatus used for the present chapter was modified to be equipped with a temperature-controlling device. The same pre-stretching procedure was conducted; the final nominal pre-strain was set as 1.8 with an interval of 0.05 so that there were 37 simulations in total, including one non-pre-stretched case.

Eq. (8.4) and (8.5) were applied to the simulation data respectively of one non-pre-stretched and 36 stretched cases. In total, 37 sets of the Ogden parameters were identified; these values are shown in Figure 8.6 showing grey and black colour bars which respectively indicate the μ and α identifications at each pre-stretched state. As an example, three sets of the Ogden parameters are chosen from Figure 8.6: $\mu_{[1]}$ = 1.55 MPa & $\alpha_{[1]}$ = 0.10 at $e_{x,p0}$ = 0, $\mu_{[3]}$ = 1.27 MPa & $\alpha_{[3]}$ = 2.21 at $e_{x,p0}$ = 0.10 and $\mu_{[6]}$ = 1.27 MPa & $\alpha_{[6]}$ = 2.21 at $e_{x,p0}$ = 0.25. Their nominal stress-strain curves are presented in Figure 8.7. The red curve is the part of the one-term Ogden curve made by $\mu_{[1]}$ and $\alpha_{[1]}$, i.e. non-pre-stretched case. The final strain is defined by the deformation range as explained above. It

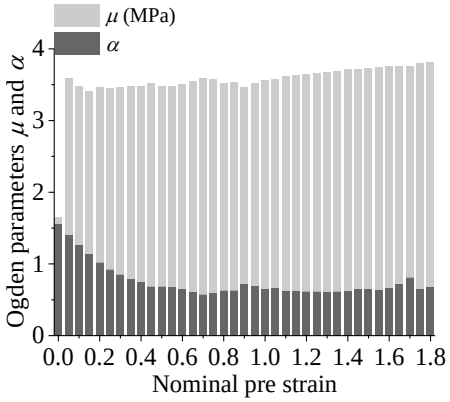

Figure 8.6 Identification of μ and α of NVFM 2 of one non-pre-stretched and 36 pre-stretched simulations.

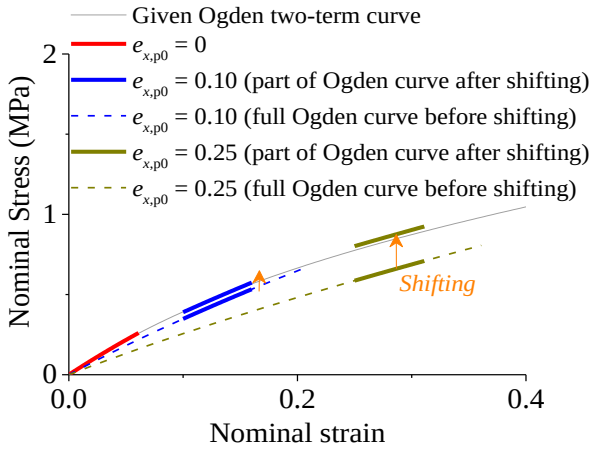

Figure 8.7 Given Ogden two-term curve and the part of the Ogden one-term curves from the chosen parameters identified by NVFM 2 at $e_{x,p0}$ = 0, 0.10 and 0.25 before and after the shifting procedure.

can be observed that the red curve is well matched with the initial part of the given two-term Ogden curve (grey solid line). The blue dash line is made with $\mu_{[3]}$ and $\alpha_{[3]}$. Clearly, this curve is not matched with the given (two-term) curve but it can be seen that the part of this blue dash line between nominal strain of 0.10 (its pre strain) and 0.16 (defined by the deformation range) has a similar curve shape as the given curve under the same strain range. The same trend can be observed on the curve (gold colour) made with $\mu_{[6]}$ and $\alpha_{[6]}$. Thus, what NVFM 2 identifies from the drop-weight simulations is the part of the curve shape of the given model within each deformation range between the pre and final strains.

In order to approximate the original curve shape from these partial one-term Ogden curves, a vertical shifting procedure is applied. The first curve of the non-pre-stretched case does not need to be shifted so it is initially fixed. Then, the next curve of $\mu_{[3]}$ and $\alpha_{[3]}$ is moved vertically by adding a stress shifting factor, $N^{[3]}_{x,\text{factor}}$, which is given by the following minimization procedure. (1) The shifting factor is initially given as

$$N^{[i]}_{x,\text{factor}} = 0 \tag{8.7}$$

(2) The nominal stresses of the fixed and shifting curves are generated by their identified parameters and the one-term Ogden uniaxial equation, f_{Ogden1}, defined by Eq. (5.3)

$$\begin{aligned}\widehat{\mathrm{N}}_{x,[\mathrm{fixed}]} &= f_{\mathrm{Ogden1}}(\mu_{[\mathrm{fixed}]}, \alpha_{[\mathrm{fixed}]}, \hat{e}_x^{[\mathrm{fixed}]}) \\ \widehat{\mathrm{N}}_{x,[\mathrm{moved}]} &= f_{\mathrm{Ogden1}}(\mu_{[\mathrm{moved}]}, \alpha_{[\mathrm{moved}]}, \hat{e}_x^{[\mathrm{moved}]})\end{aligned} \tag{8.8}$$

In these equation, $\hat{e}_x^{[i]}$ is a vector of the nominal strains from the pre-strain to the final deformation range with an interval of 0.001; similarly, $\widehat{\mathrm{N}}_{x,[i]}$ is a vector of the nominal stress generated by the model function and the strain range. (3) The given strain range and generated stress vectors are collected to form the total vector data as shown below

$$\widehat{\mathrm{N}}_x = \begin{Bmatrix} \mathrm{N}_{x,[\mathrm{fixed}]}(e_{x,1^{\mathrm{st}}}^{[\mathrm{fixed}]}) \\ \mathrm{N}_{x,[\mathrm{fixed}]}(e_{x,2^{\mathrm{nd}}}^{[\mathrm{fixed}]}) \\ \vdots \\ \mathrm{N}_{x,[\mathrm{fixed}]}(e_{x,\mathrm{final}}^{[\mathrm{fixed}]}) \\ \mathrm{N}_{x,[\mathrm{moved}]}(e_{x,1^{\mathrm{st}}}^{[\mathrm{moved}]}) + \mathrm{N}_{x,\mathrm{factor}}^{[\mathrm{moved}]} \\ \vdots \\ \mathrm{N}_{x,[\mathrm{moved}]}(e_{x,\mathrm{final}}^{[\mathrm{moved}]}) + \mathrm{N}_{x,\mathrm{factor}}^{[\mathrm{moved}]} \end{Bmatrix}, \quad \hat{e}_x = \begin{Bmatrix} e_{x,1^{\mathrm{st}}}^{[\mathrm{fixed}]} \\ e_{x,2^{nd}}^{[\mathrm{fixed}]} \\ \vdots \\ e_{x,\mathrm{final}}^{[\mathrm{fixed}]} \\ e_{x,1^{\mathrm{st}}}^{[\mathrm{moved}]} \\ \vdots \\ e_{x,\mathrm{final}}^{[\mathrm{moved}]} \end{Bmatrix} \tag{8.9}$$

(4) These collected stress and strain vectors are then fitted to the Ogden one-term uniaxial equation, Eq. (5.3), using the following objective function, in order to find the optimized parameter, μ* and α*.

$$\min_{\mu^*,\alpha^*} \Phi = \sum \left(f_{\mathrm{Ogden1}}(\mu^*, \alpha^*, \hat{e}_x) - \widehat{\mathrm{N}}_x \right)^2 \tag{8.10}$$

(5) Next, the goodness of this fitting is evaluated by the root-mean-square error, RMSE, defined as

$$\mathrm{RMSE} = \left(\mathrm{mean} \left[\sum \left(f_{\mathrm{Ogden1}}(\mu^*, \alpha^*, \hat{e}_x) - \widehat{\mathrm{N}}_x \right)^2 \right] \right)^{1/2} \tag{8.11}$$

The procedure of Eq. (8.8)-(8.11) is written as one function, which could be expressed as

$$\mathrm{RMSE} = f_{\mathrm{Ogden\_fit}}(\mu_{[\mathrm{fixed}]}, \alpha_{[\mathrm{fixed}]}, \mu_{[\mathrm{moved}]}, \alpha_{[\mathrm{moved}]}, \mathrm{N}_{x,\mathrm{factor}}) \tag{8.12}$$

(6) The last step is to find the optimized shifting factor, $\mathrm{N}_{x,\mathrm{factor}}$, giving the minimization of RMSE; this procedure can be written as

$$\min_{\mathrm{N}_{x,\mathrm{factor}}} \mathrm{RMSE} = f_{\mathrm{Ogden\_fit}}(\mu_{[\mathrm{fixed}]}, \alpha_{[\mathrm{fixed}]}, \mu_{[\mathrm{moved}]}, \alpha_{[\mathrm{moved}]}, \mathrm{N}_{x,\mathrm{factor}}) \tag{8.13}$$

The minimization procedure of Eq. (8.13) was conducted by the MATLAB built-in

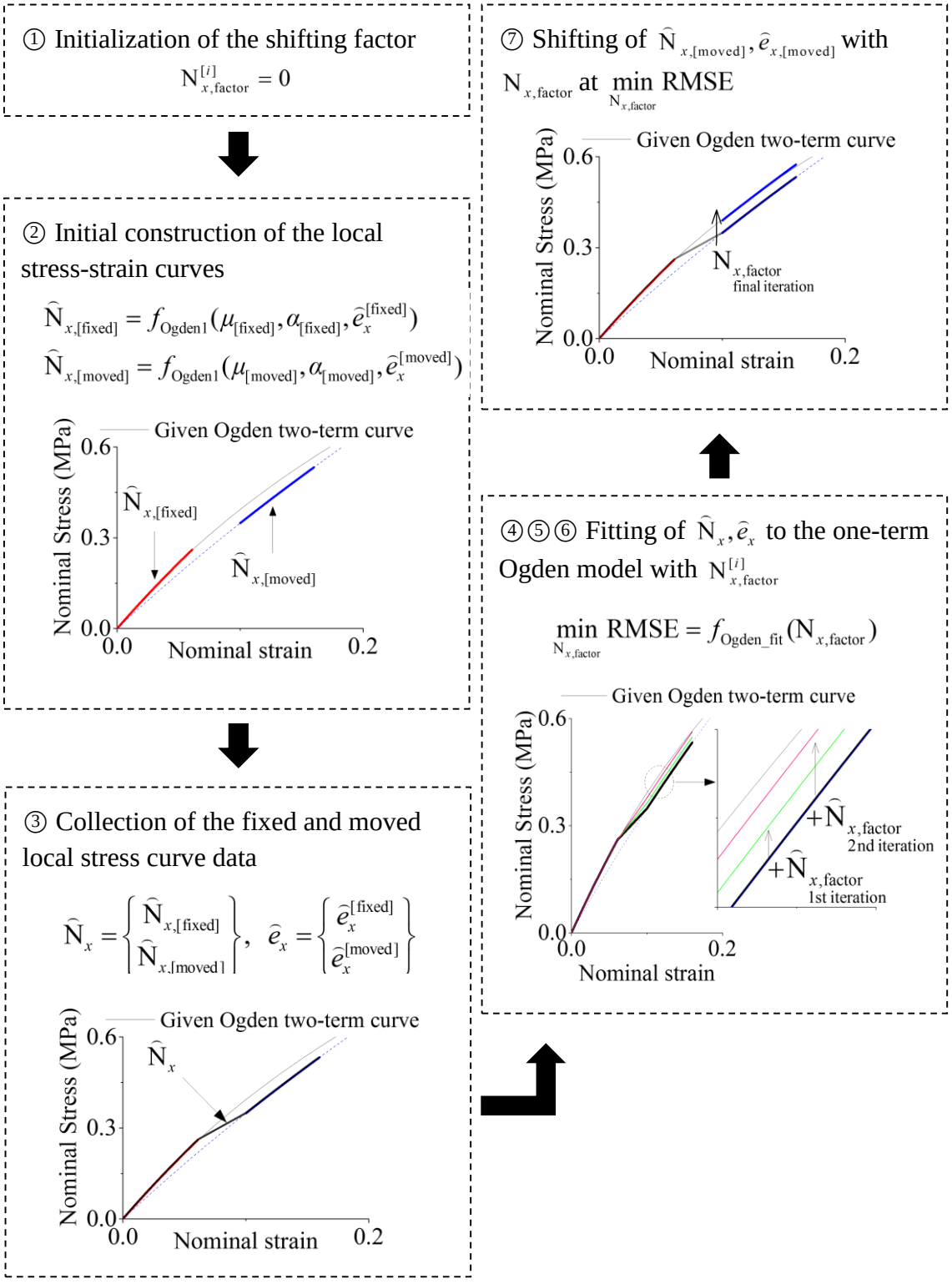

Figure 8.8 Description of the shifting procedure for a local stress curve with respect to the fixed one.

function, *fminunc*. After $\mathrm{N}_{x,\mathrm{factor}}^{[i]}$ is determined for the i^{th} pre-stretching, the shifted stress and same strain vectors become the fixed data for the next shifting procedure. For example, if $\mathrm{N}_{x,\mathrm{factor}}^{[2]}$ is obtained through the shifting procedure between the non-pre-stretching, $\widehat{\mathrm{N}}_{x,\mathrm{fixed}}^{[1]}$, and second pre-stretching cases, $\widehat{\mathrm{N}}_{x,\mathrm{moved}}^{[2]}$, the vector of $\widehat{\mathrm{N}}_{x,\mathrm{moved}}^{[2]} + \mathrm{N}_{x,\mathrm{factor}}^{[2]}$ is used as $\widehat{\mathrm{N}}_{x,\mathrm{fixed}}^{[2]}$ for the determination of $\mathrm{N}_{x,\mathrm{factor}}^{[3]}$ in order to shift $\widehat{\mathrm{N}}_{x,\mathrm{moved}}^{[3]}$. This shifting procedure is graphically described in Figure 8.8.

The Ogden parameter sets presented in Figure 8.6 were used in the shifting procedure explained above. Four shifting cases were conducted with different pre-stretching steps. For example, the first case is when all of the 47 pre-stretching simulation data are used for the shifting procedure. In the second case, it is assumed that the pre-strain interval increases to 0.10 so the shifting procedure is conducted between *i* and i+2^{th} pre-stretching data. For the third and fourth cases, 0.15 and 0.25 pre-strain intervals were respectively used. These different cases are to show the effect of the number of the pre-stretching in the identification of the curve shape.

The shifting results of these four cases are presented in Figure 8.9. The interpolated curves made by linearly connecting these shifted curves are shown together in Figure 8.10. It can be observed that the shape features of the given two-term Ogden curve, including the decreasing tangent slope at the nominal strain range of 0-0.5 and the increasing trend after about 1.0 nominal strain, are well described by all of the shifted curves. However, the degree of the exact equivalence between the given and shifted curves depends on the number of the pre-stretching steps involved in the shifting procedure as Figure 8.10 shows that the shifted curve becomes deviated upward as the step interval increased. The reason of this deviation could be because large numbers of the local shifting curves are required

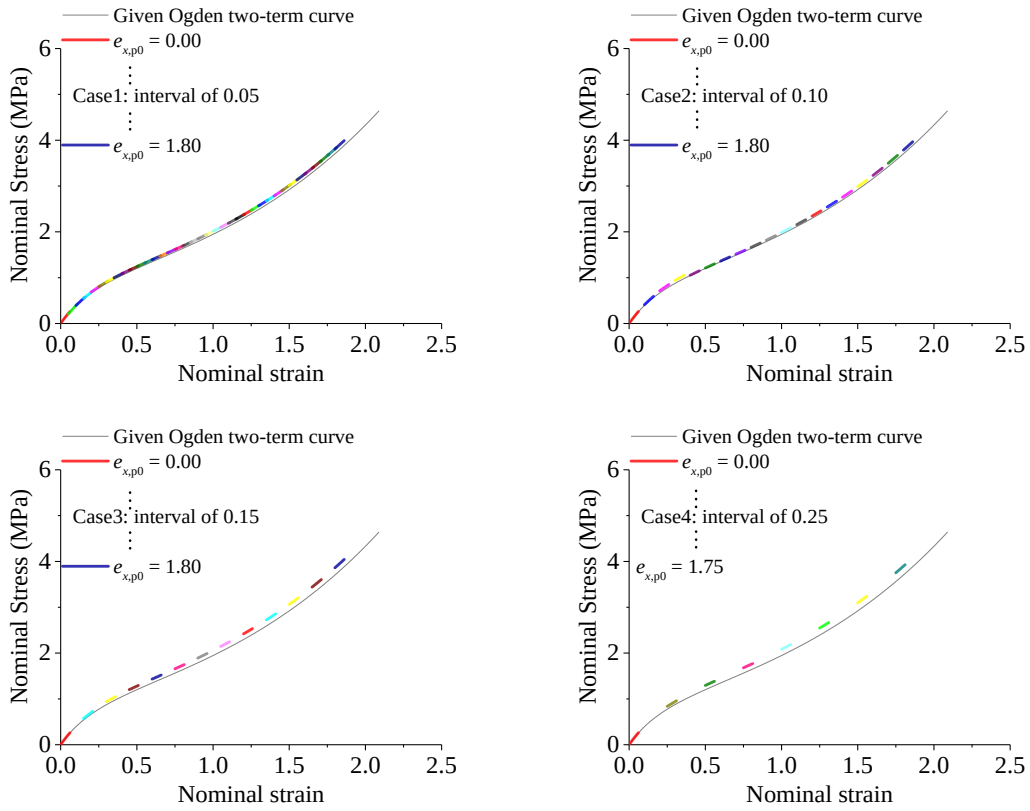

Figure 8.9 Use of the shifting procedures on the local one-term Ogden curves (small colourful curves) obtained by NVFM2 and the given two-term Ogden curves (grey solid line).

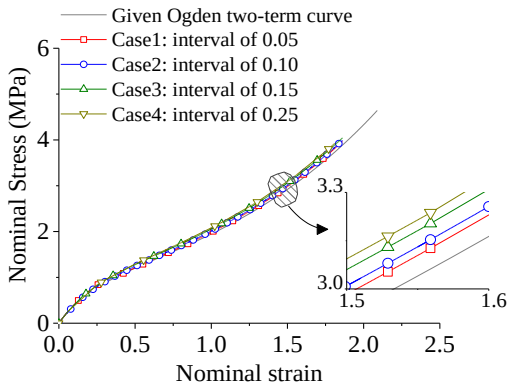

Figure 8.10 Linearly interpolated curves of the local one-term Ogden curves shown in Figure 8.9.

to produce a good fitting on the nominal strain range of 0 to 1 where the significant change in the tangent slopes is exhibited.

The same simulation study and the application of NVFM 2 and the shifting procedure were conducted with a different hyperelastic model. In order to generate a model which can show a stress-strain curve different from the given two-term Ogden model, the

second-order polynomial (second-order Mooney-Rivlin) models, Eq. (2.17) were adopted; the strain energy density is written as

$$W = C_{10}(I_1 - 3) + C_{01}(I_2 - 3) + C_{20}(I_1 - 3)^2 + C_{11}(I_1 - 3)(I_2 - 3) + C_{02}(I_2 - 3)^2 \quad (8.14)$$

This hyperelastic model is available in ABAQUS and for its five parameters, the values: (C_{11} = 0.59 (MPa), C_{01} = -3.90e-2, C_{20} = -2.84e-3, C_{11} = 7.62e-3 and C_{02}=-7.71e-4) given in a previous paper (Sasso et al., 2008) where rubber specimens were statically tested were borrowed. Their shifting results are presented in Figure 8.11. As can be observed in these figures, the current method is able to approximate the stress-strain curve made by the polynomial model for all four interval cases. Figure 8.12 shows the linearly interpolated lines for all cases; it seems that the deviation sensitivity with respect to the interval step is less than the case of the Ogden model simulation. This lower sensitivity is due to the fact that the stress-strain curve made by the present polynomial model has

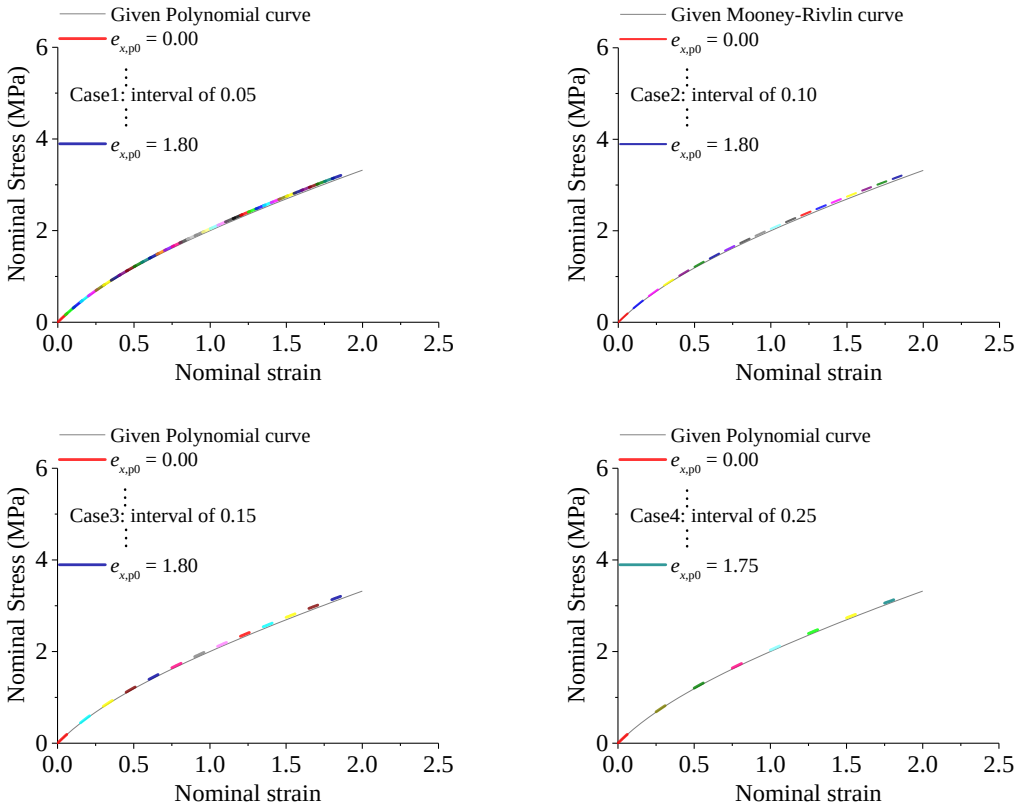

Figure 8.11 Use of the shifting procedures on the local one-term Ogden curves (small colourful curves) obtained by NVFM2 and the given second-order term polynomial model (grey solid line).

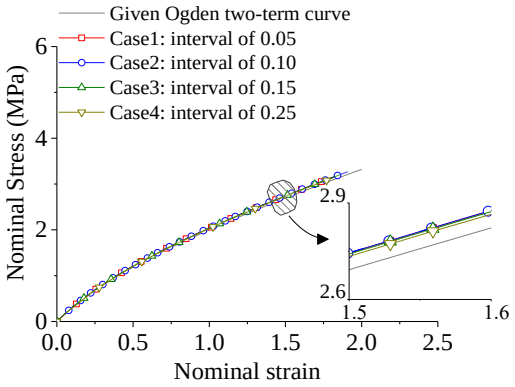

Figure 8.12 Linearly interpolated curves of the local one-term Ogden curves shown in Figure 8.11.

only one trend of the tangent slope change, which continuously decreases.

It should be mentioned that the application of NVFM 2 and the shifting procedure is to approximate the curve shape but not to characterize the stress-strain curve at a particular strain rate. The reason is due to the strain rate variation. As shown in Figure 8.5(a), it is found that the global strain rate fluctuates and for some loading periods, e.g. 0.8-1 ms, the specimen experiences a slight unloading as indicated by a negative global strain rate. The strain-rate state during the drop-weight loading is complex, and it is not easy to define a constant strain rate. Thus, the present method should be used for the approximation of the curve shape. The characterization of a precise stress-strain curve at a particular strain rate should be conducted by the technique presented in Chapter 7, i.e. VFM 2, but with the aid of the evaluation of the curve shape from the present method for the determination of a constitutive model in the optimization procedure.

The simulation data used above was generated with a rate-independent hyperelastic model. Therefore, the difference due to the strain-rate variation between the stress-strain curves made by the present shifting procedure and VFM 2 should not appear. The same simulation data given by the two-term Ogden model was applied to the procedure of VFM 2 as explained in Chapter 7. The data range used in VFM 2 is limited to the initial loading period, 0-0.6 ms. The collection of the nominal modulus *NE*, when 0.25 (case 4) interval

of a nominal pre-strain is applied, is presented in Figure 8.13. Through this figure, it is also possible to observe the feature of the curve shape of the given two-term Ogden model. When $e_{x,p0}$ = 0.25 is applied, the resulting instantaneous nominal modulus (blue profile) significantly decreases compared to the non-pre-stretching case (red profile); this reduction indicates the trend of the decreasing tangent slope of the given stress-strain curve under the same nominal strain range. The increasing trend is also observed when comparing the two profiles obtained at $e_{x,p0}$ = 1.50 and 1.75, showing that the nominal modulus profile is higher as the pre-strain increases from 1.50 to 1.75. This increment is an opposite trend when the pre-strain increases from 0 to 0.25 and represents the increasing tangent slope after 1.00 of a nominal strain of the given stress-strain curve.

The same optimization procedure using Eq. (7.15) in order to obtain the model parameters was conducted on the averaged nominal moduli. For the strain energy density W in Eq. (7.15), the two-term Ogden model was chosen so there were four parameters, μ_1, α_1, μ_2 and α_2 to be identified. The averaging period for the nominal moduli was fixed (0.3-0.4 ms) as shown in Figure 8.13, although the length of the stable estimation period of each pre-stretching case is different, in order to simplify the laborious averaging period for many identification profiles. An unstable identification of the case of $e_{x,p0}$ = 1.75 at

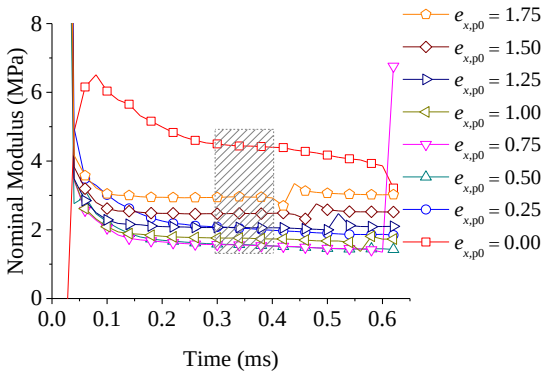

Figure 8.13 Nominal moduli identifications at each pre-strain location using VFM 2 on the same simulation data of the two-term Ogden model.

Table 8.1 Identified two-term Ogden parameters from VFM 2.

Pre-strain interval	μ_1 (MPa)	α_1	μ_2 (MPa)	α_2
0.05	0.15	4.35	1.35	-3.47
0.10	0.15	4.36	1.35	-3.46
0.15	0.14	4.39	1.36	-3.54
0.25	0.15	4.35	1.36	-3.51
Given Parameters	0.10	4.66	1.51	-3.62

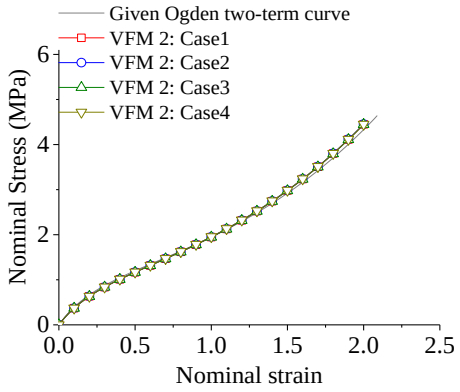

Figure 8.14 Reconstructed two-term Ogden curves using the identified parameters in Table 8.1 and the given curve.

around 0.4 ms is an indication of the stress wave arrival at the fixed end. The same four cases of the different pre-strain interval steps were respectively analysed by VFM 2 and the optimization procedure. Their identified model parameters are listed in Table 8.1 and Figure 8.14 presents the all reconstructed two-term Ogden curves showing a good match with the given model.

The comparison between the shifting results in Figure 8.10 and the application of VFM 2 in Figure 8.14 does not show a significant difference because of, as mentioned, the use of rate-independent hyperelastic model in the simulation. It is necessary to conduct the same simulation but using rate-dependent models. In order to simulate the viscoelastic behaviour with the given two-term Ogden model, the Prony series model, Eq. (2.21), was adopted. The parameters of this Prony model were obtained through the DMA experiment and time-temperature superposition using the same nitrile rubber, a detailed explanation is provided in the second part of this chapter. The normalized

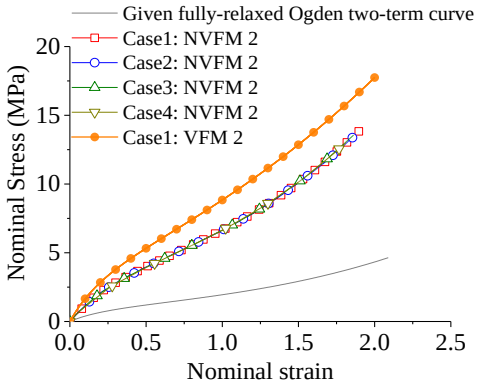

Figure 8.15 Interpolated curves of the shifted local one-term Ogden curves from NVFM 2 of the four interval step cases and the reconstructed two-term Ogden curve from VFM 2 with the visco-hyperelastic simulation data.

shear term, g_i, and relaxation time, τ_i, were listed in Table 8.3 (page. 234) in Section 8.3.2. The two-term Ogden model used in the simulation work above was assumed to be a long-term behaviour, i.e. fully relaxed behaviour. The same drop-weight simulation was conducted and the data were analysed by the present method, NVFM 2 and the shifting procedure, and VFM 2. Figure 8.15 shows the shifted curves of the local one-term Ogden curves obtained from NVFM 2 and the reconstructed two-term Ogden curves obtained from VFM 2. In the case of VFM 2, the reconstructed curves with the different interval steps are almost coincident so only the result with an interval of 0.05 pre-strain is shown here. The curve shapes of both NVFM 2 and VFM 2 are similar to each other but it can be seen that the VFM 2 curve is stiffer than that of NVFM 2. The softer curves of NVFM 2 are a result of the complex loading state where dynamic loading and a short period of unloading are involved in the analysis of NVFM 2. This simulation result shows that the present NVFM 2 and the shifting procedure application on the drop-weight experiment should be used for the approximation of the curve shape, rather than the actual characterization at a particular strain rate. The approximated curve shape can give an opportunity to evaluate the determination of a constitutive model for use in VFM 2.

In summary, the present simulation work leads to the following conclusions:

- The combined linear and nonlinear VFM is able to approximate the curve shape of the two-term Ogden model by means of the relatively simple one-term Ogden model.
- The combined method is also capable of identifying the curve shape when a different constitutive model (i.e. the polynomial model), which shows a totally different curve shape from the Ogden style model.
- The combined method with the drop-weight experiment should be used for a curve shape approximation rather than an actual parameter identification as strain rate variation is inevitable with the current experiment system.

8.2.4 Application of NVFM 2: experiment

The same drop-weight experiment and imaging procedures presented in Chapter 5 were applied on the same nitrile rubber used for the quasi-static experiment shown in Section 8.2.1. As shown in Figure 8.4, the loading duration involved in the analysis of NVFM 2 is much longer than the previous cases of the linear VFMs. In addition, in order to generate a possible change in the curve shape due to different temperatures, a simple temperature-controlling device was designed and installed on the drop-weight apparatus. The picture of this temperature device is shown in Figure 8.16. This device consists of a cooling fan (TDEX3132, Thermo Electric Devices), Peltier stage (MCPF-127-14-11, Multicomp) and cuboid-shape copper block. A Peltier stage is a thermoelectric device by which heat can be transferred from one side to the other when DC current flows into the device. The stage was attached to a heat sink so that the heat could be dissipated. The other side of the Peltier stage was bonded to the copper block by means of a thermal tape (Thermal Adhesive Tape 8940, 3M). The other side of the copper block is also covered with the tape but with its coating film in order to reduce friction between the specimen and the block. The temperature measurement was conducted using a K-type thermocouple,

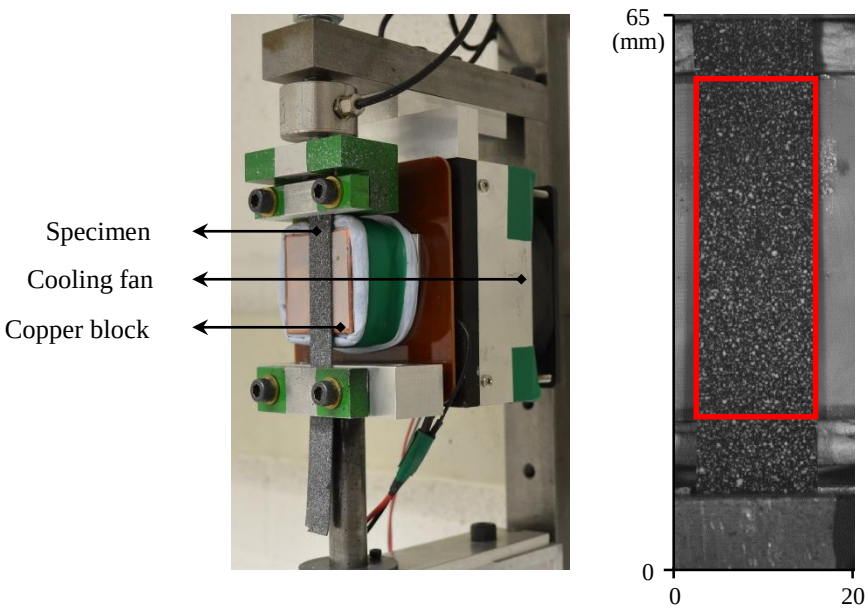

Figure 8.16 (left) Temperature-controlling device installed on the drop-weight apparatus and (right) the *in-situ* high-speed image and the analysis area indicated by the red rectangle.

the data from which was collected by a USB thermocouple data collecting device (USB TC01, National Instruments). The detailed temperature measurement procedure is explained in the second part of this chapter.

Three drop-weight experiments at temperatures of 10, 21 and 62 °C were performed. As mentioned, the same imaging procedure was applied but the temporal fitting procedure to smoothen the acceleration fields was modified to consider the longer duration of the drop-weight loading. The modified method is described in Section 8.3.3. In addition, as can be seen in Figure 8.16, the copper block does not cover the whole surface of the specimen. In order to avoid a large temperature difference, only part of the specimen area covered by the block was used for the VFM analysis, although the length reduction can give a slight overestimation of the Young's modulus as described in Figure 4.13 in Section 4.2.2. The reduced analysis area is described in Figure 8.16 (right) showing the *in-situ* image of the nitrile rubber specimen. It can be seen that the length of the specimen is much longer than those used in the previous chapters. This longer dimension is due to the modification of the drop-weight apparatus for the installation of the temperature

device behind the specimen. The data reduction was applied only for the case of the hot and cold temperatures.

The full-field data obtained from the drop-weight tests was analysed by NVFM 2 and the shifting procedure as explained in the simulation work; the length of the data period was identically given by the definition in Figure 8.5. Figure 8.17 (a) shows the results of NVFM 2 and the shifting procedure of the three temperature cases, and Figure 8.17 (b-d) presents the one- and two-term Ogden fits. The value of RMSE of each fit with respect to the interpolated curves can be used as the evaluation of the fitting quality of the chosen constitutive models. Each RMSE value is provided in the legends of Figure 8.17(b-d). It is clear that for the cases of 21 and 62 °C, the fitting quality of the two-term Ogden model is better than that of the one-term one as its RMSE value is lower. However, the fitting qualities for the case of 10 °C are not significantly different; these similar fitting

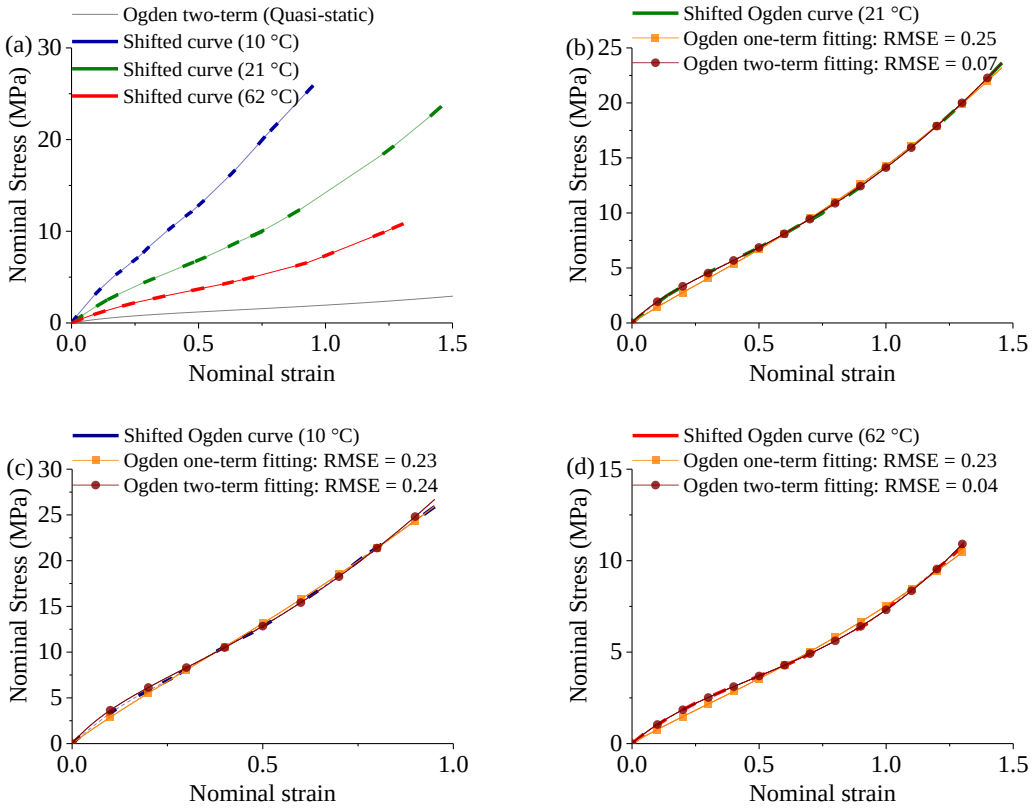

Figure 8.17 (a) Linearly interpolated curves of the shifted local one-term Ogden curves of the drop-weight experiments at 10, 21 and 62 °C; the one- and two-term Ogden fittings on the interpolated curves of (b) 21, (c) 10, and (d) 62 °C.

results can be explained by the observation that the shifted curve does not show a clear strain hardening compared to the other cases.

As explained above, the application of NVFM 2 and the shifting procedure to the drop-weight test data should be used for the approximation of the curve shape due to the difficulty of defining a definitive value of the strain rate and the complex strain state of dynamic loading followed by a short period of unloading. Thus, in this actual application of NVFM 2 on the experimental data, the evaluations of the curve shapes shown above

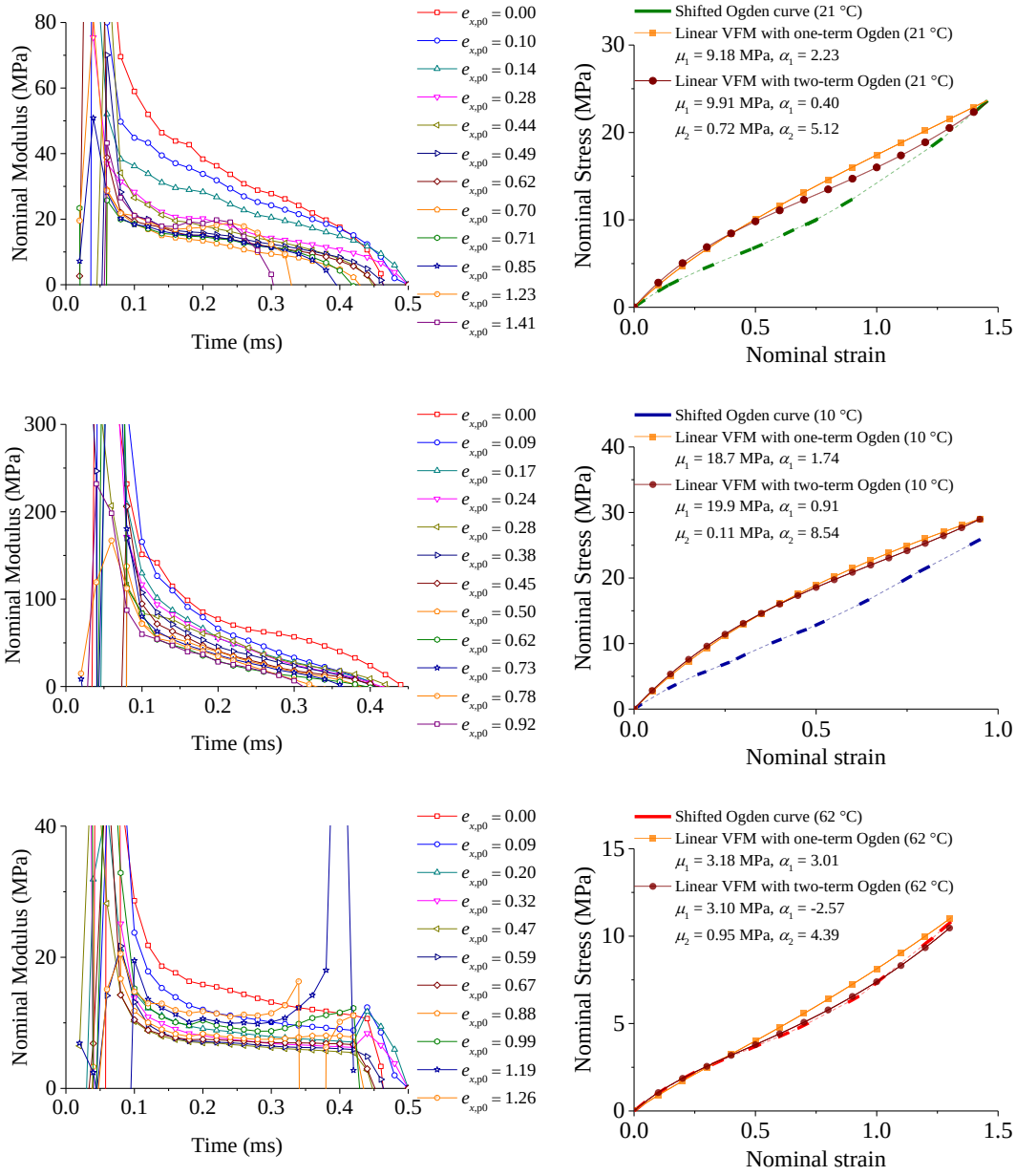

Figure 8.18 (left) Collections of the identification profiles of the nominal moduli and (right) reconstructed one- and two-term Ogden curves using VFM 2 on the drop-weight experiment data of 21, 10 and 62 °C.

using the RMSE values were used for the choice of a constitutive model in the optimization procedure of VFM 2. According to the RMSE values in Figure 8.17, the two-term Ogden model should be used for the case of 21 and 62 °C, and either the one- or two-term model seems acceptable for 10 °C.

The identification procedure of VFM 2 was applied to the same experimental data but the data range is limited to the first incident loading period. Their reconstructed Ogden curves are presented in Figure 8.18(right) with the identified parameters obtained from the optimization procedure using both of the one- and two-term models for comparison. As expected, it can be observed that the reconstructed curves are stiffer than the shifted ones except for the case of 62 °C. The small difference in this case is due to the fact that the relaxation gradient at this high temperature range is much lower than the other cases as can be observed in the storage moduli versus temperature profile shown in Figure 8.20(b). The RMSE values of the case of 21 and 62 °C from the one- and two- term model fittings show a large difference in Figure 8.17; these differences can be also observed in the dissimilarity of their one- and two-term reconstructed curves of VFM 2

Table 8.2 Averaged nominal modulus, longitudinal strain rate and nominal pre strains of the drop-weight tests with the three different temperatures of 21, 10 and 62 °C.

Temperature 21 °C			Temperature 10 °C			Temperature 62 °C		
NE (MPa)	$\dot{\varepsilon}_x$ (s^{-1})	$e_{x,p0}$	*NE* (MPa)	$\dot{\varepsilon}_x$ (s^{-1})	$e_{x,p0}$	*NE* (MPa)	$\dot{\varepsilon}_x$ (s^{-1})	$e_{x,p0}$
30.0	71	0.00	61.4	38	0.00	11.8	80	0.00
26.4	70	0.10	43.1	41	0.09	9.25	86	0.09
22.2	66	0.14	36.1	43	0.17	7.33	93	0.20
15.8	87	0.28	34.6	44	0.24	6.43	93	0.32
14.3	83	0.44	36.7	40	0.28	5.69	100	0.47
13.1	80	0.49	30.3	45	0.38	6.15	103	0.59
12.2	87	0.62	25.2	47	0.45	6.96	101	0.67
10.2	88	0.70	23.6	45	0.50	7.78	91	0.88
12.2	81	0.71	16.8	44	0.62	9.78	90	0.99
12.7	79	0.85	21.6	53	0.73	10.5	85	1.19
17.6	78	1.23	26.8	50	0.78	11.5	83	1.26
19.2	67	1.41	25.8	51	0.92			
Average $\dot{\varepsilon}_x$ = 78 s^{-1}			Average $\dot{\varepsilon}_x$ = 45 s^{-1}			Average $\dot{\varepsilon}_x$ = 91 s^{-1}		

as shown in Figure 8.18(right). The RMSE values of the 10 °C case are not significantly different, and consequently its reconstructed curves of VFM 2 are almost similar. However, for the case of 10 °C as well, the two-term Ogden model seems a more suitable choice for the optimization procedure because the trend of the averaged nominal modulus change (as listed in Table 8.2), i.e. tangent slope, initially decreases but, after 0.62 nominal pre-strain, starts to increase. As mentioned, this complex tangent slopes should be fitted by a higher order-term model.

8.2.5 Explanation of the identification variation

As can be seen in Figure 8.18, the identification of the nominal modulus is varied; the identification is not constant but gradually decreases. This variation is especially significant for the case of 10 and 21 °C, and the identification of the 62 °C case is rather stable. From this difference, the reason for this variation can be explained. The DMA data of a nitrile rubber shown in Figure 8.20(b) shows the temperature dependence of the modulus. It can be seen that the relaxation gradient with respect to temperature at 10 and 21 °C is much higher than that at 60 °C. The difference corresponds to that of the variation shown in Figure 8.18. That is, when the material is close to a glass transition temperature, the modulus gradient is high and the admissible relaxation amount is also large. In the case of silicone rubber, this variation is not large as shown in Figure 7.9 from Chapter 7. The reason is because the relaxation gradient is not as high as that for the nitrile rubber at room temperature.

The same variation can be shown using FEM simulation. Two simulations were conducted using the same condition that were employed for producing Figure 8.13 but the material is assumed to be linear. The first material is linear elastic with E = 30 MPa and ν = 0.499; the second one is linear-viscoelastic with the same parameters (for the long-term response) and the Prony series parameter of nitrile rubber shown in Table 8.3.

Figure 8.19 shows the results of these two simulations. The viscoelastic case shows a similar variation to that for the experimental result (Figure 8.18) whereas the variation in the elastic case is much less and not representative of the experimental result. This difference clearly explains the reason of the variation and its degree shown in Figure 8.18.

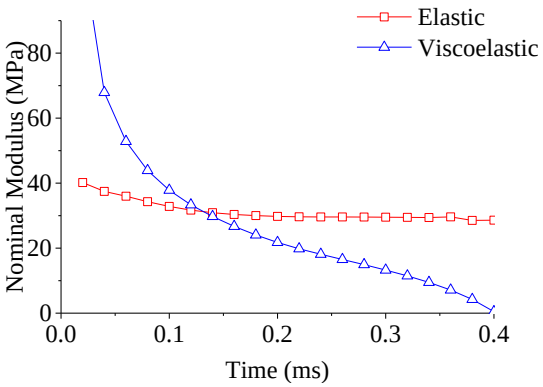

Figure 8.19 Identification results of the nominal moduli from the simulation with pure and visco-linear elastic material.

8.3 Application of the nonlinear VFM with a rate-dependent model

8.3.1 DMA tests on nitrile and silicone rubbers

The same nitrile rubber used in the first section of this chapter was characterized by the DMA and time-temperature superposition procedures. The overall procedures are the same as the one shown in the previous chapters but, in the present work, a different control mode was adopted in the DMA testing device. Previously, the storage versus temperature profiles at three different frequencies were obtained using temperature ramp & frequency sweep, in which a specimen is continuously heated with a linear heating rate and simultaneously loaded with a number of given frequencies. For the current data, temperature step & frequency sweep was available. In this loading mode, isothermal frequency sweeps were performed at different temperatures, in this case from -65 to 65 °C in 2 °C increments; the isothermal duration was given as 1 min for each step; and the five frequencies were used: 2, 5, 10, 15, 20, 30 and 35 Hz. The silicone rubber was retested for the present work as a new batch was manufactured, and the properties could be slightly

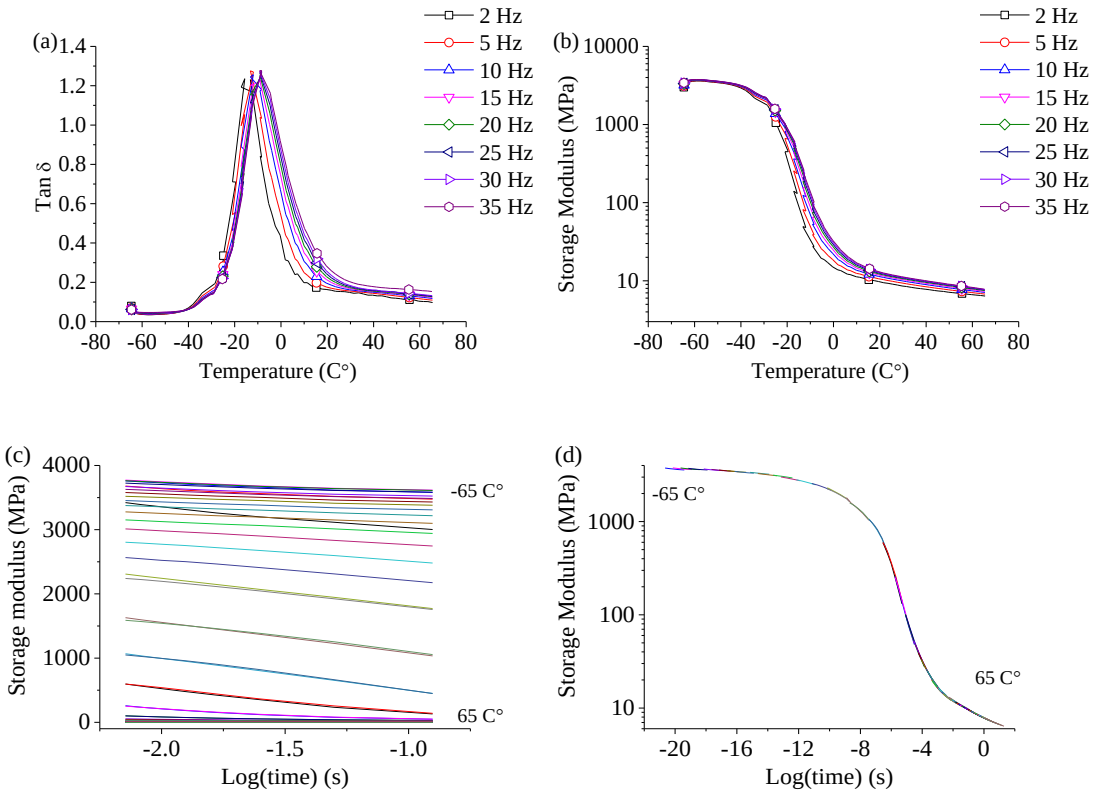

Figure 8.20 Nitrile rubber: (a) storage moduli and (b) tan δ versus temperature at the five frequencies; (c) isotherm of storage modulus and (d) master curve versus the logarithmic time.

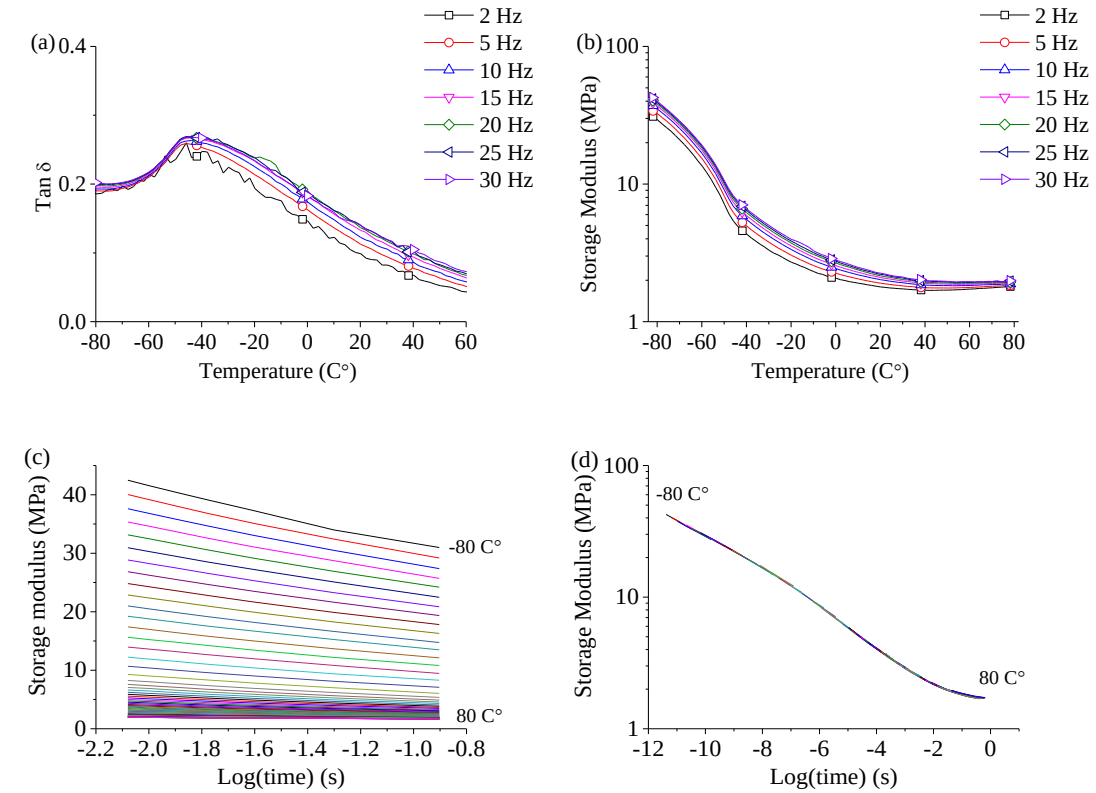

Figure 8.21 Silicone rubber: (a) storage moduli and (b) tan δ versus temperature at the five frequencies; (c) isotherm of storage modulus and (d) master curve versus the logarithmic time.

different. For the silicone rubber, the same DMA procedure was applied with the temperature range -80 to 80 °C and only the first four frequencies were used, as the behaviour at 35 Hz was very unstable. In order to obtain the relaxation curve, the same time-temperature superposition procedure was manually conducted using the isotherm curves at each temperature step. The DMA results from these two rubbers are presented in Figure 8.20 and Figure 8.21. The relaxation curves Figure 8.20(d) and Figure 8.21(d) as a result of the time-temperature superposition were used for the material property in the simulation and experiment works in the next sections.

8.3.2 Nonlinear VFM for the identification of a relaxation curve: simulation

As mentioned in the first section, there are further useful data from the drop-weight experiment for the identification of rate-dependent behaviour of rubbers: strain rate variation at a particular time step and multiple reloading with a larger deformation range. In the present work, the aim of the identification is to attempt to characterize the relaxation curve in the vicinity of an initial deformation range. It is necessary to define the time scale for this characterization prior to applying the nonlinear VFM. First, the relaxation behaviour at a small time scale is limited by the imaging speed. The same imaging speed, 50 000 fps, was used for the present work; thus, the time step Δt between each picture is 2×10^{-5} s and in logarithmic scale -4.7 ($\approx \log(2\times10^{-5})$). The relaxation

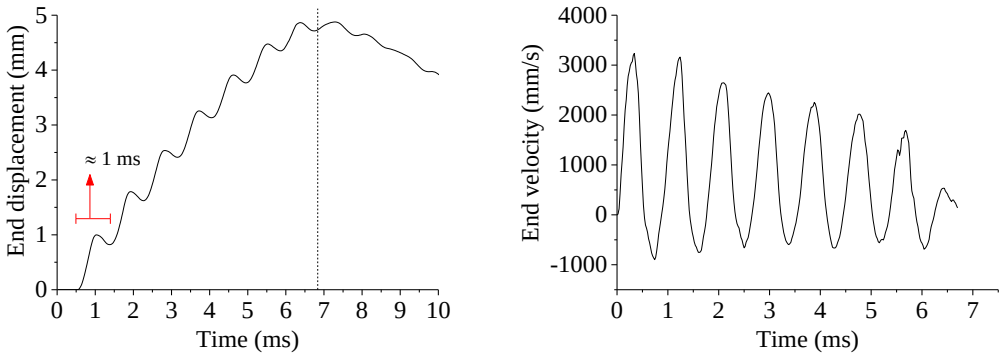

Figure 8.22 (a) End displacement and (b) velocity profile of the drop-weight test on a nitrile rubber at 9 °C (the dash line indicates the final data range for the present simulation study).

behaviour associated with logarithmic time scales smaller than -4.7 is impossible to characterize because its physical behaviour is not observed. With regard to the upper limit, it is assumed that the relaxation behaviour that can be characterized by the dynamic VFM is clearly exhibited within each reloading period because the non-uniform deformation state (consequently, acceleration field) is re-generated when each reloading is initiated at the ends of a specimen. The period of each reloading is approximately 1 ms, as indicated by the red arrow in Figure 8.22. The logarithmic time of 1 ms is -3, which is used for the upper limit of the time scale.

The overall simulation procedure was the same as in the previous drop-weight work. In order to simulate the viscoelastic behaviour, the actual relaxation data shown in Figure 8.20(d) and Figure 8.21(d) was applied. The relaxation behaviour in ABAQUS can be described by the Prony series model. Prior to applying this model, the master relaxation curves (Figure 8.20(d) and Figure 8.21(d)) formed by the manual shifting were smoothed by fitting it to the WLF model, Eq. (2.34), by which the shifting factor of each isotherm is described with respect to its temperature with a given reference temperature and two parameters of C_1 and C_2. The manual shifting factor versus temperature profile was made and fitted to Eq. (2.34) with the reference temperature of 20 °C. Then, using the optimized C_1 and C_2, the shifting factor versus temperature profile was reconstructed by Eq. (2.34).

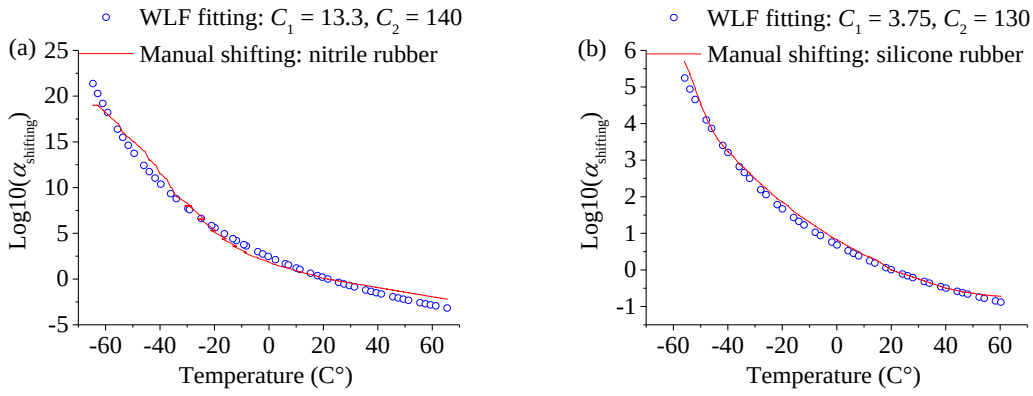

Figure 8.23 WLF model fitting on the manual shifting factor versus temperature profiles of the nitrile and silicone rubbers.

This procedure is described in Figure 8.23. The reconstructed shifting factors were used to generate the smoothed master curves which were used to obtain the parameters of the Prony series. The smoothed master curves are given in Figure 8.24 as a scatter line. A similar procedure was used in a previous study of (Kaliske and Rothert, 1997).

The parameters of the Prony series were obtained by fitting these smoothed relaxation curves. The Prony series model, Eq. (2.21), is used as a normalized form; that is, it describes the relaxation behaviour from a non-dimensional instantaneous modulus value of 1. For example, the relaxation curve of the nitrile rubber was normalized by their largest modulus. The normalized curve was then fitted by Eq. (2.21) with fixed 20 relaxation time terms given as $\tau_1 = 1\times10^{-19}$, $\tau_2 = 1\times10^{-18}$, …, $\tau_{20} = 1$ in order to obtain the corresponding normalized modulus term, g_i. The fitting procedure was conducted in a

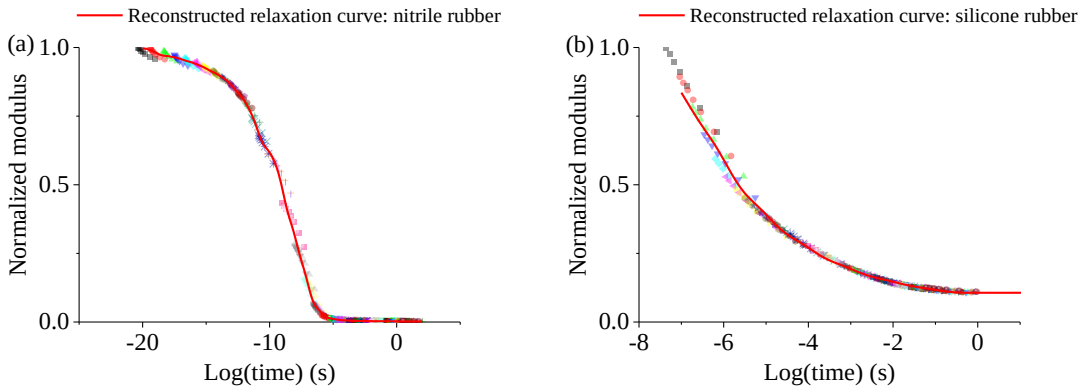

Figure 8.24 Normalized relaxation curves of the DMA relaxation data (scatter lines) and the fitted profiles using the Prony series (red solid line).

Table 8.3 Prony series parameters: given relaxation time terms τ and optimized normalized-relaxation terms g obtained from the DMA data of the nitrile and silicone rubbers.

Nitrile rubber											
$\log(\tau_i)$	-19	-18	-17	-16	-15	-14	-13	-12	-11	-10	-9
g_i	0.028	0.004	0.014	0.014	0.024	0.020	0.046	0.047	0.149	0.027	0.201
$\log(\tau_i)$	-8	-7	-6	-5	-4	-3	-2	-1	0		
g_i	0.156	0.198	0.056	0.010	0.003	0.001	0.001	0.0002	0.001		
Silicone rubber											
$\log(\tau_i)$	-7	-6	-5	-4	-3	-2	-1				
g_i	0.216	0.280	0.163	0.103	0.066	0.038	0.029				

similar way to that used for the stress-strain curve fitting. The same fitting procedure was applied to the silicone rubber data. The two sets of the Prony parameters are listed in Table 8.3, and their reconstructed relaxation curves are presented in Figure 8.24 with their normalized experimental data. These two viscoelastic properties were used in the two separate simulation works applied to the same present VFM analysis for comparison.

In both of the simulation cases, the relaxation behaviour is now defined as explained above. Their long-term behaviours, i.e. when the materials are fully relaxed ($t = \infty$), were assumed to be described by the one-term Ogden model. It should be mentioned that only the initial deformation range, which can be produced by the drop-weight experiment, was explored without the pre-stretching procedure in the present study. Therefore, the use of the one-term Ogden model could be sufficient to describe the behaviour of rubbers at small strain, where the nonlinearity is less complex, for the fully relaxed state. For the μ_∞ term of the one-term model, the quasi-static uniaxial tests were conducted at a very low strain rate of 0.001 %/s on both rubbers with the usual test procedure used in the previous chapters. The total strain was limited to 0.001 true strain up to which the stress-strain behaviour was observed to be reasonably linear. The experimental results are shown in Figure 8.25, in which the linear fitting lines are also provided. The slopes of each linear line of the silicone and nitrile rubbers are obtained as 1.1091 and 2.8307 MPa for their

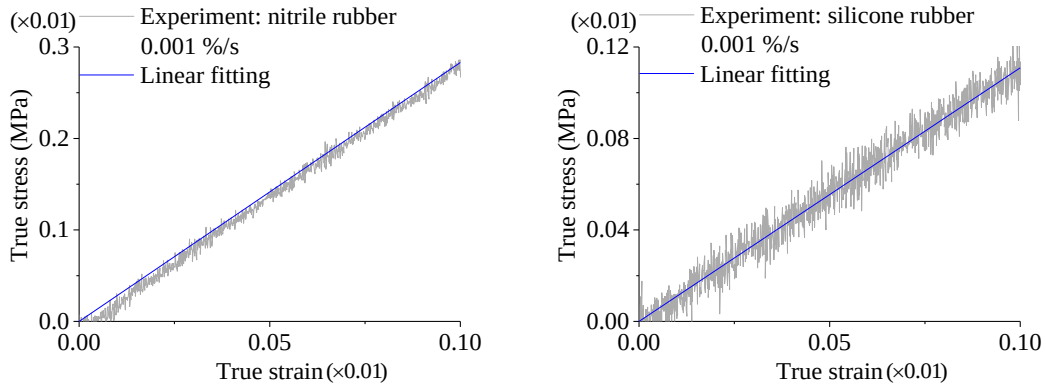

Figure 8.25 Quasi-static uniaxial tests at a strain rate of 0.001 %/s on the nitrile and silicone rubbers.

Young's modulus. The μ_∞ terms are calculated by dividing them by 3 using the assumption of incompressibility; the values are 0.37 and 0.94 MPa respectively for the silicone and nitrile rubbers. In ABAQUS, only the modulus term of a hyperelastic model is associated with the viscoelastic model, as explained in Section 2.1.2, through Eq. (2.25); the strain hardening term is assumed to be rate-independent. The α term in the present model is assumed to be 4 for both cases.

In addition to the mechanical properties, thermal properties were given to the materials in order to simulate the application of the time-temperature superposition on the present drop-weight experiment. The thermal conductivity and specific heat of the present silicone rubber were found as 0.18 W m^{-1} K^{-1} and 1100 J kg^{-1} K^{-1} (Erickson et al., 2003). Although there were two simulation cases respectively for the viscoelastic behaviour of the two rubbers, these thermal properties were also used for the nitrile rubber case as the heat transfer is not important in the current simulation. The resemblance of the mechanical property changes due to temperature and loading rate is the assumption made for the principle of the time-temperature superposition. This relationship in ABAQUS is described by the WLF model of Eq. (2.34) requiring the parameters of C_1 and C_2, and the parameters obtained in Figure 8.23 were used.

The same simulation works were conducted as in the first part of this chapter but without the pre-stretching procedure. For the boundary condition, the end velocity, Figure 8.22(b), calculated from the displacement data of Figure 8.22(a) was applied. For the application of the time-temperature superposition, 19 temperatures were applied over the whole specimen as an initial condition. The temperature condition ranges from -12 to 60 °C with an interval of 4 °C. As mentioned in the first part, when the temperature-controlling device was used, only part of the specimen area was covered by the device. This experiment condition was also applied to the present simulation by reducing the data

area 7 mm from the both ends, as described in the left-hand side of Figure 4.9, for all temperature cases.

The same data processing was applied with use of 50 000 fps for the data field extractions so the time step Δt between each data is 2×10^{-5} s. The field data were analysed by the nonlinear VFM presented in Chapter 6. The one-term Ogden model is used for a hyperelastic behaviour and the Prony series model for a viscoelastic property. The combination of these two models was given by the formulation initially proposed by Simo (1987); this method was similarly adopted in previous VFM work (Sasso et al., 2013). In the present work, it is assumed that global experiment coordinate and principal directions are coincident ($\lambda_x = \lambda_1$). First, the instantaneous- and long-term hyperelastic behaviours are given as, in terms of true stress,

$$\sigma_{x,0} = \frac{2\mu_0}{\alpha}\left(\lambda_x^{\alpha} - \lambda_x^{-0.5\alpha}\right) \tag{8.15}$$

$$\sigma_{x,\infty} = \frac{2\mu_\infty}{\alpha}\left(\lambda_x^{\alpha} - \lambda_x^{-0.5\alpha}\right) \tag{8.16}$$

where the subscripts '0' and '∞' respectively indicate the instantaneous and long-term related terms. For the α term, there is no indication by any subscript as it is assumed that the same α term is shared between these two behaviours. The total stress at a time step n is expressed using the following formulation

$$\sigma_{x,n}^{i} = \sigma_{x,n-1}^{i}\exp\left(-\frac{\Delta t}{\tau_i}\right) + g_i\exp\left(-\frac{\Delta t}{2\tau_i}\right)\left(\sigma_{x,0,n+1} - \sigma_{x,0,n}\right) \tag{8.17}$$

$$\sigma_{x,n} = \sigma_{x,\infty,n} + \sum_i \sigma_{x,n}^{i} \tag{8.18}$$

where 'i' is the number of the terms involved in the Prony series model. In total, five terms were made and, for each term, the following relaxation time terms were assumed using the definition of the upper and lower time scale range: $\tau_{1,2,3,4,5} = 1\times10^{-5}$, 5×10^{-5}, 1×10^{-4}, 5×10^{-4} and 1×10^{-3} s. The total stress σ_{xx} is converted to the PK1 stress using the

relation $\Pi_{xx} = \sigma_{xx} / \lambda_x$, which is then used in the PVW, Eq. (6.1), of the nonlinear VFM with the first set of the virtual fields. After applying the PVW, the parameters to be obtained are g_i, corresponding to each τ_i, α and μ_0; the μ_∞ term is determined by the relation of $\mu_\infty = \mu_0 \times (1 - \Sigma g_i)$. The identified μ_0 and μ_∞ are not the instantaneous and long-term shear modulus of the materials in an actual time scale but in the defined drop-weight experiment time scale. For comparison, the linear elastic constitutive model was also used. The same formulation was used with the following constitutive relation

$$\sigma_{x,0} = Q_{xx,0}\varepsilon_{xx} + Q_{xy,0}\varepsilon_{xy} \tag{8.19}$$

$$\sigma_{x,\infty} = Q_{xx,\infty}\varepsilon_{xx} + Q_{xy,\infty}\varepsilon_{xy} \tag{8.20}$$

$$\begin{aligned} Q_{xx,\infty} &= E_\infty / (1-\nu^2),\ Q_{xy,\infty} = \nu E_\infty / (1-\nu^2) \\ Q_{xx,0} &= E_\infty / (1-\nu^2),\ Q_{xy,0} = \nu E_0 / (1-\nu^2) \end{aligned} \tag{8.21}$$

For this linear elastic model, Poisson's ratio, ν, is assumed to be 0.5.

The nonlinear VFM explained above was applied to the simulation data given by the one-term Ogden model with the two relaxation behaviours. There were two different nonlinear VFMs using the viscoelastic constitutive formulations with the one-term Ogden and the linear elastic model. The identified parameters for these two cases are listed in Table 8.4. Using these identified parameters, the local relaxation curves were reconstructed. First, the normalized local relaxation curve was plotted using Eq. (2.21) and multiplied by the instantaneous shear modulus term μ_0. The reconstructed relaxation curves from the two simulation cases are presented in Figure 8.26(a and c) and indicated by a red-rectangle symbol. The same reconstruction procedure was used on the parameters identified from the nonlinear VFM with the linear elastic model. One difference is that the value of μ_0 to be multiplied to the normalized curve is obtained by dividing the identified E_0 by 3. Its results are presented by a blue-circular symbol curve.

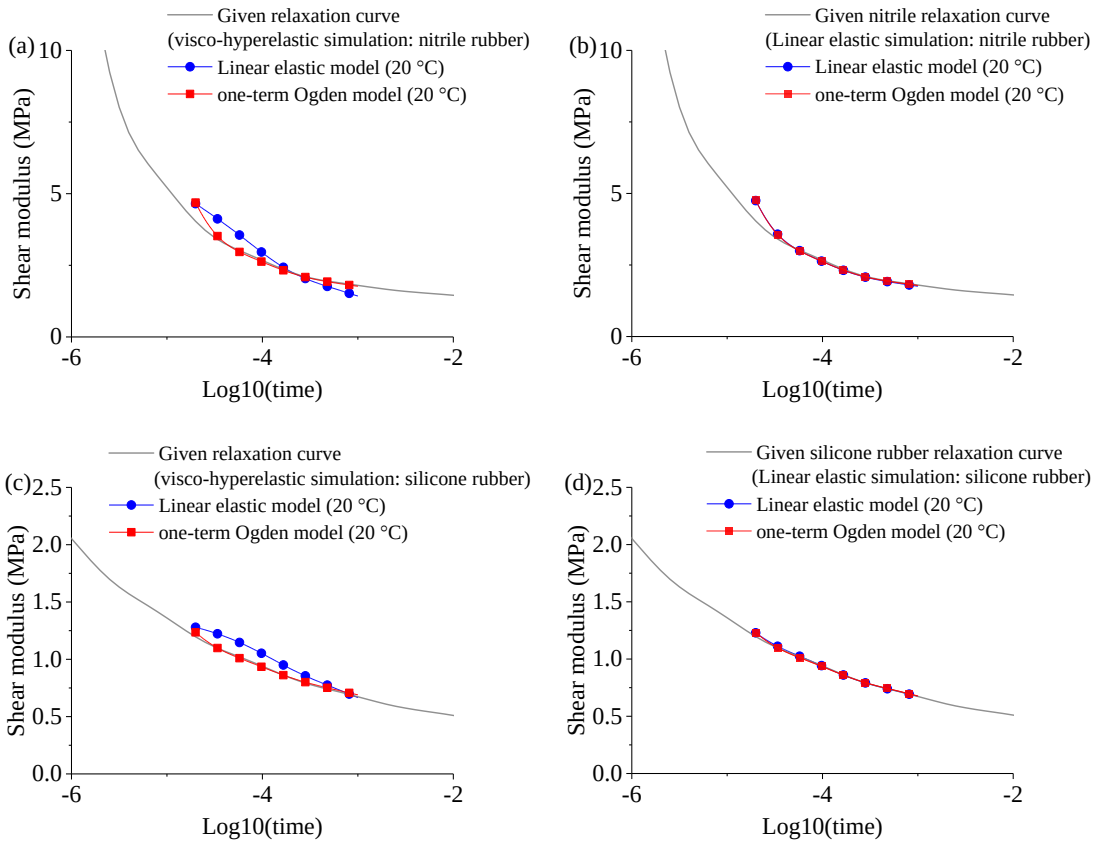

Figure 8.26 Identification of a local relaxation curve from the nonlinear VFM using the linear elastic and one-term Ogden model on the simulation data with the nitrile and silicone rubber relaxation behaviour.

Table 8.4 Identified Ogden and Prony model parameters from the viscoelastic simulations at 20 °C.

Nitrile rubber Simulation at 20 °C		Silicone rubber Simulation at 20 °C	
μ_0 (MPa)	13.3	μ_0 (MPa)	2.10
α	3.42	α	3.55
g_1	0.719	g_1	0.431
g_2	0.027	g_2	0.042
g_3	0.087	g_3	0.112
g_4	0.024	g_4	0.041
g_5	0.022	g_5	0.072

Figure 8.26(a and c) clearly shows the difference between the two nonlinear VFMs in that the use of the one-term Ogden model gives a better matching on the part of the given relaxation curves. The results in Figure 8.26(b and d) were obtained by the same nonlinear VFM on the simulation conducted with the linear elastic model instead of the Ogden model by converting the given μ_∞ to E_∞ and ν = 0.499. In this simulation case, the two

reconstructed curves are almost matched. The comparison between Figure 8.26(a and c) and Figure 8.26(b and d) indicates that in the present nonlinear VFM application for the viscoelastic behaviour of rubbers, the use of a nonlinear constitutive model can give a better identification result.

The analysis results shown above were obtained from the simulation data at 20 °C. The length of the relaxation curve is limited by the time scale defined in the previous section. At this point, the time-temperature superposition principle (TTSP) was utilized in order to extend the length of the identified relaxation curves. The first step of the TTSP application is to collect the reconstructed local relaxation curves obtained at different temperatures. When TTSP was applied to the isotherm data obtained from the DMA test, the manual shifting was conducted. In this DMA case, the temperature step can be small enough so that the part of each relaxation curve still has a similar shape to those obtained from the next temperature step, and this resemblance is very useful to visually evaluate the quality of the manual shifting. However, it was difficult to precisely control the temperature by the simple device, Figure 8.16(left), as much as the DMA. The local relaxation curve obtained from the present drop-weight experiment may not have a good resemblance to the next curve or each curve could not be connected even after manual shifting because of a large temperature step. In order to overcome this expected

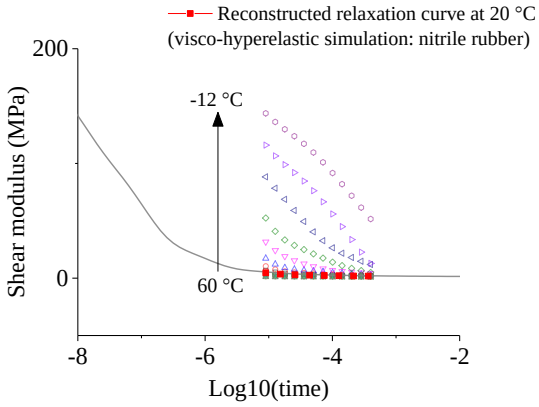

Figure 8.27 Collection of the local reconstructed relaxation curves obtained from the nonlinear VFM applied on the viscoelastic simulations with the temperature range of -12 to 60 °C with an interval of 4 °C.

experimental difficulty, the shifting procedure used in Section 8.2 was similarly applied to the present case, and this procedure is explained below.

(1) The local relaxation curve at 20 °C (red-rectangle symbol in Figure 8.27) is fixed at its initial location. This reference curve is mathematically expressed as

$$\begin{aligned} \hat{\mu}_{[20°C]} &= f_{\text{Relaxation}}(\mu_{0,[20°C]}, g_{1\ldots5,[20°C]}, \hat{t}_{[\text{fixed}]}) \\ \log10(\hat{t}_{[\text{fixed}]}) &= \begin{Bmatrix} -4.7 \\ \vdots \\ \text{interval of } 0.01 \\ \vdots \\ -3 \end{Bmatrix} \end{aligned} \tag{8.22}$$

(2) The curve shifting is horizontally conducted; the shifting factor in this case is the logarithmic time, $\log10(t_{\text{factor}})$, denoted as β_{factor}, and initialized to be zero. For example, when the relaxation curve at 16 °C, which is the next step after 20 °C, is to be shifted, it can be expressed as

$$\begin{aligned} \hat{\mu}_{[16°C]} &= f_{\text{Relaxation}}(\mu_{0,[16°C]}, g_{1\ldots5,[16°C]}, \hat{t}_{[\text{fixed}]}) \\ \log10(\hat{t}_{[16°C]}) &= \log10(\hat{t}_{[\text{fixed}]}) + \beta_{\text{factor},[16°C]} \end{aligned} \tag{8.23}$$

(3) The data in Eq. (8.22) and (8.23) are collected in a vector form, written as

$$\begin{aligned} \hat{\mu} &= \begin{Bmatrix} \hat{\mu}_{[16°C]} \\ \hat{\mu}_{[20°C]} \end{Bmatrix} \\ \log10(\hat{t}) &= \begin{Bmatrix} \log10(\hat{t}_{[\text{fixed}]}) + \beta_{\text{factor},[16°C]} \\ \log10(\hat{t}_{[\text{fixed}]}) \end{Bmatrix} \end{aligned} \tag{8.24}$$

(4) It is assumed that the good shifting of $\mu_{[16°C]}$ with respect to $\mu_{[20°C]}$ is achieved when $\beta_{\text{factor},[16°C]}$ is found by which the data of Eq. (8.24) is well fitted to the one-term exponential model shown below

$$\hat{\mu} = a\exp\left(b\log10(\hat{t})\right) \tag{8.25}$$

The goodness of this fitting was evaluated by the value of RMSE. This fitting procedure can be conducted by the built-in MATALB function, *fit*, and RMSE can be also obtained from this function. This procedure to find a proper $\beta_{\text{factor},[16°C]}$ can be expressed as

$$\min_{\beta_{\text{factor},[16°C]}} \text{RMSE} = f_{\text{exponential\_fit}}(\hat{\mu}, \log10(\hat{t}), \beta_{\text{factor},[16°C]}) \tag{8.26}$$

This minimization was conducted by using the *fminunc* function. Once the curve of $\mu_{[16°C]}$ is properly shifted and this shifted data is used as a reference curve for the shifting of the next relaxation curve using the same procedure. A similar shifting procedure was used in the previous work of (Sihn and Tsai, 1999).

Using the procedure explained above, the local curves at each temperature were shifted to extend the length of the relaxation curves. The results from the nitrile and silicone rubber simulations are presented in Figure 8.28. The red-rectangle scatter line is the local relaxation curve obtained at 20 °C. Starting from this reference curve, the shifting procedure was separately processed for the cold (20 to -12 °C) and hot temperature (20 to 60 °C) ranges. The most right- and left-hand side curves are respectively obtained from the simulation data at 60 and -12 °C. As can be observed in this figure, the shifted data and the given nitrile and silicone relaxation curves are well matched. The present nonlinear VFM on the drop-weight data is able to identify the part of the relaxation

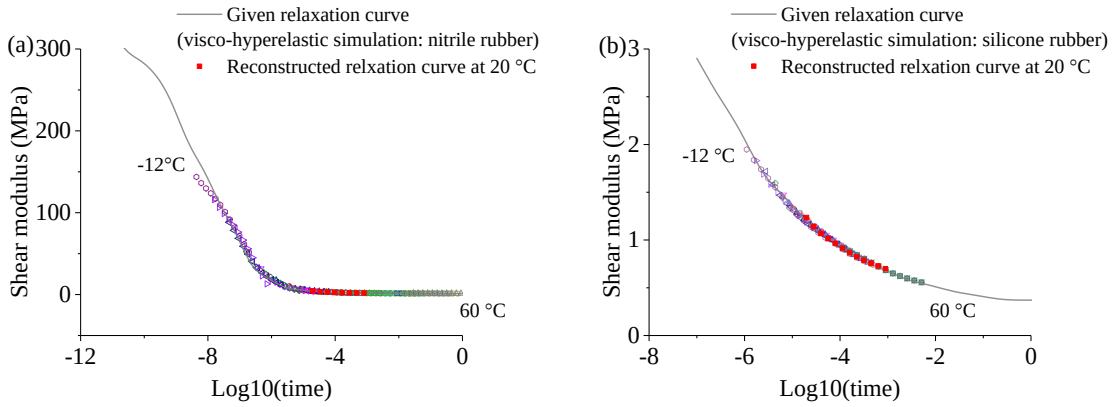

Figure 8.28 Shifted local relaxation curves obtained from the drop-weight simulations at the temperature ranges from 60 to -12 °C and the given nitrile and silicone rubber relaxation curves.

behaviour of rubber-like materials.

The simulation work presented above can be summarized as follows:

- The present nonlinear VFM is able to identify a local relaxation curve of the two different simulation materials
- It is possible to extend the time range of a relaxation curve when time temperature superposition is applied.
- The time scale of a local relaxation curve identified by the present nonlinear VFM depends on the imaging speed. When 50 000 fps is adopted, the lower and upper logarithmic time (s) boundaries are -4.7 and -3.
- It is found that a good identification of the local relaxation behaviour of rubber models requires the use of a hyperelastic model combined with the Prony series in the nonlinear VFM.

8.3.3 Nonlinear VFM for the identification of a relaxation curve: experiment

The nitrile and silicone rubbers were tested by the same drop-weight experiment and imaging procedure but, as shown in Figure 8.22, a longer period of the test data was recorded. The last data step was defined as indicated by a dash line in this figure. The temperature measurement was conducted by the same K-type thermocouple and USB thermocouple data collector used in the work of the first part of this chapter. The thermocouple was held at the end of a camera arm which was fixed around the top of the drop-weight apparatus. Prior to applying the drop-weight loading, the temperature of the specimen was measured by contacting the thermocouple to the centre of the specimen surface facing the high-speed camera. Then, the lamp used for the high-speed imaging was turned on and, at the same time, the temperature was monitored. One of the temperature records taken from the silicone rubber is shown in Figure 8.29. There was a slight temperature increase starting at around 60 s approximately at which the light was

on. It is possible to drop the weight within 20 s after turning the light on. It is therefore assumed that the definitive temperature measurement is an averaged value of the temperature record for 20 s after it starts to clearly rise. The hatched area in Figure 8.29 indicates the approximate averaging period of the temperature data. After measuring the temperature, the light was off, and the thermocouple was removed from the specimen surface. Then, there was a 5-minute delay before conducting the actual drop-weight experiment in order to make the temperature reach its initial level.

The identical nonlinear VFM was used on each set of test data at different temperatures. The same data range reduction described in Figure 8.16(right) was also adopted. In order to obtain the acceleration field data, the temporal fitting procedure introduced in Chapter 4 was applied to the displacement field data with a 9-degree polynomial. One difference

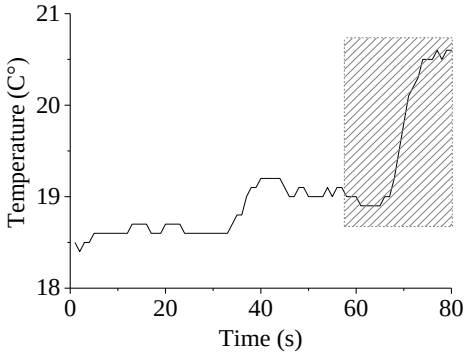

Figure 8.29 Temperature measurement using the K-type thermocouple applied on the silicone rubber during the application of the imaging lamp.

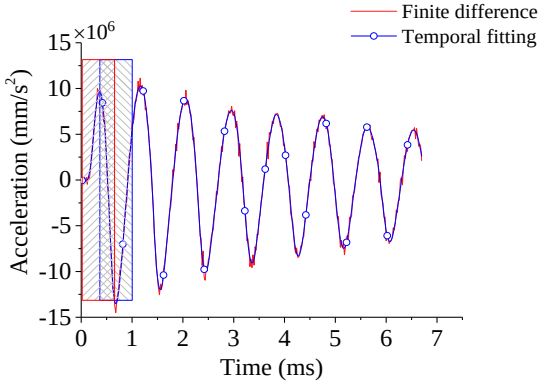

Figure 8.30 Two spatially averaged acceleration profiles from the finite difference and temporal fitting calculation methods.

of the temporal fitting used in this present work is that the fitting was separately conducted on each reloading period. This procedure is visually described in Figure 8.30, showing the two spatially averaged acceleration profiles. The red solid line is an acceleration profile obtained by the simple finite different method of Eq. (4.1); the blue-circle line indicates the acceleration profile from the temporal fitting procedure. In this figure, the red- and blue-colour hatched rectangles represent the first and second period for the temporal fitting. The acceleration data obtained from these two separate periods were individually stored. It can be observed that half of the area of these two rectangles overlap each other. This overlapped area was divided into a half again; then, the acceleration data of the left-hand side of this overlapped area is given by the first period (red rectangle) and

Table 8.5 Identified viscoelastic parameters using the nonlinear VFM with the one-term Ogden and Prony series model on the drop-weight experiments on the nitrile and silicone rubber.

Nitrile rubber							
Temperature °C	μ_0 (MPa)	α	g_1	g_2	g_3	g_4	g_5
10	97.8	6.23	0.628	0.001	0.370	0.009	0.000
14	103	0.83	0.711	0.001	0.236	0.058	0.000
17	84.3	1.48	0.818	0.013	0.065	0.109	0.002
21	55.2	0.47	0.795	0.018	0.054	0.103	0.019
24	47.3	0.09	0.824	0.020	0.001	0.164	0.013
28	31.1	1.04	0.799	0.002	0.001	0.208	0.009
32	9.70	0.13	0.346	0.095	0.020	0.585	0.012
39	5.19	0.22	0.086	0.010	0.006	0.970	0.005
49	4.30	0.72	0.008	0.002	0.002	0.865	0.211
54	3.65	0.21	0.000	0.000	0.000	0.319	0.842
65	3.47	1.72	0.032	0.001	0.001	0.050	0.992

Silicone rubber							
Temperature °C	μ_0 (MPa)	α	g_1	g_2	g_3	g_4	g_5
9	3.71	2.29	0.385	0.147	0.053	0.037	0.455
14	2.72	3.44	0.273	0.112	0.046	0.230	0.234
20	3.04	0.09	0.354	0.089	0.109	0.135	0.123
22	2.38	3.32	0.230	0.111	0.181	0.063	0.096
30	2.82	6.03	0.276	0.175	0.200	0.044	0.052
41	2.77	2.79	0.447	0.105	0.034	0.007	0.365
49	1.70	2.75	0.189	0.065	0.119	0.028	0.359
60	1.70	2.02	0.242	0.093	0.036	0.067	0.283

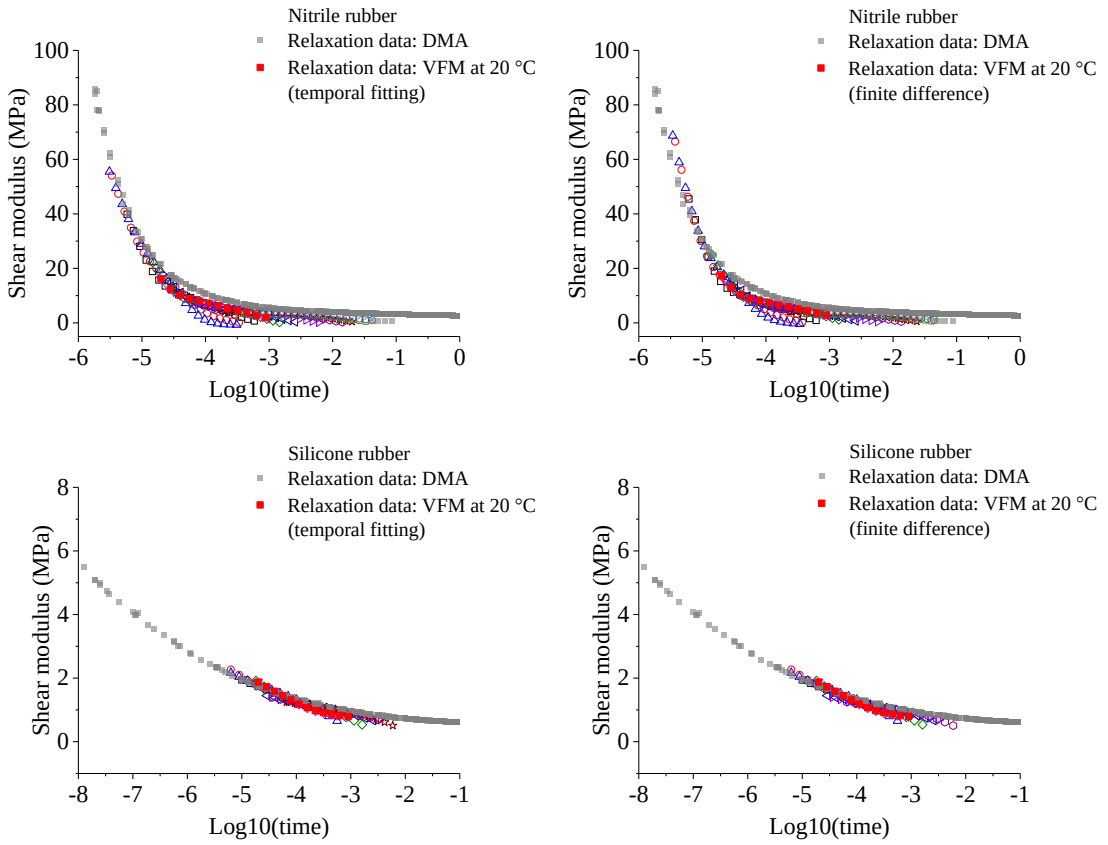

Figure 8.31 Shifted local relaxation curves obtained from the drop-weight experiments and the nitrile and silicone rubber relaxation curve obtained from the DMA (the acceleration calculation methods are given in the legend of each figure).

the second period (blue rectangle) data was used for the other side. Using this procedure, it was possible to remove a spurious acceleration data which was calculated at the end of each averaging period. This separate averaging procedure was repeated for all loading period.

Table 8.5 provides the identified parameters of the nitrile and silicone rubbers and also the temperatures measured from each test. Using these parameters and the shifting procedure, the extended relaxation curves of the nitrile and silicone rubbers are given in Figure 8.31. The raw relaxation data obtained from the DMA test are also presented in this figure; the DMA test was conducted in a tension mode so the storage modulus shown in Figure 8.20(d) and Figure 8.21(d) was divided by 3 to be converted to the shear modulus. For both cases in Figure 8.31, it can be seen that the shifted relaxation curves are well matched with the part of the DMA curves. Also, the present nonlinear VFM can

identify the different relaxation curve shapes (behaviour) of the nitrile and silicone rubber. The identified values of μ_0 in Table 8.5 explain this identification result in that the higher μ_0 is identified for the lower temperature. The acceleration calculation methods are indicated in the legend of each figure; it seems that the effect of the acceleration fitting is not significant.

8.4 Summary

Section 8.2 (the first part) introduces the further application of the drop-weight experiment which is applied to the nonlinear VFM combined with the incremental method (VFM 2). In the previous chapters, the drop-weight data were analysed by the linear VFM and the optimization procedure which includes a given constitutive model. The determination of the given model was based on the observation of a quasi-static behaviour of rubbers and the assumption that under medium strain rates the overall shape of stress-strain curves does not significantly changes. However, this assumption could be valid only to the materials tested in the previous chapters. The prior knowledge of a constitutive model from one test at a specific strain rate could not be applicable on the situation with a different strain rate or even temperature. In order to overcome the limitation, a new VFM, in which the PVWs of VFM 2 and the nonlinear VFM are combined, is utilized to approximate the curve shape. The same drop-weight experiment and pre-stretching procedures were conducted on nitrile rubbers. The combined VFM was applied to each pre-stretching data to identify the shape of a local stress-strain curve. The one-term Ogden model was adopted in this VFM with the assumption that this model is sufficient to describe the nonlinearity under the deformation range produced by the drop-weight experiment. The local stress-strain curves were reconstructed by each identified parameters. Each local curve was shifted with respect to the fixed stress-strain curve (non-pre-stretched case) in order to complete the whole stress-strain curve.

The stress-strain curve resulting from this procedure provides an opportunity to evaluate the possible choice of a constitutive model to be used in the optimization procedure of VFM 2. The shifted stress-strain curve made by the present drop-weight experiment should not be considered as the behaviour at a particular strain rate because of complex strain-rate states of the present drop-weight experiment, in which multiple loading and short periods of unloading coexist. For this reason, the shifted curve was used for the model evaluation, and the stress-strain behaviour for a definitive strain rate was obtained by applying VFM 2 on the first initial loading period and with a proper choice of a material model in the optimization procedure. However, it does not mean that the present VFM has to be used for the model evaluation. If the drop-weight apparatus is modified so that a similar deformation range can be produced but without oscillations, the shifted curve can be considered as the behaviour characterized at a particular strain rate.

Section 8.3 introduces the application of the nonlinear VFM for the identification of a viscoelastic behaviour of rubbers. The identification aim was to characterize a local relaxation behaviour of rubbers during the initial deformation range produced by the drop-weight experiment. The time scale of the local relaxation was defined by the imaging speed and the period of each multiple loading period. The one-term Ogden model was adopted in the PVW of the nonlinear VFM and modified to include the viscoelastic model described by the Prony series. The present nonlinear VFM was validated by the simulation work with the relaxation behaviours obtained from the same nitrile and silicone rubbers. In order to extend the period of the identified relaxation curve, the time-temperature superposition principle was utilized. The same drop-weight experiments were conducted but several different temperatures were applied on the specimens. The local relaxation curves identified at each temperature were shifted with respect to the

reference one measured at room temperature. The extended relaxation curve as a result of the shifting are well matched with the part of the relaxation behaviour measured from the DMA test for both of the nitrile and silicone rubber cases.

The lower limit of the time scale can be further extended if a higher imaging speed is adopted. However, the extension of the lower limit needs a careful consideration because increasing the imaging speed gives a higher amplitude of spatial noise as shown in Figure 5.3. For example, if 250 000 fps is adopted, the lower limit increases to -5.4 from -4.7 in terms of the logarithmic scale but the noise amplitude on the axial displacement becomes about 20 times higher. Instead, the application of lower temperatures could be effective. At the moment, the present temperature device is only able to cool down to 9 °C. It is expected that if a lower temperature can be applied, the identified relaxation curve can be further extended. For the extension of the lower limit of the time scale, a higher temperature range can be also applied.

Chapter 9 CONCLUSIONS

Contributions and findings of the proposed experimental techniques and analysis methods are summarised at the end of the respective chapters. All of these summaries are presented here again in Section 9.1 in a condensed form.

The dynamic VFMs proposed in this thesis show possible ways to overcome the experimental difficulties of dynamic tests on soft materials. However, opportunities for further research still remain in terms of new materials, modifications of experimental apparatus and more advanced formulations of the dynamic VFM. A list of suggested future studies is presented in Section 9.2.

9.1 Summaries

9.1.1 Chapter 3-5: Linear VFM (VFM 1)

The dynamic VFM is proposed as a solution to the experimental limitations of current dynamic tests (e.g. Hopkinson bar test) on rubbers. Two representative difficulties are described: (1) long period of non-equilibrium state and (2) large noise-to-signal ratio of a force measurement; these experimental difficulties are severe when rubbers are tested in tension. The use of the dynamic VFM can remove both of these difficulties because a real force measurement is no longer required. Instead, the measurement of acceleration field is used as a virtual force measurement. Chapter 3 explains the analysis method of the dynamic VFM by assuming a mathematical tension-type geometry with a soft elastic material. This geometry is subject to a dynamic tensile loading and the data (strain and acceleration fields) at a particular time step are calculated. These data are applied to the principle of virtual work equation (PVW) specially expressed for dynamic loading using the two virtual fields introduced in previous research. It is found that the assumed material properties, Young's modulus and Poisson's ratio, are inversely obtained by the present dynamic VFM.

In Chapter 4, the description of the dynamic VFM was applied to the FEM data, the configuration of which was given by the actual drop-weight experiment. The first simulation was conducted with a linear elastic material. The data field, calculated by the displacement field, was applied to the same dynamic VFM as explained in the previous chapter; the given material properties were precisely obtained. The importance of a proper choice of the conjugate coordinate system was studied by comparing the identification results between the initial and current coordinate; the former one shows a significant underestimation from the given Young's modulus. The same simulation was extended to a 3D case. Several experimental factors were studied in order to see the effect of a specimen thickness and data area reductions. The same 2D simulation was explored further to show the effect of white Gaussian noise on the identification. The pure displacement data were polluted by artificial Gaussian noise, and the resulting quality of the identification was presented. The simulation work was extended to reflect rubber-like behaviour. The one-term Ogden hyperelastic model was adopted for the same 2D simulation. Here, the pre-stretching procedure was introduced, in which the material is statically pre-stretched up to a certain strain and applied to dynamic loading. The dynamic VFM is modified to consider the static stress due to the pre-stretching. Several pre-stretches were applied to the hyperelastic simulation, and each data field was analysed by the dynamic VFM in order to identify the Young's modulus and Poisson's ratio at each static strain level. Young's moduli were used in the optimization procedure in which the assumption is made in that the identified Young's moduli are tangent slopes of a true stress-strain of a given constitutive model. The one-term model was chosen in this optimization procedure with the assumption that the overall stress-strain behaviour is known from a quasi-static test. The identified Ogden parameters were well matched with the values given to the simulations.

The next chapter presents the same VFM procedure applied to the actual drop-weight experiment. For a test material, silicone rubber was chosen. Quasi-static tests were conducted to observe the stress-strain curve at low strain rates. It was found that the one-term Ogden model is sufficient to describe the quasi-static curves. The experimental procedure of the drop-weight experiment is described, including the configurations of the high-speed imaging. The imaging speed was chosen based on the noise amplitude of axial displacement fields obtained from the static images. The DIC parameter, subset size, was determined by the VFM analysis on one of the drop-weight tests. The chosen subset size was the one able to produce a Poisson's ratio close to the incompressibility and a low noise amplitude of the axial strain fields. The identified Young's moduli from each pre-stretching experiment were identically used in the optimization procedure. Using the identified parameters, the one-term stress-strain curves were reconstructed. The comparison between the quasi-static and dynamic curves clearly shows the rate dependency of silicone rubbers. For a further comparison study, the same material was characterized by the DMA test; it is found that the increment ratio between the initial Young's moduli of the quasi-static and dynamic tests is comparable to that obtained from the relaxation curve of the DMA.

9.1.2 Chapter 6: Nonlinear VFM

A different way of applying the dynamic VFM is proposed in Chapter 6. Instead of using the drop-weight apparatus, a gas-gun experiment was utilized, by which one end of a rubber specimen was dynamically loaded in tension by a movement of an aluminium block impacted by a high-speed projectile. Longer and faster deformations were generated, and these data were applied to the nonlinear VFM. In this VFM, nonlinear constitutive models can be directly adopted, and its calculation of the PVW is conducted by the optimization with respect to all deformation history in contrast to the linear VFM

in which material parameters are linearly calculated at each time step. A similar FEM simulation was conducted to show the procedure of the nonlinear VFM application. The simulation configuration was given by the actual gas-gun experiment. The one-term Ogden model was assumed to describe the simulation material; it is found that the use of the nonlinear VFM with the same model is able to precisely identify the material parameters of this nonlinear model. Further simulations were conducted in order to show the effects of a specimen thickness, data area reduction and spatial noise on the parameter identifications. EPDM rubbers were adopted to describe the actual application of the gas-gun and nonlinear VFM. The same procedure of the DIC parameter choice was conducted by considering the noise amplitude and Poisson's ratio. Four EPDM specimens were tested at different impact speeds. The analysis of the test data was processed by the same nonlinear VFM and one-term Ogden model. The identified parameters were used to reconstruct the four stress-strain curves. Different dynamic behaviours are clearly observed even between these gas-gun tests and also compared to the quasi-static curve.

9.1.3 Chapter 7: Incremental VFM (VFM 2)

When the pre-stretching procedure is applied, the linear VFM, referred to as VFM 1, in Chapter 5 requires the measurement of a static force which is used in the calculation of PVW. Chapter 7 proposed another way of applying the linear VFM, in which the incremental equation of motion was used to derive the new PVW. This new PVW is able to identify instantaneous nominal moduli, which is the tangent slope of a nominal stress-strain curve, without consideration of static forces due to pre-stretching. This new analysis method is referred to as VFM 2. The same simulation works were conducted and analysed by VFM 1 and 2; their identification results were almost identical when the pure data field were applied. Further simulations were presented in that expected experimental error sources were introduced: static force and strain measurements. It is found that the

identification of the VFM 1 procedure is more sensitive than VFM 2 as it is involved with the two sets of static data but for VFM 2 only static strain data are included. The same VFM 1 and 2 procedures were applied on the same experimental data used in Chapter 5 and Chapter 6. It is observed that the stress-strain curve identified from VFM 1 seems slightly softer than that of VFM 2. The underestimation of the static force measurement due to stress relaxation could be one reason as the simulation work showed a similar result. When the identified true stress-strain curves are converted to nominal values, the silicone and EPDM rubbers show distinctive curve shapes: convex and concave-upward shapes. It can be concluded that the present VFMs are able to identify the mechanical behaviour of the two different rubbers. The effect of the relaxation times after pre-stretching was investigated. Three different relaxation times (3, 15, 30 min) were given to the silicone and EPDM rubbers after stretching. Then, their identification results obtained from VFM 2 are shown and indicate that the relaxation time is not significant. At the end of this chapter, the SHPB test data of the same silicone rubber is presented to be compared with the compressive curve made by the parameters obtained from the linear (VFM 2) and nonlinear VFM results. The comparison shows that the results are reasonably comparable but the SHPB results seem stiffer than those from the VFM. The possible reason for this observation could be lateral friction in the compressive tests. The effect of friction is shown using a simple finite element model updating technique.

9.1.4 Chapter 8: Further applications of the VFM

In the first part of this chapter, it is attempted to give a solution to the possible question of whether the assumption of a constitutive model, based on the observation of a quasi-static behaviour, used in the optimization procedure of the linear VFM is valid. It is assumed that the overall curve shape of the silicone and EPDM rubbers are almost similar between quasi-static and medium strain rates. This assumption was based on the

observation in several previous research works. In the present work, a nitrile rubber was adopted; its quasi-static curve was well described by the two-term Ogden model, not by the one-term one. The same pre-stretching simulations were conducted with the two-term model. The simulation data was analysed by the new VFM procedure. This new VFM is based on VFM 2 and the nonlinear VFM. The non-pre-stretching data was analysed by the nonlinear VFM using the one-term model with the assumption that this model is sufficient to describe the nonlinearity of the deformation range produced by the drop-weight experiment. The data with the pre-stretching was applied to the combined VFM (VFM 2 and the nonlinear VFM) with the same assumption. The identified one-term Ogden parameters were used to reconstruct the local nonlinear stress-strain curves. Each curve was shifted with respect to the fixed initial curve (non-pre-stretching case). Using this shifting procedure, the given two-term Ogden curve is well predicted without the use of this model. It is pointed out that this new VFM procedure is not to identify the behaviour at a particular strain rate due to complex strain rate states but should be used for the determination of a constitutive model used in the optimization procedure of VFM 2. The present procedure was used on the drop-weight test on the nitrile rubber. The two-term Ogden style curve shape was estimated using the shifting procedure. For comparison, the same technique was applied to the data produced at cold (10 °C) and hot (62 °C) temperatures. Their different nonlinearities are well approximated. The shifted curves were evaluated for the choice of the material model. The shifted curves of the room and hot temperatures are well described by the two-term model, and no significant difference is found for the cold temperature. The VFM 2 analysis shows similar results in that the stress-strain curves made by the optimization procedure using the one- and two-term models are clearly different for the room and hot temperature cases, and for the cold temperature the two curves are almost similar.

The second part describes the application of the nonlinear VFM for the viscoelastic behaviour of rubbers. The PVW of the present nonlinear VFM is used with the one-term Ogden model which is combined with the viscoelastic model using the Prony series. The aim of this VFM is to identify the local relaxation curve at around the initial deformation range. The time scale for the local relaxation curve is defined by the imaging speed and the period of an incident loading duration. The same drop-weight simulation was conducted but without the pre-stretching procedure. The material model was given by the one-term Ogden model and the relaxation behaviour of the nitrile and silicone rubbers obtained by the DMA test. The local relaxation curve was reconstructed by the material parameters and well matched with the part of the given relaxation behaviour. In order to extend the length of the local relaxation curve, the time-temperature superposition principle was applied to the several local relaxation curves identified at different temperatures. The automated shifting procedure is introduced by which the local relaxation curves are horizontally shifted with respect to the fixed curve obtained at the reference temperature. The extended curves show a good match with the given relaxation curves of both of the silicone and nitrile rubbers. The same VFM technique was used on the drop-weight experiments of the two rubbers. The temperature-controlling device was adopted to cool and heat the drop-weight specimens. The same drop-weight experiment was performed, and their full-field data obtained at each temperature were identified by the present nonlinear VFM in order to characterize the material parameters. These parameters were identically used for the reconstruction of the local relaxation curves and the shifting procedure. It is found that the part of the raw relaxation data obtained from the DMA is well described by the extended relaxation curve obtained from the present nonlinear VFM and shifting procedures.

9.2 Future work

9.2.1 Strain calculation

When the actual experiment data is applied to the VFM, the strain field was directly obtained from the DIC software, the calculation method of which is given by Eq. (5.7). According to the simulation works, the current noise level generated from the experiments does not have a significant influence on the parameter identifications. However, especially in the case of the nonlinear VFM, the strain noise level can be further amplified if the image resolution becomes low as a result of a longer imaging distance in order to capture a larger deformation of rubbers. Some of the gas-gun experiments were not fractured at their final strain; instead, the specimen moved outside of the field of view. Some rubbers could exhibit deformations much larger than those presented in this thesis. The use of the nonlinear VFM for this case can be significantly affected by the strain noise level. With regard to this issue, new strain calculation methods can be used. For example, it would be interesting to apply the two strain calculation methods introduced by Avril et al (2010), in which the displacement fields are shaped by FEM style meshes or polynomial functions, and the shaped fields are used for the numerical differentiation.

The DIC procedure including the error assessment of strain and displacement and the determination of subset size was conducted on a given speckle pattern. That is, the ideal DIC parameters were chosen with respect to a given pattern, but the quality of pattern in terms of image correlation has not been assessed. In particular, the size of a speckle was not rigorously considered in the present research. For example, some of the speckles shown in Figure 5.4 are too small (less than 3 pixels). It is known that a small speckle size can increase the systematic error of DIC induced from intensity interpolation, which is required to resample the intensity level of a subset at a non-integer pixel location (Lecompte et al., 2007). Resampling of a small speckle induces a large aliasing effect so

that the distinctive pattern can be blurred. An optimal pattern size should be chosen with the consideration of an interpolation error; if it is difficult to control the size of pattern, a different interpolation function from a bilinear function, which was adopted in the present research, can be applied.

9.2.2 Experiment apparatus

One advantage of the drop-weight experiment is that the imaging resolution can be relatively high because of the small deformation amplitude. However, the pre-stretching procedure can be laborious and might induce some inelastic effects such as Mullin's effect. In addition, the achievement of high strain rates is difficult with the current drop-weight system. In contrast, the gas-gun experiment is able to apply very high-speed deformation for a long period. For this reason, the gas-gun data was used in the nonlinear VFM without the pre-stretching method. However, as explained, the image resolution is lower than the drop-weight experiment. Moreover, the gas-gun experiment requires the manufacture of a projectile and aluminium block for every test so it is not suitable when multiple tests are required. It is planned to develop a new experimental apparatus that can combine the advantages of the drop-weight and gas-gun experiments. A split Hopkinson tension bar style system will be designed to satisfy requirements that medium to high strain rates are possible; the pre-stretching procedure is available; and constant strain rates are generated until a target displacement. If the last requirement is achieved, the technique of the curve shape approximation introduced in Section 8.2 can be used for the actual identification of the stress-strain curve at a constant strain rate. The new experiment system will be also equipped with a high-frequency force sensor. This force sensor will be used for the nonlinear VFM, the PVW of which is modified to include the traction force term as well as the inertial one. It is expected that if the traction force term is included, the

identification could be still reliable even when the acceleration field is not clear due to wave attenuation as explained in Chapter 6.

9.2.3 Other strain state

It is usual that the mechanical characterization of rubbers is performed in several loading states such as uniaxial, pure shear and biaxial strain states. Two previous VFM works on quasi-static experiments on rubbers were performed in order to produce different loading states such as uniaxial, pure shear and biaxial states or simultaneous mixture of these (Palmieri et al., 2011; Promma et al., 2009). The simultaneous use of various strain states allows the VFM to obtain the parameters which can describe all of these loading states The present drop-weight apparatus would be able to perform the pure shear experiment using a very wide specimen. A preliminary simulation work showed that when a wide specimen is dynamically loaded, the strain state is not purely shear but is a mixture of shear and uniaxial states. Also, this work found that the use of the linear elastic model in the PVW is not sufficient to describe this heterogeneous state. For this case, the neo-Hookean model can be an alternative choice as this model has one material parameter so the linear calculation is still possible. In addition, when such a wide specimen is used, it is worthwhile to see the effect of the number of independent virtual fields applied on the PVW of VFM 2 and the nonlinear VFM, in which only one virtual field was used on the axial stress term.

9.2.4 Anisotropic behaviour

In the present thesis, it is assumed that the stress-strain relationship of rubbers is isotropic and described by isotropic hyperelastic models. However, an initially isotropic rubber can be anisotropic due to the loading history or the addition of a reinforcement filler. It is expected that the present experiment technique is very suitable for the characterization of the dynamic anisotropic behaviour of rubbers because a relatively

larger size specimen can be tested in which anisotropic mechanical features are clearly exhibited. A preliminary simulation was conducted using one of the anisotropic hyperelastic models (Gasser et al., 2006) available in ABAQUS. The simulation data was analysed by the linear VFM with the in-plane orthotropic linear elastic model. The analysis result showed that the anisotropic behaviour at an initial strain range was well characterized. It is interesting to apply the pre-stretching procedure to obtain an anisotropic behaviour for a large deformation range. As mentioned in the above section, the number of independent virtual fields could affect the identification quality for anisotropic behaviour.

9.2.5 Rate-dependent model

Rubbers used in an actual engineering application would experience various loading rates. Thus, in order to conduct a FEM simulation on some engineering component made by rubbers, which is subjected to dynamic loadings, the material model should be capable of describing a stress-strain relationship for various strain rates. The simple visco-hyperelastic model adopted in Section 8.3 may not be able to accommodate high-rate behaviour for a large deformation due to the assumption of the strain-independent relaxation behaviour, i.e. linear viscoelasticity (Mott et al., 2011). Several rate-dependent hyperelastic models have been developed for high-strain rate behaviour and finite deformation (Hoo Fatt and Ouyang, 2007; Khajehsaeid et al., 2014; Petiteau et al., 2012; Pouriayevali et al., 2012; Quintavalla and Johnson, 2004; Shim and Mohr, 2011; Yang et al., 2000). The identification results at several strain rates obtained from the present VFM technique can be fitted by these rate-dependent models. Instead of this indirect way, it is interesting to directly adopt these models in the present dynamic VFM. As mentioned in Section 8.3, strain rate variations exist during a dynamic loading period. These variations could be directly used for the parameter identification of the high-rate dependent models.

One of these models suggested a strain-dependent relaxation function (nonlinear viscous response); the application of the nonlinear VFM in Section 8.3 at different pre strain levels can provide useful experimental data for this nonlinear function.

9.2.6 Optimized piecewise virtual fields

The optimized piecewise virtual fields (PVF) were applied only on the linear VFM (VFM 1) presented in Chapter 3-5. It is interesting to apply the PVF to the incremental VFM (VFM 2) and the nonlinear VFM. The application of the PVF on VFM2 will be a simple modification of the PVF procedure in Section 3.3.2 in order to make the denominator of Eq. (7.13) to be one. For the current nonlinear VFM, the PVF that has been developed for elasto-plastic material (Pierron et al., 2010) can be considered.

9.2.7 Unloading

From some of the gas-gun experiments, it was possible to capture a clear unloading behaviour when only the moving end was clearly fractured. The unloading data also showed a similar wave propagation starting from the unloaded end. A preliminary nonlinear VFM application on this unloading data produced material parameters from which the reconstructed curve seemed reasonable. A preliminary simulation work was conducted using the model (Mullin's effect) giving a distinctive unloading behaviour; it was found that the application of the nonlinear VFM was able to identify the unloading stress-strain curve. The unloading experiment data from the present gas-gun test was obtained by chance; it is necessary to develop some experimental system that can trigger and produce a stable unloading dynamic deformation.

From some of the gas-gun experiments, it was possible to capture a clear unloading behaviour when only the moving end was clearly fractured. The unloading data also showed a similar wave propagation starting from the unloaded end. A preliminary nonlinear VFM application on this unloading data produced material parameters from

which the reconstructed curve seemed reasonable. A preliminary simulation work was conducted using the model (Mullin's effect) giving a distinctive unloading behaviour; it was found that the application of the nonlinear VFM was able to identify the unloading stress-strain curve. The unloading experiment data from the present gas-gun test was obtained by chance; it is necessary to develop some experimental system that can trigger and produce a stable unloading dynamic deformation.

REFERENCES

ABAQUS, 2011. ABAQUS 6.11 analysis user's manual. Abaqus 6.11 Doc.

Anthony, R.L., Caston, R.H., Guth, E., 1943. Equations of State for Natural and Synthetic Rubber-Like Materials. I Unaccelerated Natural Soft Rubber. Rubber Chem. Technol. doi:10.5254/1.3540117

Arruda, E.M., Boyce, M.C., 1993. A three-dimensional constitutive model for the large stretch behavior of rubber elastic materials. J. Mech. Phys. Solids 41, 389–412. doi:10.1016/0022-5096(93)90013-6

Ashby, M.F., 1989. Overview No. 80: On the engineering properties of materials. Acta Metall. 37, 1273–1293. doi:10.1016/0001-6160(89)90158-2

Aster, R., Borchers, B., Thurber, C., 2013. Parameter estimation and inverse problems, Book.

ASTM International, 2014. ASTM D1566-14 Standard Terminology Relating to Rubber, in: Annual Book of ASTM Standards. doi:10.1520/D1566

Avril, S., Bonnet, M., Bretelle, A.-S., Grédiac, M., Hild, F., Ienny, P., Latourte, F., Lemosse, D., Pagano, S., Pagnacco, E., Pierron, F., 2008. Overview of Identification Methods of Mechanical Parameters Based on Full-field Measurements. Exp. Mech. 48, 381–402. doi:10.1007/s11340-008-9148-y

Avril, S., Feissel, P., Pierron, F., Villon, P., 2010. Comparison of two approaches for differentiating full-field data in solid mechanics. Meas. Sci. Technol. 21, 015703. doi:10.1088/0957-0233/21/1/015703

Avril, S., Grédiac, M., Pierron, F., 2004. Sensitivity of the virtual fields method to noisy data. Comput. Mech. 34, 439–452. doi:10.1007/s00466-004-0589-6

Avril, S., Huntley, J.M., Pierron, F., Steele, D.D., 2008. 3D Heterogeneous Stiffness Reconstruction Using MRI and the Virtual Fields Method. Exp. Mech. 48, 479–494. doi:10.1007/s11340-008-9128-2

Bacon, C., 1998. An Experimental Method for considering Dispersion and Attenuation in a Viscoelastic Hopkinson Bar. Exp. Mech. 38, 242–249. doi:10.1177/001448519803800402

Bastawros, A., 2000. Experimental analysis of deformation mechanisms in a closed-cell aluminum alloy foam. J. Mech. Phys. Solids 48, 301–322. doi:10.1016/S0022-5096(99)00035-6

Bechir, H., Chevalier, L., Chaouche, M., Boufala, K., 2006. Hyperelastic constitutive model for rubber-like materials based on the first Seth strain measures invariant. Eur. J. Mech. - A/Solids 25, 110–124. doi:10.1016/j.euromechsol.2005.03.005

Bergström, J.S., Boyce, M.C., 1998. Constitutive modeling of the large strain time-dependent behavior of elastomers. J. Mech. Phys. Solids 46, 931–954. doi:http://dx.doi.org/10.1016/S0022-5096(97)00075-6

Bertholf, L.D., Karnes, C.H., 1975. Two-dimensional analysis of the split Hopkinson pressure bar system. J. Mech. Phys. Solids 23, 1–19. doi:10.1016/0022-5096(75)90008-3

Blatz, P.J., Ko, W.L., 1962. Application of Finite Elastic Theory to the Deformation of Rubbery Materials. J. Rheol. (N. Y. N. Y). 6, 223. doi:10.1122/1.548937

Boyce, M.C., Arruda, E.M., 2000. Constitutive Models of Rubber Elasticity: A Review. Rubber Chem. Technol. 73, 504–523. doi:10.5254/1.3547602

Bradley, G.L., Chang, P.C., Mckenna, G.B., 2001. Rubber modeling using uniaxial test data. J. Appl. Polym. Sci. 81, 837–848. doi:10.1002/app.1503

Briscoe, B.J., Nosker, R.W., 1984. The influence of interfacial friction on the deformation of high density polyethylene in a split Hopkinson pressure bar. Wear 95, 241–262. doi:10.1016/0043-1648(84)90140-6

Brown, R., 2006. Physical Testing of Rubber. Springer Science & Business Media.

Casem, D., Weerasooriya, T., Moy, P., 2005. Inertial effects of quartz force transducers embedded in a split Hopkinson pressure bar. Exp. Mech. 45, 368–376. doi:10.1007/BF02428167

Chalal, H., Avril, S., Pierron, F., Meraghni, F., 2006. Experimental identification of a nonlinear model for composites using the grid technique coupled to the virtual fields method. Compos. Part A Appl. Sci. Manuf. 37, 315–325. doi:10.1016/j.compositesa.2005.04.020

Chen, D.J., Chiang, F.P., Tan, Y.S., Don, H.S., 1993. Digital speckle-displacement measurement using a complex spectrum method. Appl. Opt. 32, 1839–1849. doi:10.1364/AO.32.001839
Chen, W., Lu, F., Zhou, B., 2000. A quartz-crystal-embedded split Hopkinson pressure bar for soft materials. Exp. Mech. 40, 1–6. doi:10.1007/BF02327540
Chen, W., Song, B., 2011. Split Hopkinson (Kolsky) Bar, Mechanical Engineering Series. Springer US, Boston, MA. doi:10.1007/978-1-4419-7982-7
Chen, W., Zhang, B., Forrestal, M.J., 1999. A split Hopkinson bar technique for low-impedance materials. Exp. Mech. doi:10.1007/BF02331109
Cheng, M., Chen, W., 2003. Experimental investigation of the stress-stretch behavior of EPDM rubber with loading rate effects. Int. J. Solids Struct. 40, 4749–4768. doi:10.1016/S0020-7683(03)00182-3
Chevalier, L., Calloch, S., Hild, F., Marco, Y., 2001. Digital image correlation used to analyze the multiaxial behavior of rubber-like materials. Eur. J. Mech. - A/Solids 20, 169–187. doi:10.1016/S0997-7538(00)01135-9
Connesson, N., Clayton, E.H., Bayly, P. V, Pierron, F., 2015. Extension of the optimised virtual fields method to estimate viscoelastic material parameters from 3D dynamic displacement fields. Strain 51, 110–134. doi:10.1111/str.12126
Daly, S., Rittel, D., Bhattacharya, K., Ravichandran, G., 2008. Large Deformation of Nitinol Under Shear Dominant Loading. Exp. Mech. 49, 225–233. doi:10.1007/s11340-008-9178-5
Davidson, J.S., Fisher, J.W., Hammons, M.I., Porter, J.R., Dinan, R.J., 2005. Failure Mechanisms of Polymer-Reinforced Concrete Masonry Walls Subjected to Blast. J. Struct. Eng. 131, 1194–1205. doi:10.1061/(ASCE)0733-9445(2005)131:8(1194)
Day, J.R., Miller, K.A., 2000. Equibiaxial stretching of elastomeric sheets, an analytical verification of experimental technique, in: ABAQUS 2000 User's Conference Proceedings. Newport, Rhode Island. May 30-June.
Delpueyo, D., Grédiac, M., Balandraud, X., Badulescu, C., 2012. Investigation of martensitic microstructures in a monocrystalline Cu-Al-Be shape memory alloy with the grid method and infrared thermography. Mech. Mater. 45, 34–51. doi:10.1016/j.mechmat.2011.09.007
Diani, J., Fayolle, B., Gilormini, P., 2009. A review on the Mullins effect. Eur. Polym. J. 45, 601–612. doi:10.1016/j.eurpolymj.2008.11.017
Erickson, D., Sinton, D., Li, D., 2003. Joule heating and heat transfer in poly(dimethylsiloxane) microfluidic systems. Lab Chip 3, 141–149. doi:10.1039/b306158b
Ferry, J.D., 1961. Viscoelastic properties of polymers. Wiley.
Field, J.E., Walley, S.M., Proud, W.G., Goldrein, H.T., Siviour, C.R., 2004. Review of experimental techniques for high rate deformation and shock studies, International Journal of Impact Engineering. doi:10.1016/j.ijimpeng.2004.03.005
Forsberg, F., Siviour, C.R., 2009. 3D deformation and strain analysis in compacted sugar using x-ray microtomography and digital volume correlation. Meas. Sci. Technol. 20, 095703. doi:10.1088/0957-0233/20/9/095703
Gasser, T.C., Ogden, R.W., Holzapfel, G. a., 2006. Hyperelastic modelling of arterial layers with distributed collagen fibre orientations. J. R. Soc. Interface 3, 15–35. doi:10.1098/rsif.2005.0073
Gendy, a. S., Saleeb, a. F., 2000. Nonlinear material parameter estimation for characterizing hyper elastic large strain models. Comput. Mech. 25, 66–77. doi:10.1007/s004660050016
Genovese, K., Lamberti, L., Pappalettere, C., 2006. Mechanical characterization of hyperelastic materials with fringe projection and optimization techniques. Opt. Lasers Eng. 44, 423–442. doi:10.1016/j.optlaseng.2005.06.003
Ghosh, R., Gupta, S., Dickinson, A., Browne, M., 2012. Experimental validation of finite element models of intact and implanted composite hemipelvises using digital image correlation. J. Biomech. Eng. 134, 081003. doi:10.1115/1.4007173
Godara, A., Raabe, D., 2007. Influence of fiber orientation on global mechanical behavior and mesoscale strain localization in a short glass-fiber-reinforced epoxy polymer composite during tensile deformation investigated using digital image correlation. Compos. Sci. Technol. 67, 2417–2427. doi:10.1016/j.compscitech.2007.01.005

Goldrein, H.., Palmer, S.J.., Huntley, J.., 1995. Automated fine grid technique for measurement of large-strain deformation maps. Opt. Lasers Eng. 23, 305–318. doi:10.1016/0143-8166(95)00036-N

Grédiac, M., Pierron, F., 2006. Applying the Virtual Fields Method to the identification of elasto-plastic constitutive parameters. Int. J. Plast. 22, 602–627. doi:http://dx.doi.org/10.1016/j.ijplas.2005.04.007

Grédiac, M., Pierron, F., Vautrin, A., 1994. The Iosipescu in-plane shear test applied to composites: A new approach based on displacement field processing. Compos. Sci. Technol. 51, 409–417. doi:10.1016/0266-3538(94)90109-0

Grédiac, M., Toussaint, E., Pierron, F., 2002a. Special virtual fields for the direct determination of material parameters with the virtual fields method. 1—Principle and definition. Int. J. Solids Struct. 39, 2691–2705. doi:http://dx.doi.org/10.1016/S0020-7683(02)00127-0

Grédiac, M., Toussaint, E., Pierron, F., 2002b. Special virtual fields for the direct determination of material parameters with the virtual fields method. 2 - Application to in-plane properties. Int. J. Solids Struct. 39, 2707–2730. doi:10.1016/S0020-7683(02)00128-2

Greenwood, J.A., Tabor, D., 1958. The Friction of Hard Sliders on Lubricated Rubber: The Importance of Deformation Losses. Proc. Phys. Soc. 71, 989–1001. doi:10.1088/0370-1328/71/6/312

Haddadi, H., Belhabib, S., 2008. Use of rigid-body motion for the investigation and estimation of the measurement errors related to digital image correlation technique. Opt. Lasers Eng. 46, 185–196. doi:10.1016/j.optlaseng.2007.05.008

Han, B., Post, D., Ifju, P., 2005. Moiré interferometry for engineering mechanics: current practices and future developments. J. Strain Anal. Eng. Des. doi:10.1243/0309324011512568

Harrigan, J.J., Ahonsi, B., Palamidi, E., Reid, S.R., 2014. Experimental and numerical investigations on the use of polymer Hopkinson pressure bars. Philos. Trans. A. Math. Phys. Eng. Sci. 372, 20130201. doi:10.1098/rsta.2013.0201

Holt, W.L., 1931. Behaviour of Rubber under Repeated Stresses 1,2. Ind. Eng. Chem. 23, 1471–1475. doi:10.1021/ie50264a043

Holzapfel, G., 2000. Nonlinear solid mechanics: A continuum approach for engineering. Wiley.

Holzapfel, G.A., 1996. On large strain viscoelasticity: continuum formulation and finite element applications to elastomeric structures. Int. J. Numer. Methods Eng. 39, 3903–3926. doi:10.1002/(SICI)1097-0207(19961130)39:22<3903::AID-NME34>3.0.CO;2-C

Hoo Fatt, M.S., Ouyang, X., 2007. Integral-based constitutive equation for rubber at high strain rates. Int. J. Solids Struct. 44, 6491–6506. doi:10.1016/j.ijsolstr.2007.02.038

Ienny, P., Caro-Bretelle, A.-S., Pagnacco, E., 2012. Identification from measurements of mechanical fields by finite element model updating strategies. Eur. J. Comput. Mech. Eur. Mécanique Numérique.

Isihara, A., Hashitsume, N., Tatibana, M., 1951. Statistical Theory of Rubber-Like Elasticity. IV. (Two-Dimensional Stretching). J. Chem. Phys. 19, 1508. doi:10.1063/1.1748111

ISO, 2003. ISO. Plastics—determination of tensile properties at high strain rates. A draft of ISO/CD 18872.

Jerabek, M., Major, Z., Lang, R.W., 2010. Strain determination of polymeric materials using digital image correlation. Polym. Test. 29, 407–416. doi:10.1016/j.polymertesting.2010.01.005

Jiang, T.Z., Xue, P., Butt, H.S.U., 2015. Pulse shaper design for dynamic testing of viscoelastic materials using polymeric SHPB. Int. J. Impact Eng. 79, 45–52. doi:10.1016/j.ijimpeng.2014.08.016

Johnson, W., 1983. Impact strength of materials. Edward Arnold, London.

Kabanikhin, S.I., 2008. Definitions and examples of inverse and ill-posed problems. J. Inverse Ill-Posed Probl. 16, 317–357. doi:10.1515/JIIP.2008.019

Kajberg, J., Lindkvist, G., 2004. Characterisation of materials subjected to large strains by inverse modelling based on in-plane displacement fields. Int. J. Solids Struct. 41, 3439–3459. doi:10.1016/j.ijsolstr.2004.02.021

Kajberg, J., Wikman, B., 2007. Viscoplastic parameter estimation by high strain-rate experiments

and inverse modelling – Speckle measurements and high-speed photography. Int. J. Solids Struct. 44, 145–164. doi:10.1016/j.ijsolstr.2006.04.018
Kaliske, M., Rothert, H., 1997. Formulation and implementation of three-dimensional viscoelasticity at small and finite strains. Comput. Mech. 19, 228–239. doi:10.1007/s004660050171
Kang, J., Wilkinson, D.S., Jain, M., Embury, J.D., Beaudoin, A.J., Kim, S., Mishira, R., Sachdev, A.K., 2006. On the sequence of inhomogeneous deformation processes occurring during tensile deformation of strip cast AA5754. Acta Mater. 54, 209–218. doi:10.1016/j.actamat.2005.08.045
Kanyanta, V., Ivankovic, A., 2010. Mechanical characterisation of polyurethane elastomer for biomedical applications. J. Mech. Behav. Biomed. Mater. 3, 51–62. doi:http://dx.doi.org/10.1016/j.jmbbm.2009.03.005
Kar, K.K., Bhowmick, A.K., 1997. High-strain hysteresis of rubber vulcanizates over a range of compositions, rates, and temperatures. J. Appl. Polym. Sci. 65, 1429–1439. doi:10.1002/(SICI)1097-4628(19970815)65:7<1429::AID-APP21>3.0.CO;2-O
Kavanagh, K., Clough, R., 1971. Finite element applications in the characterization of elastic solids. Int. J. Solids Struct. 7, 11–23.
Kendall, M.J., Drodge, D.R., Froud, R.F., Siviour, C.R., 2014. Stress gage system for measuring very soft materials under high rates of deformation. Meas. Sci. Technol. 25, 075603. doi:10.1088/0957-0233/25/7/075603
Khajehsaeid, H., Arghavani, J., Naghdabadi, R., Sohrabpour, S., 2014. A visco-hyperelastic constitutive model for rubber-like materials: A rate-dependent relaxation time scheme. Int. J. Eng. Sci. 79, 44–58. doi:10.1016/j.ijengsci.2014.03.001
Kim, B., Lee, S.B., Lee, J., Cho, S., Park, H., Yeom, S., Park, S.H., 2012. A comparison among Neo-Hookean model, Mooney-Rivlin model, and Ogden model for chloroprene rubber. Int. J. Precis. Eng. Manuf. 13, 759–764. doi:10.1007/s12541-012-0099-y
Kim, J.H., Lee, G.A., Lee, M.G., 2015. Determination of dynamic strain hardening parameters using the virtual fields method. Int. J. Automot. Technol. 16, 145–151. doi:10.1007/s12239-015-0016-3
Kim, J.-H., Serpantié, A., Barlat, F., Pierron, F., Lee, M.-G., 2013. Characterization of the post-necking strain hardening behavior using the virtual fields method. Int. J. Solids Struct. 50, 3829–3842. doi:10.1016/j.ijsolstr.2013.07.018
Kolsky, H., 1949. An Investigation of the Mechanical Properties of Materials at very High Rates of Loading. Proc. Phys. Soc. Sect. B 62, 676–700. doi:10.1088/0370-1301/62/11/302
LaVision, 2007. DaVis 7.2 Software: Product-Manual.
Le Cam, J.B., 2012. A review of the challenges and limitations of full-field measurements applied to large heterogeneous deformations of rubbers. Strain 48, 174–188. doi:10.1111/j.1475-1305.2011.00830.x
Le Magorou, L., Bos, F., Rouger, F., 2002. Identification of constitutive laws for wood-based panels by means of an inverse method. Compos. Sci. Technol. 62, 591–596. doi:10.1016/S0266-3538(01)00149-X
Lecompte, D., Bossuyt, S., Cooreman, S., Sol, H., Vantomme, J., 2007. Study and generation of optimal speckle patterns for DIC. Proc. Annu. Conf. Expo. Exp. Appl. Mech. 1643–9.
Lecompte, D., Smits, A., Bossuyt, S., Sol, H., Vantomme, J., Van Hemelrijck, D., Habraken, A.M., 2006. Quality assessment of speckle patterns for digital image correlation. Opt. Lasers Eng. 44, 1132–1145. doi:10.1016/j.optlaseng.2005.10.004
Leendertz, J.A., 1970. Interferometric displacement measurement on scattering surfaces utilizing speckle effect. J. Phys. E. 3, 214–218. doi:10.1088/0022-3735/3/3/312
Lion, A., 1997. On the large deformation behaviour of reinforced rubber at different temperatures. J. Mech. Phys. Solids. doi:10.1016/S0022-5096(97)00028-8
Louëdec, G. Le, Pierron, F., Sutton, M. a., Reynolds, a. P., 2013. Identification of the Local Elasto-Plastic Behavior of FSW Welds Using the Virtual Fields Method. Exp. Mech. 53, 849–859. doi:10.1007/s11340-012-9679-0
Marckmann, G., Verron, E., 2006. Comparison of Hyperelastic Models for Rubber-Like Materials. Rubber Chem. Technol. 79, 835–858. doi:10.5254/1.3547969

Martins, P. a. L.S., Natal Jorge, R.M., Ferreira, a. J.M., 2006. A Comparative Study of Several Material Models for Prediction of Hyperelastic Properties: Application to Silicone-Rubber and Soft Tissues. Strain 42, 135–147. doi:10.1111/j.1475-1305.2006.00257.x

Meijer, R., Douven, L., Oomens, C., 1999. Characterisation of anisotropic and non-linear behaviour of human skin in vivo. Comput. Methods Biomech. Biomed. Engin. 2, 13–27.

Meuwissen, M., Oomens, C., Baaijens, F.P.., Petterson, R., Janssen, J.., 1998. Determination of the elasto-plastic properties of aluminium using a mixed numerical–experimental method. J. Mater. Process. Technol. 75, 204–211. doi:10.1016/S0924-0136(97)00366-X

Mooney, M., 1940. A Theory of Large Elastic Deformation. J. Appl. Phys. 11, 582–592.

Mott, P.H., Twigg, J.N., Michael Roland, C., Nugent, K.E., Hogan, T.E., Robertson, C.G., 2011. Comparison of the transient stress-strain response of rubber to its linear dynamic behavior. J. Polym. Sci. Part B Polym. Phys. 49, 1195–1202. doi:10.1002/polb.22292

Moulart, R., Pierron, F., Hallett, S., Wisnom, M., 2011. Full-Field Strain Measurement and Identification of Composites Moduli at High Strain Rate with the Virtual Fields Method. Exp. Mech. 51, 509–536. doi:10.1007/s11340-010-9433-4

Mullins, L., 1948. Effect of Stretching on the Properties of Rubber. Rubber Chem. Technol. 21, 281–300. doi:10.5254/1.3546914

Nie, X., Song, B., Ge, Y., Chen, W.W., Weerasooriya, T., 2008. Dynamic Tensile Testing of Soft Materials. Exp. Mech. 49, 451–458. doi:10.1007/s11340-008-9133-5

Niemczura, J., Ravi-Chandar, K., 2011a. On the response of rubbers at high strain rates—I. Simple waves. J. Mech. Phys. Solids 59, 423–441. doi:10.1016/j.jmps.2010.09.006

Niemczura, J., Ravi-Chandar, K., 2011b. On the response of rubbers at high strain rates—II. Shock waves. J. Mech. Phys. Solids 59, 442–456. doi:10.1016/j.jmps.2010.09.007

Niendorf, T., Dadda, J., Canadinc, D., Maier, H.J., Karaman, I., 2009. Monitoring the fatigue-induced damage evolution in ultrafine-grained interstitial-free steel utilizing digital image correlation. Mater. Sci. Eng. A 517, 225–234. doi:10.1016/j.msea.2009.04.053

Notta-Cuvier, D., Langrand, B., Markiewicz, E., Lauro, F., Portemont, G., 2013. Identification of Johnson-Cook's Viscoplastic Model Parameters Using the Virtual Fields Method: Application to Titanium Alloy Ti6Al4V. Strain 49, 22–45. doi:10.1111/str.12010

Ogden, R.W., 2007. Incremental statics and dynamics of pre-stressed elastic materials. Waves nonlinear pre-stressed Mater. doi:10.1007/978-3-211-73572-5

Ogden, R.W., 1984. Non-linear elastic deformations. E. Horwood.

Ogden, R.W., 1972. Large Deformation Isotropic Elasticity - On the Correlation of Theory and Experiment for Incompressible Rubberlike Solids. Proc. R. Soc. London. A. Math. Phys. Sci. 326, 565–584. doi:10.1098/rspa.1972.0026

Ogden, R.W., Saccomandi, G., Sgura, I., 2004. Fitting hyperelastic models to experimental data. Comput. Mech. 34, 484–502. doi:10.1007/s00466-004-0593-y

Pagnacco, E., Moreau, a., Lemosse, D., 2007. Inverse strategies for the identification of elastic and viscoelastic material parameters using full-field measurements. Mater. Sci. Eng. A 452-453, 737–745. doi:10.1016/j.msea.2006.10.122

Palmieri, G., Sasso, M., Chiappini, G., Amodio, D., 2011. Virtual Fields Method on Planar Tension Tests for Hyperelastic Materials Characterisation. Strain 47, 196–209. doi:10.1111/j.1475-1305.2010.00759.x

Pan, B., 2011. Recent Progress in Digital Image Correlation. Exp. Mech. 51, 1223–1235. doi:10.1007/s11340-010-9418-3

Pan, B., Qian, K., Xie, H., Asundi, A., 2009. Two-dimensional digital image correlation for in-plane displacement and strain measurement: a review. Meas. Sci. Technol. 20, 062001. doi:10.1088/0957-0233/20/6/062001

Pannier, Y., Avril, S., Rotinat, R., Pierron, F., 2006. Identification of elasto-plastic constitutive parameters from statically undetermined tests using the virtual fields method. Exp. Mech. 46, 735–755. doi:10.1007/s11340-006-9822-x

Parry, D.J., Dixon, P.R., Hodson, S., Al-Maliky, N., 1994. Stress Equilibrium Effects Within Hopkinson Bar Specimens. J. Phys. IV; Colloq. C8, Suppl. auf J. Phys. III 4, C8_107–C8_112. doi:10.1051/jp4:1994816

Périé, J.N., Leclerc, H., Roux, S., Hild, F., 2009. Digital image correlation and biaxial test on

composite material for anisotropic damage law identification. Int. J. Solids Struct. 46, 2388–2396. doi:10.1016/j.ijsolstr.2009.01.025

Petiteau, J.-C., Verron, E., Othman, R., Sourne, H., Sigrist, J.-F., Barras, G., 2012. Large strain rate-dependent response of elastomers at different strain rates: convolution integral vs. internal variable formulations. Mech. Time-Dependent Mater. 17, 349–367. doi:10.1007/s11043-012-9188-7

Petrović, Z.S., Ferguson, J., 1991. Polyurethane elastomers. Prog. Polym. Sci. 16, 695–836. doi:10.1016/0079-6700(91)90011-9

Pierron, F., Alloba, E., Surrel, Y., Vautrin, A., 1998. whole-field assessment of the effects of boundary conditions on the strain field in off-axis tensile testing of unidirectional composites. Compos. Sci. Technol. doi:10.1016/S0266-3538(98)00027-X

Pierron, F., Avril, S., Tran, V.T., 2010. Extension of the virtual fields method to elasto-plastic material identification with cyclic loads and kinematic hardening. Int. J. Solids Struct. 47, 2993–3010. doi:10.1016/j.ijsolstr.2010.06.022

Pierron, F., Forquin, P., 2012. Ultra-High-Speed Full-Field Deformation Measurements on Concrete Spalling Specimens and Stiffness Identification with the Virtual Fields Method. Strain 48, 388–405. doi:10.1111/j.1475-1305.2012.00835.x

Pierron, F., Grédiac, M., 2012. The virtual fields method : extracting constitutive mechanical parameters from full-field deformation measurements. Springer, New York.

Pierron, F., Sutton, M. a., Tiwari, V., 2011. Ultra High Speed DIC and Virtual Fields Method Analysis of a Three Point Bending Impact Test on an Aluminium Bar. Exp. Mech. 51, 537–563. doi:10.1007/s11340-010-9402-y

Pierron, F., Zhu, H., Siviour, C., 2014. Beyond Hopkinson's bar. Philos. Trans. R. Soc. A Math. Phys. Eng. Sci. 372, 20130195. doi:10.1098/rsta.2013.0195

Porter, J.R., Dinan, R.J., Hammons, M.I., Knox, K.J., 2002. Polymer coatings increase blast resistance of existing and temporary structures. AMPTIAC Q. 6, 47–52.

Post, D., Han, B., Ifju, P., 1994. High Sensitivity Moire: Experimental Analysis for Mechanics and Materials, Mechanical Engineering Series.

Pouriayevali, H., Guo, Y.B., Shim, V.P.W., 2012. A constitutive description of elastomer behaviour at high strain rates – A strain-dependent relaxation time approach. Int. J. Impact Eng. 47, 71–78. doi:10.1016/j.ijimpeng.2012.04.001

Promma, N., Raka, B., Grédiac, M., Toussaint, E., Le Cam, J.B., Balandraud, X., Hild, F., 2009. Application of the virtual fields method to mechanical characterization of elastomeric materials. Int. J. Solids Struct. 46, 698–715. doi:http://dx.doi.org/10.1016/j.ijsolstr.2008.09.025

Pyne, J.D., Genovese, K., Casaletto, L., Vande Geest, J.P., 2014. Sequential-digital image correlation for mapping human posterior sclera and optic nerve head deformation. J. Biomech. Eng. 136, 021002. doi:10.1115/1.4026224

Quintavalla, S.J., Johnson, S.H., 2004. Extension of the Bergström-Boyce Model to High Strain Rates. Rubber Chem. Technol. 77, 972–981. doi:10.5254/1.3547863

R. Jones and C. Wykes, 1989. Holographic and Speckle Interferometry, Cambridge University Press. publisherNameCambridge University Press.

Rajan, V.P., Rossol, M.N., Zok, F.W., 2012. Optimization of Digital Image Correlation for High-Resolution Strain Mapping of Ceramic Composites. Exp. Mech. 52, 1407–1421. doi:10.1007/s11340-012-9617-1

Ramesh, k. t., 2008. High Strain Rate and Impact Experiments, in: Springer Handbook of Experimenatl Solid Mechanics. pp. 929–960.

Rao, S., Shim, V.P.W., Quah, S.E., 1997. Dynamic mechanical properties of polyurethane elastomers using a nonmetallic Hopkinson bar. J. Appl. Polym. Sci. 66, 619–631. doi:10.1002/(SICI)1097-4628(19971024)66:4<619::AID-APP2>3.0.CO;2-V

Rastogi, 2000. Photomechanics, Photomechanics.

Rey, T., Chagnon, G., Le Cam, J.-B., Favier, D., 2013. Influence of the temperature on the mechanical behaviour of filled and unfilled silicone rubbers. Polym. Test. 32, 492–501. doi:10.1016/j.polymertesting.2013.01.008

Rivlin, R.S., 1948. Large Elastic Deformations of Isotropic Materials. IV. Further Developments

of the General Theory. Philos. Trans. R. Soc. A Math. Phys. Eng. Sci. 241, 379–397. doi:10.1098/rsta.1948.0024
Rodgers, B., Waddell, W., 2005. Science and Technology of Rubber, Science and Technology of Rubber. Elsevier. doi:10.1016/B978-012464786-2/50017-1
Roland, C.M., Twigg, J.N., Vu, Y., Mott, P.H., 2007. High strain rate mechanical behavior of polyurea. Polymer (Guildf). 48, 574–578. doi:10.1016/j.polymer.2006.11.051
Russell, B.P., Karthikeyan, K., Deshpande, V.S., Fleck, N. a., 2013. The high strain rate response of Ultra High Molecular-weight Polyethylene: From fibre to laminate. Int. J. Impact Eng. 60, 1–9. doi:10.1016/j.ijimpeng.2013.03.010
Sarva, S.S., Deschanel, S., Boyce, M.C., Chen, W., 2007. Stress–strain behavior of a polyurea and a polyurethane from low to high strain rates. Polymer (Guildf). 48, 2208–2213. doi:10.1016/j.polymer.2007.02.058
Sasso, M., Chiappini, G., Rossi, M., Cortese, L., Mancini, E., 2013. Visco-Hyper-Pseudo-Elastic Characterization of a Fluoro-Silicone Rubber. Exp. Mech. 54, 315–328. doi:10.1007/s11340-013-9807-5
Sasso, M., Palmieri, G., Chiappini, G., Amodio, D., 2008. Characterization of hyperelastic rubber-like materials by biaxial and uniaxial stretching tests based on optical methods. Polym. Test. 27, 995–1004. doi:10.1016/j.polymertesting.2008.09.001
Shams, M., Destrade, M., Ogden, R.W., 2011. Initial stresses in elastic solids: Constitutive laws and acoustoelasticity. Wave Motion 48, 552–567. doi:10.1016/j.wavemoti.2011.04.004
Shergold, O.A., Fleck, N.A., Radford, D., 2006. The uniaxial stress versus strain response of pig skin and silicone rubber at low and high strain rates. Int. J. Impact Eng. 32, 1384–1402. doi:http://dx.doi.org/10.1016/j.ijimpeng.2004.11.010
Shi, X.Q., Pang, H.L.J., Zhang, X.R., Liu, Q.J., Ying, M., 2004. In-Situ Micro-Digital Image Speckle Correlation Technique for Characterization of Materials' Properties and Verification of Numerical Models. IEEE Trans. Components Packag. Technol. 27, 659–667. doi:10.1109/TCAPT.2004.838907
Shim, J., Mohr, D., 2011. Rate dependent finite strain constitutive model of polyurea. Int. J. Plast. 27, 868–886. doi:10.1016/j.ijplas.2010.10.001
Sihn, S., Tsai, S., 1999. Automated shift for time-temperature superposition. 12th Int. Com. Compos. Mater. 51.
Simo, J.C., 1987. On a fully three-dimensional finite-strain viscoelastic damage model: Formulation and computational aspects. Comput. Methods Appl. Mech. Eng. 60, 153–173. doi:10.1016/0045-7825(87)90107-1
Siviour, C.R., 2009. A measurement of wave propagation in the split Hopkinson pressure bar. Meas. Sci. Technol. 20, 065702. doi:10.1088/0957-0233/20/6/065702
Sjödahl, M., Benckert, L.R., 1993. Electronic speckle photography: analysis of an algorithm giving the displacement with subpixel accuracy. Appl. Opt. 32, 2278–84. doi:10.1364/AO.32.002278
Song, B., Chen, W., 2004. Dynamic stress equilibration in split Hopkinson pressure bar tests on soft materials. Exp. Mech. 44, 300–312. doi:10.1007/BF02427897
Song, B., Chen, W., 2003. One-Dimensional Dynamic Compressive Behavior of EPDM Rubber. J. Eng. Mater. Technol. 125, 294. doi:10.1115/1.1584492
Sutton, M., Wolters, W., Peters, W., Ranson, W., McNeill, S., 1983. Determination of displacements using an improved digital correlation method. Image Vis. Comput. doi:10.1016/0262-8856(83)90064-1
Sutton, M.A., Orteu, J.-J., Schreier, H., 2009. Image Correlation for Shape, Motion and Deformation Measurements. Springer US, Boston, MA. doi:10.1007/978-0-387-78747-3
Tang, S., 1967. Wave propagation in initially-stressed elastic solids. Acta Mech.
Timmel, M., Kolling, S., Osterrieder, P., Du Bois, P.A., 2007. A finite element model for impact simulation with laminated glass. Int. J. Impact Eng. 34, 1465–1478. doi:10.1016/j.ijimpeng.2006.07.008
Tobolsky, A. V., 1956. Stress Relaxation Studies of the Viscoelastic Properties of Polymers. J. Appl. Phys. 27, 673. doi:10.1063/1.1722465
Toki, S., Sics, I., Ran, S., Liu, L., Hsiao, B.S., Murakami, S., Senoo, K., Kohjiya, S., 2002. New

Insights into Structural Development in Natural Rubber during Uniaxial Deformation by In Situ Synchrotron X-ray Diffraction. Macromolecules 35, 6578–6584. doi:10.1021/ma0205921

Treloar, L.R.., 1975. The Physics of Rubber Elasticity. Oxford University Press, USA.

Treloar, L.R.G., 1944. Stress-Strain Data for Vulcanized Rubber under Various Types of Deformation. Rubber Chem. Technol. doi:10.5254/1.3546701

Treloar, L.R.G., 1943. The elasticity of a network of long-chain molecules?II. Trans. Faraday Soc. 39, 241. doi:10.1039/tf9433900241

Tung, S.-H., Shih, M.-H., Kuo, J.-C., 2010. Application of digital image correlation for anisotropic plastic deformation during tension testing. Opt. Lasers Eng. 48, 636–641. doi:10.1016/j.optlaseng.2009.09.011

Valanis, K.C., 1967. The Strain-Energy Function of a Hyperelastic Material in Terms of the Extension Ratios. J. Appl. Phys. 38, 2997. doi:10.1063/1.1710039

Wang, L.-R., Lu, Z.-H., 2003. Modeling Method of Constitutive Law of Rubber Hyperelasticity Based on Finite Element Simulations. Rubber Chem. Technol. 76, 271–285. doi:10.5254/1.3547739

Warren, T.L., Forrestal, M.J., 2009. Comments on the Effect of Radial Inertia in the Kolsky Bar Test for an Incompressible Material. Exp. Mech. 50, 1253–1255. doi:10.1007/s11340-009-9322-x

Wattrisse, B., Chrysochoos, A., Muracciole, J.-M., Némoz-Gaillard, M., 2001. Analysis of strain localization during tensile tests by digital image correlation. Exp. Mech. 41, 29–39. doi:10.1007/BF02323101

Williams, M., Landel, R., Ferry, J., 1955. The temperature dependence of relaxation mechanisms in amorphous polymers and other glass-forming liquids. J. Am. Chem. Soc. 679. doi:10.1021/ja01619a008

Yang, L.M., Shim, V.P.W., Lim, C.T., 2000. A visco-hyperelastic approach to modelling the constitutive behaviour of rubber. Int. J. Impact Eng. 24, 545–560. doi:10.1016/S0734-743X(99)00044-5

Yoneyama, S., Kitagawa, A., Iwata, S., Tani, K., Kikuta, H., 2007. Bridge deflection measurement using digital image correlation. Exp. Tech. 31, 34–40. doi:10.1111/j.1747-1567.2006.00132.x

Zhang, D., Eggleton, C.D., Arola, D.D., 2002. Evaluating the mechanical behavior of arterial tissue using digital image correlation. Exp. Mech. 42, 409–416. doi:10.1007/BF02412146

Zhao, J., Knauss, W.G., Ravichandran, G., 2008. Applicability of the time–temperature superposition principle in modeling dynamic response of a polyurea. Mech. Time-Dependent Mater. 11, 289–308. doi:10.1007/s11043-008-9048-7

Zhu, H., 2015. A novel methodology for high strain rate testing using full-field measurements and the virtual fields methods. Troyes.